# A Superradiant Laser and Spin Squeezed States: Collective Phenomena in a Rubidium Cavity QED System for Enhancing Precision Measurements

by

**Justin G. Bohnet**

B.S., University of Northern Iowa, 2008

M.S., University of Colorado at Boulder, 2011

A thesis submitted to the
Faculty of the Graduate School of the
University of Colorado in partial fulfillment
of the requirements for the degree of
Doctor of Philosophy
Department of Physics
2014

This thesis entitled:
A Superradiant Laser and Spin Squeezed States: Collective Phenomena in a Rubidium Cavity QED System for Enhancing Precision Measurements
written by Justin G. Bohnet
has been approved for the Department of Physics

James K. Thompson

Jun Ye

Date

The final copy of this thesis has been examined by the signatories, and we find that both the content and the form meet acceptable presentation standards of scholarly work in the above mentioned discipline.

Bohnet, Justin G. (Ph.D., Physics )

A Superradiant Laser and Spin Squeezed States: Collective Phenomena in a Rubidium Cavity QED
System for Enhancing Precision Measurements

Thesis directed by Prof. James K. Thompson

By allowing a large ensemble of laser cooled and trapped $^{87}$Rb atoms to interact collectively with an optical cavity, I have explored two phenomena that may prove useful for enhancing precision measurements: superradiant lasing and spin squeezing.

Superradiant lasers have been proposed as future ultrastable optical frequency references, with predicted linewidths $< 1$ millihertz. These lasers operate in an unusual regime of laser physics where collective emission from an atomic ensemble maps the quantum phase stored in the atoms onto the optical cavity field. I will give an overview of my experimental work using a cold-atom, superradiant Raman laser as a model system to confirm a number of the key predictions concerning superradiant lasing, including the possibility of coherent emission with $< 1$ intracavity photon on average and greatly reduced sensitivity to cavity frequency noise.

I also present work using cavity-aided, coherence-preserving measurements of the atomic state population to create entanglement between atoms. The entanglement enables more precise estimation of the quantum phase at the heart of nearly all precision measurements and sensors utilizing quantum objects. By utilizing a cycling transition for the quantum non-demolition probe, we have reduced by several orders of magnitude the measurement induced back-action caused by spontaneous Raman transitions. We directly observe, with no background subtraction, a spin squeezed state with sensitivity to measuring a quantum phase enhanced 10.5 times in variance (i.e. 10.2 dB) beyond the standard quantum limit for an unentangled state. This experimental breakthrough demonstrates that quantum-aided sensing techniques can realize large enough enhancements to have a substantial impact on precision measurements and may aid advances in technology as well as searches for new physics.

# Dedication

To my wife, Cassy, who has been with me from the beginning of this endeavor.

# Acknowledgements

One of the primary lessons I learned over the course of my degree was how very rarely great achievements are the product of an isolated individual. So many people in my life have played important parts in realizing this doctoral dissertation. First, I would like to thank my parents, Mark and Denise, who provided a loving, safe, encouraging home where I could feel confident to try many different activities. They impressed upon me the attitude that I would always have to work hard for my achievements, but that they would still love me no matter the outcome of my efforts.

I also need to thank my wife, Cassy, who has been such a steady and encouraging partner throughout my education. She has always encouraged me to become the best I could be in any endeavor, and I feel that having her with me has allowed me to achieve much more than I could have alone. She was willing to move to Boulder with me, without a job in sight for her, and I'm very thankful for all of the things she has sacrificed for me to pursue graduate school.

I also must give much credit to my PhD advisor, James. As a science mentor, he has been unmatched, with knack for understanding and explaining complex topics simply and clearly. I greatly appreciate how closely he worked with me and how much he taught me in these past few years. I can see in James not only a passion to do great science, but to train great scientists. And in all of that, I felt like he treated us graduate students with a lot of respect and dignity.

I also want to acknowledge one of my earliest scientific mentors, Paul Shand. While doing my undergraduate work at the University of Northern Iowa, Paul introduced me to what doing science was really all about by inviting me to work with him on a summer research project, studying the magnetic properties of nanocrystalline materials. My love of doing experimental research was really born in that lab, opening up so many exciting opportunities in my life. It is easy to see that the experiences and the training provided by Paul are culminating in this dissertation.

Of course, so much of what is contained in this manuscript is a joint product with the team of amazing graduate students I worked with over the years, Zilong, Phoenix, Josh, Kevin and Matt. In particular, I need to acknowledge Zilong, from whom I learned so much of my atomic physics knowledge and laboratory techniques. His unwavering precision and patience has been vital for me to develop while tempering my hasty tendencies.

# Contents

**Chapter**

**Appendix**

# Tables

**Table**

# Figures

**Figure**

# Chapter 1

# Introduction

## 1.1 Classical and quantum correlations enhancing precision measurements

In this dissertation, I describe fundamental investigations of collective effects in atomic ensembles, contributing to the fields of quantum control and precise quantum measurements. My studies took the form of two different projects that both utilized an ensemble of laser cooled and trapped $^{87}$Rb atoms collectively interacting with a single mode of an optical cavity.

The first project focuses on non-destructive, coherence-preserving measurements of the collective pseudo-spin of the $^{87}$Rb atoms. We use this measurement to generate entangled states, called spin squeezed states, with modified quantum noise properties. In spin squeezed states, the quantum noise of one atom can partially cancel quantum noise in another, due to the quantum correlations between atoms, making the collective entangled state useful for improving quantum sensors. The primary advance in my work is the implementation of a measurement scheme that nearly eliminates the dominant source of measurement back-action that limited our previous attempts to create spin squeezed states. With this advance, we achieve a direct observation of ensembles with phase noise 10.5 times lower in variance than the limit set by the uncorrelated quantum noise for an equivalent ensemble of unentangled atoms. The enhancement in phase sensitivity is nearly an order of magnitude greater than our previous proof-of-principle experiments [35] and to our knowledge represents the largest entanglement-enhancement in matter systems observed to date.

In the second project, I studied collectively-enhanced emission, known as superradiance, in the ensemble of $^{87}$Rb atoms. Ultimately, my work has led to realizing a Raman laser operating in an unusual regime of laser physics where the coherence of the gain medium, in this case the atoms, is several orders of magnitude better than the coherence of the cavity field. This Raman laser serves as a good model system for exploring the physics of proposed ultranarrow linewidth lasers [114, 33], such as their insensitivity to cavity vibration, quantum-limited linewidth, and amplitude stability. Using this model system as a framework, we also investigated the link between the quantum-limited linewidth of a laser (the well known Schawlow-Townes linewidth [136]) and the quantum limits on the precision of the phase of the field radiated by an ensemble of atoms. With the potential to posses a sub-millihertz quantum-limited linewidth and many orders of magnitude reduced sensitivity to cavity vibrations, superradiant lasers may be an important next-generation optical frequency reference.

These two projects share the common connection of applying collective phenomena to the field of precision measurement. The collective phenomena arise from the effective interactions between the atoms mediated by a cavity mode. Such interactions between quantum systems can be seen as another degree of freedom in the system that, if properly controlled and manipulated, can result in new tools for science and technology that fundamentally cannot be realized with individual quantum systems.

Historically, research to improve precise quantum measurements has focused on controlling and manipulating quantum objects to purify their internal states, control their motional states, and remove perturbations associated with the external environment and also interactions between individual quantum objects. For example, optical pumping and NMR techniques were developed to allow precise initialization and control of the internal quantum states of atoms. Later, laser cooling and trapping techniques were developed to gain control over the external atomic motional degrees of freedom with the goal of decreasing doppler broadening and enhancing measurement coherence times. To mitigate interactions between atoms, precise quantum measurements have been done with single ions or atoms, or using dilute gases where collisions are sufficiently reduced to avoid systematic errors.

Eliminating interatomic interactions, along with mastery over the internal and external degrees of freedom of these quantum objects has resulted in some of the most precise and accurate measurements ever made [132, 74, 19]. These precision quantum measurements have led to a number of advances in science, including tests of the standard model [83] and searches for new physics [16, 8, 128, 75]. The impacts of precision measurement tools based on quantum sensors also impacts everyday technologies such as GPS, cellular telephones, biological sensors, and the internet [89, 44]. At the heart of many of these advances is precision time or frequency standards.

Quantum systems serve as excellent time standards because their quantum nature guarantees that all atoms or ions are identical, the transitions can be precisely measured, and systems can be chosen that are insensitive to external perturbations. Laser-cooled atoms can realize the current definition of the second [165], and along with the invention of the femto-second laser frequency comb [153, 40], new trapped atomic optical frequency standards (so called optical lattice clocks) can have fractional frequency uncertainties approaching 1 part in $10^{18}$ [74, 19]. In the future, optical lattice clocks may be able to use the sensitivity of time to gravity as predicted by the theory of general relativity to serve as gravimeters for advancements in geodesy [38].

The optical lattice clock serves as a pinnacle example of the paradigm of controlling both the internal and external degrees of freedom of single atoms (Fig. 1.1). Interactions between the atoms are kept to a minimum by working at low densities or possibly in the future by utilizing 3D optical lattices with at most one atom per lattice site.

However, as optical atomic clocks continue to mature, they are approaching fundamental limitations, which serve as a good examples of the fundamental limitations for all atomic sensors. One such limitation is the quantum noise that arises from the projection of the atomic wavefunction from a superposition into a discrete atomic state. Another limitation comes in the form of noise in the frequency of the laser light used to probe the atoms in the optical lattice trap. Looking forward, one possible way to address these limitations is to leverage the additional degree of freedom provided by inter-atomic interactions.

It has long been recognized that particular interactions in the ensemble can give rise to interesting and useful collective states with enhanced measurement properties. Interactions between

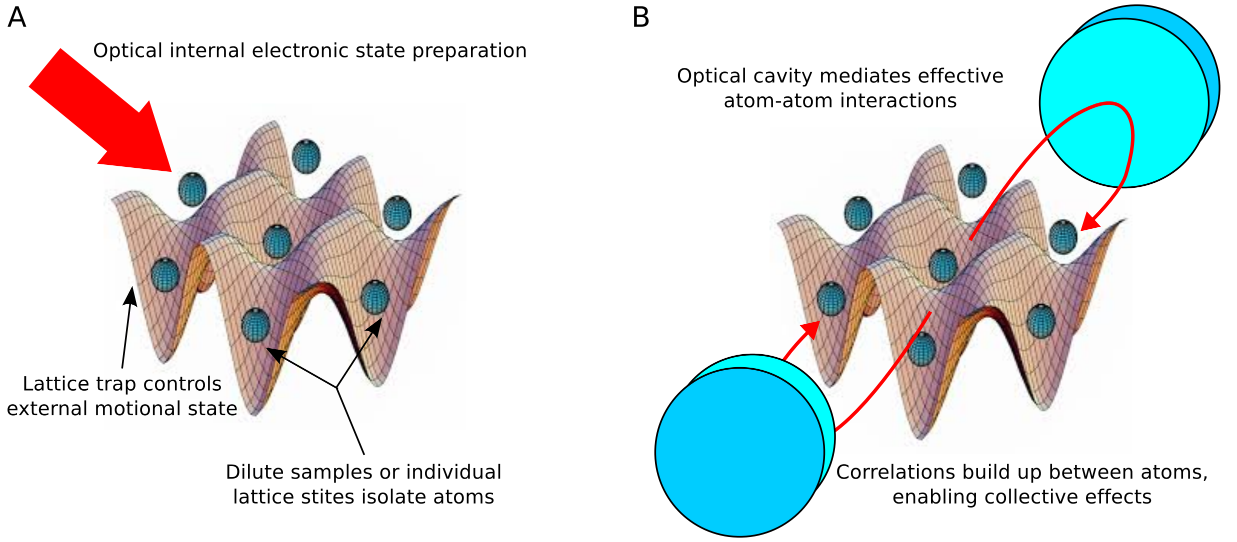

Figure 1.1: (A) The laser trapped and cooled sample of neutral atoms in an optical lattice clock serves as an example of the variety of single particle control techniques used extensively in precision measurements with cold atoms. The optical lattice trap nearly eliminates all motional perturbations from the system, controlling the atoms' external states and optical pumping techniques control the internal electronic states of the atoms. Lattice clocks can also operate with fermions in dilute samples that can nearly remove collisional interactions between atoms. (B) By adding a nearly-resonant optical cavity mode, we can introduce controlled atom-atom interactions and take advantage of this additional degree of freedom in the ensemble. The collective state of the ensemble is more than just many independent realizations of an experiment, possessing, for example, modified quantum noise properties that produce enhanced sensitivity for precision measurements with the same resources (in this case, the number of atoms).

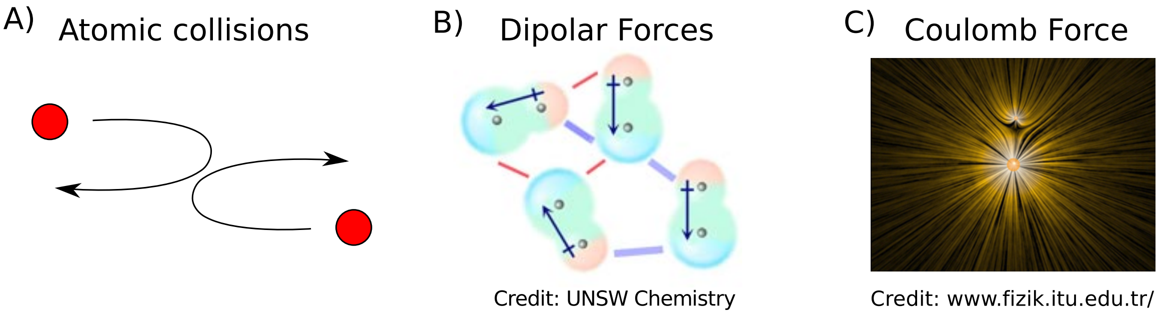

Credit: UNSW Chemistry

Credit: www.fizik.itu.edu.tr/

Figure 1.2: Examples of common interactions used for quantum simulation and generation of interesting collective states. A) Atomic collisions have a short range of interaction $\propto r^{-6}$, and although they can be tuned with techniques such as magnetic Feshbach resonances, can be difficult to quickly and completely extinguish. B) Dipolar forces are slightly longer range $\propto r^{-3}$, but also anisotropic. C) Coulomb interactions can be relatively long range $\propto r^{-1}$, but systems that take advantage of Coulomb coupling, like ion traps, have proved difficult to scale to large atom numbers.

the quantum objects, such as collisions, are often treated as a perturbation to be eliminated from a precision measurement system, because of the systematic errors they can introduce. Thus a key advance in the field of quantum information is to extend the precise manipulation and control over the quantum system to include inter-particle interactions in order to both create and apply these useful collective states while controlling or avoiding systematic errors.

Controlled interactions open up a wide range of interesting quantum many-body phenomena for study and for applications that cannot be realized in purely classical systems. As an ensemble of quantum objects is allowed to interact, correlations build up throughout the system so that the ensemble can no longer be described just as many copies of a single quantum object, but must instead be described by a new collective state. In addition to applications in precise quantum measurements, controlled interactions are at the heart of the fields of quantum simulation [18, 15], quantum computation [100], quantum memories [80], quantum teleportation [5, 129], and quantum cryptography [59]. Of primary interest in this thesis will be collective states with enhanced emission properties (superradiance) and reduced quantum noise (spin squeezed states).

Useful inter-particle interactions can take many forms, but for the precision measurement applications envisioned here, the interactions should be both strong and long range. Strong interactions allow the useful correlations to develop quickly compared to any decoherence effects that often tend to destroy the collective state. Long range interactions allow the correlations to build up homogeneously throughout the ensemble. In addition, the interaction should have rapid dynamic control. This allows one to use interactions to create useful collective states, but then quickly extinguish the interactions to allow the collective state to evolve during a sensing period free from systematic errors produced by interactions.

The atoms collectively interacting with a cavity mode can meet these criteria for generating useful collective states. The cavity provides a common communication bus between the atoms, creating infinite range, effective interactions between the atoms (Fig. 1.1). In principle, atoms can interact through the a cavity mode, even when separated by many millimeters or centimeters, a much longer range than the typical ranges of interactions for s-wave collisions or dipole-dipole interactions. The optical cavity can greatly enhance the interaction of atoms with the light field by confining the light to a small volume. The strength of the interactions can be varied in real time as simply as turning off the optical field providing the coupling, with the time scale limited only by the cavity ring down time, typically $< 1$ microsecond. The tunability and range of interactions offer distinct advantages compared with other types of interactions that are intrinsically much shorter-range in nature and/or more difficult to control, such as direct collisions [49, 130, 62, 28, 108, 69], magnetic and electric dipolar interactions [148, 168], and Coulomb interactions between ions [164, 117] illustrated in Fig. 1.2.

As another point of comparison, the top-down nature of the collective states realized in cavity QED systems means that interesting collective phenomena can emerge in large ensembles composed of hundreds to millions of neutral atoms. Collective cavity QED technicques have also recently been applied to ensembles of ions [71]. The emergent nature of the correlations that develop in the cavity QED systems mean that the ensemble size is easier to scale to a large number of quantum objects than the deliberate correlations that are built in through pair-wise quantum logic gate operations in ensembles of trapped ions, for example. In both the spin squeezing and superradiance studies, we are going to leverage the ability to use large ensembles to enhance the collective interaction with the cavity mode required to create the correlations.

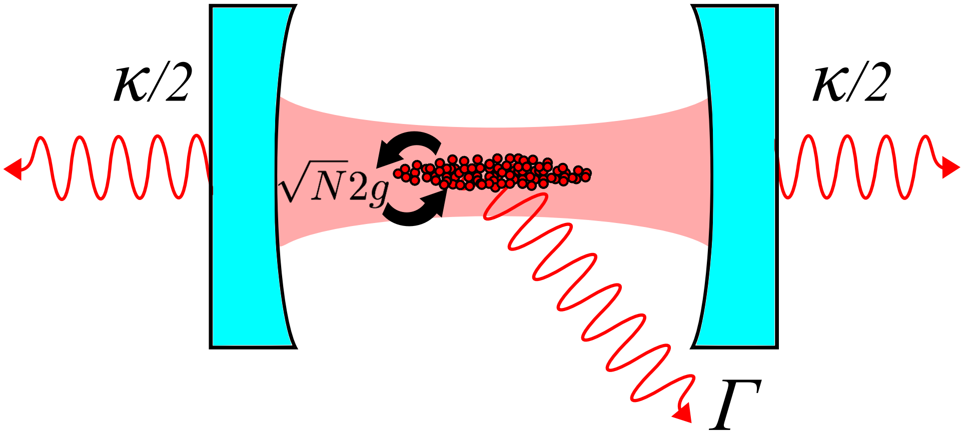

Figure 1.3: Atom-cavity coupling is a competition between coherent exchange of excitations between the atoms and cavity at a rate $\sqrt{N}2g$, and loss of excitations through decay through free space scattering $\Gamma$ and spontaneous decay through both cavity mirrors $\kappa$. The enhanced atom-cavity coupling rate arises from a constructive interference for emission and absorption with respect to the cavity mode due to correlations among the individual atoms, the same physics underlying the phenomena of Dicke superradiance [43].

Collective coupling means that the ensemble of atoms interacts much more strongly with the cavity than a single atom. One atom in the cavity absorbs and reemits a photon into the cavity at a characteristic frequency $2g$, given by the atomic dipole moment and the electric field of a photon in the cavity mode. The strength of the coupling relative to the coupling of the atom to all other non-cavity modes is characterized by the single particle cooperativity $C \equiv \frac{4g^2}{\kappa\Gamma}$, where $\kappa$ is the spontaneous decay rate of the cavity field and $\Gamma$ is the spontaneous decay rate of the atomic excited state. The relevant rates are illustrated in Fig. 1.3. The single particle cooperativity can be interpreted as a ratio of the atom-cavity coupling rate to the rates of losing a photon through the cavity mirrors or through spontaneous free-space scattering, after which the photon never returns to interact with the atoms. Another useful interpretation of $C$ is as the fraction of the time that a single atom in the excited state decays by emitting a photon into the cavity mode. Our system operates in the weak single particle coupling limit with $C \sim 0.5 \times 10^{-3}$.

However, if $N$ atoms are in the cavity, then the atoms can collectively absorb a cavity photon and reemit it at frequency $\sqrt{N}2g$. The system then has a collective cooperativity $NC = \frac{4Ng^2}{\kappa\Gamma}$ which can be much greater than 1, meaning the coherent exchange of excitations between the atoms and cavity field can dominate over the decay processes. The collective cooperativity $NC$, or the effective optical depth, also gives the fraction of time that excitations from the ensemble are emitted into the cavity mode.

As the ensemble of atoms exchanges photons with an optical mode collectively, strong correlations can build up between atoms. The correlations arise from a fundamental ambiguity of the atoms interacting with the optical mode, as there is no way to assign photon emission and absorption to a single atom. These correlations can be simply classical, or quantum, indicating entanglement.

Collective emission and correlations play the central role in both of the experiments described in this thesis. The enhanced emission into the cavity mode in a spin squeezing experiment allows for more collective information to be extracted for the same amount of free space scattering that causes decoherence. Non-classical correlations generated from such a measurement reduce the quantum noise of the resulting entangled state, as correlated fluctuations can cancel. In the case of the superradiant laser, the classical correlations between atoms spontaneously synchronize their emission, providing the collective enhancement in the ensemble's scattering rate necessary to extract a useful amount of output power. In this thesis, we will study these two collective effects in detail, particularly how they can advance precision measurements. As we will see, the correlations between atoms introduced by their interactions in the atom-cavity system may enable precision measurements that go beyond the limits to the single particle precision measurement paradigm that has already been so influential and fruitful. The rest of this introduction will introduce these two topics in detail and give a basic outline of the content of the thesis.

## 1.2 Coherence Preserving Measurements to Create Spin Squeezed States

The first body of work I will describe is the generation of conditional spin squeezed states in ensembles of laser cooled $^{87}$Rb atoms confined in an optical cavity. The squeezed state generation depends on coherence-preserving, collective measurements of atomic populations enhanced by the optical cavity. The key experimental advance described in my work is the reduction of measurement induced back-action on the population states of the atoms. We reduced measurement back-action by probing the atom-cavity system near an optical cycling transition, suppressing probe-induced Raman scattering between internal atomic states by several orders of magnitude. The process of performing a collective measurement on the ensemble can be thought of as building quantum correlations, or entanglement, between the atoms through their effective interaction with the optical cavity. The measurement is used to record the value of the correlation of quantum noise in a given trial. The information gained can then be used to essentially subtract out the quantum noise in subsequent measurements within the same trial.

### 1.2.1 Quantum Projection Noise

Quantum noise is the price we pay for the benefits associated with metrology using quantum objects. While quantum mechanics guarantees that each quantum object, like a $^{87}$Rb atom, will have the same, well-defined transition frequencies, we must cope with an unavoidable source of noise that provides the fundamental limitation to many state of the art precision measurements.

One way to understand the source of quantum noise in atomic sensors is by considering the probabilistic nature of the measurement process. Atomic sensors encode their information in a quantum phase $\phi(t)$, a relative phase that accumulates in the wavefunction of a two level system placed in the superposition of the two quantum states $|\Psi\rangle = \cos((\pi/2-\theta)/2)\,|\uparrow\rangle + e^{i\phi}\sin((\pi/2-\theta)/2)\,|\downarrow\rangle$. The state of such a two level system can be directly mapped onto a Bloch-vector[51] of length $|\mathbf{J}| = J = 1/2$, whose tip lies on a sphere and whose orientation is given by the azimuthal angle $\phi$ and a polar angle $\theta$, here measured from the equator as shown in Fig. 1.4. The value of $\phi$ is most often estimated by measuring the population of atoms in different quantum states after $\phi$ is mapped onto $\theta$ at the end of a Ramsey sequence (see Fig. 1.4). The angle $\theta$ can then be simply estimated by measuring the probability that the atom is in $|\uparrow\rangle$ $P_\uparrow$ or $|\downarrow\rangle$ $P_\downarrow$, i.e. the projection of the Bloch vector onto the $z$-axis $J_z = (P_\uparrow - P_\downarrow)/2$, as in the small angle limit $\theta \approx J_z/J$.

The quantum phase $\phi$ evolves continuously while an atom or qubit is in a superposition of

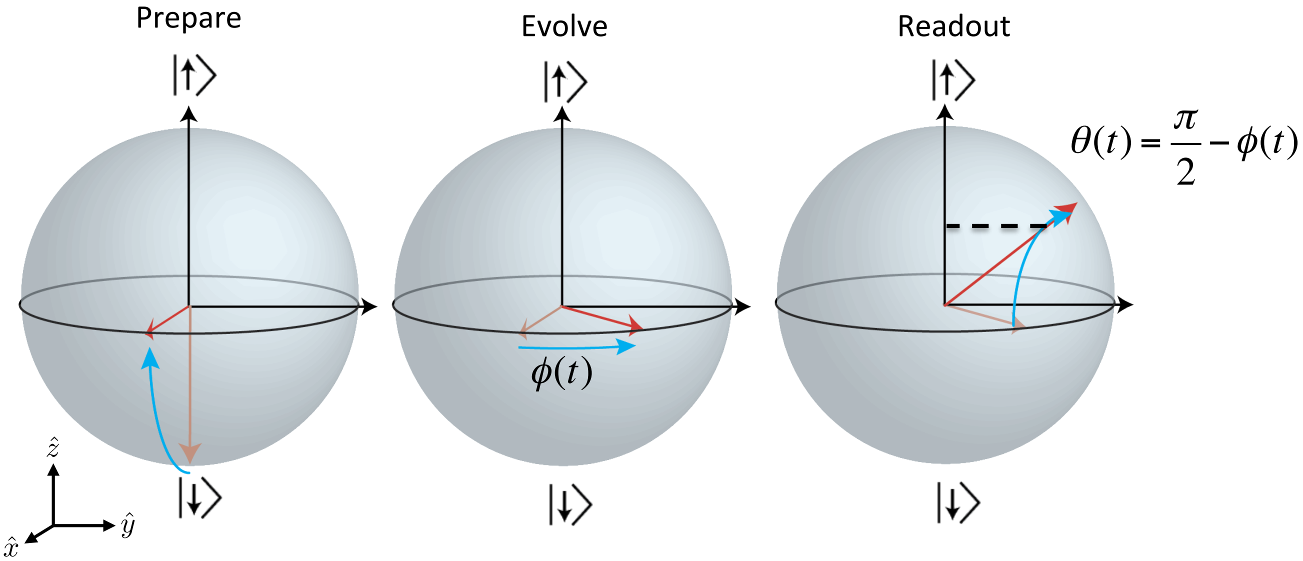

Figure 1.4: Illustration of a Ramsey sequence with a two level system represented by a Bloch sphere. The first step is optical pumping the atoms all into $|\downarrow\rangle$ (light red arrow), then performing a $\pi/2$ rotation about $-\hat{y}$ axis to place the Bloch vector along $\hat{x}$. The Bloch vector then precesses around the $\hat{z}$ axis at a rate proportional to the energy difference between $|\uparrow\rangle$ and $|\downarrow\rangle$. The Bloch vector precession represent the evolution of the quantum phase in the wavefunction $|\Psi\rangle = \cos((\pi/2-\theta)/2)\,|\uparrow\rangle + e^{i\phi(t)}\sin((\pi/2-\theta)/2)$ that we ultimately wish to measure. The second $\pi/2$ pulse performs another rotation about $-\hat{y}$ and maps the $\phi(t)$ onto the coefficients of the population states, or equivalently onto the polar angle of the Bloch sphere. The quantum phase $\phi(t)$ can then be inferred by measuring the state of the two level system. Quantum randomness in the projection onto the population basis results in fundamental quantum noise limiting the resolution of the angle $\phi(t)$.

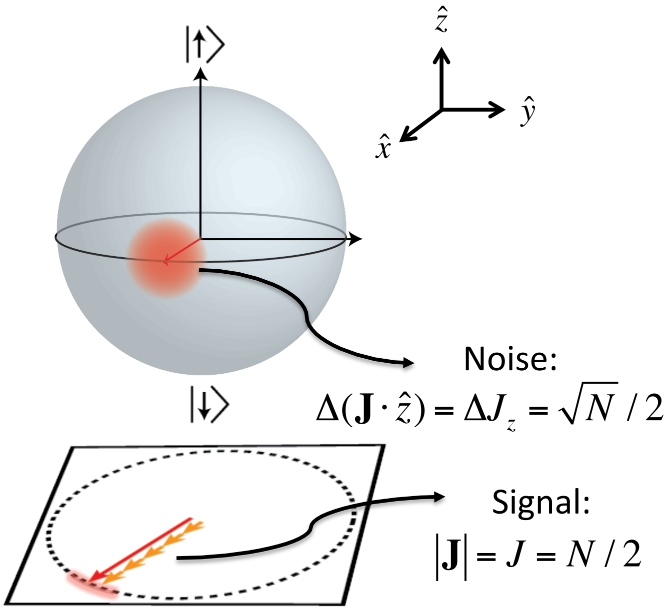

Figure 1.5: The standard quantum limit for a coherent spin state. Quantum noise appears as an uncertainty in the pointing location of the classical Bloch vector $\mathbf{J}$, represented by the blurry red region at the tip of the vector. The signal, that is, the change in the $z$ projection of $\mathbf{J}$ for a given angular rotation, increases linearly with $N$. However, the standard deviation in a measurement of the $z$ projection from quantum noise grows as $\sqrt{N}$.

its two spin states, but the measurement process always finds an atom in one of the two population states $|\uparrow\rangle$ or $|\downarrow\rangle$, or equivalently $\theta = \pm\pi/2$. Thus for an atom in an equal superposition of spin states, the readout has fundamental fluctuations that require repeated measurements over identical experiments in order to precisely estimate the probabilities $P_\uparrow$ and $P_\downarrow$. This noise is often called quantum projection noise[76], associated with the notion of the measurement projecting the superposition state onto one of the population states.

Using ensembles of $N$ identical atoms is equivalent to running many independent experiments in parallel in order to more precisely determine the probabilities $P_\uparrow$ and $P_\downarrow$. We can conveniently represent the measurement resolution of the collective state using a collective Bloch vector of length $|\mathbf{J}| = N/2$, as shown in Fig. 1.5. Averaging the outcomes of the $N$ parallel experiments, quantum projection noise limits the uncertainty in the estimate of $\theta$ (and therefore $\phi$) to a variance $(\Delta\theta)^2 \geq (\Delta\theta_{SQL})^2 = 1/N$, a limit known as the standard quantum limit (SQL) for a coherent

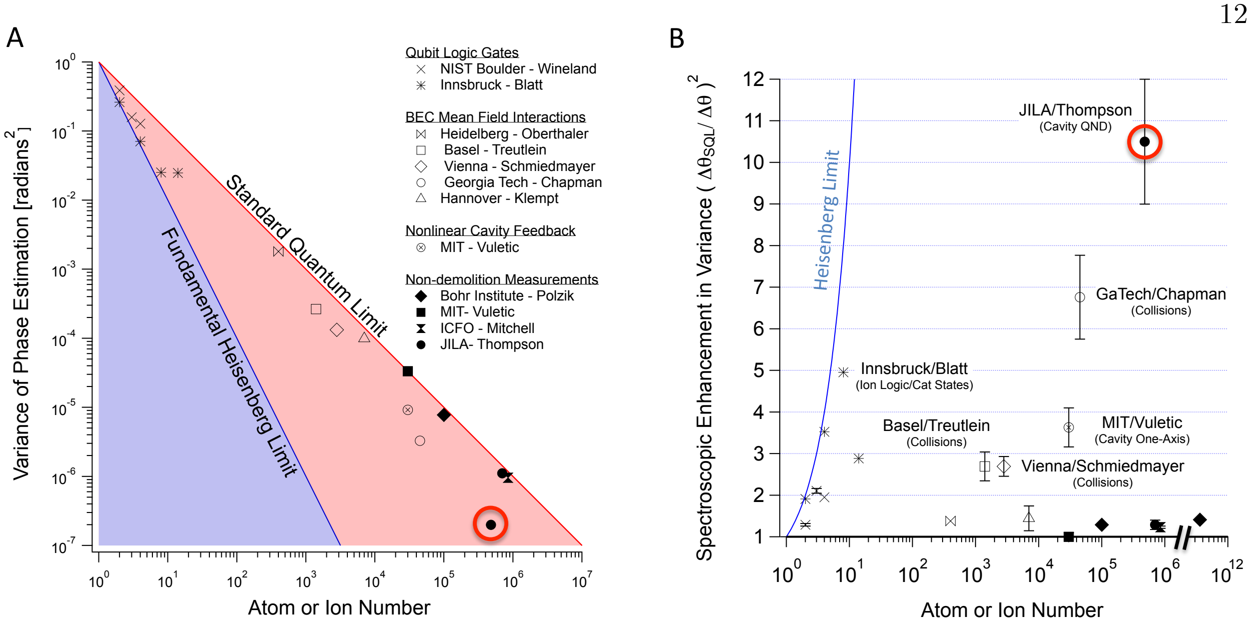

Figure 1.6: A summary of results for the observed entanglement-enhanced sensitivity for measuring a quantum phase across a variety of physical systems and mechanisms. The solid points indicate results that use coherence preserving pre-measurements, the most relevant results for comparison to this work. The result from this work is highlighted with a red circle. (A) Absolute observed phase resolution of an ensemble, emphasizing the improvement in the absolute sensitivity from simply starting with a large ensemble of atoms. Though our result is far from the Heisenberg limit, the large ensemble size allows improvement for an already highly resolved phase. (B) The observed enhancement of phase resolution relative to the SQL. The blue line indicates the fundamental Heisenberg limit. Compared to previous work, which observed interesting, but small entanglement-enhanced sensitivities, we have observed over an order of magnitude enhancement in a system readily applicable to precision measurement experiments such as optical lattice atomic clocks. To date, our result is the largest enhancement in any system using matter as spins. The other results can be found in Refs. [116, 102, 117] for experiments using ions, Refs. [49, 130, 62, 28, 108, 69, 104] for experiments using one-axis twisting, and Refs. [4, 159, 141, 139, 35] for non-demolition measurements.

spin state (CSS). Throughout the thesis the notation $\Delta X$ indicates the standard deviation of the quantity $X$ over many independent trials. Thus, the primary way to mitigate quantum projection noise is to use as many atoms, or photons in the case of optical interferometry, as possible.

However, scaling up the system size also has limitations. In the case of photons, this limitation may not be immediately apparent as the photons don't interact with one another. However, high power effects like parametric instabilities [50] and radiation pressure back-action (recently observed in optomechanical systems [123]) can make photon shot noise a limitation in precision measurement experiments such as gravitational wave detectors LIGO [1] and GEO600 [2].

In atomic sensors, the limitations to system size are much more apparent. Collisions between atoms can cause perturbations to atomic transitions [29], affecting the accuracy of the sensor. Other times, the desire for high spatial resolution of a sensor can constrain the trap dimensions, limiting the ensemble size.

Ultimately, for an optimal number of quantum objects, quantum projection noise sets the fundamental phase precision. Both atomic sensors and the optical interferometers used for gravitational wave detection are nearly or already limited by quantum noise, so entanglement-enhanced metrology would improve some of the most precise measurements of external fields [93], rotations [66], and time [74], and will advance searches for new physics [120].

### 1.2.2 Squeezed states

By entanglement-enhanced metrology, we mean the use of non-classical correlations between individual members of the ensemble to improve the fundamental precision. It has long been recognized that non-classical states can have modified quantum noise properties, which could enhance the resolution of sensors and interferometers beyond the SQL [31, 164].

Squeezed states are non-classical states with modified quantum noise properties first investigated in the field of optics. It was theoretically shown and experimentally demonstrated that entanglement in the optical field could reduce quantum noise in one quadrature of the field at the expense of added noise in the orthogonal quadrature. For instance, the quantum noise can be squeezed out of the field's phase quadrature for enhanced phase measurements in an interferometer. The quantum noise is squeezed into the amplitude quadrature, but this quadrature is not relevant for making phase measurements. Represented on a phasor diagram, shown in Fig. 1.7, the quantum uncertainty of the most classical state, a coherent state, is represented by a classical probability distribution that smears out the tip of the classical vector. Here the distribution is visualized as a circle with equal quantum noise in both quadratures. The entangled state has an elliptical shape. The Heisenberg uncertainty relationships require that the total area defining the

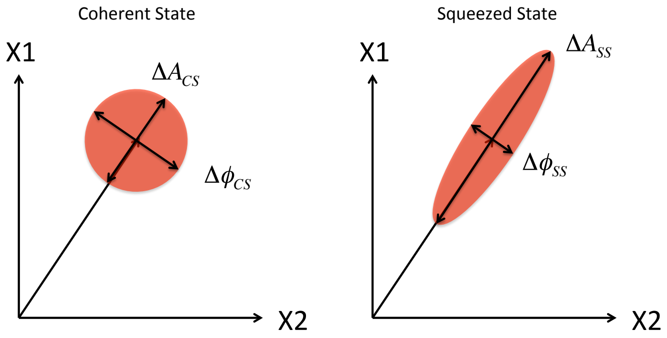

Figure 1.7: Squeezing in an optical field, or equivalently a harmonic oscillator, with the two conjugate variables on the $X_1$ and $X_2$. Both the coherent and squeezed states can be represented as a classical phasor with quantum uncertainty. The area of uncertainty is constant, but can be distributed among the different quadratures. In this case, the squeezed state has a reduced phase uncertainty $\Delta\phi_{SS}$ at the expense of increased uncertainty in the amplitude $\Delta A_{SS}$.

size of the quantum noise must remain constant. So the uncertainty in one quadrature can be pushed into the other, giving the squeezed state its name.

Squeezed states in optics were long considered a solution looking for a problem, as many times the quantum noise of a coherent state could more easily be mitigated by using more optical power than implementing squeezing protocols. Currently however, squeezed states are actively being used to improve searches for gravitational waves using optical interferometers [1]. Another possible use of squeezed light is microscopy in biological systems where intense light can damage biological system [150]. As discussed previously, the situation is different for sensors that use ensembles of atoms or ions.

Spin squeezed states, referring to the squeezing of the pseudo-spin formed by any two level system, were first produced and shown to operate below the projection noise limit for two ions [116]. Spin squeezed states have a direct analogy to optical squeezing, except that the noise in one spin projection, say $J_z$ is reduced at the expense of increased noise in an orthogonal spin projection, $J_y$ for example. The impressive degree of coherence and state control allowed ion system to realize other non-classical states (such as NOON or cat states) with altered noise properties and/or phase accumulation rates [102, 117] realizing the fundamental noise limit even for entangled states, known as the Heisenberg limit, where $\Delta\theta^2 \geq \Delta\theta_H^2 = 1/N^2$ (see Fig. 1.6B).

Though entangled states of a few ions have been demonstrated at the fundamental Heisenberg limit, their phase precision can be surpassed by classical states that simply use more atoms (Fig. 1.6). The atomic fountain clocks that realize SI second use of order $10^5$ atoms per experimental trial, and optical lattice clocks, good candidates for future time standards, use of order $10^3$ to $10^5$ neutral atoms. Sensors with many neutral atoms are promising because they possess an intrinsically small quantum-limited noise floor. In addition, the potential enhancement in measurement precision from a squeezed state can be much larger in systems with large ensemble size because of the $1/N$ relative scaling in phase variance between the SQL and the Heisenberg limit. As a result, techniques that can can generate a large degree of squeezing systems such as optical lattice clocks [74, 19], could make a large impact on precision metrology.

One approach to generating spin squeezing in atomic systems is to non-destructively pre-measure the quantum fluctuation in $J_z$ before each Ramsey sequence, and then subtract the measurement outcome from the measurement outcome for $J_z$ obtained at the end of the Ramsey sequence. The quantum noise will be common to the two measurements, while any phase accumulated during the Ramsey sequence will not be common [99]. While the resulting state of the ensemble is sometimes termed a conditional spin-squeezed state, the reduction in noise is essentially deterministic with no discarding of trials necessary. My work here uses this pre-measurement approach. The essential idea is illustrated in Fig. 1.8.

The pre-measurement scheme stands in contrast with other techniques to generate squeezed states where appropriate interactions between atoms generate correlations without the need for noise subtraction. For comparison, these results are included in Fig. 1.6. In systems of ions, interactions mediated by the Coulomb force produce the entanglement [164, 117]. In neutral atoms, squeezed states have been generated using atomic collisions in ensembles of degenerate gas to produce the desired interactions [49, 130, 62, 28, 108, 69]. Notably, it was also demonstrated that effective atom-atom interactions mediated by cavity-based optical feedback could also produce squeezed states [104]. Note that there is an intellectual connection with the pre-measurement technique presented in this thesis and the cavity feedback technique in that cavity feedback can be understood as the cavity measuring the $J_z$ spin-projection and then creating a $\hat{z}$ rotation of the spin proportional to the measured value. This rotation causes a shearing of the state uncertainty, similar to the original one-axis twisting proposal put forth by Kitagawa and Ueda [87].

The pre-measurement approach relies on measurement back-action, the ability of a measurement to change the state of the system being measured. For example, a measurement of a system in a superposition of two states causes the system to project, or collapse, into one of the two discrete states, resulting in quantum projection noise. Measurements performed on an ensemble, however, can project the ensemble into an entangled state when only collective quantities are measured. For example, using two spins each in a superposition state, a joint measurement that only revealed that one of the two spins was in spin-up, but not which one, is projected into the entangled state $|\Psi\rangle = \left(|\uparrow_1\downarrow_2\rangle + |\downarrow_1\uparrow_2\rangle\right)/\sqrt{2}$. Any information about the spin-state of a single atom that leaks to the environment due to imperfections in the collective measurement reduces entanglement as the collapse of state of the individual atoms means the previous entangled state becomes either one of the two unentangled states $|\uparrow_1\downarrow_2\rangle$ or $|\downarrow_1\uparrow_2\rangle$. Such collective or joint measurements arise in a wide range of applications, including quantum teleportation [119], quantum information protocols [91], studies of strongly-correlated quantum systems [48], Dicke superradiance [43], and entanglement generation in optical [65], solid state [131] and atomic systems [39].

A collective pre-measurement of the spin state of an ensemble can precisely measure the quantum noise, while preserving the coherence between states that is required for sensing a quantum phase [99]. The collective pre-measurements invoked here are intimately tied to the notion of quantum state preparation and quantum non-demolition measurements. To make a non-destructive measurement of the atomic state, often an optical beam is passed through the ensemble. The light-atom interactions cause the state of the field (for instance, it's polarization state or quadrature amplitudes) to become entangled with the state of the atoms, such that a subsequent destructive measurement of the light field can give the state of the ensemble. After the destructive measurement

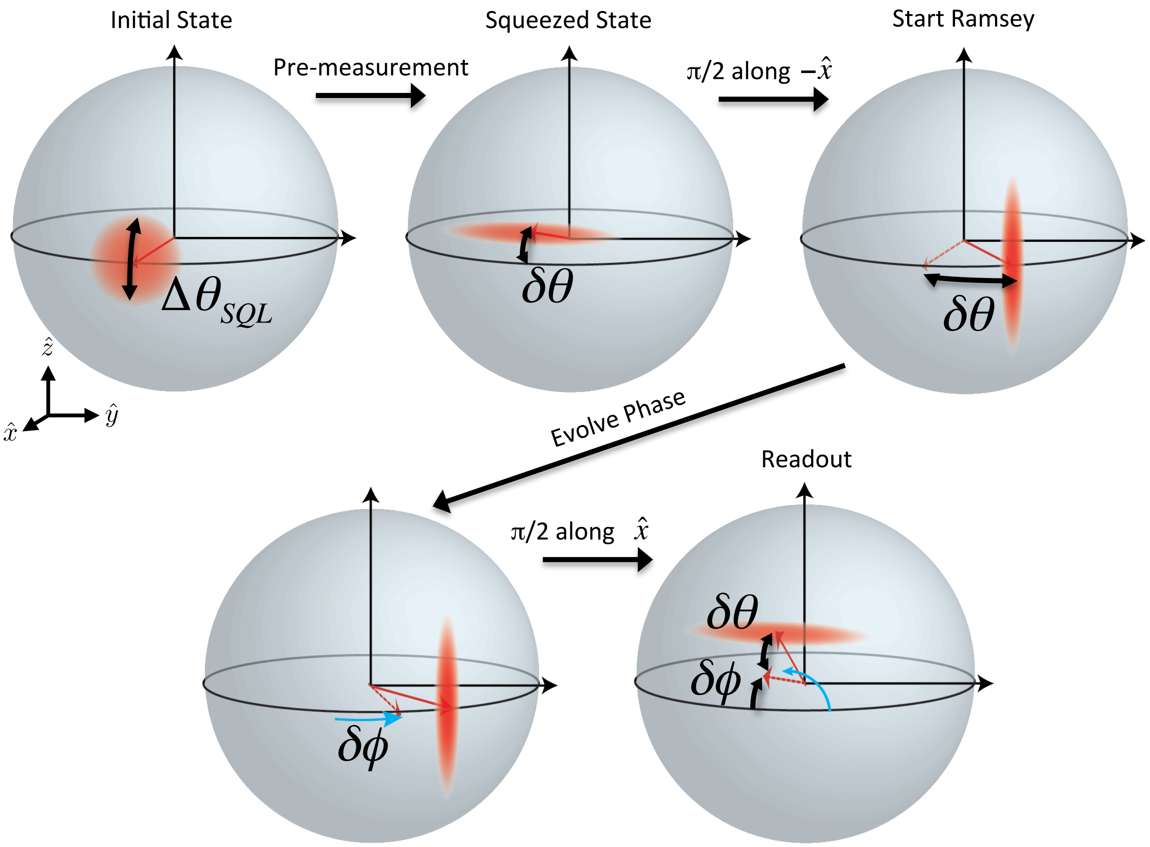

Figure 1.8: Generating a squeezed state with a coherence-preserving pre-measurement for a Ramsey sequence. A coherent spin state has an initial uncertainty in the azimuthal angle of the Bloch vector $\Delta\theta_{SQL}$ set by quantum noise that defines the SQL for phase resolution of the state. By performing a measurement on the polar angle $\theta$ using a population readout with resolution below the quantum noise limit, the deviation of the Bloch vector from the equator on that particular trial, $\delta\theta$, can be recorded. Another $\pi/2$ pulse rotates the quadrature with a known quantum fluctuation into the the azimuthal quadrature and the Ramsey sequence can begin. A noiseless vector going through the Ramsey sequence is shown as a dashed line. While the final output of the interferometer will still exhibit quantum fluctuations $\Delta\theta_{SQL}$ about the average output polar angle $\delta\phi$, the fluctuations can be subtracted on a trial by trial basis due to the knowledge of the initial state from the pre-measurement. Effectively the state has an uncertainty set by the measurement resolution, determining the precision which one can measure the initial quantum fluctuation.

of the light field, the atomic ensemble is projected into an eigenstate of the measurement. As described above, a measurement of a collective quantity can then result in projection into an entangled state.

While measurement back-action can work to our benefit in the case of preparing a state with reduced quantum noise properties, this does not need to be the case. Fundamental measurement back-action requires added noise in the orthogonal quadrature to the measurement. Fortunately, in spin systems, the orthogonal degree of freedom does not couple back into the measured quadrature, unlike in mechanical systems, where a position measurement adds uncertainty to the momentum, which affects the position at a later time [26].

However, there can be additional sources of back-action in a spin system. One example is atoms individually scattering probe light out of the cavity mode, projecting them into a definite population state and taking them out of the collective ensemble, leading to a shortening of the Bloch vector $\mathbf{J}$. This back-action makes the ensemble less sensitive to a quantum phase, as the observable signal $J_z$ is proportional to Bloch vector length in the small squeezing limit $J_z = |\mathbf{J}|\theta$ for the same rotation $\theta$. In addition, a scattering event can also cause an atom to change its spin state, resulting in added noise in the quantity $J_z$ being measured. The added noise in $J_z$ from population diffusion can reduce the correlation between the pre- and final measurements of $J_z$, limiting the degree of noise reduction in the differential spin projection measurements. Ultimately, the spectroscopic enhancement $W^{-1}$ relative to the SQL that can be achieved, quantified here as the ratio of the SQL to the observed angular variance $W^{-1} = (\Delta\theta_{SQL}/\Delta\theta)^2$, is a combination of reduction in noise and the loss of signal caused by the pre-measurement.

The degree to which atoms appear indistinguishable to the measurement, i.e. only collective information is obtained, sets the limit on these two forms of back-action. Thus one figure of merit for the measurement is the degree of indistinguishability, quantified by the collective optical depth $NC$. Free space ensembles with high optical depth provided by trapping and/or high densities have been shown to be able to generate conditional spin squeezed states [4, 159, 141].

An optical cavity enhances the optical depth by a factor of the cavity finesse $F$. Compared to free space measurements, significant enhancements on the optical depth can be achieved at lower atomic densities, critical for sensors to avoid inaccuracies associated with collisions in high density samples. The collective scattering of the atomic sample into the cavity mode means that the rate of obtaining collective information is enhanced relative to the rate of single particle scattering. Thus operation deep in the strong collective coupling regime, $NC \gg 1$, is important.

First proof-of-principle experiments, both in free space [4, 159, 141] and in optical cavities [139, 35], have generated conditional spin-squeezed states by using collective pre-measurements, with results shown in Fig. 1.6. However, measurement-induced back-action has limited direct observations of spectroscopic enhancement to only $W^{-1} \leq 1.4$ [159]. Note that larger stated improvements appear in these papers, but most often these values include background subtractions and do not represent the actual obtained spectroscopic enhancement. Such modest improvements are not useful for precision measurements, as the added cost and complexity to a device are likely not worth such small improvement. If entanglement-enhanced metrology is to continue to advance, we must show it is possible to realize metrologically relevant degrees of spectroscopic enhancement using entanglement, such as the order of magnitude improvement realized in this work. Importantly, the results presented here can be mapped directly onto several atomic species used in optical lattice clocks, such as Sr and Yb.

In Chapter 2, I describe our atom-cavity system, giving technical details regarding the optical cavity and trapping and cooling the atoms. This chapter serves as a foundation for both the squeezing experiment and the superradiant laser experiment. Then in Chapter 3, I describe the generation of spin squeezed states of $\sim 5 \times 10^5$ atoms with precision enhanced by $W^{-1}$ up to 10.5 beyond that of an entangled state using a method compatible with state of the art optical lattice clocks. I give the specific setup of the squeezing experiment, focusing on the improvements to the previous implementation of measurement-induced spin squeezing that allowed us to improve the directly observed spectroscopic enhancement by nearly an order of magnitude beyond our previous result.

## 1.3 Superradiant lasers

The second class of experiments covered in my thesis is the development of a superradiant Raman laser using the laser-cooled $^{87}$Rb cavity QED system. Our system operates very deep in the bad-cavity regime where the atomic linewidth $\gamma_\perp$ is much less than the cavity linewidth $\kappa$, similar to an active hydrogen maser [60]. In this regime, the correlations between individual atomic dipoles that result in the collectively enhanced emission, or superradiance, arise spontaneously through emission into the cavity mode, building a collective coherence that can exceed the coherence of a single particle alone. As a result of operating in this unusual regime of laser physics, we observe a variety of interesting phenomena, including lasing and linewidth narrowing with on average less than 1 photon inside the laser cavity. Such a collectively-emitting ensemble of cold atoms is at the heart of proposals for future millihertz linewidth lasers where the gain medium would consist of alkaline-earth atoms with narrow optical transitions[115, 33], and we confirm a number of key predictions for superradiant lasing relevant for these proposed millihertz linewidth lasers.

### 1.3.1 New frontiers in ultrastable lasers

Frequency stable lasers are our primary rulers for space and time. In particular, narrow linewidth lasers are crucial ingredients in optical clocks [45, 118, 74, 19] and their comparison [132, 118], timing signal distribution [54], and precision tests of fundamental physics [38]. Most neutral atom optical clocks work by stabilizing the frequency of a probe laser to the nearly forbidden optical transition in alkaline-earth atoms using high-resolution laser spectroscopy. In state of the art clocks, the frequency stability of the probe laser is currently the primary limitation to the clocks' precision. The finite frequency stability of the laser both limits the spectroscopy interaction time and introduces additional noise during the dead time in the measurement cycle while atoms are being re-loaded in the clock. Consequently, enabling a next generation of ultra-stable, narrow-linewidth lasers would impact a wide range of technical and fundamental scientific applications, including communications, navigation, geodesy [38], determining the fundamental constants of nature [53] and searches for physics beyond the standard model [17].

Lasers stabilized to highly engineered Fabry-Perot cavities have achieved remarkable levels of frequency stability. However, even in state-of-the-art stable lasers, the mirrors of the reference cavity to which they are stabilized vibrate due to thermal noise, causing time-integrated phase drifts that limit the laser linewidth to between 0.04 and 0.3 Hz [78, 84].

Superradiant lasers offer an alternative, complementary path forward. Recent proposals[115, 33, 114, 113] suggest that superradiant laser oscillators utilizing very narrow optical transitions in atoms can be orders of magnitude more spectrally pure than current lasers. When $\kappa \gg \gamma_\perp$, the optical atomic transition acts as the repository for phase coherence and the laser frequency and linewidth is set by the atomic transition. In essence, the man-made artifact of the reference cavity is replaced with a quantum reference. Deep in this bad-cavity regime, the laser can be primarily viewed as a very coherent ensemble of atoms where the emission rate of the gain medium is enhanced by superradiance [43, 63]. Therefore, I use the terms bad-cavity regime and superradiant regime interchangeably.

### 1.3.2 Superradiance

Superradiance is a constructive interference effect where the correlations among the individual atomic dipoles results in an enhancement by $N$ of the excited state decay rate, and thus the total power emitted by the ensemble. For an ensemble of 2-level atoms confined within an optical wavelength, the indistinguishability of the atoms with respect to the emitted radiation results in the ensemble emitting collectively. The ensemble can store many excitations, making it a source of multiple photons with a well-defined phase relationship as they reflect the coherence of the correlations stored in the ensemble.

Even in an extended sample, correlations between atoms (in this case, a spatially dependent phase relationship between the optical dipoles of the atoms) can result in constructive interference along preferred directions. The correlations spontaneously form as excitations are emitted into optical modes in which the sample has high optical depth. This can be viewed again as a condition

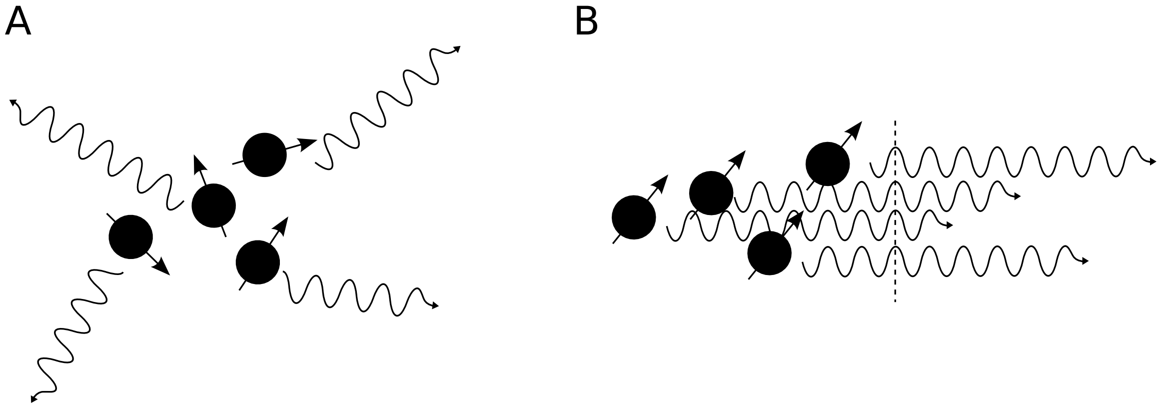

Figure 1.9: A cartoon representation of superradiance in an extended ensemble of atoms. For a collection of atoms radiating with independent phases (A), the light is isotropic and the total power emitted goes as $NP_0$, where $P_0$ is the power emitted by a single atom. For ensembles with spatially correlated radiating phases (B), represented by the synchronization of the arrows on the atoms, the emitted light can constructively interfere along certain directions, resulting in an $N^2$ enhancement of the power radiated along this direction. The cooperativity parameter $C$ serves as a measure of the range of directions (fractional solid angle) over which the constructive interference occurs. The total power radiated due to this constructive interference is then proportional to $N^2CP_0$, i.e. NC larger than for the total power from non-correlated radiation.

for indistinguishability of the emitted excitation giving rise to the correlations between atomic dipoles. As a result, superradiance in extended samples have a directionality to the enhanced emission (Fig. 1.9).

The addition of an optical cavity provides a very high effective optical depth mode for the collective emission. Although the visual representation of correlations present in the atomic dipoles becomes more complex, the addition of the cavity mode actually greatly simplifies the system as the single cavity mode easily becomes preferred over all other spatial modes. Thus, in a superradiant laser, the cavity serves primarily as a way to establish and maintain the synchronization between the atoms.

### 1.3.3 Good Cavity, Bad Cavity: opposite extremes in laser physics

Previously, most optical lasers have operated in the good-cavity regime of laser physics defined by the condition $\kappa/2 \gg \gamma_\perp$ (see the left side Fig. 1.10). In other words, the cavity field is more coherent than the gain medium. High rates for excited-state decay in optical transitions in atoms, combined with transition broadening from repumping, lattice interactions in solid state gain mediums, or Doppler effects in gases, have prevented lasers from operating with $\kappa/2 \gg \gamma_\perp$. In the good-cavity regime, the phase coherence is primarily stored in the cavity light field, and the polarization of the gain medium adiabatically follows the state of the cavity field. As a result, the laser frequency and linewidth is determined primarily by the cavity properties, with the familiar quantum-limited linewidth given by the Schawlow-Townes limit [136] as $\Delta f_{GC} \propto \frac{\kappa}{M_c}$ where $M_c$ is the average number of intracavity photons. The Schawlow-Townes limit can be made quite small in optical lasers, and the linewidth is instead limited by the laser cavity stability or the stability of an external optical reference cavity.

Deep in the bad-cavity limit, the roles of the atoms and photons have been reversed in some ways. Here the cavity field rapidly decays, and the phase coherence resides primarily in the atom's robust collective coherence. The cavity field adiabatically follows the polarization. In fact, such lasers are predicted to operate with a very small intracavity field – just enough to maintain the synchronization between the individual atomic dipoles. This means that the laser frequency properties are determined largely by the atoms (right side of Fig. 1.10). In this limit, the Schawlow-Townes linewidth is set by atomic properties $\Delta f_{BC} \propto \frac{\gamma_\perp}{N}$, analogous to the good-cavity case, but with the number of atomic quanta $N$ replacing the photonic quanta $M_c$ and the cavity damping rate $\kappa$ replaced by the atomic decoherence rate $\gamma_\perp$.

Additionally, the laser frequency is mainly determined by the atomic transition frequency, with the sensitivity to cavity frequency changes being reduced by the ratio $P = 2\gamma_\perp/\kappa$. The laser emission frequency is $f_l \approx f_a + P(f_c - f_a)$, where $f_a$ is the atomic transition frequency and $f_c$ is the cavity resonance frequency. This insensitivity could be important for operating optical frequency sources in high vibration applications such as communications, geodesy, space-based interferometry, and GPS.

The correlation among dipoles in the gain medium exists in both good-cavity and bad-cavity lasers, but the difference is largely how the correlations arise. In a good cavity laser the very strong, coherent cavity field locks the 'forgetful' atomic dipoles into a well defined phase relationship, forcing them to emit in phase with the cavity field. However, the cavity field can be greatly impacted by vibrations of the cavity mirrors. Conversely, in the superradiant laser, the atoms are very coherent and will largely stay in phase on their own, sustained by the spontaneous build up of correlations as a result of the ensemble collectively emitting into the cavity mode. In the superradiant case, it is the cavity mode that is 'forgetful', so the intracavity field is directly locked to the atomic coherence.

At microwave frequencies, masers typically operate in the bad-cavity regime with a long history of contributions to precision spectroscopy [60, 90, 127]. Because the system actively oscillates, the linewidth is narrowed by the presence of many atoms oscillating and can be much narrower than both the broadened linewidth and potentially the atomic decay linewidth. Because of the thermal photon occupation at microwave frequencies, cryogenic operation is required for optimal stability [9]. In contrast, an optical system can potentially access quantum limits on performance, can operate in a novel regime with less than single quanta on average in the cavity-field, and can overcome fundamental thermal limitations on current optical light sources.

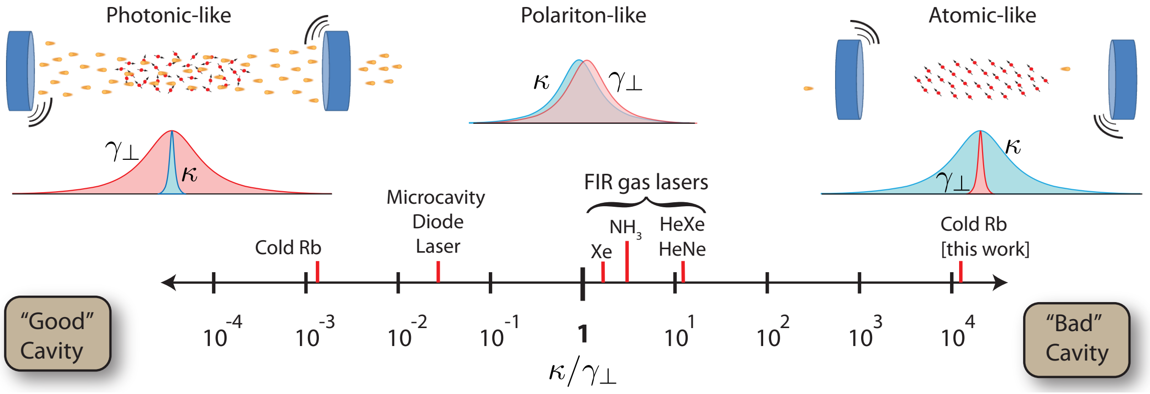

Figure 1.10: (Left) In the good-cavity limit, the atomic coherence rapidly decays, and the photon field is the primary reservoir of phase information in the laser. As a result, perturbations which disturb the cavity resonance frequency, such as thermal mirror vibrations (drawn as curved lines near the mirrors), limit the frequency stability of the laser. (Right) At the other extreme, the bad-cavity, or superradiant, laser presented here operates in a regime where the atomic coherence decay rate $\gamma_\perp$ is much less than the cavity power decay rate $\kappa$. In this regime, the atomic gain medium is the primary reservoir of phase memory in the laser, a fact represented by the aligned dipoles of the atoms and a cavity mode nearly devoid of light quanta. Because the emission frequency is primarily determined by the atoms, perturbations from fluctuations in the cavity frequency are suppressed. (Middle) Near the crossover regime, the phase coherence is jointly stored by the atoms and the cavity photons, making it a polariton-like excitation. Most optical lasers operate in the good-cavity limit (one example is the cold atom Raman laser of Ref. [156]), with microcavity diode lasers [12] and far infrared (FIR) gas lasers, using Xe [30], $NH_3$ [70, 162], and HeXe/HeNe [97], operating in the vicinity of the crossover, polariton-like regime. Our cold atom Raman laser is unique both in terms of operating so deeply into the bad-cavity regime, and also in that the steady-state intracavity photon number can be made much less than one.

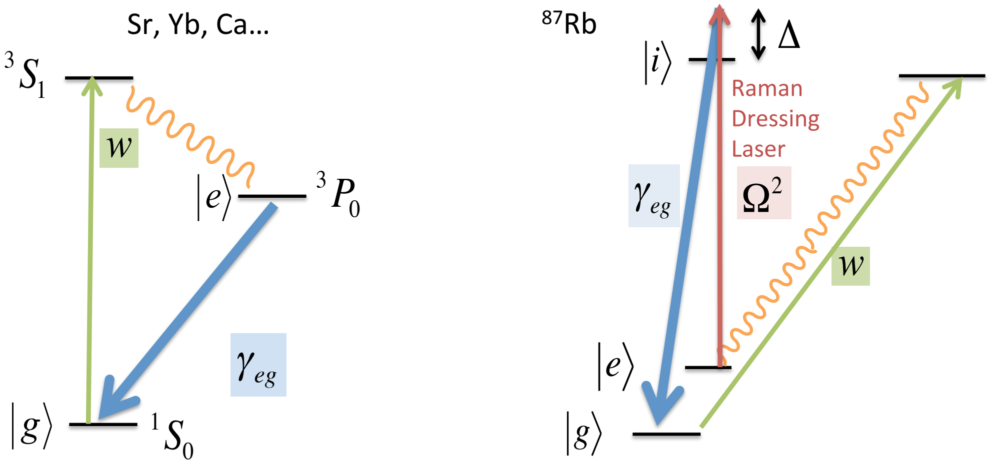

Figure 1.11: The long lived, nearly forbidden $^3P_0$ to $^1S_0$ transition in elements like Sr, Yb or Ca, with excited state decay rate $\gamma_{eg}$, is mimicked by a two photon Raman transition between hyperfine ground states in $^{87}$Rb. The Raman dressing laser, with Rabi frequency $\Omega$, is detuned from an optically excited intermediate state $|i\rangle$ to induce an optical decay from $|e\rangle$ to $|g\rangle$ at rate $\gamma_{eg}$, mimicking the naturally occurring decay on the left hand side. This decay rate can be tuned over a wide range by adjusting the dressing laser intensity and/or detuning from the intermediate state. In both cases, population inversion is maintained by incoherently repumping the atoms back to the excited state $|e\rangle$ using another laser that excites atoms in the ground state $|g\rangle$ to a short-lived optically excited state after which they quickly spontaneously decay to $|e\rangle$. The collective blue laser emission in both cases is resonant with the optical cavity mode, while the single-particle spontaneous emission for repumping (yellow) is not resonant and is scattered into free space.

Until recently, attempts to observe the features of optical lasers in the bad-cavity regime have been limited to operation near the cross-over regime (i.e. where the cavity linewidth is approximately equal to the linewidth of the gain medium). In the cross-over regime, the excitation of the oscillator is described best as a polariton, possessing significant atomic and photonic contributions (Fig. 1.10 center). Kuppens *et al.* [97, 98] studied HeNe and HeXe infrared gas lasers in the good-cavity to bad-cavity crossover regime $2\gamma_\perp/\kappa = 6$ to 0.2, with $2\gamma_\perp \approx 2\pi \times (100$ to $500)$ MHz, and with $M_\mathrm{c} \gg 1$ intracavity photons. They observed linewidths up to an order of magnitude below the naive linewidth limit expected in the good cavity regime $\Delta f_\mathrm{GC}$. Other work with far infrared gas lasers investigated the mapping of the Lorenz model onto the laser equations, observing signatures of chaos [67, 162]. Microcavity lasers, such as VCSELs, have operated near the bad-cavity regime [12], but their usefulness as a state-of-the-art phase reference is limited due to the linewidth broadening inherent in semiconductor gain media.

The utilization of nearly forbidden optical atomic transitions, along with advances in laser cooling and trapping, have opened up the possibility to access the superradiant regime in the optical domain. To minimize inhomogeneous broadening of the atomic transition, proposed narrow-linewidth superradiant lasers would use trapped, laser-cooled atoms as the gain medium [115, 33]. The first use of cold atoms as a laser gain medium was reported in Ref. [73]. Recently, the spectral properties of a cold-atom Raman laser were studied in a high finesse cavity, deep into the so-called good-cavity regime [156]. Clouds of cold atoms can also simultaneously provide gain and feedback for distributed feedback lasing [138] and random lasing [6]. Cold atoms have also been used as the gain medium in four-wave mixing experiments [61, 7, 13] and in collective atomic recoil lasing [94].

### 1.3.4 A superradiant Raman laser

In my thesis work, we use our $^{87}$Rb cavity QED system to realize a superradiant Raman laser as a controllable, model system to explore the physics of proposed superradiant optical lasers. By dressing a meta-stable ground state, we use a two-photon Raman transition to demonstrate operation deep into the optical bad-cavity regime, achieving $2\gamma_\perp/\kappa \sim 10^{-4}$. An energy level diagram showing the analogy between the two systems is shown in Fig. 1.11. Previously, Raman lasers using laser-cooled, untrapped atoms have operated in the good-cavity limit [156], or in the bad-cavity limit without studying the spectral properties of the light, with $M_{\mathrm{c}} \gg 1$ intracavity photons, and with no distinction between the Raman dressing laser and repumping laser[73, 64, 32]. Additionally, optomechanical forces have made interpretation of previous results difficult [32]. Four-wave mixing [64, 13] was used to observe a discrete quantum symmetry-breaking phase transition [7].

Starting in Chapter 4, I introduce a theoretical model of a superradiant laser, deriving the steady-state behaviors of the laser's atomic inversion, atomic polarization, and light field amplitude. Then in Chapter 5, I give the first experimental results using the apparatus described in Chapter 2, where we demonstrate lasing deep in the bad cavity regime with less than one intracavity photon and observe cavity frequency pulling coefficients $P$ as small as $5 \times 10^{-5}$. In Chapter 7, I identify relaxation oscillations and dynamic cavity feedback that can serve to damp or enhance oscillatory behavior of the laser field's amplitude, as well as the atomic inversion and polarization. The research into laser amplitude stability is supported by the linear response theory of a superradiant laser contained in Chapter 6. Finally, in Chapter 8, I connect the two topics of this thesis by exploring the connection between the Schawlow-Townes linewidth and the standard quantum limit for phase estimation. Because the coherence of a superradiant laser is stored primarily in the atomic ensemble, the laser light can be viewed as a continuous, non-destructive readout of a collective quantum phase. In this last chapter, I theoretically explain the optimal estimator of the quantum phase from the light field measurement and experimentally demonstrate using the superradiant readout for Ramsey spectroscopy, which has lead to additional work as a superradiant magnetometer [160].

# Chapter 2

# Apparatus

In this chapter, I describe the apparatus used to perform the experiments discussed in the later chapters, common to both the spin squeezing and superradiant experiments. First, I describe the laser systems, including the lasers, frequency stabilization, and frequency distribution to the experiment. Next, I describe the details of the science chamber, including the optical cavity used for the experiments. I give the schemes used for the optical trapping that prepares the atoms for the subsequent experiments. Finally, I give an overview of the detectors and electronics that are used to detect and process signals from the experiments. Technical details for specific experiments will be provided in subsequent chapters.

## 2.1 Laser Systems

Lasers are the primary way we control and manipulate the atoms' internal and external degrees of freedom in our experiment. The laser system used can be subdivided into three modules that operate mostly independently from one another. Two laser subsystems operate on the D2 line of $^{87}$Rb at 780 nm. The final subsystem uses lasers operating at both 795 nm (the D1 line in $^{87}$Rb ) and 823 nm (for an off-resonant optical lattice trap), combined into a single system using a stabilized Fabry-Perot cavity to transfer frequency stability to the trap laser and ultimately to the science cavity. In this section, I first describe the general external cavity diode laser (ECDL) design used throughout the experiment, then give the details on the individual laser subsystems. The section concludes with a description of the laser beatnote phase locks and RF signal generation

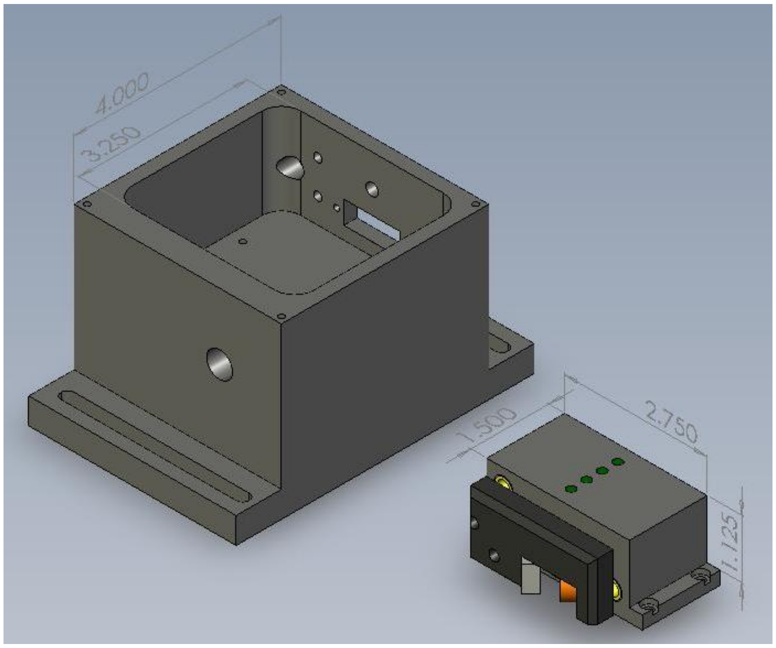

Figure 2.1: A CAD model of the custom ECDL used throughout the laser systems in our lab. The laser diode is mounted in the lens tube assembly. The diffraction grating (white) provides frequency selective optical feedback to the narrow the laser linewidth. The grating is mounted on the adjustable pivot. A piezoelectric slab provides a method of feeding-back to the grating position for wideband laser frequency tuning by pivoiting the assembly. The grating can also be manually adjusted with the two screws that push on the pivot. The 45° mirror out-couples the laser light (out-coupling lens not shown). The temperature control Peltier device rests under the mount as it sits in the external enclosure.

used to control the laser frequencies.

### 2.1.1 General ECDL design

All the lasers, except for the 780 nm narrow DBR lasers, are the same ECDL originally designed by graduate student Shannon Sankar and machined in the JILA instrument shop, shown in Fig. 2.1. The laser diodes are mounted in the internal mount, which is housed in the external enclosure. The different laser diodes used are described in their respective sections. The mount holding the laser diode is temperature controlled with a Melcor Peltier device (PN: UT8-12-25-F2) separate from the laser diode itself. The laser mount has an adjustable diffraction grating providing optical feedback to the laser diode. The gratings can be adjusted manually to optimize feedback into the diode which is critical for robust single mode operation of the lasers. The optimum alignment is associated with the lowest threshold current for lasing. A separate piezoelectric control provides tuning of the angle of the grating, adjusting the frequency of the optical feedback into the laser diode to provide wideband, mode-hop-free tuning when used in conjunction with a feedforward to the laser current. We observe at least 6 GHz mode-hop free tuning for the laser frequency for time scales on the order of seconds, turning the laser lock point by hand. The feedforward is the limit on the tuning range. We have observed rapid single mode frequency tuning (1.184 GHz per ms) for short frequency sweeps, on the order of 70 MHz, used in the experiments described in Ref. [35]. For these sweeps we assume only the current is changing and the grating tuning is not needed.

After exiting the ECDL enclosure, the beams pass through an opto-isolator, either from Electro Optics Technology (PN: WT-04-I-780-MP) for the 780 nm MOT and state preparation lasers or a Optics For Research (OFR) opto-isolator (PN: IO-3-795-HP). The output is coupled into single mode optical fibers for distribution throughout the experiment. All fiber optics used for laser signals are OZ optics (PN: PMJ-3AF3AF-780-5/125) single mode optical fibers. The fibers have an 8° angled output to avoid back reflections off the fiber tip. In addition, fibers that directly face the ECDL have an in-house AR coating applied to the tips. We avoid using fiber patch cord connectors as we noticed back-reflections that can modify the laser linewidth for the better or worse, but in a manner that drifts in time.

### 2.1.2 780 nm MOT and state preparation lasers

One laser system in our experiments serve primarily to generate the magneto-optical trap (MOT), to perform optical state preparation, and to maintain population inversion through incoherent pumping in the superradiant Raman laser experiments. The trapping and state prep laser system operates on the D2 line in $^{87}$Rb near 780 nm and consists of three ECDLs. Each one use a non-AR coated Sanyo laser diode (PN: DL-7140-201S) nominally selected for a lasing at 780 nm. An overview of the MOT and state preparation laser system is shown in Fig. 2.2.

The system starts with with the 780 nm Reference laser, which serves only as a reference for the other lasers and does not interact with atoms in the science chamber. The 780 nm Ref-

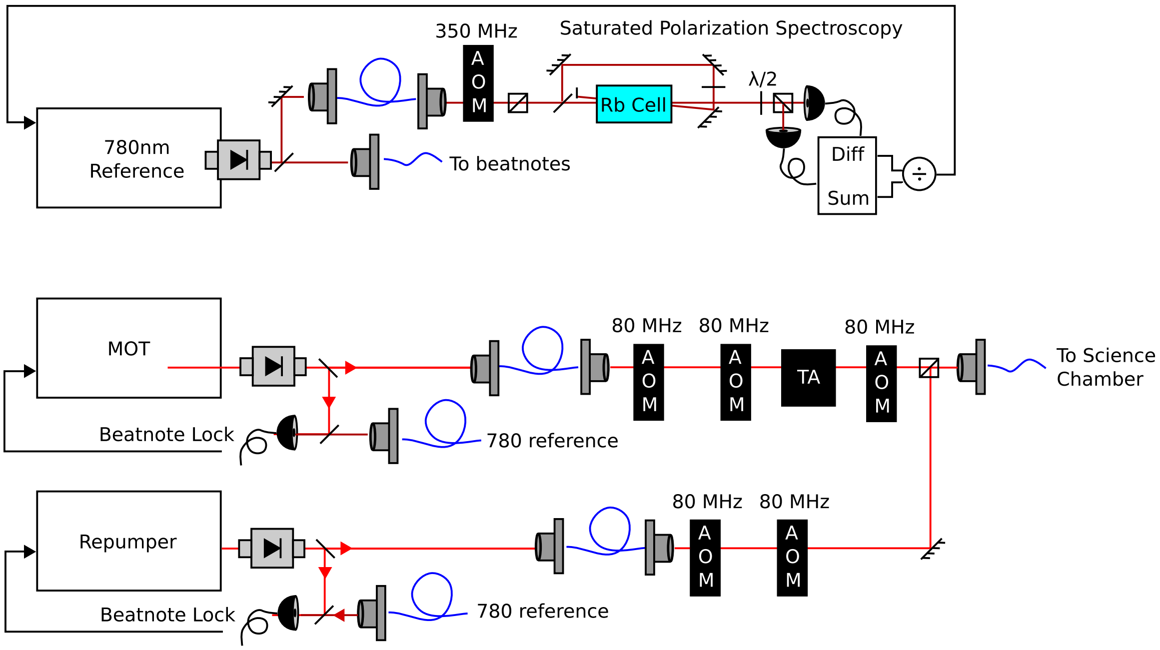

Figure 2.2: A schematic of the 780 nm laser subsystem used to generate the magneto-optical trap and perform state preparation using the D2 transition of $^{87}$Rb . The system consists of 3 ECDL lasers, labeled 780 nm Reference, MOT and Repumper. The 780 nm Reference laser is stabilized to an atomic frequency reference using a Doppler-free polarization spectroscopy. Both the MOT and Repumper lasers are beatnote stabilized to the Reference laser (not shown). Feedback loops are indicated by the black line leading back to the lasers.

| State | MOT ($F = 2$) BN [MHz] | Repumper ($F = 1$) BN [MHz] |
|---|---|---|
| F=0’ | – | 810 |
| F=1’ | 934 | 738 |
| F=2’ | 777 | 581 |
| F=3’ | 510 | 314 |

Figure 2.3: RF beatnote frequencies used to set the MOT and Repumper lasers to resonance from their respective hyperfine ground state to the excited states of the $^{87}$Rb D2 line.

erence laser frequency is stabilized to an absolute atomic reference using polarization saturation spectroscopy [122], locked to the F=2 to F=3’ transition of $^{87}$Rb. The lasers we call the MOT and Repumper lasers operate on the F=2 ground hyperfine state to excited state and F=1 ground hyperfine state to excited state respectively. The lasers are stabilized to the atomic reference using a laser beatnote lock, described in Section 2.1.5. We can control the frequency of both the MOT and Repumper laser using the beatnote reference frequency, giving us the ability to address the entire excited state structure from the ground hyperfine state associated with each laser. The beatnote frequencies needed for the two lasers are given in Table 2.3.

The MOT laser is amplified with an Eagleyard tapered amplifier (PN:EYP-TPA-0780-01000-3006-CMT03). After passing through Isomet AOMs (PN: 1205C-1) which act as a fast switch, the beam is split to produce 6 beams each containing 3 mW of power. The beams form 3 pairs of counter-propgating beams to trap in all three spatial dimensions. The details of the MOT are described in Section 2.3.

The Repumper laser is combined with the MOT beam just before being split to 6 beams to maintain separate control over the Repumper beam power. The light co-propagates with the MOT laser to provide repumping for atoms in the F=1 hyperfine ground state. There is enough power such that each of the six paths contains 0.5 mW of repumping light.

In an attempt to vary the density of the atomic ensemble in the trap, we added an additional set of MOT trapping beams that only confine the atomic ensemble in two dimensions. These beams are generated by picking off 30% of the MOT light and directing it into two beam perpendicular to each other and the cavity axis. The beams are retro-reflected to provide the 2D confinement. These beams were used for the superradiant laser experiments and were not used for the spin squeezing results. The orientation of the beams is given in Section 2.3.

### 2.1.3 780 nm Narrow DBR Lasers

The key technical advance for the coherence preserving, non-destructive population measurement in this work was the implementation of probing the atomic population on a cycling transition of $^{87}$Rb , which only exists for the D2 transition. However, the hyperfine ground states associated with the cycling transition have a significantly reduced coherence time compared to so-called clock transition used in our previous work [35]. The reduced coherence time requires a faster measurement sequence, which then imposes constraints on the laser frequency noise beyond what we could achieve with the ECDL setups described previously.

We have implemented a second D2 laser system to produce a narrow linewidth probe laser (Fig. 2.4. The system uses two distributed Bragg grating reflector (DBR) lasers with an extra long external cavity feedback setup to generate a narrow linewidth probe laser. We label the two lasers as the DBR Reference and DBR Probe. Both lasers start with a Photodigm DBR laser in a long eternal cavity setup [106] to provide optical feedback to the laser diode, resulting in good short term frequency stability properties. Measurements indicated both lasers have linewidths of $\sim$ 5 kHz. The DBR Reference laser is stabilized to an atomic rubidium reference frequency for long term stability using modulation transfer spectroscopy (MTS) [110]. The MTS locks the laser to the $F = 3$ to $F = 4'$ transition in $^{85}$Rb and provides both high frequency feedback to the laser diode current and low frequency feedback to the length of the external cavity through a Thorlabs piezo stack (PN: AE050D08F).

The DBR Probe laser is frequency offset locked, or beatnote locked, to the DBR reference laser, providing us the flexibility to set DBR Probe laser frequency to any $F = 2$ to excited state transition. A beatnote of $-1.246$ GHz places the probe laser on resonance with the $F = 2$ to $F = 3'$ transition in $^{87}$Rb. In the squeezing experiments where a DBR probe laser detuning from the transition by $+200$ MHz was used, the beatnote was set to $-876$ MHz to account for the AOMs

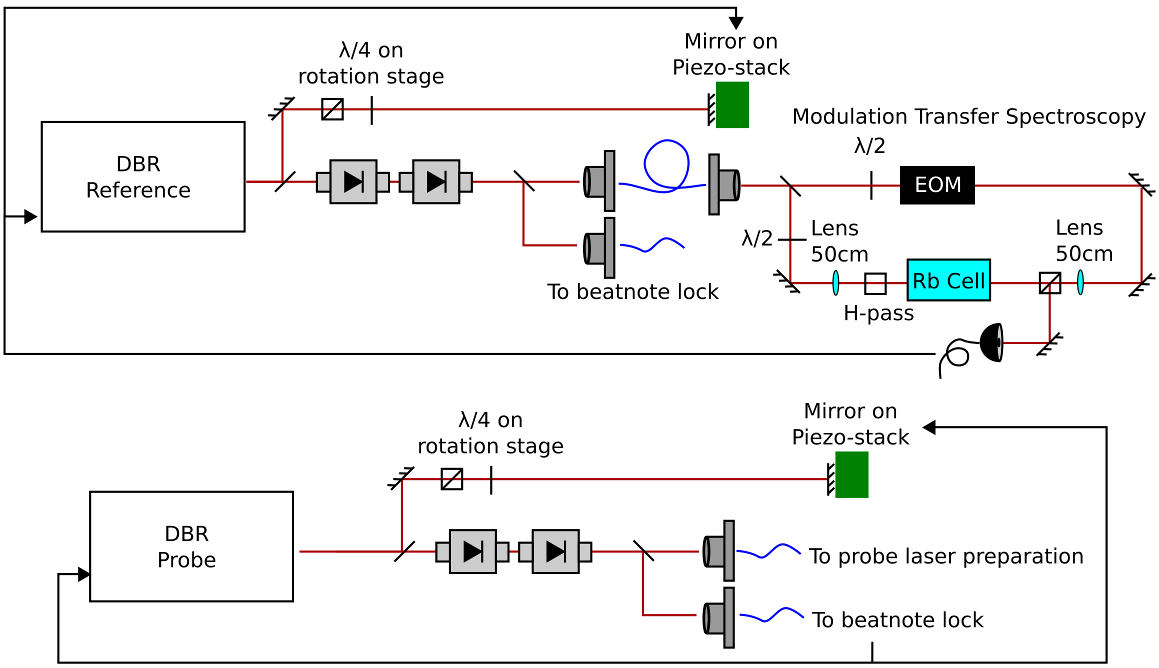

Figure 2.4: A schematic of the 780 nm narrow linewidth DBR laser subsystem used to generate the probe laser on the D2 transition of $^{87}$Rb for the spin squeezing experiment. The system consists of 2 Photodigm DBR lasers, labeled DBR Reference and DBR probe. The DBR lasers have improved short term stability properties due to the optical feedback provided by the long external free space cavity, of length $\sim 0.5$ m. We can tune the magnitude of the optical feedback using the $\lambda/4$ waveplate and polarizing beam cube in the feedback path. The reference laser provides long term frequency stability by locking to an atomic reference with MTS. The probe laser is then beatnote locked to the reference laser, giving us tunable control over the probe frequency over a range of 3.2 GHz.

and EOM in the probe path, described in detail in Chapter 3. We can also sweep the laser frequency by sweeping the beatnote lock reference RF frequency, controlled by our direct digital synthesis system, described in Section 2.1.6.

Tuning of the long external cavity feedback is largely empirical. We start by looking at the beatnote on a wideband spectrum analyzer, with either the 780 nm Reference ECDL laser in the case of the DBR Reference, or with the DBR Reference in the case of the DBR Probe. As the optical cavity feedback is increased by changing the $\lambda/4$ waveplate, peaks start to appear in the beatnote, separated by the external cavity free spectral range of 50 MHz. The feedback is increased until the point where the laser oscillates at multiple longitudinal modes of the external cavity when the feedback loop is engaged. Then the waveplate is turned slightly to decreases the optical feedback so the laser can operate on a single mode. Fine tuning of the laser spectrum is performed by forming the probe heterodyne signal with the bare cavity (described in detail in Chapter 3), and minimizing the detection noise by changing the feedback loop parameters.

The presence of multiple external cavity modes impacts the laser spectrum by adding small noise bumps appearing at $\sim$ 50 MHz from the optical carrier. In our heterodyne measurement of the probe beam, the signal can appear at an RF frequency between 0 and 200 MHz, so care must be taken to avoid the noise bump near 50 MHz to preserve the highest signal to noise of the heterodyne detection.

### 2.1.4 795 nm and 823 nm Science Cavity lasers

In this section, I described the laser system that generates the beams used for trapping the atoms in the optical lattice, frequency stabilizing the science optical cavity, probing the cavity resonance frequency on the D1 line at 795 nm, and creating the effective optically excited state by dressing the ground hyperfine state used for the superradiant Raman laser. This system consists of four ECDL lasers with the same design as was described earlier. We call these lasers the 795 nm Reference, Dressing, Transfer, and Lattice lasers.

The 795 nm Reference laser provides an absolute frequency reference for long term frequency stability. The frequency stability is extended to the lattice trap laser, and ultimately the science cavity, using the Transfer laser and a second Fabry-Perot optical cavity called the transfer cavity. A simplified schematic is shown in Fig. 2.5. The basic idea is that the Transfer laser is beatnote locked to the 795 nm Reference laser, and the transfer cavity length is stabilized with the Transfer laser. The Lattice laser is then frequency locked to a lower longitudinal mode of the transfer cavity, and the science cavity is finally locked to the lattice laser, stabilizing it with respect to atomic resonance. Therefore, changing the Transfer laser beatnote ultimately changes the science cavity frequency. The details are described below.

The Reference, Dressing, and Transfer lasers all use Eagleyard anti-reflection (AR) coated laser diodes at 795 nm (PN:EYP-RWE-0840-06010-1500-SOT02-0000) in the ECDL setup. The 795 nm Reference laser is stabilized to the $F = 3$ to $F = 2' - 3'$ crossover signal of $^{85}$Rb with frequency modulation saturation spectroscopy [68]. The Dressing and Transfer lasers are stabilized to the 795 nm Reference laser using a beatnote lock. The Dressing laser is a versatile laser which functions as both the Raman dressing laser and a cavity resonance frequency probe in the superradiance experiments described in subsequent chapters. The output of the Dressing laser has three important outputs to the science chamber. The first is the Dressing beam path, which after passing through an Isomet AOM to act as a fast switch, goes directly to the science cavity. The beatnote lock of 845 MHz places the Dressing beam on resonance with the $F = 2$ to $F = 2'$ transition on the D1 line of $^{87}$Rb . While running superradiance, the beatnote was most often set to $-255$ MHz to place the dressing laser $+1.1$ GHz detuned from the $F = 2$ to $F = 2'$ transition, though the beatnote allowed for flexible changing of the detuning ranging from $\sim \pm 3$ GHz.

Early in the dressing laser path, half of the power is split off to form the the probe and superradiance heterodyne beams. The light passes through an EO Space phase modulator (PN: PM-OK5-PFU-800-UL). The modulator can generate frequency components more than $\pm 6.8$ GHz from the optical carrier, bridging the hyperfine splitting so that the probe beam can be resonant with the optical science cavity resonance that is usually $\sim 1.1$ GHz detuned from the $F = 1$ to $F = 2'$ atomic transition. The two frequency components on the heterodyne beam also allow us to

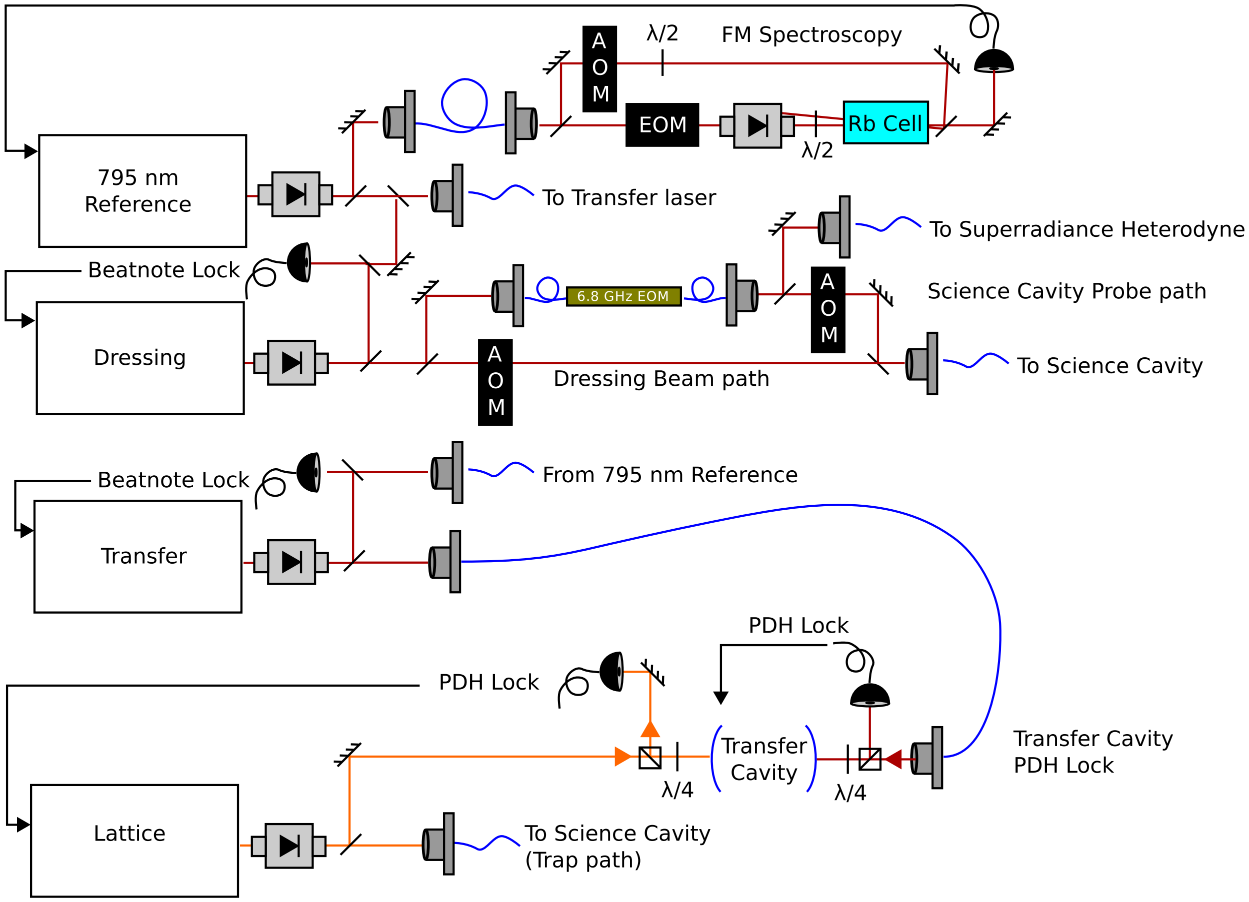

Figure 2.5: The 795 and 823 nm laser subsystem. The subsystem consists of three ECDLs at 795 nm (the 795 nm Reference, Dressing, and Transfer lasers) and one ECDL at 823 nm (the Lattice laser). All are ultimately referenced to the $F = 2 - 3$ to $F = 3'$ crossover signal of $^{85}$Rb through beatnote locks in the case of the Dressing and Transfer lasers, and using the transfer cavity in the case of the Lattice laser. The transfer cavity is locked to the Transfer laser using a PDH lock to stabilize the cavity length, then the Lattice laser is PDH locked to a longitudinal mode of the transfer cavity near 823 nm. The Dressing laser is split into three functions, generating the Raman dressing light for inducing superradiance, probing the science cavity resonance frequency, and providing the heterodyne reference beam in the superradiance experiments. The difference in the dressing laser frequency and the probe frequency is bridged by a EO Space phase modulator driven near the hyperfine splitting frequency. The Heterodyne beam is path is also phase modulated, so that RF beatnotes of both the superradiantly emitted light and the dressing light can be obtained.

form detection signals of both the dressing light ($\sim +1.1$ GHz detuned from the $2-2'$ transition) and the emitted light ($\sim +1.1$ GHz from the $1-2'$ transition). The probe light is recombined with the dressing light for most of the superradiance results, as both go to the science cavity.

The optical lattice trap is generated by injecting a laser that is far red-detuned from atomic resonance along the cavity cavity axis to build up a standing wave inside the science cavity. This Lattice laser uses another Eagleyard AR coated laser diode that is nominally wavelength selected to 820 nm. Measurements with an optical wavemeter indicate that the wavelength we use is near 823 nm. The frequency of the laser is stabilized with respect to the 795 nm reference laser using a transfer cavity, as shown in Fig. 2.5. The optical lattice trap confines the atoms to the waist of the optical cavity $\text{TEM}_{00}$ mode, near the center of the cavity as described later in Section 2.3.3.

The transfer cavity is a Fabry-Perot cavity with a length of 3 cm and a finesse of 5000. The cavity mirrors are glued to piezo-electric stacks which are mounted on a Zerodur spacer. The transfer cavity length is stabilized using a Pound-Drever-Hall (PDH) lock [46, 14] to the frequency-stabilized Transfer laser. When in lock, tuning the reference frequency of the Transfer laser beatnote lock allows us to change the transfer cavity length. We found that adjusting the resonance frequency of the cavity by more than $\kappa$ put the cavity outside of the PDH lock range, and the cavity would become unlocked from the laser and unable to re-capture lock without manual tuning.

With the transfer cavity frequency stabilized to the atomic reference at 795 nm, the cavity provides a series of resonances separated by the free spectral range, about 7 GHz. We again use a PDH lock to now stabilize the 823 nm laser to one of these resonances, fixing the lattice trap laser in frequency with respect to an atomic transition. Finally, we use another PDH lock to stabilize the science cavity (described in Section 2.2), controlled by Piezomechanik piezoelectric stacks (PN: PZT-5H). We can use the transfer cavity to then ultimately change the optical cavity resonance frequency, setting it to the desired detuning from atomic resonance. The change in the trap frequency is small enough to be negligible for the purposes of the off-resonant trapping light.

### 2.1.5 Details of laser beatnote locks

Laser beatnote locks are used to stabilize trapping and probing lasers with respect to the reference lasers. The laser beatnote locks give agile control over the laser frequencies during the experiment. The beatnote typically is detected with high speed Hamamatsu GaAs photodiodes (PN: G4176-01, TO-18 package) connected to a Mini Circuits Bias Tee (ZX85-12G-S+) providing +5 V of DC bias (exceeding 10 V kills the diode immediately). The signal is amplified using a microwave frequency SBW5089 MMIC amplifier. This detector provides the VCO signal for a Hittite HMC 440S16G phase frequency detector, with a reference signal provided by the Analog Devices DDS boards (PN: AD9959) described in Section 2.1.6. Although the minimum reference frequency specified by the HMC 440QS16G is 10 MHz, we found a square wave reference frequency was needed to operate below 20 MHz.

### 2.1.6 Direct Digital Synthesis

We use a series of versatile, phase coherent Analog Devices direct digital synthesis (DDS) chips (PN: AD9959) to generate RF frequencies ranging from a few MHz to 200 MHz for use throughout the experiment. The chips are integrated in evaluation boards purchased from Analog Devices. In principle, the DDS can produce frequencies up to 500 MHz using the digital image frequencies, but a high-order 200 MHz low pass filter is included on the output of our boards to reject the high frequency image signal. The DDS boards share a common 500 MHz clock derived from the 5x multiplication of a Wenzel 100 MHz crystal oscillator (PN: 501-16843), with long term stability provided by a rubidium atomic clock from Stanford Research Systems (PN: FS725). The 5x multiplier is constructed using surface mount PIN diodes (PN: BPF-B503+) [151]. The same 100 MHz oscillator also provides the phase stable microwave frequencies used to manipulate the ground states in $^{87}$Rb using the microwave source described in detail in Ref. [36]. For RF frequencies that do not need sweeps of the frequency or ramps of the power, we control the DDS chips via serial communication from our Labview experimental control and data acquisition software.

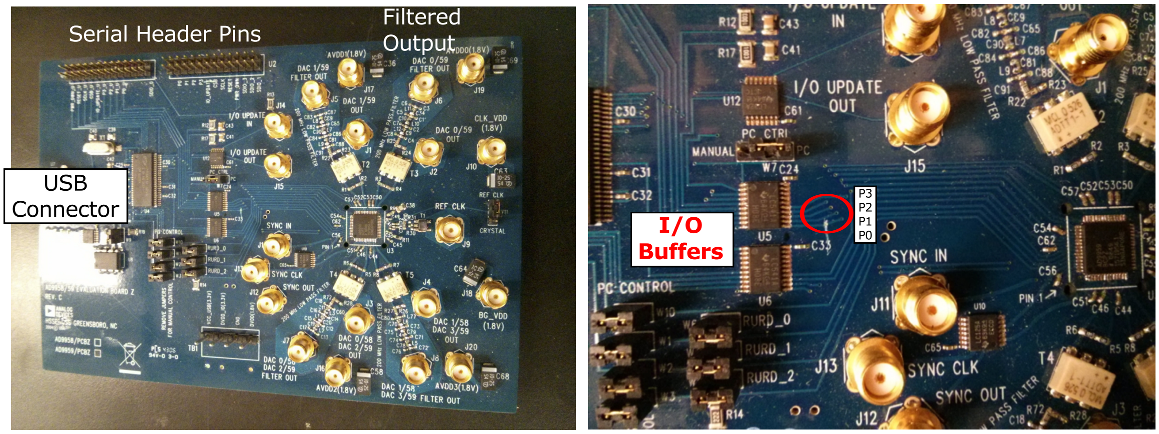

Figure 2.6: The Analog Devices AD9959 direct digital synthesis evaluation board shown fully on the left and zoomed in on the right. The evaluation board has two modes of control, either serial control through the header pins at the top of the picture, or through a USB control on the left side of the picture. To enable pre-programmed ramps of the frequency, amplitude, or phase of the DDS channels using an external TTL signal, we modified the evaluation board. The ramps are controlled by profile pins to the DDS chip, P0, P1, P2, and P3. These pins connect to the serial header, but the I/O buffer (chip U5, PN: 74LVC5414A) connects the USB profile inputs (PX_U) to the profile pins. By cutting the traces from the IO Buffer (chip U5, pins 11-14), the profile pins are freed to be controlled by the serial headers. In the photograph on the right, the traces corresponding to the profile pins are circled in red. Here only the trace for profile pin P0, corresponding to pin 11 on U5, has been cut.

For measuring cavity resonance frequencies, a probe laser frequency is often swept in time by using a triggered sweep of a DDS frequency to vary a laser beatnote lock reference frequency. We have two DDS boards dedicated to sweeping, each with four output channels. These boards are not controlled with serial communication, but use the evaluation software included with the evaluation board and interfaced through a USB controller. In principle, we should be able to control sweep functions by serial commands from Labview as well, but for unknown reasons, repeated attempts to add this functionality failed. To allow the chips to have sweeps triggered by an external TTL signal that did not come through the USB channel, we disconnected the DDS profile pin connections to the USB sweep trigger lines. This allows us to preprogram sweeps using the USB software, while triggering them with TTL signals provided by our Labview data acquisition system. The details are described in Fig. 2.6.

## 2.2 Optical Cavity and Science Chamber

In this Section, I give an overview of the Fabry-Perot optical cavity used in both of the projects described in the thesis. This includes details of the cavity mirrors, their mounting and stabilization, and the vacuum chamber that houses the optical cavity. The optical cavity is shown in Fig. 2.7, and the vacuum chamber is shown in Fig. 2.12.

### 2.2.1 Optical Cavity

The optical cavity is a nearly confocal Fabry-Perot cavity. The mirrors are dielectric coated mirrors produced by Advanced Thin Films. The super-polished substrates are 7.75 mm in diameter with a 5 cm radius of curvature. The dielectric coating produced highly reflecting mirrors at wavelengths ranging from 750 nm to $> 850$ nm. The mirrors had a specified transmission coefficient of 2500 ppm, and the delivered mirrors were measured to have transmission coefficients at 780 nm and 795 nm of $T_{780} = 2011$ ppm and $T_{795} = 2122$ ppm respectively.

The length of the optical cavity is controlled using piezoelectric stacks from Piezomechanik (PN: PZT-5H), one on each side of the cavity. The piezo stacks have a tubular geometry. Mirrors fit inside cylindrical piezo tubes and are held in place with the Torr Seal. The piezos have free-standing axial/radial resonance frequency of 80/75 kHz. After one set of wires that apply voltage to the piezo stacks shorted, arcing through vacuum, we restricted the operating range of the voltage applied to the piezo stacks. In the future, we could include separate vacuum feedthroughs for each piezo. Then in the case that one piezo fails, we can still drive the other. After the arc, we noticed an increase in the cavity linewidth associated with increased losses from the cavity mirrors, reflected in the cavity finesse $F$ in Table 2.10.

In Tables 2.9 and 2.10, I give a table summarizing the important properties of the cavity modes for the three wavelengths of interest. The numbers are based primarily on the specifications given by ATF for the mirrors and measurements performed of the cavity mode resonant structure at 795 nm.

Figure 2.7: Photograph showing the optical cavity spacer, piezos and mirrors inside the glass cell vacuum chamber. The smaller coils of copper wire are the initial, symmetric MOT coils. The larger wire coils provide bias magnetic fields in all three directions.

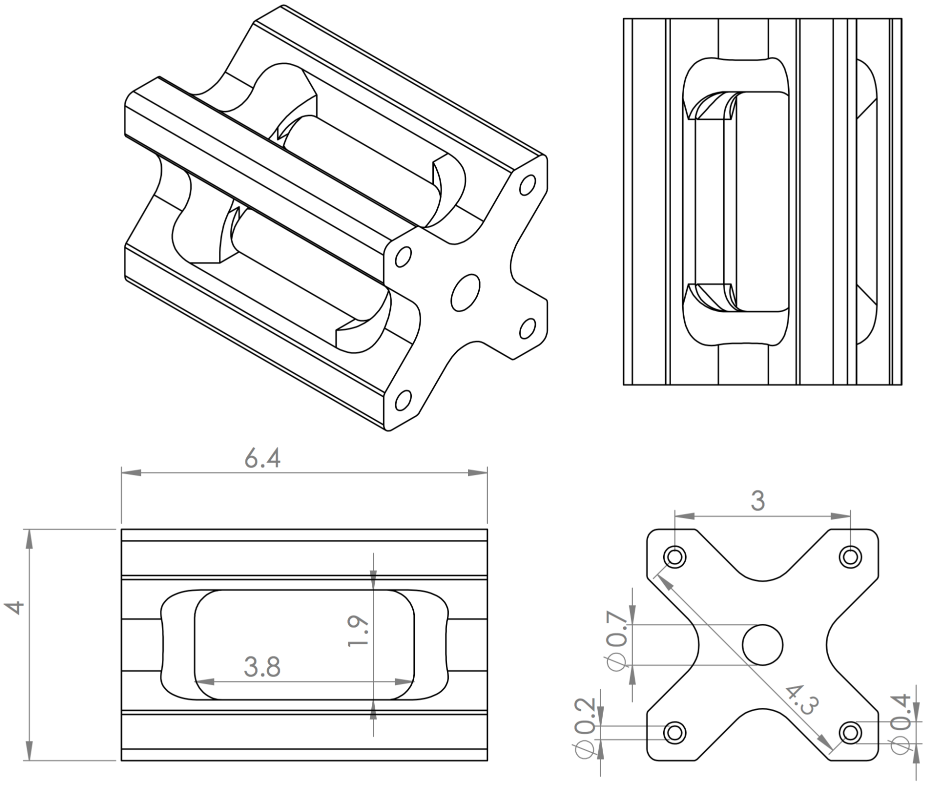

Figure 2.8: A drawing of the cavity spacer. All dimensions are given in units of cm. The spacer was machined from a single piece of Zerodur. The spacer is supported by four rods at the midpoint of the cavity. The holes for the support rods are symmetric on both ends of the spacer for common mode rejection of vibration. The angled cutouts on either end of the cavity allow for better optical access for the angled MOT beams.

| **Parameter** | |
|---|---|
| Free spectral range $f_{FSR}$ | 7828(1) MHz |
| Transverse mode spacing | 2257(1) MHz |
| Cavity length $L$ | 1.9149(2) cm |
| Mirror radius of curvature | 5.00(1) cm |
| Rayleigh range $Z_R$ | 1.967(2) cm |

Figure 2.9: List of science cavity parameters that are constant across wavelength.

| **Parameter** | 780 nm | 795 nm | 823nm |
|---|---|---|---|
| Measured Linewidth [MHz] | $11.8 \times 10^6$ | $11.1 \times 10^6$ | – |
| Finesse $F$ | 663 | 705 | – |
| Mode waist [$\mu$m] | 69.9 | 70.6 | 71.8 |
| Mode Volume [cm$^3$] | $7.35 \times 10^{-5}$ | $7.49 \times 10^{-5}$ | $7.75 \times 10^{-5}$ |

Figure 2.10: Science cavity parameters for the relevant wavelengths in including the spin squeezing probe at 780 nm, the superradiance at 795 nm, and the trap at 823 nm.

The mirrors and piezo tubes are mounted to a spacer machined from a solid piece of Zerodur. The vertical cavity orientation and spacer support points located midway between the mirror give common-mode rejection of vibrations to passively stabilize the cavity length. The spacer rests on Viton spheres for additional vibration damping. A drawing of the cavity spacer is shown in Fig. 2.8. The machining was performed by Hans Greene in the JILA machine shop.

The spacer is supported by four support rods that attach to a vibration damping system in the vacuum chamber, seen in Fig. 2.12. The spacer supports connect to the support damping structure inside the spherical cube. The support structure also rests on three Viton spheres for damping. The long pendulum that hangs down off the support structure serves to lower the resonance frequency of of any vibrations the would shift the cavity position. We found that in practice, low frequency vibrations in the floor of the building, caused by an air conditioning fan, would cause 17 Hz vibrations in the cavity damping structure, and modulating the coupling of our probe beam to the cavity. This appeared as fluctuations in the reflected and transmitted power, as the coupling into single mode optical fibers from the cavity was very sensitive to laser pointing stability.

### 2.2.2 Vacuum System

The heart of the vacuum system is the spherical square from Kimball Physics (PN: MCF450-SS20400) that sits just above the optical table. The bottom of the cube connects to the vacuum pumps, and the top connects to a metal-to-glass transition that holds the glass cell containing the cavity spacer. One of the side ports is occupied with a valve connected to the source of rubidium, which is kept between 40 and 50 C° to provide a rubidium vapor throughout the vacuum chamber. A second port of the optical cube is used for electrical feedthroughs to drive the piezoelectric tubes that position the cavity mirrors. Finally, the third port is a window to allow laser light to bounce off a 45° mirror at the center of the spherical cube and propagate upwards to the cavity. The system was initially pumped down with Varian turbo pump (PN: Turbo V 81-M, IDP-3 Dry Scroll Pump). The vacuum is maintained with a Varian VacIon Starcell 50L/s ion pump (PN: 9191340). We measure pressure with a Varian Ion gauge (PN: UHV-24P).

## 2.3 Magneto Optical Trap and Lattice Trap

In this section, I describe the procedure for trapping and cooling approximately $10^6$ atoms near the middle of the optical cavity and localizing them near the radial center of the cavity mode as well. The procedure starts with a magneto-optical trap (MOT) [124] which is then loaded into a 1D optical lattice formed by the resonant standing wave at 823 nm created by the optical cavity. After the lattice trap is loaded, the sample is sub-Doppler cooled using polarization gradient cooling (PGC) and the experiments begin.

### 2.3.1 Beams

Optical molasses for the MOT is provided by the six MOT beams, derived from the MOT laser described in Section 2.1.2. Each beam has a characteristic diameter of 1.2 cm. Repumping light co-propagates with each MOT beam to close the cycling transition. The six beams intersect at the center of the optical cavity as shown in Fig. 2.11.

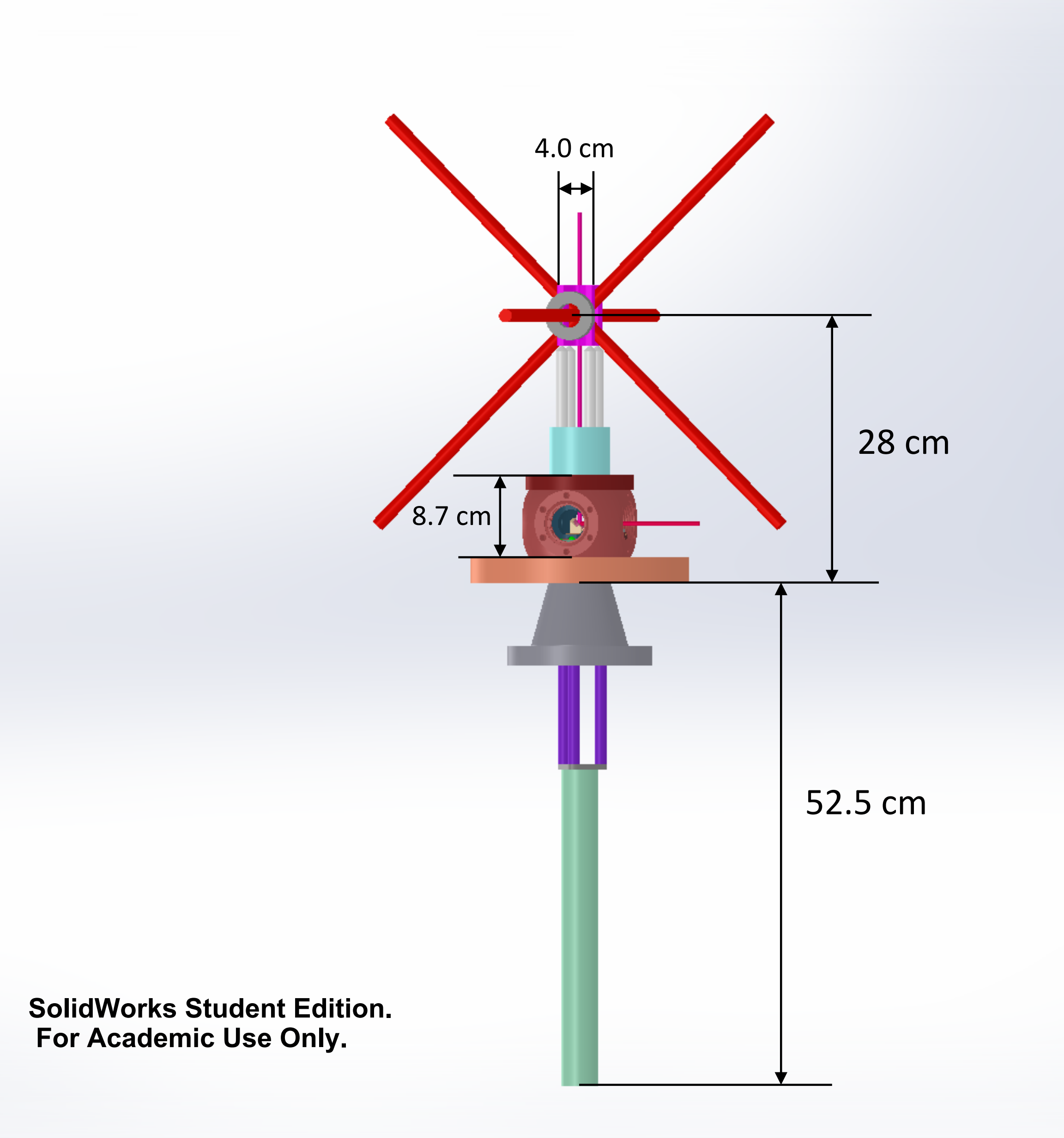

Figure 2.11: A drawing of the complete vacuum system (the glass cell surrounding the cavity spacer is not shown). The vacuum chamber below the reducer fitting (grey) is not shown. The cavity spacer is in magenta, the MOT coil is in light grey, the spacer supports are in white, and Kimball Physics spherical square in dark red. The damping pendulum hangs off the support structure with the purple rods. The pendulum weight is colored light green. The three pairs of MOT beams intersect at the center of the cavity spacer. The cavity axis beam path is shown entering the spherical square and exiting out the top of the optical cavity. The distance to the center of the cavity and the end of pendulum are both measured from the top of the optical table.

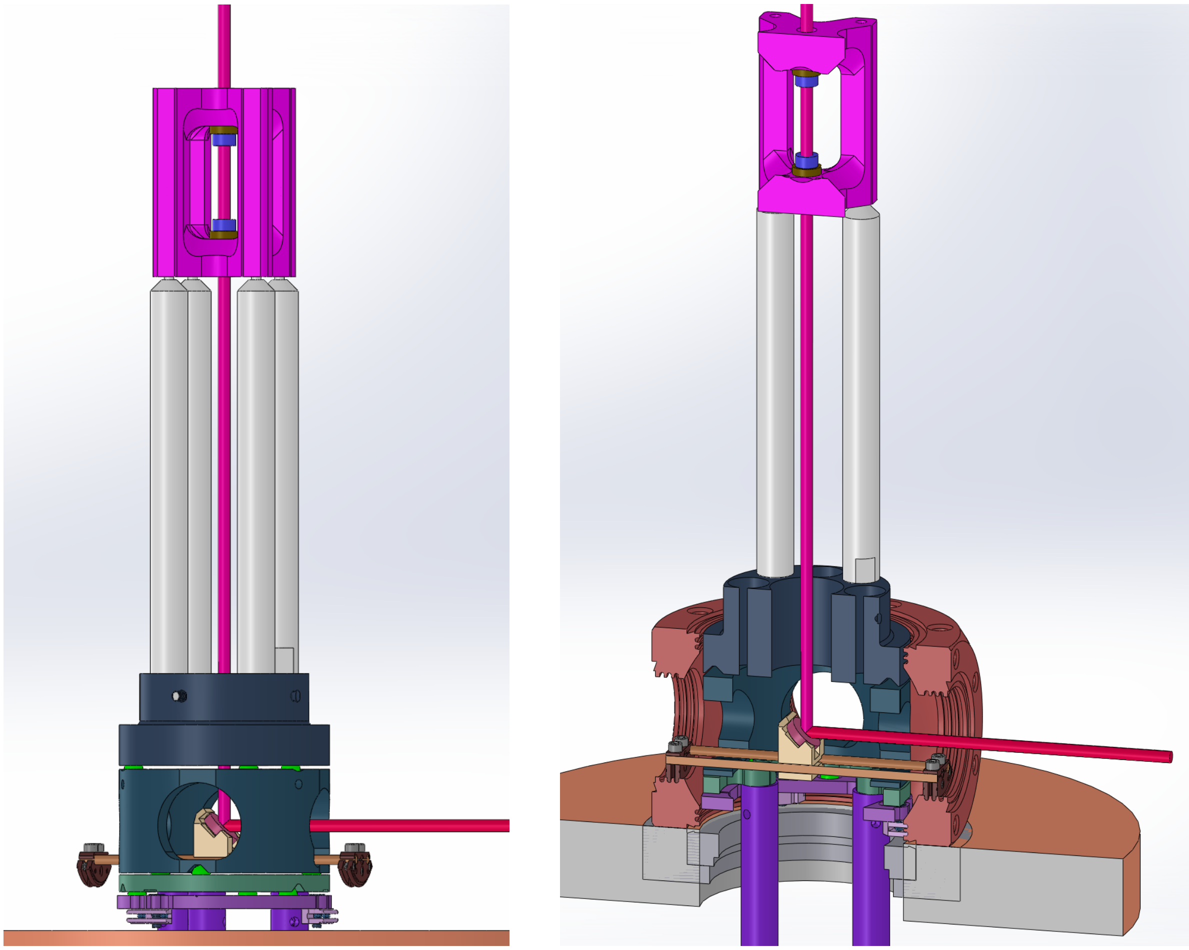

Figure 2.12: (Left) The CAD model of the vacuum chamber, cavity support system, and cavity spacer. A probe laser beam is shown entering a vacuum port, bouncing off the 45° mirror and coupling to the cavity. (Right) A cutaway view of the cavity support structure. The cylindrical support structure (dark grey) links the cavity spacer supports (white) to the damping pendulum (purple). The damping pendulum (seen in Fig. 2.11) hangs off the support structure, which rests on 3 Viton spheres (bright green) for damping. The 45° mirror is mounted on rails connected to the vacuum chamber with Groove Grabbers.

One additional pair of MOT and Repumping beams were added perpendicular to the original horizontal beams. By leaving on only these two pairs of beams, we found that we could create a 2D MOT which would allow atoms to spread out along the cavity axis and load into about twice as many lattice sites as with the 3D MOT alone. In the loading sequence, this 2D MOT step was on for 5 ms after initial 3D lattice step, and then the atoms were loaded into the lattice.

### 2.3.2 Coils and Drivers

The addition of the magnetic field provides the true confinement to the MOT. In the experiments described here, we have primarily used a pair of asymmetric coils of wire to provide the magnetic quadrapole field needed for trapping. The MOT coils are elongated with the goal of providing an elongated MOT to allow more atoms to be confined in the optical lattice with the same atomic density by spreading them over more lattice sites utilizing the 2D MOT beams. A schematic of the coils are included in Fig. 2.13. The current in the coils is $\sim 2$ Amps for the circular coils and $\sim 3$ Amps for the elongated coils. The current is driven with high voltage power MOSFETs from Advanced Power Technology (PN: APL501J). The gradient established by the MOT coils is $\sim 34$ G/cm.

Three pairs of additional coils are used to apply small bias fields, such that the total current flowing is 0.75 to 1 Amp. The bias coils are seen in Fig. 2.7. The bias field typically applied to define a quantization axis is 3 Gauss.

### 2.3.3 Lattice Trap

The optical lattice trap is operated with intracavity lattice powers ranging from 0.3 W circulating in the spin squeezing experiment to up to 1 W circulating in the superradiance experiments. In the spin squeezing experiments, 26 mW was delivered to the 50/50 beamsplitter that directs lattice light to both the cavity and the path length fluctuation measurement (see Chapter 3 for details, particularly Fig. 3.8). In the superradiance experiments, all the lattice light was directed to the cavity alone, allowing us to reach 1 W circulating powers only directing $\sim 40$ mW to the

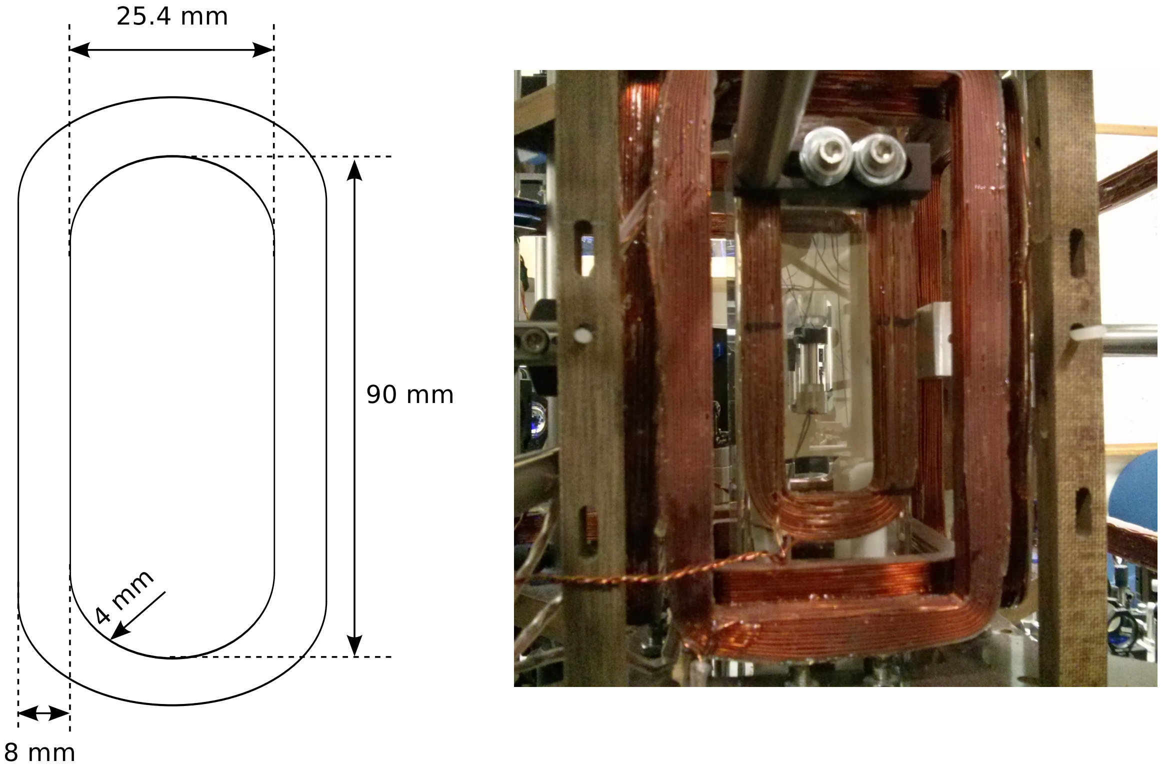

Figure 2.13: (left) A basic schematic of the elongated MOT coils used for most of the experiments presented in this thesis. The Coil is composed of 128 turns of Belden 20 AWG magnet wire. The individual turns are held together with Araldite 2011 Epoxy. Each layer of the coil is 12 turns, making the coil 10.7 mm deep. The rounded inside corners have a radius of curvature of 4 mm. (right) A photograph showing the elongated MOT coil mounted in the experiment. The coil sits inside the larger bias coil.

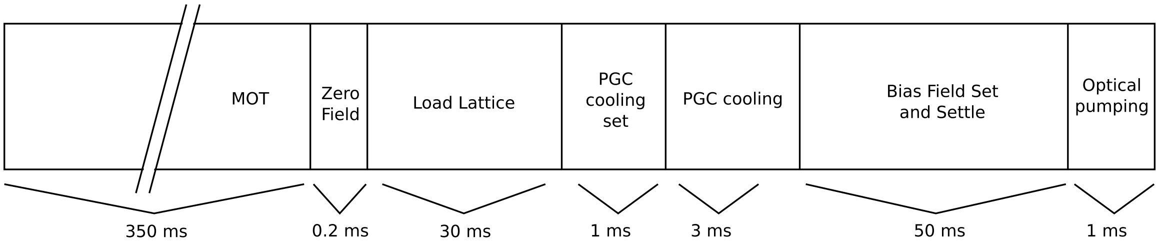

Figure 2.14: A general time sequence that begins each of the experiments in this dissertation (not to scale). Maybe a chart showing what lasers are on and what the B-field is doing here would be useful?

dichroic mirror that overlapped the Dressing laser and the Lattice laser. The given intracavity powers result in lattice trap frequencies of 180 kHz and 335 kHz for the squeezing and superradiance experiments respectively. The intracavity power is stabilized by detecting the transmitted light and feeding back to the power of the RF drive of an AOM acting as an amplitude modulator.

### 2.3.4 Loading Sequence, PGC cooling

Fig. 2.14 shows a general time sequence that contains the usual experimental sequence that prepares the atoms in the optical lattice trap and in a well-defined internal state to begin the experiments. Over the course of the experiments, some timings or details of the applied laser power may vary slightly, but this diagram gives the overall procedure.

We start by forming the MOT directly from the rubidium vapor between the optical cavity mirrors. The MOT laser was set to be slightly red detuned from the 2-3' transition, and the Repumper laser set slightly red of the 1-2' transition. Both laser frequencies are empirically tuned to maximize the atom number loaded in the trap. For the usual 1 Hz repetition rate for the experiments, this step was about 350 ms, though to vary the atom number $N$ ultimately loaded into the lattice, we would increase or decrease this time. We also varied $N$ by changing the power in the MOT beams during this step.

With a healthy MOT formed, we then load into the lattice trap by eliminating the magnetic quadrapole field and using the bias coils to zero the magnetic field at the location of the atoms. We jump the MOT light to 50 MHz to the blue of the 2-2' transition. During this time, the intensity of the MOT and Repumping light is stepped downward. Then the F=2 MOT light is stepped even further down for the remaining loading time. Note that the lattice light is always on all throughout the process. The optimal time to load the lattice has varied from 30 to 50 ms over the course of this and is manually tuned for a given experiment.

After the lattice trap loading period, the MOT laser is adjusted to +20 MHz detuned from the 2-2' transition for the polarization gradient cooling step. All light is extinguished for 1 ms while the laser frequencies settle. Polarization gradient cooling [41] allows us to reach measured temperatures of 10-25 $\mu$K.

After the final cooling step in the lattice, all light except for the trap is extinguished and a bias magnetic field specific to the particular experiment is applied to the ensemble, usually with a magnitude of about 3 G. We usually allow about 30 to 50 ms for all magnetic fields and induced eddy currents to settle after this change, especially for experiments with magnetic field sensitive transitions. The final state preparation using optical pumping takes about 1 ms, although the details of the state preparation are particular to each experiment and described in detail in their respective chapters.

## 2.4 Detection and Signal Chain

Here I describe components common to both experiments used in detecting signals from the science cavity, electronically processing those signal and recording them into the computer.

### 2.4.1 APD detector

A simple avalanche gain photodiode provides a good first look at the light transmitted through the cavity and superradiant emission. For detecting these small signals, we used a Hammamatsu avalanche photodiode (PN: S2381). The avalanche gain was $\sim 98$ at a bias voltage of -150 V. The detector uses a transimpedance amplifier (PN: OPA656U) with 0.8 M$\Omega$ of gain. The detector has a bandwidth of about 1 MHz, allowing us to see the initial superradiant pulses that were taking place on timescales of a few microseconds.

### 2.4.2 Fast heterodyne detector

For low noise detection that includes sensitivity to the frequency of the detected light, we also implemented heterodyne detection schemes in the various experiments, described in detail in the chapters of their respective experiments. In each experiment, the heterodyne detection uses a Hamamatsu photodiode (PN: S5973) with 1 GHz intrinsic bandwidth. We removed the uncoated glass cover to gain about 8% in quantum efficiency. The photodiode sensitivity without glass is 0.54 A/W at 795 nm corresponding to internal photodiode quantum efficiency of 84%.

The photocurrent generated at the photodiode is converted to electric voltage with a 240 MHz Analog Devices transimpedance amplifier (PN: AD8015). In assembling the photodiode circuit, we found that all the ground connections for the AD8015 must be connected close to the ground pins. When not properly grounded, we observed oscillations around 300 MHz in the output voltage. We obtained the best high bandwidth performance when the path from the photodiode to the transimpedance amplifier was made as short as possible to reduce parasitic capacitance and inductance. The design used in the experiment has the output of the S5973 connect to the AD8015 input pin in free space through an ac coupling capacitor, bypassing the surface mount trace on the circuit board. A circuit diagram of the photodiode is included in Appendix D.

### 2.4.3 IQ demodulators

The signal from the high frequency photodiode is split and frequency filtered as we often have more than one signal contained in different frequency beatnotes. For example, in addition to a signal that passed through the atomic sample, we may also have a path length reference signal that did not interact with the atoms but contains information on path length fluctuations. Each separate signal gets its own IQ demodulation channel and reference frequency derived from the DDS. Each demodulator splits the signal again and demodulates to near DC using an Analog Devices IQ demodulator (PN: ADL5385) or a Linear Technologies IQ demodulator (PN: LT5517) for RF frequency signals below 50 MHz. The IQ demodulators provide two orthogonal quadratures

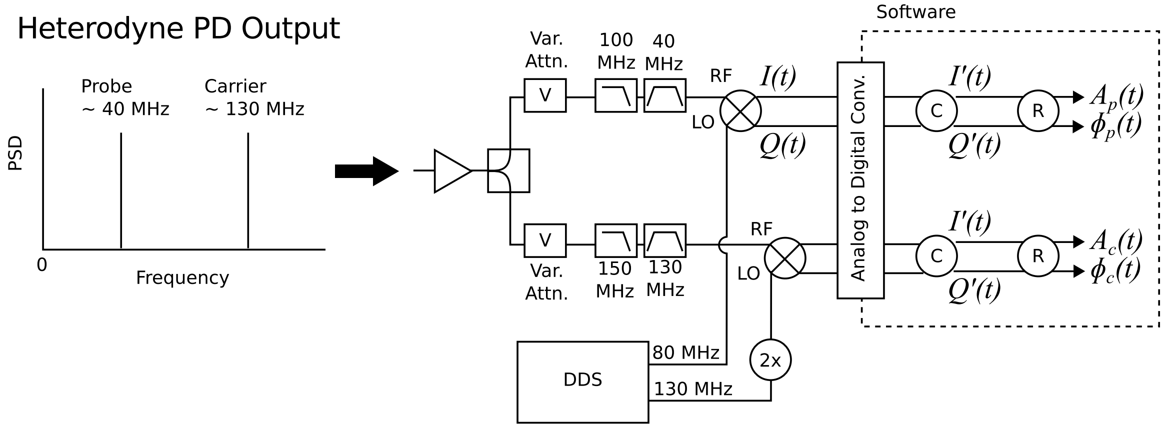

Figure 2.15: An example schematic of the heterodyne data acquisition system. The output of the heterodyne photodiode can have multiple signals separated in RF frequency. We split the signal after amplification, then have separate paths for each frequency in which we can separately attenuate the signals to keep the inputs to the IQ demodulators. The signals are demodulated with RF frequencies from the DDS. The corrections to account for imbalances in each IQ demodulator is applied in software (circle with 'C'), giving the corrected signals $I'(t)$ and $Q'(t)$ from which the amplitude $A(t)$ and phase $\phi(t)$ of each signal can also be calculated.

of the signal with respect to the reference frequency. These two orthogonal quadratures, which we call $I(t)$ and $Q(t)$ are read into the computer with a National Instruments analog to digital converter (PN: PCI-6133).

In software, we apply corrections to the $I(t)$ and $Q(t)$ channels to correct for small imperfections in the demodulation hardware, including average offsets between the channels, scale factors between the channels, and higher order corrections. After applying corrections to the individual $I(t)$ and $Q(t)$ traces, we form the amplitude $A(t)$ and the phase $\phi(t)$ quadratures. We tune the corrections by applying test signals from the DDS boards. First, an overall voltage offset is removed by applying no test signal to the RF input. Then the average voltage on the $I(t)$ and $Q(t)$ channels give the individual DC offsets $y_I$ and $y_Q$. The exact corrections applied to the $I(t)$ and $Q(t)$ quadratures are given below. First, each quadrature is corrected for an offset $y$ and an amplitude $K$ error, then a curvature $\beta$ correction is applied

$$I' = K_I(I + y_I) \tag{2.1}$$

$$Q' = K_Q(Q + y_Q) \tag{2.2}$$

$$I'' = I' - \beta_I(I'^2 + Q'^2) \tag{2.3}$$

$$Q'' = Q' - \beta_Q(I'^2 + Q'^2) \tag{2.4}$$

Finally, a relative angle error $\theta$ between the two quadratures can also be corrected

$$I''' = I'' \tag{2.5}$$

$$Q''' = \frac{Q'' - I'' \sin(\theta)}{\cos(\theta)} \tag{2.6}$$

The coefficients are choosen empirically by driving the RF input with a test signal that differs from the LO frequency by $\sim 1$ kHz. Imbalance between the two quadratures appears as oscillations in amplitude quadrature $A(t) = \sqrt{I'''(t)^2 + Q'''(t)^2}$ as the actual input voltage oscillates from $I(t)$ to $Q(t)$ and back. The deviations show up as peaks in the Fourier transform of the amplitude at harmonics of the frequency offset between the two test signals. Tuning the coefficients, we can push the size of these peaks into the detection noise floor. Higher order corrections, $\epsilon_i$ and $\phi_i$ are also applied to the phase quadrature $\phi(t)$ as

$$\phi(t) = \arctan(\frac{Q'''}{I'''}) + \sum_{i=3} \epsilon_i \cos\left(i \arctan\left(\frac{Q'''}{I'''}\right) + \phi_i\right) . \tag{2.7}$$

We normally apply only the $i = 3$ correction term.

The corrected amplitude $A(t)$ and phase $\phi(t)$ then reflects the electric field coming from the cavity, either as a result of a probe laser or superradiant emission. We calculate the scale factor to be able to quantify $A(t)$ in units such as average intracavity photons $M_c$ or photons transmitted from a probe beam $M_t$. The calibration also depends on the average power contained in the heterodyne reference beam. This beam is responsible for the DC current generated by the photodiode that we detect separately from the IQ detection, and read in through the analog to digital converter.

# Chapter 3

# Reducing measurement back-action to generate spin squeezed states with phase sensitivity 10 times beyond the standard quantum limit

## 3.1 Experimental System

In this chapter, I describe collective measurements of a cavity field that is entangled with the total number of spin-1/2 atoms in spin up (Fig. 3.1A). The measurement uses an optical cycling transition to reduce the measurement back-action on the atomic system. The high readout precision and small measurement back-action allows us to use the measurement to generate a spin squeezed state by subtracting the pre-measurement result from subsequent measurements. The degree to which the measurement precision has been improved is quantified by the spectroscopic enhancement $W^{-1} = \frac{\Delta\theta_{SQL}}{\Delta\theta}$, which is equal to the ratio of the phase variance at the standard quantum limit (SQL) to the measured phase variance $\Delta\theta$. We directly observe a state with spectroscopic enhancement $W^{-1} = 10.5(1.5)$ times beyond the SQL for phase estimation of a coherent spin state composed of $N = 4.8 \times 10^5$ $^{87}$Rb atoms. This result reflects no background subtraction or corrections for finite probe detection efficiency, which is critical for the realization of practical applications of entangled states.

The experimental system consists of an ensemble of $N$ pseudo-spin-1/2s formed by the hyperfine ground states $|\uparrow\rangle \equiv |F = 2, m_f = +2\rangle$ and $|\downarrow\rangle \equiv |F = 1, m_f = +1\rangle$ in $^{87}$Rb, separated by 6.8 GHz. The quantum state of the ensemble can be approximated as a single collective spin or Bloch vector $\mathbf{J} \equiv \langle\hat{\mathbf{J}}\rangle$, in an abstract space defined by the collective spin operator $\hat{\mathbf{J}} = \hat{J}_x\hat{x}+\hat{J}_y\hat{y}+\hat{J}_z\hat{z}$ (Fig. 3.1B). The spin projection operator $\hat{J}_z = \hat{N}_\uparrow - N/2$ can be written in terms of the measurable

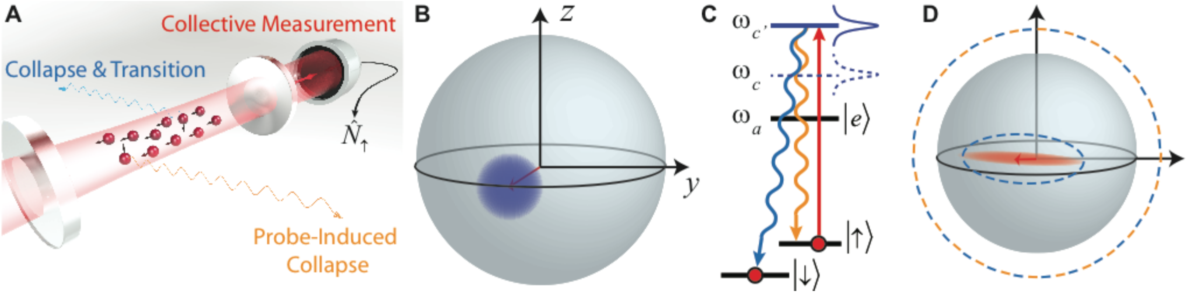

Figure 3.1: **Spin-squeezing and measurement back-action** (**A**) Atoms collectively interact with light in an optical cavity. A measurement of the phase of the probe field (red) is sensitive to the total number of atoms in spin up, and projects the ensemble into an entangled state, conditioned on the measurement outcome. Probe photons can be scattered into free space, causing atoms to collapse to spin up (orange in A, C, and D) and can also cause state-changing transitions (blue in A, C, and D). (**B**) A coherent spin state can be visualized by a Bloch vector (red), with a pointing uncertainty set by quantum noise, represented by the shaded uncertainty disk. (**C**) Atoms in $|\uparrow\rangle$ with optical transition frequency $\omega_a$ couple to the detuned cavity mode with resonance frequency $\omega_c$. The coupling results in a dressed cavity mode with resonant frequency $\omega_{c'}$, so probing $\omega_{c'}$ measures the total number of atoms in $|\uparrow\rangle$, and hence the Bloch vector's spin projection $J_z$, without measuring the state of individual atoms. Probing on a cycling transition suppresses back-action from scattering events that change an atom's state to $|\downarrow\rangle$ (blue), limiting back-action to collapse (orange). (**D**) After a pre-measurement, back-action modifies the noise distribution on the Bloch sphere. Fundamental back-action appears along $\hat{y}$. Back-action from non-ideal measurements, indicated by dashed lines, include reduction in length $J$ of the collective Bloch vector and added noise in $J_z$ caused by state-changing transitions.

quantities: total atom number $N$ and the spin up population operator $\hat{N}_\uparrow = \Sigma_{i=1}^{N} |\uparrow_i\rangle \langle\uparrow_i|$, where $i$ labels individual atoms. The length of the vector is $J = \left|\left\langle \hat{\mathbf{J}} \right\rangle\right|$. For an unentangled CSS, $J = N/2$.

The quantum projection noise and standard quantum limit can be understood as arising from uncertainty in the orientation of the Bloch vector (Fig. 3.1B). This quantum uncertainty can be visualized as a quasi-probability distribution perpendicular to the mean vector. When the Bloch vector is oriented along $\hat{x}$, the degree of uncertainty in the orthogonal spin projections is constrained by a Heisenberg uncertainty relationship $\Delta J_z \Delta J_y \geq N/4$, where $\Delta X$ indicates the standard deviation of repeated measurements of $X$. For a CSS of atoms, $\Delta J_z = \Delta J_y = \Delta N_{CSS} = \sqrt{N}/2$. For the polar angle $\theta \approx J_z/J = 2N_\uparrow/N - 1$ measured from the equator of the Bloch sphere, the SQL is set by the projection noise fluctuations to $\Delta\theta_{SQL} = 1/\sqrt{N}$.

## 3.2 Creating a Squeezed State with a Collective Premeasurement

The squeezed state is created by first preparing a CSS along $\hat{x}$ and then making a collective pre-measurement $\hat{N}_\uparrow$, with measurement outcome labeled $N_{\uparrow p}$, and subtracting the result from a subsequent final measurement $\hat{N}_\uparrow$, labeled $N_{\uparrow f}$. The differential quantity $N_{\uparrow f} - N_{\uparrow p}$ can possess reduced noise relative to the projection noise fluctuations $\Delta N_{CSS}$ appearing in the two separate measurements. The spin noise reduction is calculated as $R = (\Delta(N_{\uparrow f} - N_{\uparrow p}))^2/\Delta N_{CSS}^2$. By making a collective or joint measurement, any rotation of the vector's polar angle $\theta$ that occurs between the two measurements will still modify the differential quantity $N_{\uparrow f} - N_{\uparrow p}$, leading to the desired enhancement in the estimation of applied phase shifts.

To measure the collective state population $N_\uparrow$, the atomic ensemble is coupled to the $\text{TEM}_{0,0}$ mode of an optical cavity. The coupling is characterized by an effective single-atom coupling $g = 2\pi \times 450(20)$ MHz. The details of inhomogeneous coupling to the probe in our standing wave cavity are handled as in Refs. [139, 35]. With no atoms present, the cavity has a resonant frequency $\omega_c$ and decay rate $\kappa = 2\pi \times 11.8(1)$ MHz. We detune the cavity frequency from an atomic transition by $\delta = \omega_c - \omega_a = 2\pi \times 200$ MHz, where $\omega_a$ is the frequency of the atomic transition from $|\uparrow\rangle$ to an optically excited state $|e\rangle \equiv |F = 3', m_f = +3\rangle$. The radiative decay rate of $|e\rangle$ in free space is

$\Gamma = 2\pi \times 6.07$ MHz. Atoms in $|\uparrow\rangle$ produce a dressed atom-cavity resonance at frequency $\omega_{c'}$, such that $\omega_{c'} - \omega_c = (\sqrt{\delta^2 + 4g^2 N_\uparrow} - \delta)/2$ (Fig. 3.1C). We measure $\omega_{c'}$ with a probe laser (frequency $\omega_p$) to determine $N_\uparrow$. The strength of the collective measurement is characterized by the average number of probe photons $M_t$ transmitted through the cavity along with the average number of photons scattered into free space $M_s$. The transmitted probe provides collective population information corresponding to the total number of atoms in $|\uparrow\rangle$, without providing individual atomic state information. Detailed schematics of the probe measurement scheme are provided in section 3.4.

The information gained from a pre-measurement $\hat{N}_\uparrow$ causes back-action on the system, illustrated in Fig. 3.1D. First, the measurement reduces the collective spin projection uncertainty to $\Delta J_z = \Delta N_{\uparrow m}$, where $\Delta N_{\uparrow m}$ is the measurement imprecision. The Heisenberg uncertainty relationship requires fundamental back-action to appear in the orthogonal spin projection $\Delta J_y \geq (N/4)/\Delta N_{\uparrow m}$, referred to as anti-squeezing. Because $J_z$ is not coupled to the back-action quadrature $J_y$, the ideal measurement is intrinsically back-action evading[26].

However, real systems experience at least two additional sources of probe-induced back-action, also illustrated in Fig. 3.1D. Both are caused by photons spontaneously scattered from the probe into free space, with average number of scattered photons $M_s$ scaling linearly with the measurement strength $M_s \propto M_t$. One source of back-action arises from free-space scattered photons leaking single-atom information to the environment, projecting an individual atom into $|\uparrow\rangle$ or $|\downarrow\rangle$ for every free-space scattered photon. The result is a shortening of the Bloch vector such that a subsequent angular deflection $\theta$ will produce a reduced change of the measured population $N_{\uparrow f}$.

Another source of probe-induced back-action is spontaneous Raman transitions between ground states driven by the same free-space scattering. Quantum randomness in the number of transitions between states adds noise to the measurement of $N_\uparrow$ as the population diffuses amongst ground states. The added noise $\Delta N_{\uparrow D}$ scales as $(\Delta N_{\uparrow D})^2 \propto pM_t$, where $p$ is the probability an atom changes state if it scatters a photon into free-space. The optimum spin-noise reduction $R$ is fundamentally limited by the need to balance the decrease in measurement noise $\Delta N_{\uparrow m} \propto 1/\sqrt{M_t}$ versus the increase in diffusion noise $\Delta N_{\uparrow D} \propto \sqrt{M_t}$. This balancing is analogous to radiation pressure back-action that sets the SQL for measurements of mechanical position[26].

The key experimental advance enabling the results presented here is the elimination of state-changing transitions as a limitation on the spectroscopic enhancement $W^{-1}$. This is achieved by creating a system in which collective coupling to the probe mode is enhanced relative to single-atom processes. The approach uses the medium finesse optical cavity $F = 660$ to enhance the collective coupling, with the figure of merit $NC \approx 6 \times 10^3$, where $C = 1.1(1) \times 10^{-2}$ is the single-atom cooperativity [139, 35]. In addition, we suppress state-changing transitions by using $\sigma^+$ polarized probe light on a cycling transition [134, 4, 170, 34]. If a photon is scattered into free space, the ground-state transition probability $p$ is $\sim 1/150$ that of our previous work [35]. As a result, previously ignored noise sources, described in Sec. 3.4.4, now dominate the probe-induced back-action on the measurement $\hat{N}_\uparrow$.

## 3.3 Results

In Fig. 3.2, we directly sense an externally-applied phase shift with resolution below the SQL. We apply a small rotation $\psi$ of the polar angle $\theta$ using a microwave pulse. In one case, the rotation is applied to a CSS with no pre-measurement. In a second case, the rotation is applied just after the pre-measurement of $N_\uparrow$ prepares a conditional spin-squeezed state. The deflection of $N_{\uparrow f}$ is slightly smaller for the spin-squeezed state due to probe-induced collapse during the pre-measurement $N_{\uparrow p}$. However, the reduction in noise in the quantity $N_{\uparrow f} - N_{\uparrow p}$ allows the rotation angle to be estimated with an enhancement $W^{-1} = 7.5(9)$ in this example data set with measurement strength $M_t = 2.7(1) \times 10^4$ and $N = 4.3 \times 10^5$. No background subtractions or corrections are applied. In a single-shot, the fractional error rate in determining whether the phase shift of $\psi = 2.3(1)$ mrad was applied is reduced from 0.27(1) without the pre-measurement to 0.022(7) with the pre-measurement.

More generally, we can identify an optimum spectroscopic enhancement by measuring both the spin noise reduction $R$ and the fractional shortening of the Bloch vector $\mathcal{C} = J/(N/2)$ as a function of measurement strength $M_t$, shown in Fig. 3.3A. First we consider the spin noise

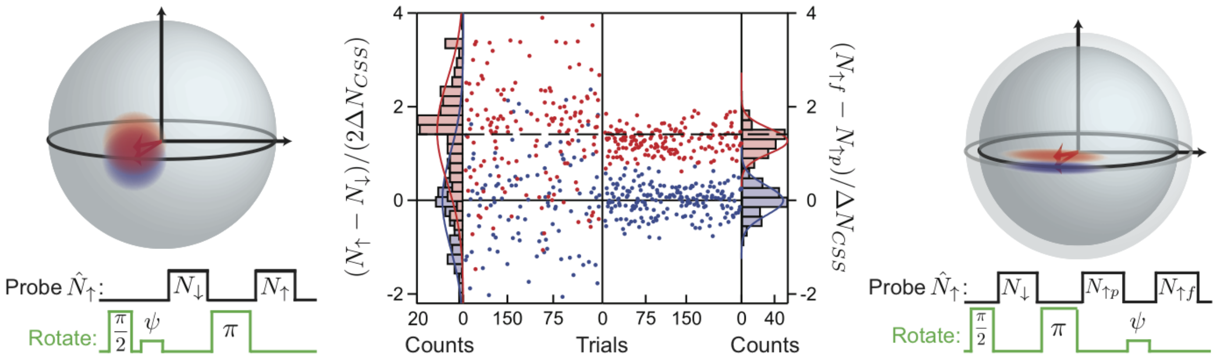

Figure 3.2: **Detection of a quantum phase with entanglement-enhanced sensitivity.** We apply a small rotation $\psi$ to the polar angle $\theta$ of both a CSS and a spin-squeezed state, with data and representative Bloch spheres shown on the left and right sides respectively. Red data points show experimental trials with $\psi = 2.3(1)$ mrad, and blue data points show trials with $\psi = 0$. The data are represented both as histograms and Gaussian curves generated from the average and standard deviation of the measurements. The experimental timing sequence consists of probe pulses (black) and microwave rotation pulses (green). For the CSS, the rotation $\psi$ is applied immediately after preparing the CSS along $\hat{x}$. The rotation $\psi$ appears as a change in the quantity $N_\uparrow - N_\downarrow$, which is normalized to the total projection noise that appears in this differential quantity. In the case of the spin-squeezed state, we perform the rotation $\psi$ after a pre-measurement $N_{\uparrow p}$. The rotation then appears as a change in $N_{\uparrow f} - N_{\uparrow p}$, where the projection noise largely cancels. The spin-squeezed state has a precision $W^{-1} = 7.5(9)$, even though the change in $N_{\uparrow f} - N_{\uparrow p}$ is slightly smaller than in the CSS due to free-space scattering during the pre-measurement. The loss of signal is represented by a smaller Bloch sphere for the spin-squeezed state.

reduction. The maximum $R^{-1}$ observed, with no background subtraction, is $R^{-1} = 16(2)$ at $M_t = 4.1 \times 10^4$. The contributions of various noise sources are quantified using a fit to the observed $R$ versus $M_t$. The model, $R = r_{PSN}/M_t + R_{tf} + r_q M_t + r_c M_t^2$, includes four noise contributions: photon shot noise $r_{PSN}$, a technical noise floor $R_{tf}^{-1} = 73(34)$ independent of $M_t$, probe-induced quantum back-action $r_q$, and probe-induced classical back-action $r_c$. Photon shot noise dominates at low $M_t$ so that $R^{-1}$ initially increases as $M_t$ increases. However, the rise in classical back-action $r_c M_t^2$ eventually limits $R^{-1}$. At the optimum $M_t$, the classical back-action $r_c$ alone would limit $R^{-1}$ to 67(15). The quantum back-action $r_q$ is statistically consistent with zero.

Raman transitions between hyperfine ground states have been effectively eliminated as a substantial source of back-action in the current experiment. The noise added due to population diffusion from state-changing transitions, described in Sec. 3.4.4, is estimated to only limit $R^{-1}$ to $1.7(3) \times 10^3$ as measured by probe-induced optical pumping between different ground-states. Also, the inferred contribution to $r_c$ due to the observed classical fluctuations in probe power would only limit $R^{-1}$ to $3.2(4) \times 10^4$. The equivalent transition probability is $p \leq 4.4(8) \times 10^{-3}$. For comparison, the clock states in our previous work had a transition probability $p = 2/3$ which, in our current system, would limit $R^{-1}$ to 1.9(2). With population noise considerably suppressed, other sources of back-action, including optomechanical effects (Fig. 3.3B), appear to dominate the probe induced back-action on $R$.

Free-space scattering also leads to a reduction in the Bloch vector length $J$, and the resulting loss of signal must be accounted for to determine the spectroscopic enhancement. To determine $J$, the polar angle of the Bloch vector $\theta$ is varied after the pre-measurement $N_{\uparrow p}$ using a microwave pulse. The population $N_\uparrow$ is then recorded versus the rotation angle, shown in Fig. 3.3C. The fractional reduction in length of the Bloch vector is determined from the fitted contrast $\mathcal{C} = 2J/N$ of the observed fringe. The initial contrast at $M_t = 0$ is $\mathcal{C}_i = 0.97(3)$, and $\mathcal{C}$ monotonically decreases as a function of $M_t$, close to the limit from wave function collapse due to free space scattering (Fig. 3.3A). We believe uncanceled inhomogeneous probe light shifts are responsible for the additional small loss of contrast.

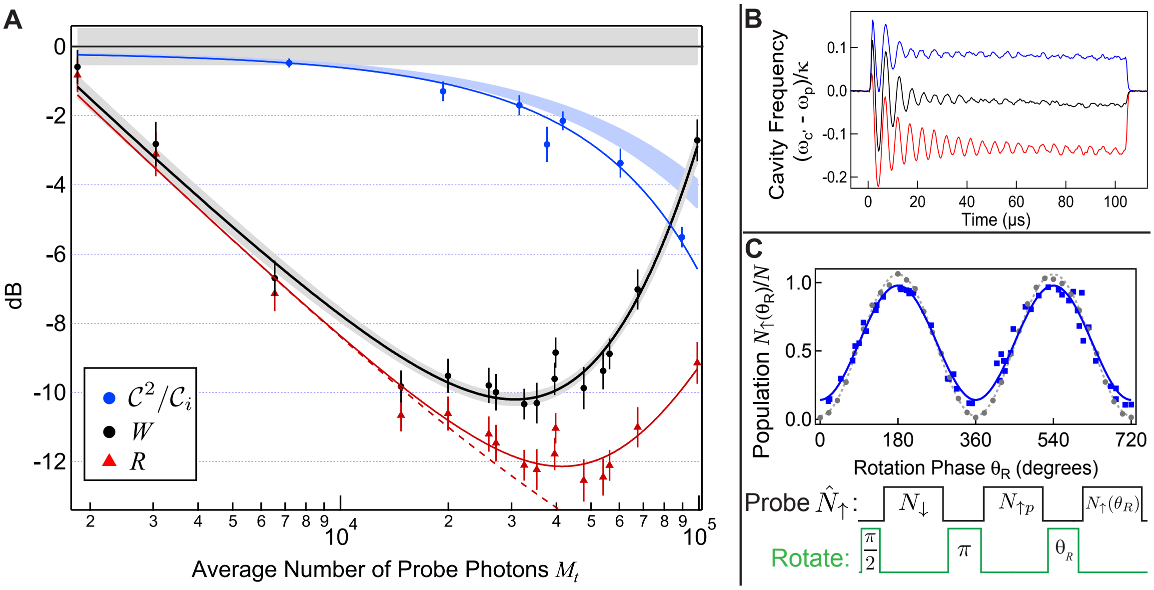

Figure 3.3: **Spin-squeezing and probe-induced back-action.** (**A**) Scaling of the spin noise reduction $R$ (red), loss of signal $\mathcal{C}^2/\mathcal{C}_i$ (blue), and the inverse of the spectroscopic enhancement $W$ (black) versus probe intensity $M_t$ for $N = 4.8 \times 10^5$. The red, blue, and black curves are fits to the data. The data for $W$ is calculated from $R$ data and the fit to $\mathcal{C}^2/\mathcal{C}_i$. The 68% confidence band for the $W$ fit and the SQL is in grey. The dashed red curve shows the fitted $R$ assuming no probe-induced added noise ($r_c = r_q = 0$). The light-blue region is the predicted $\mathcal{C}^2/\mathcal{C}_i$ due to free space scattering. All error bars are 1 std. dev. We use the usual convention for expressing a ratio $X$ in dB units, $x$ (dB) $= 10 \log_{10} X$. (**B**) Examples of optomechanical oscillations in the dressed cavity frequency $\omega_{c'}$. The relative detuning of $\omega_{c'}$ and $\omega_p$ results in increased or decreased oscillation damping rates, a source of probe-induced back-action noise (see supplementary text). Each curve is the average of 30 experimental trials. (**C**) Example data and experimental sequence for the measurement of the contrast $\mathcal{C}$. Probe pulses (black) are measurements $\hat{N}_\uparrow$. Microwave pulses (green) rotate the polar angle $\theta$ of the Bloch vector. After the pre-measurement of $N_{\uparrow p}$, a variable rotation $\theta_R$ is applied and $N_\uparrow(\theta_R)$ is recorded. The contrast $\mathcal{C}$ is determined from the amplitude of the $N_\uparrow(\theta_R)$ fringe (curves are a fit to the data), with two examples shown in blue and grey for $M_t = 3.0 \times 10^4$ and $M_t = 0$ respectively.

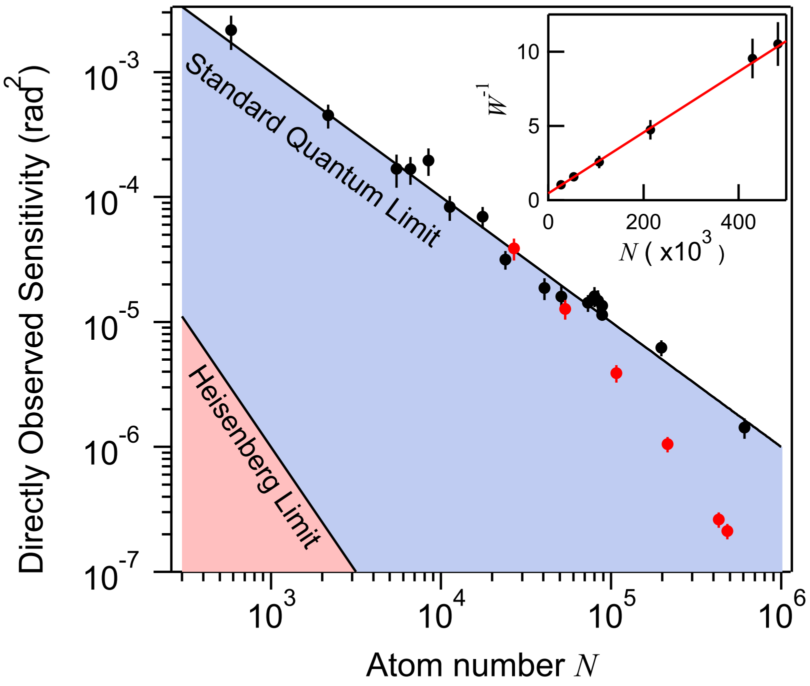

Figure 3.4: **Absolute phase sensitivity versus *N*.** The red points are the observed spin-squeezed state phase sensitivities (optimized with respect to measurement strength $M_t$) for different atom numbers $N$. The data show the predicted $1/N^2$ scaling for probing on a cycling transition [134, 34], equivalent to a linear scaling of the spectroscopic enhancement $W^{-1}$ versus $N$, shown in the inset. The red line is a linear fit to the data. The SQL is confirmed by measuring the projection noise that appears in $N_\downarrow - N_{\uparrow p}$ (black points, each 100 trials) and observing $1/\sqrt{N}$ scaling. Error bars indicate 68.3% confidence intervals.

Taken together, the decrease in spin noise and loss of contrast quantify the spectroscopic enhancement of the spin-squeezed state $W^{-1} = R^{-1}\mathcal{C}^2/\mathcal{C}_i$, as calculated in Refs. [4, 139, 35]. The optimum observed improvement corresponds to $W^{-1} = 10.5(1.5)$ or 10.2(6) dB. This value includes no measurement background noise subtraction, and thus represents the actual realized improvement in phase sensitivity.

Further confirmation that our collective measurement is near the cycling transition limit is the observed $\Delta\theta^2 \propto 1/N^2$ scaling of the absolute phase resolution[4, 34], shown in Fig. 3.4. For comparison, the optimal phase resolution when state-changing processes are the dominant limitation on $W$ scales as $N^{-3/2}$. This more favorable scaling with $N$ is important for practical applications where absolute phase resolution is the figure of merit.

When the spectroscopic enhancement $W^{-1} \geq 1$, the ensemble is guaranteed to be entangled. We also compute from Ref. [144] the multi-partite entanglement witness $\xi = 100 >> 1$ with the physical interpretation that a system of consisting of 100 spin-1/2 atoms that undergo ideal two-axis twisting[88] would exhibit the same spin-noise reduction and contrast as we observe in our system. Maximally entangled ensembles can achieve phase estimation precision of $\Delta\theta_{HL}^2 = 1/N^2$, known as the Heisenberg limit, which has been realized with small ensembles[117]. Our system is far from the Heisenberg limit for $N = 4.8 \times 10^5$ atoms. However, the absolute phase sensitivity is equivalent to $\sim$ 44000 copies of a maximally-entangled 11 atom ensemble, emphasizing the massive parallelism achievable by collective measurements to generate entanglement in neutral atom ensembles.

The optical nature of our approach, among others[4, 139, 159, 104, 141], offers the advantage that the probe or squeezing laser can be completely extinguished after the squeezed state is generated. In contrast, a potential challenge for squeezing generated using atomic collisions is whether the interactions that generate entanglement can be sufficiently reduced to avoid loss of accuracy and precision during the subsequent sensing period.

The collective measurement approach is compatible with a wide array of atomic sensors but is particularly appealing for optical lattice clocks[74], where systematic errors and atom loss may place a limit on the ensemble size. The probe also provides a low-noise, non-destructive readout method, similar to Ref. [170]. We achieve a readout sensitivity at the SQL while only imparting 0.007(1) photon recoils per atom, and hence very little loss of atoms from the trap due to heating. This may provide a purely classical improvement for sensors limited by measurement dead time associated with reloading the atomic ensemble in between trials, a crucial issue for advancing optical lattice clock stability [163].

Straightforward technical improvements could both decrease the technical measurement noise floor and increase the total probe detection efficiency from 8(5)% (see Table 3.5) to > 50%, allowing us to reach $W^{-1} \sim 100$ in our current system with only a medium finesse optical cavity. However, to realize even further spectroscopic enhancement, previously unimportant forms of probe-induced back-action will likely require additional study.

| **Common to both paths** | |
|---|---|
| Cavity mirror losses | 0.42 |
| Heterodyne detection | 0.5 |
| Photodetector (S5973) | 0.865 |
| **Transmission Path** | |
| Path efficiency | 0.69 |
| Detector electronic noise | 0.80 |
| Added noise from 823 nm path length reference | 0.9 |
| Total transmission path efficiency | 0.046 |
| **Reflection Path** | |
| Path efficiency | 0.54 |
| Detector electronic noise | 0.83 |
| Added noise from carrier path length reference | 0.9 |
| Total reflection path efficiency | 0.037 |

Figure 3.5: The measured detection efficiencies for the spin squeezing experiment.

## 3.4 Experimental Details

### 3.4.1 Atom-Cavity System

The optical cavity used for the collective measurements has a measured free spectral range of 7.828(1) GHz and a measured transverse mode spacing of 2.257(2) GHz, determining the cavity length to be $L = 1.9149(3)$ cm and the mode waist to be $w_{780} = 69.90(4)$ $\mu$m at 780 nm. With no atoms in the cavity, the cavity frequency is denoted $\omega_c$ and the measured cavity linewidth or power decay rate is $\kappa = 2\pi \times 11.8(1)$ MHz, giving a cavity finesse $F = 663(5)$. The power decay rate from factory-specified mirror transmission alone is $\kappa_\circ = 2\pi \times 5.02$ MHz.

The cavity is also used to generate the one-dimensional, intra-cavity optical lattice trap at wavelength $\lambda_l = 823$ nm, with a mode waist $w_{823} = 71.78(4)$ $\mu$m and an axial trap frequency $\omega_{ax} = 2\pi \times 150$ kHz. The atoms are polarization-gradient-cooled to 10(2) $\mu$K in the trap, putting them in the Lamb-Dicke regime along the cavity axis. A magnetic field with magnitude $|\mathbf{B}| = 0.73(1)$ G is oriented along the cavity axis. A simplified diagram of the cavity setup is shown in Fig. 3.6, and a more detailed schematic of the system is shown in Fig. 3.8.

The atomic ensemble is prepared and probed using the D2 line in $^{87}$Rb at 780 nm (Fig S2). The hyperfine ground states $|{\downarrow}\rangle \equiv \left|5\ ^2S_{1/2}, F = 1, m_f = 1\right\rangle$ and $|{\uparrow}\rangle \equiv \left|5\ ^2S_{1/2}, F = 2, m_f = 2\right\rangle$

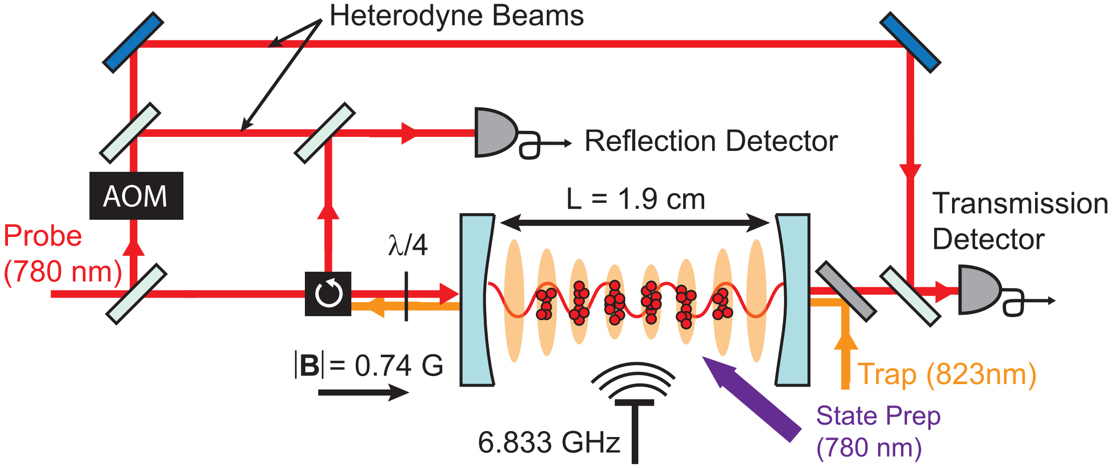

Figure 3.6: **Simplified experimental diagram.** The one dimensional optical lattice trap at $\lambda_l = 823$ nm is formed from a standing wave in the cavity (orange). We load $N_\circ = 4.0 \times 10^4$ to $7.2 \times 10^5$ $^{87}$Rb atoms into the trap and cool them to 10 $\mu$K. The atomic sample extends $\sim$ 1 mm along the axis of the $L = 1.9$ cm long optical cavity. State preparation is performed using a combination of 780 nm light (purple) for optical pumping and coherent ground state rotations performed with 6.833 GHz microwaves from the dipole antenna. A uniform magnetic field is applied to provide a quantization axis and spectrally resolve the ground state Zeeman sub-levels. The probe electric field forms a standing wave in the cavity, represented by the sinusoidal red line. The atom-cavity system is probed with 780 nm light (red), set to $\sigma^+$ polarization before entering the cavity. The probe light is separated from trap light using a dichroic mirror (grey) on the probe transmission side. The probe light is detected in both reflection and transmission with a heterodyne beam frequency shifted by an AOM.

form the pseudo-spin-1/2 system. Coherent rotations of the spin system are accomplished by coupling the ground states with a 6.833 GHz microwave field[36]. The relevant optically excited state $|e\rangle \equiv \left|5\ {}^2P_{3/2}, F' = 3, m_f = 3\right\rangle$ has a decay rate $\Gamma = 2\pi \times 6.06$ MHz.

The coupling between the cavity mode and a single atom on the $|\uparrow\rangle$ to $|e\rangle$ transition is parametrized by the single-photon Rabi frequency $2g_0 = 2\pi \times 1070(30)$ kHz, given at an antinode of the standing wave probe field at the center of the cavity both in the transverse and axial dimensions[85]. The probe coupling varies sinusoidally as $g(z) = g_0 \cos(2\pi z/\lambda_p)$, where $z$ is the spatial coordinate along the axis of the cavity. The probe field at wavelength $\lambda_p = 780$ nm is incommensurate with the trapping site spacing set by $\lambda_l$, so we define an effective single photon Rabi frequency $2g$ for the ensemble, accounting for both the axially and radially varying coupling as in [139, 35]: $2g = 2\pi \times 894(46)$ kHz (or cooperativity parameter $C = 4g^2/(\kappa\Gamma) = 1.1(1) \times 10^{-2}$). The total number of atoms confined in the optical lattice is $N_\circ$, irrespective of their coupling to the standing-wave probe mode. An effective atom number $N = 0.663(4) \times N_\circ$ with uniform coupling $2g$ produces the observed projection noise fluctuations. Throughout the main text, $N$ refers to the effective atom number.

### 3.4.2 Collective Population Measurement

The collective measurement of atomic population in $|\uparrow\rangle$, $\hat{N}_\uparrow$, is made by measuring the resonance frequency of the coupled, or dressed, atom-cavity system $\omega_{c'}$. The collective coupling of the atoms in $|\uparrow\rangle$ to the cavity mode is $\Omega_\uparrow = \sqrt{N_\uparrow}2g$, where $N_\uparrow$ is number of atoms in $|\uparrow\rangle$. The bare cavity resonance frequency $\omega_c$ is detuned $\delta = \omega_c - \omega_a = 2\pi \times 200$ MHz to the blue of the $|\uparrow\rangle \to |e\rangle$ transition at frequency $\omega_a$. The collective coupling results in a dressed cavity resonance frequency that is shifted by an amount

$$\omega_{c'} - \omega_c = \frac{1}{2}\left(\sqrt{\delta^2 + N_\uparrow (2g)^2} - \delta\right) \ . \tag{3.1}$$

We measure the frequency of the dressed atom-cavity system using $\sigma^+$ polarized light from a narrow ($< 5$ kHz) linewidth probe laser similar to that in Ref. [106], described in Chapter 2. The probe

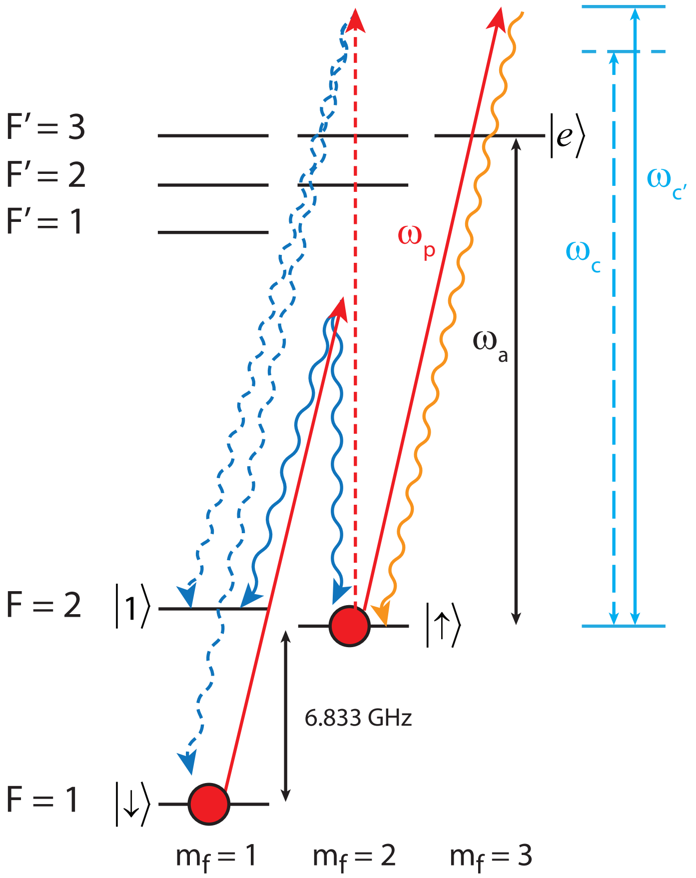

Figure 3.7: **Atomic energy level structure.** The relevant energy level structure of the $5\,^2S_{1/2}$ to $5\,^2P_{3/2}$ transition in $^{87}$Rb. The cycling transition has an optical atomic resonance frequency $\omega_a$. The cavity resonance with no atoms present (dashed light blue) with frequency $\omega_c$ is detuned to the blue of atomic resonance. The atom-cavity coupling creates a dressed cavity resonance (light blue) with frequency $\omega_{c'}$ which we probe using $\sigma^+$ laser light at frequency $\omega_p$ (red). The cycling nature of the transition means scattering primarily maintains population in $|\uparrow\rangle$ (orange). Scattering of the probe light from atoms in $|\downarrow\rangle$, detuned by $\sim 6.8$ GHz, provides the fundamental limit to the cycling transition, as atoms can scatter to both $|\uparrow\rangle$ and $|1\rangle \equiv |F = 2, m_f = 1\rangle$ (dark blue). Furthermore, imperfect polarization can lead to transitions for atoms in $|\uparrow\rangle$ to other internal states. An example of scattering from a $\pi$-polarized component of the probe is shown as the dashed red lines, with the state changing transitions in dark blue.

frequency $\omega_p$ is tuned nominally to resonance with the dressed cavity mode $\omega_{c'}$. The phases of the transmitted and reflected probe signals give the resonance frequency $\omega_{c'}$, described in detail below. The measured frequency is then used in Eqn. 3.1 to determine $N_\uparrow$. The relevant cavity and probe frequencies are schematically represented in Fig. 3.7.

The collective measurement strength is quantified by $M_t$, the average number of photons transmitted through the cavity in a single measurement $\hat{N}_\uparrow$. For each measurement, the probe light is on for 43 $\mu$s, but the measurement is an average of $\omega_{c'}$ over only 40 $\mu$s to avoid edge effects in the data acquisition. Probe-induced back-action from free space scattering is quantified by $M_s$, the number of photons scattered into free space during each measurement. $M_s$ is related to $M_t$ by $M_s = M_t \left( \frac{2\Gamma}{\kappa_\circ} \frac{N_\uparrow 4g^2}{4(\omega_{c'} - \omega_a)^2} \right)$ [34]. For the data with optimum squeezing at $N = 2N_\uparrow = 4.8 \times 10^5$, the calculated number of photons scattered into free space is $M_s = 1.0(1) \times M_t$.

Both the transmitted and reflected probe light are detected in heterodyne with respect to frequency-shifted light derived from the same probe laser (Fig. 3.8). In both cases, the probe signal appears at the photodiode output as a 50 MHz signal that is quadrature demodulated, with the in-phase $I$ and quadrature-phase $Q$ digitized and recorded by a computer. The $I$ and $Q$ amplitudes during a measurement are used to compute the phase of the detected probe light in both transmission $\phi_{pt}$ and reflection $\phi_{pr}$ as described in Chapter 2.

Fluctuations in the relative paths of the probe and heterodyne beams adds fluctuations to the measured phases, equivalent to variances two times projection noise in transmission and 15 times projection noise in reflection. We use reference beams traversing the same optical paths to remove the added phase fluctuations without introducing significant additional atomic decoherence.

The probe light at frequency $\omega_p$ that resonantly excites the dressed cavity mode is generated by phase modulating a carrier 170 MHz to the blue of the probe frequency. The modulation is performed with the EOspace phase modulator shown in Fig. 3.8. In reflection, this carrier follows the same path as the reflected probe light, and therefore can be used to cancel path length fluctuations. Because this reference beam is detuned from the dressed cavity resonance $\omega_{c'}$ by many cavity linewidths, it is primarily reflected from the cavity input and does not interact with the atoms. The carrier produces a signal in the reflection photodetector at 120 MHz, which is then quadrature demodulated, digitized, and a carrier phase is computed $\phi_{cr}$. Path length noise is removed in the differential quantity $\phi_r = \phi_{pr} - \phi_{cr}$, which is found to be very stable over time.

The carrier frequency component is not transmitted through the cavity and cannot be used to remove path length noise in the transmission heterodyne detection. Instead, we exploit the 823 nm

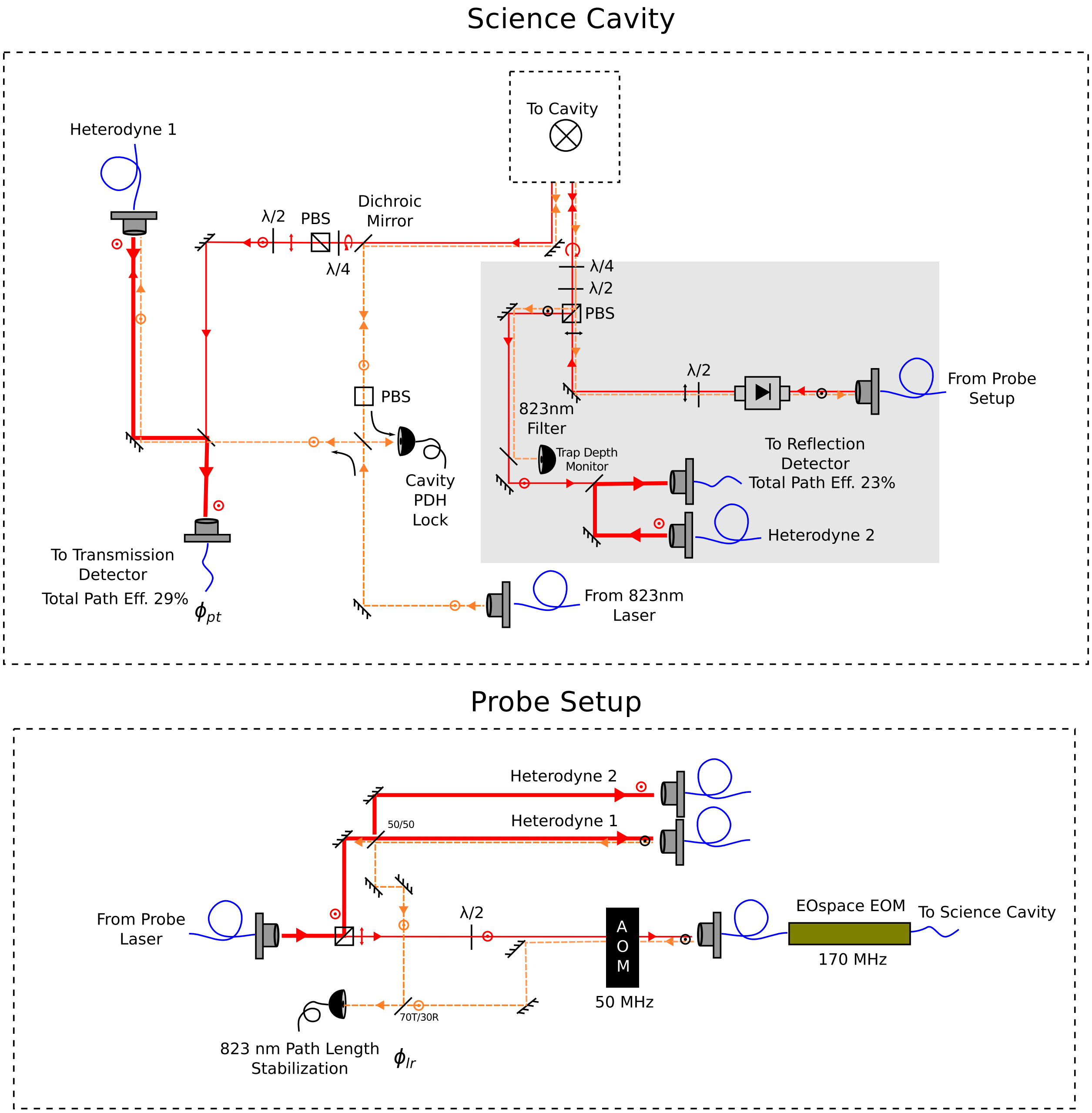

Figure 3.8: Detailed probe path documenting generation of heterodyne beams, probe quantum efficiencies to reflection and transmission detectors, and path length stabilization setup for transmission using 823 nm lattice laser. The 780 nm laser (red) is split into the heterodyne paths (thick lines) and the probe path (thin lines), which are eventually overlapped before jointly entering single mode fibers that go to the fast heterodyne detectors. The 823 nm laser (orange dashed line) that forms the optical lattice trap is also directed to largely follow, in reverse direction, the transmission heterodyne path (Heterodyne 1). Some of the path length noise is then common mode, and appears in the heterodyne detection of the 823 light in the probe setup area. The grey square indicates components on a platform raised 3 ft off the optical table surface. All other components on table surface.

optical lattice light passing through the cavity to remove path length noise from the transmission phase $\phi_{pt}$. The details are shown in Fig. 3.8. A 50/50 beam splitter takes the light from the 823 nm lattice laser path to send back through the heterodyne arm of the transmission path to the 823nm heterodyne detector, a Hamamatsu S5973 photodiode with a AD8015 transimpedance amplifier like those described in Chapter 2. The 823 nm trapp light that transmits through the cavity travels back along the path of the probe beam, with enough light leaking through the optical isolator to form a signal in heterodyne. This leakage light is then frequency shifted by an AOM to form a beatnote signal on the 823 nm photodiode at 50 MHz. The detected signal is demodulated and sampled to yield a phase $\phi_{lt}$. Path length noise in the transmission probe phase is removed by calculating the differential quantity $\phi_t = \phi_{pt} - \phi_{lt}(\lambda_l/\lambda_p)$, where $\lambda_l = 823$ nm and $\lambda_p = 780$ nm. The two heterodyne interferometers for the transmitted probe light and tracer light are made to be completely common up to two short free space paths of $\sim 0.5$ m total running along the optics table. While fluctuations in the differential path length lead to long term drifts (1 radian at 20 ms) in $\phi_t$, the drifts are not relevant to the differential measurements of populations made at short time scales (100 $\mu$s) in this work.

The measured phases are converted to detunings between the probe and cavity mode $\delta_{t,r} = \phi_{t,r}/S_{t,r}$ using separate scale factors $S_{t,r} = \mathrm{d}\phi_{t,r}/\mathrm{d}\omega_p$. The scale factors are directly measured during the experiments by jumping the probe frequency by 0.5 MHz (much less than the cavity half linewidth) and recording the change in the measured phases. In the case of transmission, an additional linear phase shift appears in $\phi_t$ and must be accounted for, because the lattice or tracer beam frequency is not changed in the scale factor calibration. $S_t$ must be adjusted accordingly. In contrast, in reflection both the probe and carrier frequency components are jumped in frequency together.

For measurements of the crucial differential quantity $N_{\uparrow f} - N_{\uparrow p}$, we construct differential detunings $\delta_{rfp} \equiv \delta_{rf} - \delta_{rp} = (\phi_{rf} - \phi_{rp})/S_r$ and similarly for transmission. Long terms drifts in $\phi_t$ cancel from this differential quantity. The final estimate for the differential detuning is calculated from a weighted average of the transmission and reflection measurements as $\delta_{fp} =$

$(\sigma_{rfp}^2\delta_{tfp}+\sigma_{tfp}^2\delta_{rfp})/(\sigma_{rfp}^2+\sigma_{tfp}^2)$. The measured noise variances in transmission $\sigma_{tfp}^2$ and reflection $\sigma_{rfp}^2$ are estimated from the variance in measurements of $\delta_{tfp}$ and $\delta_{rfp}$ performed over 100 trials at the same atom number $N$ and probe photon number $M_t$. Ideally, the weights are equal, but we find $\sigma_{rfp}^2/\sigma_{tfp}^2 = 1.65(4)$ indicating different detection efficiencies for the two paths. We calculate the differential atom number $N_{\uparrow f} - N_{\uparrow p} = \delta_{fp}\left(\mathrm{d}\omega_{c'}/\mathrm{d}N_{\uparrow}|_{N_{\uparrow rp}}\right)$, where the derivative is calculated using Eqn. 3.1 and evaluated at an atom number $N_{\uparrow rp}$ in $|\uparrow\rangle$ that is calculated from Eqn. 3.1 and the reflection measurement $\delta_{rp}$.

### 3.4.3 Spin Noise Reduction Measurement Sequence

Spin noise reduction $R$ is determined from the directly measured noise in the difference of two measurements of the population $N_{\uparrow}$. The experimental sequence for measuring $R$ is shown in Fig. 3.9. We first pre-align the probe frequency $\omega_p$ to the dressed cavity frequency $\omega_{c'}$, described in detail below. Next, we prepare a coherent spin-state on the equator of the Bloch sphere by optically pumping all atoms to $|\downarrow\rangle$ ($\mathbf{J}$ along $-\hat{z}$), then applying a $\pi/2$ microwave pulse to orient the Bloch vector along $\hat{x}$, equivalent to placing each atom in a superposition of $|\uparrow\rangle$ and $|\downarrow\rangle$. We infer the number of atoms in $|\uparrow\rangle$ by switching on the probe laser to make the first measurement of $\omega_{c'}$, and label the result $N_{\downarrow}$. After phase-coherently swapping the populations in $|\uparrow\rangle$ and $|\downarrow\rangle$ using a microwave $\pi$-pulse, we perform two successive measurements of the population in $|\uparrow\rangle$ and label the results $N_{\uparrow p}$ and $N_{\uparrow f}$. The experiment is repeated more than 100 times and the variance of the difference between the final measurement and the pre-measurement $(\Delta\left(N_{\uparrow f} - N_{\uparrow p}\right))^2$ is calculated from the measured phases as described above. The spin noise reduction $R$ is computed as $R = \frac{\left(\Delta\left(N_{\uparrow f}-N_{\uparrow p}\right)\right)^2}{N/4}$.

In Fig. 3.10, we compare measurement noise versus $M_t$ both with and without atoms in the cavity. With atoms, the contribution from photon shot noise is 4.5 dB lower because the presence of atoms creates a narrower dressed cavity resonance [34]. The difference is visible for small $M_t$ where photon shot noise dominates. However, measurement back-action with atoms present contributes noise that increases with $M_t$ and limits the maximum-achievable spin noise

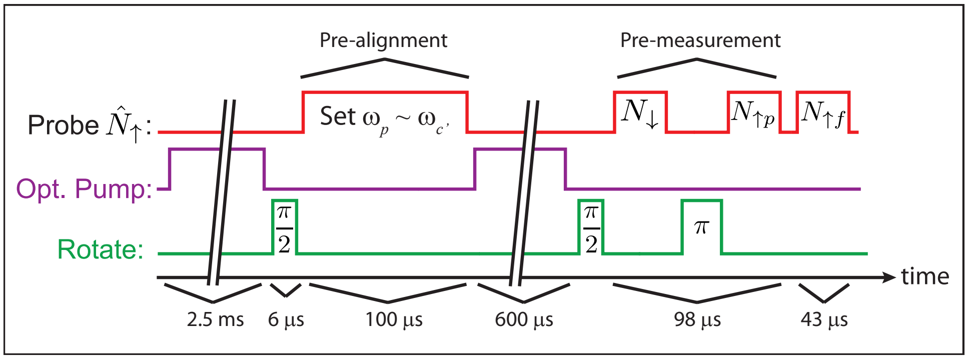

Figure 3.9: **Timing Sequence.** The experimental timing sequence showing probe laser pre-alignment and the pre-measurement that prepares a conditionally spin-squeezed state, followed by a final measurement to quantify the reduction in spin noise. Each optical pumping step (purple) prepares the ensemble in $|\downarrow\rangle$. Rotations (green) are performed by coupling $|\uparrow\rangle$ and $|\downarrow\rangle$ with a coherent microwave source. Probe laser pulses (red) correspond to individual measurements $\hat{N}_\uparrow$, with the measurement outcomes labeled as shown.

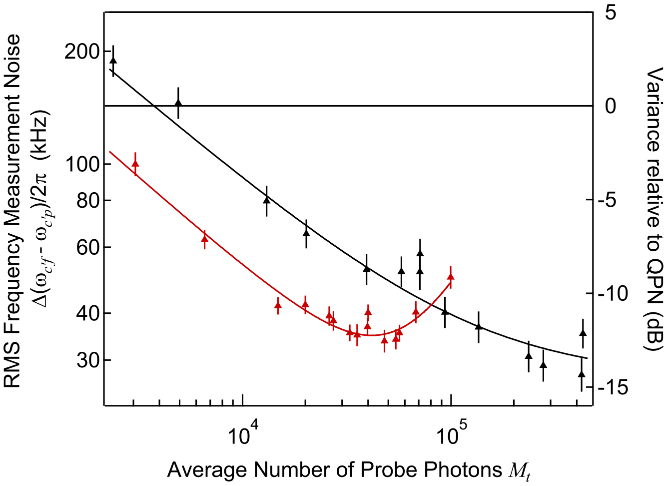

Figure 3.10: **Comparing measurement noise with and without atoms.** The fluctuations in the difference between two measurements of the dressed cavity frequency $\omega_{c'f} - \omega_{c'p}$, used to determine the difference of population measurements $N_{\uparrow f} - N_{\uparrow p}$, is plotted versus the average number of probe photons $M_t$. On the left axis, the fluctuations are expressed as the standard deviation $\Delta(\omega_{c'f} - \omega_{c'p})/2\pi$ in absolute frequency units. On the right axis, the same fluctuations are expressed as the ratio of the variance $(\Delta(\omega_{c'f} - \omega_{c'p}))^2$ to the variance $(\Delta\omega_{c'p})^2$ caused by the quantum projection noise (QPN) of a CSS. For the ensemble of $N = 4.8 \times 10^5$ atoms here, QPN causes fluctuations $\Delta\omega_{c'} = 2\pi \times 144(9)$ kHz, indicated by the line at 0 dB. Measurement noise is compared with (red) and without (black) the atoms loaded in the trap. For the case with atoms, the right axis is equivalent to $R$. The lines are fit to the data. The error bars are 1 std. dev.

reduction $R$, as described later in the supplementary text.

The role of the first measurement, labeled $N_{\downarrow}$ in Fig. 3.9, is to cancel inhomogeneous light shifts caused by the standing-wave probe light during the pre-measurement $N_{\uparrow p}$, with the $\pi$-pulse forming a spin-echo sequence. Light shift cancellation is critical for restoring coherence (i.e. length of the Bloch vector) so that a Bloch vector rotation through an angle $\theta$ after the pre-measurement will produce an observable change of the final measurement $N_{\uparrow f}$.

In principle, the first measurement can be used to enhance the spin noise reduction. However, we found that the $\pi$-pulse degraded the observed spin noise reduction when the information gained from the first measurement was utilized. The noise added by the microwave rotation results from both fluctuations in the transition frequency $|\downarrow\rangle$ to $|\uparrow\rangle$, as well as amplitude and phase noise of the applied microwave field. Neglecting the information in $N_{\downarrow}$ avoids these sources of rotation-added noise at the cost of a potential factor of 2 improvement in $R$.

Fluctuations in the atom number $N$ produce significant fluctuations in the detuning $\delta_p = \omega_p - \omega_{c'}$ of the probe from the dressed cavity resonance from one trial to the next. For scale, the atom number changes by $\sim 1\%$ peak to peak on 1 minute time scales, and can drift by 2.5% over 30 minutes. Fluctuations in $\delta_p$ can create additional technical noise that limits $R$. First, the number of transmitted photons $M_t$ changes with the detuning of the probe, modifying the small observed chirping of $\omega_{c'}$ described below. Secondly, the point of maximum measurement sensitivity is achieved when $\delta_p \ll \kappa/2$.

To mitigate these two effects, we implement a scheme to pre-align the probe laser frequency $\omega_p$ to the dressed cavity frequency $\omega_{c'}$ at the start of each trial (Fig. 3.9). After we prepare a coherent spin-state on the equator of the Bloch sphere by optical pumping and a $\pi/2$ rotation, we actively lock $\omega_p$ to $\omega_{c'}$, then hold $\omega_p$ fixed at the final frequency for all subsequent measurements within a trial. After this pre-alignment, the ensemble is optically repumped to $|\downarrow\rangle$ and the measurement sequence described previously is performed. Pre-alignment of the probe laser reduced the trial to trial standard deviation of the probe-cavity detuning during the pre-measurement $N_{\uparrow p}$ to $\Delta\delta_p = 0.045 \times \kappa/2$. For comparison, the fundamental limit set by the uncorrelated projection noise appearing in both the pre-alignment and the pre-measurement is $\Delta\delta_p = 0.034 \times \kappa/2$.

### 3.4.4 Quantifying Measurement-induced Back Action

To verify that the collective measurements generate a conditionally spin-squeezed state with enhanced phase sensitivity, we must determine the fractional reduction in the Bloch vector length $J$ caused by measurement back-action. The degree to which the measurement avoids collapse and dephasing is quantified by the contrast $\mathcal{C} = J/(N/2)$. To measure $\mathcal{C}$, we apply a variable polar angle rotation $\theta_R$ to the Bloch vector using an additional $\pi/2$ microwave pulse after the measurement of $N_{\uparrow p}$. The polar angle is changed by varying the phase of the final microwave $\pi/2$ pulse relative to that of the initial $\pi/2$ pulse. We then measure the population of $|\uparrow\rangle$ with measurement outcome labeled $N_{\uparrow}(\theta_R)$. The contrast is determined from fitting the data to its expected dependence $N_{\uparrow}(\theta_R) = (N/2)(1 + \mathcal{C}\cos\theta_R)$. Assuming each free space scattered photon causes a single atom to collapse into spin up, reducing $J$ by one unit, the predicted contrast is $\mathcal{C}_{pred} = \mathcal{C}_i e^{-M_s/N}$. The initial contrast $\mathcal{C}_i = 0.97(3)$ is the contrast measured with no probe light ($M_s = M_t = 0$) during the pre-measurement. When $M_s$ is increased such that $\mathcal{C}$ falls below $\sim 0.9$, the contrast begins to decrease more rapidly than predicted by free space scattering, as seen in Fig. 3.3A. We believe the deviation is likely due to light shifts that are not fully canceled by the spin-echo formed by the combination of measurements labeled $N_{\downarrow}$ and $N_{\uparrow p}$.

In this section, we quantify measurement back-action due to spontaneous scattering that changes the internal state of an atom. We consider limitations to the spin noise reduction from both the fundamental quantum noise, which we call population diffusion, and noise from classical fluctuations in the average change in internal state populations. For a perfect probing scheme on a cycling transition, only Rayleigh scattering is allowed, and so no change of the internal state of the atom would take place. However, as shown in Fig. 3.7 and discussed in ref. [34], atoms in $|\downarrow\rangle$ can non-resonantly Raman scatter to both $|\uparrow\rangle$ and $|1\rangle \equiv |F = 2, m_f = 1\rangle$. Another possible measurement imperfection we consider is impure probe light polarization allowing population to Raman scatter out of $|\uparrow\rangle$.

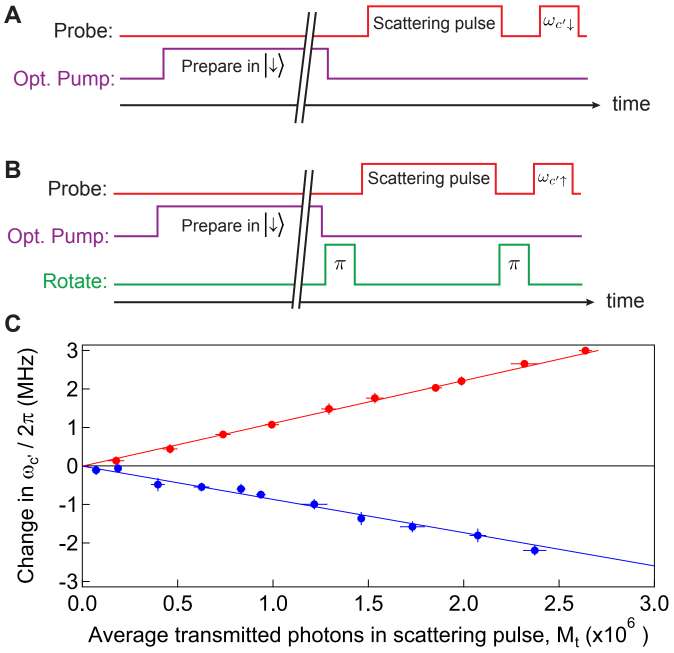

Figure 3.11: **Probe-induced population change.** (**A**) To measure the sum of transition probabilities $p_{\downarrow\uparrow} + p_{\downarrow 1}$, we first prepare atoms in $|\downarrow\rangle$ with optical pumping (purple). Next, a scattering probe pulse (red), quantified by the average number of transmitted probe photons $M_t$, causes some atoms to change state to $|\uparrow\rangle$ and $|1\rangle$. Many photons per atom in $|1\rangle$ are scattered into free space, allowing the atoms in $|1\rangle$ to transition to $|\uparrow\rangle$. Thus, the measurement of the dressed cavity frequency $\omega_{c'\downarrow}$ gives the total number of atoms scattered out of $|\downarrow\rangle$. (**B**) To measure the transition probability $p_{\uparrow\downarrow}$, we prepare atoms in $|\uparrow\rangle$ using optical pumping and a microwave $\pi$ pulse (green). The imperfection in the $\sigma^+$ polarized probe used for the scattering pulse causes some atoms to change state to $|\downarrow\rangle$. We again assume all atoms that scatter to $|1\rangle$ immediately transition back to $|\uparrow\rangle$. We swap the populations in $|\uparrow\rangle$ and $|\downarrow\rangle$ with another microwave $\pi$ pulse, so the measurement of $\omega_{c'\uparrow}$ gives the number of atoms that scattered to $|\downarrow\rangle$. (**C**) Measurements of the dressed cavity frequency due to probe-induced internal state-changing transitions, with $\omega_{c'\downarrow}$ (red) described in **A**, and $\omega_{c'\uparrow}$ (blue) described in **B**. The lines are fits to the data, yielding a change in $\omega_{c'}$ per transmitted photon $\delta\omega_{c'\downarrow} = 2\pi \times 1.11(2)$ Hz/photon (red) and $\delta\omega_{c'\uparrow} = -2\pi \times 0.86(5)$ Hz/photon (blue). Here $N = 2.1 \times 10^5$ atoms.

Our model for the added noise in $R$ considers transitions between three states, $|\uparrow\rangle$, $|\downarrow\rangle$, and $|1\rangle$. The probabilities per free space scattered photon to make a transition are denoted as $p_{\uparrow\downarrow}$, $p_{\downarrow\uparrow}$, $p_{\uparrow 1}$, and $p_{\downarrow 1}$ for the four transitions $|\uparrow\rangle \rightarrow |\downarrow\rangle$, $|\downarrow\rangle \rightarrow |\uparrow\rangle$, $|\uparrow\rangle \rightarrow |1\rangle$, and $|\downarrow\rangle \rightarrow |1\rangle$ respectively. To determine the transition probabilities, we do two experiments, shown in Fig. 3.11. In each experiment, we measure an average change in $\omega_{c'}$ per transmitted probe photon. We then convert the frequency change into a transition probability using the calculated dressed cavity shift per atom added to each state $\alpha_s = \frac{d\omega_{c'}}{dN_s}$, where $s = \uparrow, \downarrow, 1$. In one experiment, shown in Fig. 3.11A, we measure the sum $p_{\downarrow\uparrow} + p_{\downarrow 1}$ and use known branching ratios to get the individual probabilities $p_{\downarrow\uparrow} = 7.3(7) \times 10^{-4}$ and $p_{\downarrow 1} = 3.6(4) \times 10^{-4}$. In the other experiment, shown in Fig. 3.11B, we directly measure $p_{\uparrow\downarrow} = 8(1) \times 10^{-4}$. We assume $p_{\uparrow\downarrow}$ results from imperfect polarization of the probe laser. This measurement of $p_{\uparrow\downarrow}$ constrains the fraction of probe power in the non-cycling polarization to $< 6.7(8)\%$, if the imperfection is assumed to be $\sigma^-$-polarized light, and $< 1.7(2)\%$, assuming $\pi$-polarized light for the imperfection. Direct measurements more tightly constrain the fraction of power in the probe that is not in the $\sigma^+$ mode to $< 0.5\%$. The final transition probability $p_{\uparrow 1}$ can be calculated using branching ratios, known probe detuning from atomic resonance $\omega_p - \omega_a$, and $p_{\uparrow\downarrow}$, assuming a specific ratio of $\sigma^-$ to $\pi$ polarization for the probe polarization imperfection. For the full range of possibility for the polarization of the probe light imperfection (i.e. the ratio of $\sigma^-$ to $\pi$ polarized light in the probe imperfection ranging from 0 to 1), the transition probability doesn't change within its uncertainty, $p_{\uparrow 1} < 3.9(5) \times 10^{-3}$. In all cases, these independent measurements show that the transition probabilities are small $p \ll 1$, approaching the ideal cycling transition limit of $p = 0$.

The fundamental limitation on $R$ from internal state-changing scattering events comes from quantum noise in the scattering process. Specifically, if the average total number of transitions from $|\uparrow\rangle$ to $|\downarrow\rangle$ is $N_{\uparrow\downarrow} = p_{\uparrow\downarrow} M_s$, then on a given trial there will be quantum fluctuations in the total number of transitions with the standard deviation of $N_{\uparrow\downarrow}$ given by $\Delta N_{\uparrow\downarrow q} = \sqrt{p_{\uparrow\downarrow}\beta M_s}$. Here the factor of $\beta = 2/3$ accounts for the unweighted time averaging of the measurement records during the two measurements $\hat{N}_\uparrow$ that form the desired differential quantity $N_{\uparrow f} - N_{\uparrow p}$. In the limit that

$M_s/(N/2)$ is small, the noise from each process is uncorrelated, and the noise added to $R$ is the sum of the individual variance of each process

$$R_{pop,q} = \frac{\beta M_s}{N/4}\Big[p_{\uparrow\downarrow}(\alpha_\downarrow - \alpha_\uparrow)^2 + p_{\uparrow 1}(\alpha_1 - \alpha_\uparrow)^2 \\ + p_{\downarrow\uparrow}(\alpha_\uparrow - \alpha_\downarrow)^2 + p_{\downarrow 1}(\alpha_1 - \alpha_\downarrow)^2\Big]\ . \tag{3.2}$$

We assume no multiple Raman scattering, a good assumption for the low average probe photon number $M_t$ used here.

Classical fluctuations in the probe photon number $M_t$, and hence $M_s$, also introduce classical noise in the number of Raman transitions between ground states which adds noise to $N_{\uparrow f} - N_{\uparrow p}$, limiting the spin noise reduction. Also, an average population change can add technical challenges to the experiment as the dressed cavity mode frequency $\omega_{c'}$ changes or chirps during a measurement. For our experiment, the classical rms fluctuations in $M_s$ are $\Delta M_s = 0.04 M_s$. These classical fluctuations contribute a term to the total spin noise reduction

$$R_{pop,c} = \frac{\Delta M_{sc}^2}{N/4}\Big[p_{\uparrow\downarrow}(\alpha_\downarrow - \alpha_\uparrow) + p_{\uparrow 1}(\alpha_1 - \alpha_\uparrow) \\ + p_{\downarrow\uparrow}(\alpha_\uparrow - \alpha_\downarrow) + p_{\downarrow 1}(\alpha_1 - \alpha_\downarrow)\Big]^2\ . \tag{3.3}$$

The noise added by classical probe power fluctuations exhibits a fortuitous cancellation in the current experiment. The added classical noise due to the population change is reduced by a factor of $\sim 6.5$ in variance due to a cancellation of the two terms containing $(\alpha_\downarrow - \alpha_\uparrow)$ and as seen in Fig. 3.11.

The results of both the quantum and classical noise models, combined with the determination of the four transition probabilities, predict that internal-state changing transitions have been effectively eliminated as a source of probe induced back-action in this system (see Table 3.1 for constraints). Our measurements also indicate the added noise is small enough to allow for another two orders of magnitude improvement in spectroscopic enhancement for future experiments.

By suppressing internal-state transition noise, we reveal sources of probe-induced back-action that were not relevant in our prior measurement-induced spin-squeezing experiments [35]. Here we consider two sources that contribute noise to population measurements, both of which arise from the standing wave probe field in the cavity. The first source of back-action results from dispersive forces exerted on the atoms by the probe, which cause coherent oscillations of $\omega_{c'}$ (previously observed in ref. [170]). The second source results from free-space scattering of probe photons leading to photon recoil heating, which causes a change of the dressed cavity frequency $\omega_{c'}$. In this section, we describe how these two effects contribute both classical and quantum noise to our measurement of $N_{\uparrow f} - N_{\uparrow p}$. Note that neither source of back-action acts as an additional source of decoherence (i.e. a loss of contrast $\mathcal{C}$). While these sources of back-action do not fully account for the measured back-action $r_c$ in our experiment, they are interesting as sources of back-action that may limit the spin noise reduction $R$ in future work.

In our standing wave cavity, the probe induces a spatially varying light shift on the atoms, proportional to $g^2(z)$. The gradient of this light shift imparts a force on atoms not at a node or anti-node of the standing wave. When the probe is turned on, the atoms experience an impulsive momentum kick along the axial direction and oscillate at $\omega_{ax} = 2\pi \times 150$ kHz in the confinement of the trapping lattice at 823 nm. Because the coupling strength $g(z)$ is position dependent, the atomic motion causes $\omega_{c'}$ to oscillate at the same frequency. The oscillations damp in approximately 10 $\mu$s due to a spread in axial oscillation frequencies caused by the spread in radial position of the atoms in the confining optical lattice.

The oscillation is phase coherent between trials, and each measurement $\hat{N}_\uparrow$ largely averages over the oscillations. Nonetheless, variation in initial conditions lead to measurement noise in the differential quantity $N_{\uparrow f} - N_{\uparrow p}$ by causing variation in the collective oscillation. For example, classical and quantum fluctuations in $N_\uparrow$ cause variation in the probe detuning from the dressed cavity mode $\delta_p = \omega_p - \omega_{c'}$. The detuning $\delta_p$ determines the nature of dynamic optomechanical effects on the atoms [140]. If $\omega_{c'} > \omega_p$, the collective oscillation experiences optomechanical damping. If $\omega_{c'} < \omega_p$, the oscillation will experience optomechanical anti-damping that lengthens the

| Noise Source | $R^{-1}$ (uncertainty) |
|---|---|
| Observed Optimum | 16(2) |
| Photon Shot Noise $r_{PSN}$ | 32(4) |
| Technical Noise Floor $R_t$ | 73(34) |
|     Laser Linewidth | 520(250) |
| Classical Noise $r_c$ | 67(15) |
|     Variable Damping $R_o$ | 620(60) |
|     Photon Recoil $R_{ext,c}$ | $4.5(5) \times 10^3$ |
|     Population Change $R_{pop,c}$ | $3.2(4) \times 10^4$ |
| Quantum Noise $r_q$ | $> 7 \times 10^5$ |
|     Photon Recoil $R_{ext,q}$ | $4.8(5)) \times 10^5$ |
|     Population Diffusion $R_{pop,q}$ | 1700(300) |

Table 3.1: Contributions to the observed spin noise reduction $R$ from a fit to the data versus probe strength $M_t$ that includes photon shot noise, a noise floor, quantum noise, and classical noise. Each value is given at the optimum spin noise reduction at $M_t = 4.1 \times 10^4$. The indented rows show the calculated contributions from the various noise sources to each term. The uncertainties are 68.3% confidence intervals.

characteristic decay time of the observed oscillations of $\omega_{c'}$ (Fig. 3.3B).

A change in the damping rate can alter the degree of cancellation of the optomechanical ringing in the differential measurement $N_{\uparrow f} - N_{\downarrow p}$. Pre-alignment of the probe frequency to the dressed cavity resonance, described previously, was important for reducing fluctuations in the probe detuning $\delta_p$ that drive these variations.

We estimate the noise contribution of probe-induced collective oscillations by comparing data with and without the oscillations. We make the comparison by applying the probe continuously, and defining measurement windows that are time shifted with respect to the turn on of the probe where the ringing of $\omega_{c'}$ is largest. We first calculate $\Delta(N_{\uparrow f} - N_{\uparrow p})$ measured using the first 86 $\mu$s of data, as was done in the spin-squeezing experiments. Then we calculate $\Delta(N_{\uparrow f} - N_{\uparrow p})$ using data starting 90 $\mu$s after the probe turn on when the collective oscillations have largely damped away. From the comparison of the two variances, we estimate that variable damping contributes a term $R_o$ to the spin noise reduction that empirically scales as $M_t^2$ and limits $R^{-1}$ to 620 (Table 3.1).

The second source of optomechanical back-action we consider here arises from free-space scattered photons heating the ensemble in a position-dependent manner. Importantly, atoms that are more strongly coupled to the cavity mode are more strongly heated due to free-space scattering. This process can be thought of as an external state-changing transition, paralleling the internal state-changing transitions discussed previously (i.e. Eqns. 3.2 and 3.3). The rise in temperature while probing changes the atoms' spatial distribution, reducing the overall coupling to the cavity and shifting $\omega_{c'}$. The average shift of $\omega_{c'}$ caused by the increase in temperature is 1.3 Hz per free space scattered photon, making it the largest average probe-induced frequency shift of $\omega_{c'}$ in our system. Thus, quantum and classical fluctuations in $M_s$ adds noise to measurements $\hat{N}_{\uparrow}$, contributing the relatively small quantum $R_{ext,q}$ and classical $R_{ext,c}$ terms to the spin noise reduction $R$ (see Table 3.1).

Again, the two identified sources of back-action, spatially-dependent photon-recoil heating and variable damping of the optomechanical ringing, fail to predict the entirety of the measured probe-induced back-action $r_c$ that scales as $M_t^2$ for data in Fig. 3.3 and 3.10. We believe the remaining added noise results from the details of the collective optomechanical oscillations, which are difficult to quantify and require further characterization. This additional noise will be important to understand for future advances but is beyond the scope of this work.

# Chapter 4

## A theoretical model for a steady-state superradiant Raman laser

In this chapter, I develop a theoretical model of a steady-state Raman laser that makes three extensions to the two-level superradiant laser model presented in Ref. [115]. These extensions are motivated by repumping and cavity tuning effects present in the experimental work of Refs. [24, 21, 23, 160], described subsequently in this thesis. The extensions include: (1) an imperfect atomic repumping scheme in which some population remains in an intermediate third level, (2) additional decoherence caused by Rayleigh scattering during repumping, and (3) a tuning of the cavity mode frequency in response to the distribution of atomic populations among the available atomic states. We initially make no assumptions about operation in the good or bad cavity regime. I explicitly show that a Raman lasing transition involving three levels can be reduced to a two level lasing transition, making the Raman system a relevant model system to explore the physics of superradiant lasers. Finally, I extend the simple Raman system to the experimental system in $^{87}$Rb, incorporating all eight atomic ground hyperfine states.

## 4.1 Three-Level Model

### 4.1.1 Deriving the Laser Equations

We begin by equations for a general three-level laser, making no assumptions about a good cavity or bad cavity regime. The three-level model for the laser presented here is pictured in Fig. 4.1. It consists of two lasing levels denoted by excited state $|e\rangle$ and ground state $|g\rangle$ separated by optical frequency $\omega_{eg}$, a third state $|3\rangle$ which the atoms must be optically pumped to before they

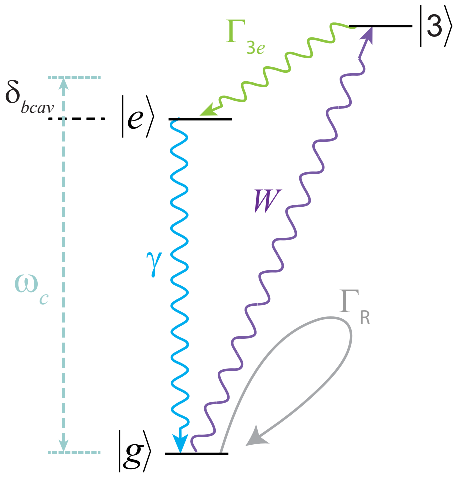

Figure 4.1: Energy level diagram of a three-level superradiant laser using the optical transition from $|e\rangle$ to $|g\rangle$. The emitted optical laser light (blue) is nearly resonant with the cavity mode (dashed lines), detuned from $\omega_c$ by $\delta_{bcav}$. The atoms are incoherently repumped to a third state at a rate $W$. Atoms in $|g\rangle$ also Rayleigh scatter at a rate $\Gamma_R$, but leaves them in state $|g\rangle$. The incoherent repumping from $|3\rangle$ to $|e\rangle$ at rate $\Gamma_{3e}$ completes the cycle.

can be optically pumped back to $|e\rangle$, and a single optical cavity mode with resonance frequency $\omega_c$. The cavity resonance is near the $|e\rangle \to |g\rangle$ transition frequency, with $\delta_{bcav} = \omega_c - \omega_{eg}$. We describe the atoms-cavity system using the Jaynes-Cummings Hamiltonian [77]

$$\hat{H} = \hbar\omega_c \hat{c}^\dagger \hat{c} + \hbar g(\hat{c}^\dagger \hat{J}_- + \hat{c}\hat{J}_+). \tag{4.1}$$

Here $2g$ is the single atom vacuum Rabi frequency that describes the strength of the coupling of the atoms to the cavity mode, set by the atomic dipole matrix element. The operators $\hat{c}$ and $\hat{c}^\dagger$ are the bosonic annihilation and creation operators for photons in the cavity mode. We have introduced the collective spin operators $\hat{J}_- = \sum_{q=1}^{N} \left|g^{(q)}\right\rangle \left\langle e^{(q)}\right|$, and $\hat{J}_+ = \sum_{q=1}^{N} \left|e^{(q)}\right\rangle \left\langle g^{(q)}\right|$ for the $|e\rangle$ to $|g\rangle$ transition, assuming uniform coupling to the cavity for each atom. The index $q$ labels the sum over $N$ individual atoms. We also define the number operator for atoms in the state $|k\rangle$, $k \in \{e, g, 3\}$, as $\hat{N}_k = \sum_{q=1}^{N} \left|k^{(q)}\right\rangle \left\langle k^{(q)}\right|$ and the collective spin projection operator $\hat{J}_z = \frac{1}{2}\sum_{q=1}^{N}(\hat{N}_e^{(q)} - \hat{N}_g^{(q)})$.

The density matrix for the atom cavity system is $\hat{\rho} = \sum_{kl}\sum_{m,n=0}^{\infty} |k, n\rangle \langle l, m|$ where the second sum is over the atomic basis states $k, l \in \{g, e, 3\}$, and the third sum is over the cavity field basis of Fock states. The time evolution of $\hat{\rho}$ is determined by a master equation for the atom cavity system

$$\dot{\hat{\rho}} = \frac{1}{i\hbar}[\hat{H}, \hat{\rho}] + \mathcal{L}[\hat{\rho}]. \tag{4.2}$$

Dissipation is introduced through the Liouvillian $\mathcal{L}[\hat{\rho}]$ [115]. Sources of dissipation and associated characteristic rates include the power decay rate of the cavity mode at rate $\kappa$, the spontaneous decay from $|e\rangle$ to $|g\rangle$ at rate $\gamma$, the spontaneous decay from $|3\rangle$ to $|e\rangle$ at rate $\Gamma_{3e}$, and Rayleigh scattering from state $|g\rangle$ at rate $\Gamma_R$. The repumping is treated as "spontaneous absorption" at rate $W$, analogous to spontaneous decay, but from a lower to higher energy level. Note that here I redefine the symbol $W$ to refer to the repumping rate, which holds throughout the rest of the thesis. Physically, this is achieved by coupling $|g\rangle$ to a very short lived excited state that decays to $|3\rangle$. The Liouvillian is written as a sum of contributions from the processes above respectively as $\mathcal{L}[\hat{\rho}] = \mathcal{L}_c[\hat{\rho}] + \mathcal{L}_{eg}[\hat{\rho}] + \mathcal{L}_{3e}[\hat{\rho}] + \mathcal{L}_R[\hat{\rho}] + \mathcal{L}_{g3}[\hat{\rho}]$. The individual Liouvillians are

$$\mathcal{L}_c[\hat{\rho}] = -\frac{\kappa}{2}(\hat{c}^\dagger\hat{c}\hat{\rho} + \hat{\rho}\hat{c}^\dagger\hat{c} - 2\hat{c}\hat{\rho}\hat{c}^\dagger) \tag{4.3}$$

$$\mathcal{L}_{eg}[\hat{\rho}] = -\frac{\gamma}{2}\sum_{q=1}^{N}(\hat{\sigma}_{eg}^{(q)}\hat{\sigma}_{ge}^{(q)}\hat{\rho} + \hat{\rho}\hat{\sigma}_{eg}^{(q)}\hat{\sigma}_{ge}^{(q)} - 2\hat{\sigma}_{ge}^{(q)}\hat{\rho}\hat{\sigma}_{eg}^{(q)}) \tag{4.4}$$

$$\mathcal{L}_{3e}[\hat{\rho}] = -\frac{\Gamma_{3e}}{2}\sum_{q=1}^{N}(\hat{\sigma}_{3e}^{(q)}\hat{\sigma}_{e3}^{(q)}\hat{\rho} + \hat{\rho}\hat{\sigma}_{3e}^{(q)}\hat{\sigma}_{e3}^{(q)} - 2\hat{\sigma}_{e3}^{(q)}\hat{\rho}\hat{\sigma}_{3e}^{(q)}) \tag{4.5}$$

$$\mathcal{L}_R[\hat{\rho}] = \frac{\Gamma_R}{4}\sum_{q=1}^{N}((\hat{\sigma}_{ee}^{(q)} - \hat{\sigma}_{gg}^{(q)})\hat{\rho}(\hat{\sigma}_{ee}^{(q)} - \hat{\sigma}_{gg}^{(q)}) - (\hat{\sigma}_{ee}^{(q)} + \hat{\sigma}_{gg}^{(q)})\hat{\rho}). \tag{4.6}$$

$$\mathcal{L}_{g3}[\hat{\rho}] = -\frac{W}{2}\sum_{q=1}^{N}(\hat{\sigma}_{g3}^{(q)}\hat{\sigma}_{3g}^{(q)}\hat{\rho} + \hat{\rho}\hat{\sigma}_{g3}^{(q)}\hat{\sigma}_{3g}^{(q)} - 2\hat{\sigma}_{3g}^{(q)}\hat{\rho}\hat{\sigma}_{g3}^{(q)}) \tag{4.7}$$

We obtain equations of motion for the relevant expectation values of the atomic and field operators using $\dot{O} = \mathrm{Tr}[\hat{O}\dot{\hat{\rho}}]$. Complex expectation values are indicated with script notation, while

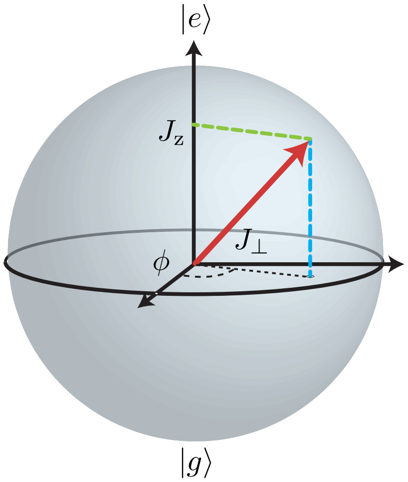

Figure 4.2: Representing the state of the $|e\rangle$, $|g\rangle$ two level system using a collective Bloch vector.

real definite expectation values are standard font, so $\dot{\mathcal{C}} = \mathrm{Tr}[\hat{c}\dot{\hat{\rho}}]$ and $\dot{\mathcal{J}}_- = \mathrm{Tr}[\hat{J}_-\dot{\hat{\rho}}]$. We assume the unknown emitted light frequency is $\omega_\gamma$ and factor this frequency from the expectation values for the cavity field and the atomic polarization, $\mathcal{C} = \breve{\mathcal{C}}e^{-i\omega_\gamma t}$ and $\mathcal{J}_- = \breve{\mathcal{J}}_- e^{-i\omega_\gamma t}$. The symbol $\breve{}$ indicates a quantity in a frame rotating at the laser frequency. The set of coupled atom-field equations is then

$$\dot{\breve{\mathcal{C}}} = -(\kappa/2 + i(\omega_c - \omega_\gamma))\breve{\mathcal{C}} - ig\breve{\mathcal{J}}_- \tag{4.8}$$

$$\dot{\breve{\mathcal{J}}}_- = -(\gamma_\perp + i(\omega_{eg} - \omega_\gamma))\breve{\mathcal{J}}_- + i2g\breve{\mathcal{C}}J_z \tag{4.9}$$

$$\begin{aligned} \dot{J}_z = &-(W+\gamma)\frac{J_z}{2} + (2\Gamma_{3e} - W + \gamma)\frac{N_3}{4} \\ &+ \frac{N}{4}(W-\gamma) + ig(\breve{\mathcal{J}}_-\breve{\mathcal{C}}^* - \breve{\mathcal{J}}_+\breve{\mathcal{C}}) \end{aligned} \tag{4.10}$$

$$\dot{N}_3 = -(\Gamma_{3e} + W/2)N_3 + W(N/2 - J_z) \tag{4.11}$$

In the above equations, we have combined the broadening of the atomic transition into a single transverse decay $\gamma_\perp = \gamma/2 + W/2 + \Gamma_R/2$. We have assumed no entanglement between the atomic degrees of freedom and the cavity field in order to factorize expectation values of the form $\langle\hat{\sigma}_{kl}\hat{c}\rangle = \langle\hat{\sigma}_{kl}\rangle\langle\hat{c}\rangle$. The equations make no assumptions about the relative sizes of the various rates, making them general equations for a three level laser, but one of the distinct differences in cold-atom lasers versus typical lasers is that the transverse decay rate is often dominated by the repumping rate $\gamma \sim W/2$.

It is useful to represent the two-level system formed by $|e\rangle$ and $|g\rangle$ as a collective Bloch vector (Fig. 4.2). The vertical projection of the Bloch vector is given by the value of $J_z$, and is proportional to the laser inversion. The projection of the Bloch vector onto the equatorial plane $J_\perp$ is given by the magnitude of atomic polarization $|\breve{\mathcal{J}}_-|$, with $J_\perp^2 = |\breve{\mathcal{J}}_-|^2$. We refer to $J_\perp$ as the collective transverse coherence of the atomic ensemble.

### 4.1.2 Steady-state Solutions

To understand how extending to this three-level model affects the fundamental operation of the laser, we now study the steady-state solutions with respect to repumping rates, cavity detuning, and Rayleigh scattering rates. The steady-state solutions assume $\gamma \ll W$, the regime of operation for proposed superradiant light sources [115, 33] and the experiments of Refs. [24, 21], but make no approximations based on the relative magnitudes of $\gamma_\perp$ and $\kappa$. Thus $\gamma_\perp \approx W/2 + \Gamma_R/2$, but otherwise the results in the section hold for both good-cavity ($\kappa \ll \gamma_\perp$) and bad-cavity ($\kappa \gg \gamma_\perp$) lasers. We first determine the steady-state oscillation frequency, starting by setting the time derivatives in Eqn. 4.8 and Eqn. 4.9 to zero. After solving for $\breve{\mathcal{C}}$,

$$\breve{\mathcal{C}} = -i\frac{g}{\kappa/2 + i\delta_0}\breve{\mathcal{J}}_- \tag{4.12}$$

where $\delta_0$ denotes the cavity detuning from the laser emission frequency $\delta_0 = \omega_c - \omega_\gamma$. Substituting the result into Eqn. 4.9, we have

$$2g^2 J_z = (\gamma_\perp + i(\omega_{eg} - \omega_\gamma))(\kappa/2 + i\delta_0)\ . \tag{4.13}$$

Since $J_z$ is always real, the imaginary part of Eqn. 4.13 must be zero. This constrains the frequency of oscillation to

$$\omega_\gamma = \frac{\omega_c}{1 + \frac{\kappa}{2\gamma_\perp}} + \frac{\omega_{eg}}{1 + \frac{2\gamma_\perp}{\kappa}}\ , \tag{4.14}$$

a weighted average of the cavity frequency and the atomic transition frequency.

We solve for the steady-state solutions of Eqns. 4.8-4.10 by setting the remaining time derivatives to zero and substituting Eqn. 4.12 for $\mathcal{C}$ in all the equations. In this work, the amplitude properties are our primary interest (as compared to the phase properties studied in Refs. [115, 24]), so we further simplify the equations, at the expense of losing phase information, by considering the magnitude of the atomic polarization $|\breve{\mathcal{J}}_{-}|$. The equation for the time derivative of $J_{\perp}^2$ is

$$\frac{d}{dt}J_{\perp}^2 = |\breve{\mathcal{J}}_{+}||\frac{d}{dt}\breve{\mathcal{J}}_{-}| + |\breve{\mathcal{J}}_{-}||\frac{d}{dt}\breve{\mathcal{J}}_{+}| \tag{4.15}$$

The steady-state output photon flux is just proportional to the square of the equatorial projection

$$\dot{M}_c = \kappa|\breve{\mathcal{C}}|^2 = J_{\perp}^2 \frac{C\gamma}{1+\delta_0'^2}\ . \tag{4.16}$$

Here we have also defined a normalized detuning $\delta_0' = \delta_0/(\kappa/2)$ and a single particle cavity cooperativity parameter

$$C = \frac{(2g)^2}{\kappa\gamma} \tag{4.17}$$

that gives the ratio of single-particle decay rate from $|e\rangle$ to $|g\rangle$ for which the resulting photon is emitted into the cavity mode, making $C$ equivalent to the Purcell factor [149].

After these substitutions and simplifications, the steady-state solutions (denoted with a bar) are

$$\bar{J}_z = \frac{2\gamma_{\perp}(1+\delta_0'^2)}{2C\gamma} \tag{4.18}$$

$$\bar{J}_{\perp}^2 = \left(\frac{N}{2}\right)^2 \left(\frac{2r}{1/2+r}\right) \left(\frac{W(1+\delta_0'^2)}{NC\gamma}\right) \left(1 - \frac{2\gamma_{\perp}(1+\delta_0'^2)}{NC\gamma}\right) \tag{4.19}$$

$$\bar{N}_3 = \frac{\bar{J}_\perp^2}{r}\left(\frac{C\gamma}{W(1+\delta_0'^2)}\right) \tag{4.20}$$

$$\dot{M}_c = \left(\frac{N}{2}\right)^2\left(\frac{2r}{1/2+r}\right)\left(\frac{W}{N}\right)\left(1-\frac{2\gamma_\perp(1+\delta_0'^2)}{NC\gamma}\right) \tag{4.21}$$

written in terms of the repumping ratio $r \equiv \Gamma_{3,e}/W$. Note that $r$ also determines the steady-state build up of population in $|3\rangle$ as $\bar{N}_3/\bar{N}_g = 1/r$. To succinctly express the modification of $\bar{J}_\perp^2$ and $\dot{M}_c$ due to inefficient repumping, we define the reduction factor

$$R(r) \equiv \frac{r}{1/2+r}\ . \tag{4.22}$$

which appears in Eqns. 4.19 and 4.21 above.

Next we discuss the behavior of these solutions for the characteristic parameters of the three-level model: $W$, $r$, $\delta_0'$, and $\Gamma_R$. The results are illustrated in Figs. 4.3-4.5.

First, we focus on the impact of repumping on the steady-state behavior. The photon flux $\dot{M}_c$ follows a parabolic curve versus the ground state repumping rate $W$ (Fig. 4.3). In the limit $\delta_0' \to 0$, $r \to \infty$, and $\Gamma_R \to 0$, Eqn. 4.21 reduces to the result for the simple two-level model of Ref. [115]. This limit is shown as the black curve in part (a) of Figs. 4.3-4.5. At low $W$, the photon flux is limited by the rate at which the laser recycles atoms that have decayed to $|g\rangle$ back to $|e\rangle$. At high $W$, the photon flux becomes limited by the decoherence from the repumping, causing the output power to decrease with increasing $W$. When the atomic coherence decays faster than the collective emission can re-establish it, the output power goes to zero. This decoherence limit is expressed in the condition for the maximum repumping threshold, above which lasing ceases:

$$W_{max} = \frac{NC\gamma}{1+\delta_0'^2} - \Gamma_R\ . \tag{4.23}$$

The output photon flux is optimized at $W_{opt} = W_{max}/2$. Notice that the maximum repumping rate is not affected by $r$. However, the additional decoherence (here in the form of Rayleigh scattering)

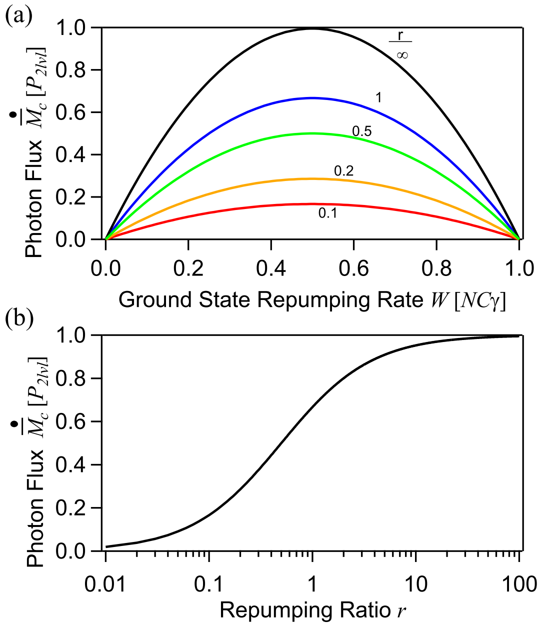

Figure 4.3: (a) Steady-state photon flux $\dot{\bar{M}}_c$ versus ground state repumping rate $W$, with a series of curves showing the effects of repumping through the additional state $|3\rangle$.The case of $r = \infty$ is the two level model of Ref. [115] (black). (b) Photon flux $\dot{\bar{M}}_c$ versus $r$ with $W = W_{opt}$. For all curves, $\delta_0' = 0$ and $\Gamma_R = 0$, and the photon flux is plotted in units of $P_{2lvl} = N^2C\gamma/8$.

lowers the turn-off threshold. If $\Gamma_R > \frac{NC\gamma}{1+\delta_0'^2}$, the decoherence will prevent the laser from reaching superradiant threshold regardless of $W$.

In Figs. 4.3-4.5, we plot Eqn. 4.21 emphasizing (a) the modification to the photon flux parabola, and (b) the optimum photon flux as a function of the population in the third state (as parameterized by the repumping ratio $r$), detuning of the cavity resonance from the emission frequency $\delta$, and additional decoherence from Rayleigh scattering $\Gamma_R$. The photon flux is plotted in units of the optimum photon flux in the two-level model of Refs. [115, 114], $P_{2lvl} = N^2C\gamma/8$.

As the repumping process becomes more inefficient and population builds up in $|3\rangle$, parameterized by $r$ as $\bar{N}_3/\bar{N}_g = 1/r$, we see from Eqns. 4.19 and 4.21 that the photon flux $\dot{\bar{M}}_c$ decreases (Fig. 4.3). A repumping ratio $r = 10$ ensures the laser operates within a few percent of its maximum output power. Notice that $\dot{\bar{M}}_c$ saturates after $r$ is greater than $\approx 2$. Although inefficient repumping suppresses $\dot{\bar{M}}_c$, the optimum and maximum repumping rates $W_{opt}$ and $W_{max}$ are not modified.

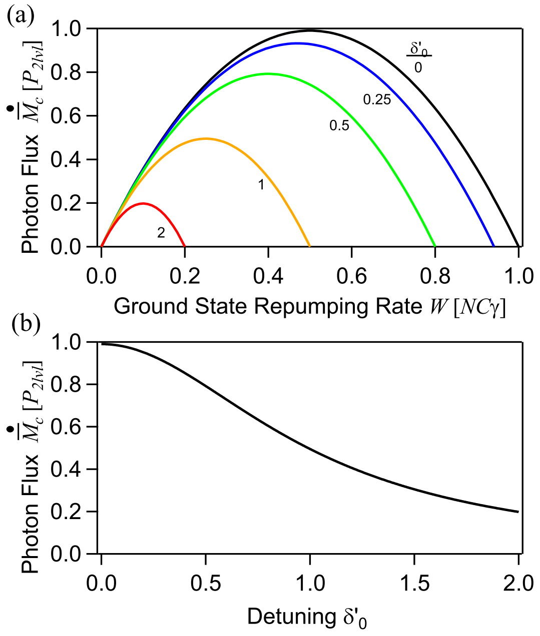

Figure 4.4: (a) Steady-state photon flux $\dot{M}_c$ versus ground state repumping rate $W$, with a series of curves showing the effects of detuning of the cavity resonance frequency from the emitted light frequency $\delta'_0$. (b) Photon flux $\dot{M}_c$ versus $\delta'_0$ with $W = W_{opt}(\delta'_0)$. The photon flux is plotted in units of $P_{2lvl} = N^2 C\gamma/8$. For all curves, $r = \infty$ and $\Gamma_R = 0$.

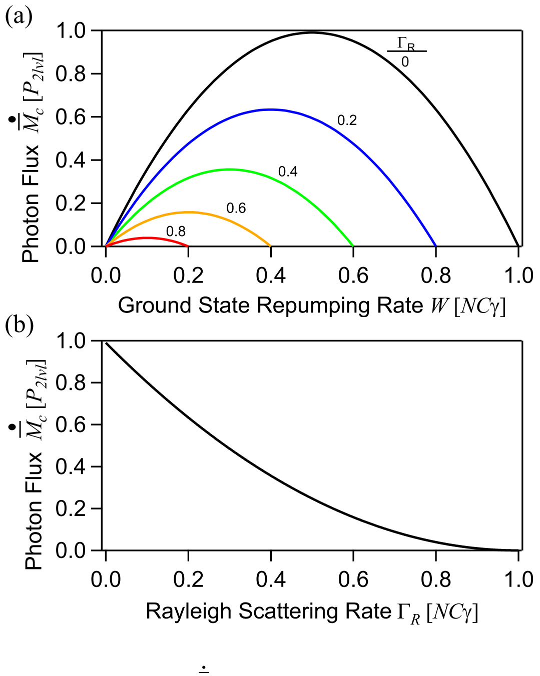

Figure 4.5: (a) Steady-state photon flux $\dot{M}_c$ versus ground state repumping rate $W$, with a series of curves showing the effects of decoherence in the form of Rayleigh scattering from the ground state $|g\rangle$. (b) Photon flux $\dot{M}_c$ versus $\Gamma_R$ with $W = W_{opt}(\Gamma_R)$. The photon flux is plotted in units of $P_{2lvl} = N^2 C\gamma/8$. For all curves, $r = \infty$ and $\delta'_0 = 0$.

The preservation of the operating range can be important, as in practice large values of $r$ can lead to added decoherence (due to intense repumping lasers for example), which does reduce the operating range. Lowering the value of $r$ allows some flexibility as some output power can be sacrificed to keep the laser operating over a wider range of $\overline{W}$.

Cavity detuning modifies both the $\dot{M}_c$ and $W_{\text{opt}}$ (Fig. 4.4). The modification arises from the $\delta_0'$ dependent cavity cooperativity

$$C' = \frac{C}{1+\delta_0'^2} \ . \tag{4.24}$$

The modified cooperativity $C'$ originates from the atomic polarization radiating light at $\omega_\gamma$, which non-resonantly drives the cavity mode with the usual Lorentzian-like frequency response. Thus, the output photon flux $\dot{M}_c$, turn-off threshold $W_{max}$, and optimum repumping rate $W_{opt}$ all scale like $1/(1+\delta_0'^2)$. This effect is symmetric with respect to the sign of $\delta_0'$. Physically, the rate a single atom spontaneously decays from $|e\rangle$ to $|g\rangle$ by emitting a photon into the cavity mode is $\Gamma_c \equiv C'\gamma$, which we use to simplify some later expressions.

Finally, we examine the effect of additional atomic broadening through $\Gamma_R$ in Fig. 4.5. Additional broadening linearly reduces $W_{opt}$ and $W_{max}$, but because we require the repumping rate to remain at $W_{opt}$ in Fig 4.5b, $\dot{M}_c$ has a $(\frac{\Gamma_R}{N\Gamma_c} - 1)^2$ dependence.

The key insight from the steady-state solutions for our three-level model is that imperfections in the lasing scheme can quickly add up, greatly reducing the expected output power of the laser. A repumping scheme should be chosen to minimize Rayleigh scattering $\Gamma_R$ and maximize the repumping ratio $r$. Added decoherence, as well as the detuning $\delta_0'$ are especially problematic because they restrict the possible range of $W$ for continuous operation. The results of this section were crucial for understanding the operation of the experiments described in Chapters 5, 7, and 8.

## 4.2 Raman laser system

In the previous section, I presented a model for a three level laser for qualitatively describing the results from recent experiments that use laser cooled $^{87}$Rb as the gain medium [24, 21, 23]. However, the $^{87}$Rb system also relies on a two-photon Raman lasing transition between hyperfine ground states, instead of a single optical transition. To address this difference, here we provide a model that has a two-photon Raman lasing transition, but a simple one-step repumping scheme directly from $|g\rangle$ to $|e\rangle$. Then in Sec. 4.3, we present a full model of the bad-cavity laser in $^{87}$Rb that has both the two-photon Raman transition and a more complex repumping scheme.

In Sec. 4.2.1, we derive equations of motion for the expectation values in the Raman model, then explicitly adiabatically eliminate the optically excited intermediate state in the Raman transition. In Sec. 4.2.2 I establish the equivalences (and differences) between the Raman and non-Raman models. We will find that the Raman transition is well described as a one-photon transition with a spontaneous decay rate $\gamma$, an effective atom-cavity coupling $g_2$, and with a two-photon cooperativity parameter $C_2$ equal to the original one-photon cooperativity parameter. The Raman system differs in the appearance of two new phenomena: differential light shifts between ground states and cavity frequency tuning in response to atomic population changes. The latter effect was inserted by hand in Sec. 4.1. As in Sec. 4.1, we first derive equations without assuming a good-cavity or bad-cavity laser, only specializing to the bad-cavity limit at the end of the section.

### 4.2.1 Adiabatic Elimination

To establish the connection between two-photon Raman lasing and one-photon lasing, we start by defining the Hilbert space for a three-level Raman system with two ground states denoted $|g\rangle$ and $|e\rangle$ (separated by only 6.834 GHz in $^{87}$Rb) and an optically excited intermediate state $|\mathrm{i}\rangle$ (Fig. 4.6). The Hilbert space also includes a single cavity mode that couples $|g\rangle$ to $|\mathrm{i}\rangle$. The density operator for the Hilbert space is $\hat{\rho} = \sum_{q=1}^{N} \sum_{kl} \sum_{mn}^{\infty} \left|k^{(q)}, n\right\rangle \left\langle l^{(q)}, m\right|$. The first sum is over individual atoms, the second is over the atomic basis states $k, l \in \{i, e, g\}$, and the third sum

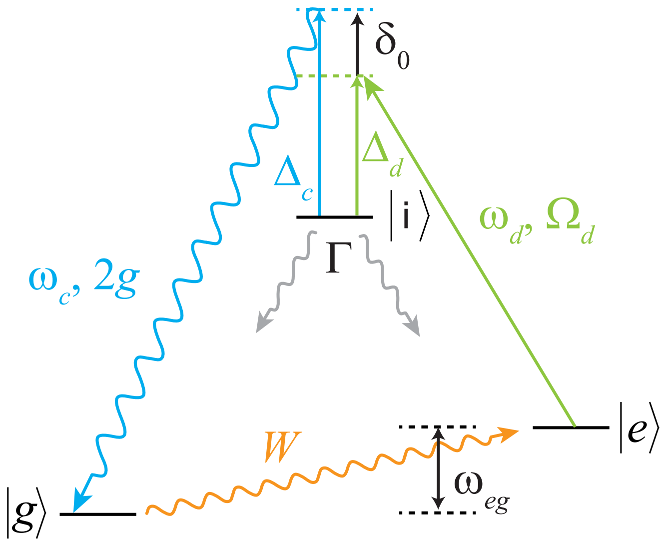

Figure 4.6: Energy level diagram for a superradiant laser enabled by an induced Raman transition. States $|e\rangle$ and $|g\rangle$ are two metastable states separated by a non-optical frequency $\omega_{eg}$. They share an optically excited state $|\mathrm{i}\rangle$ that has a linewidth $\Gamma$. Using a Raman dressing laser (green), detuned from $|\mathrm{i}\rangle$ by $\Delta_d$, we can induced a optical decay to $|g\rangle$, which, in absence of collective effects, would proceed at rate $\gamma = \frac{\Gamma}{4}\left(\frac{\Omega_d}{\Delta}\right)^2$. Including a single optical cavity mode, coupled to the $|\mathrm{i}\rangle$ to $|g\rangle$ transition with coupling constant $2g$, gives rise to collective emission. The cavity mode frequency is $\omega_c$, detuned from $|\mathrm{i}\rangle$ by $\Delta_c$, making the two-photon detuning $\delta_0 = \omega_c - (\omega_d + \omega_{eg})$. To complete the laser cycle, the atoms are incoherently repumped from $|g\rangle$ to $|e\rangle$ at a rate $W$.

is over cavity Fock, or photon-number, states. Raising and lowering operators for the cavity field and atoms are defined as in Sec. 4.1. The state occupation operators for atoms in the state $|k\rangle$ are again $\hat{N}_k = \sum_{q=1}^{N} \left|k^{(q)}\right\rangle \left\langle k^{(q)}\right|$, where the index $q$ denotes a sum over individual atoms. We also define collective atomic raising and lower operators $\hat{J}_{kl} = \sum_{q=1}^{N} \left|k^{(q)}\right\rangle \left\langle l^{(q)}\right|$.

We describe the system via the semi-classical Hamiltonian

$$\begin{aligned} H &= \hbar\omega_c \hat{c}^\dagger \hat{c} + \hbar\omega_i \hat{N}_i + \hbar\omega_e \hat{N}_e + \hbar\omega_g \hat{N}_g \\ &+ \hbar \frac{\Omega_d(t)}{2}(\hat{J}_{ei} + \hat{J}_{ie}) + \hbar g(\hat{c}^\dagger \hat{J}_{gi} + \hat{c}\hat{J}_{ig}). \end{aligned} \tag{4.25}$$

The Raman dressing laser at frequency $\omega_d$ is described by the coupling $\Omega_d(t) = \Omega_d(e^{-i\omega_d t} + e^{i\omega_d t})$, and the atoms are uniformly coupled to the dressing laser. The rotating wave approximation will be applied so that only near-resonant interactions will be considered. The dressing field is externally applied, and we assume it is unaffected by the system dynamics (i.e., there is no depletion of the field).

To reduce the Raman transition to an effective two-level system, we derive the equations of motion for expectation values of the operators that describe the field and the atomic degrees of freedom. As was done in Sec. 4.1, we use the time evolution of the density matrix obtained from the master equation (Eqn. 4.2) to derive the equations of motion $\dot{\hat{\mathcal{O}}} = \mathrm{Tr}[\hat{\mathcal{O}}\dot{\hat{\rho}}]$. The details are included in Appendix A.

After adiabatic elimination of the optically excited state, we have the set of three coupled equations analogous to Eqns. 4.8-4.10:

$$\dot{\mathcal{C}} = \left(-\kappa/2 - i\left(\frac{g^2}{\Delta}N_g + \omega_c\right)\right)\mathcal{C} - i\frac{g\Omega_d}{2\Delta}J_{ge}e^{-i\omega_d t} \tag{4.26}$$

$$\begin{aligned} \dot{J}_{ge} &= \left(-\gamma_\perp - i\left(\frac{\Omega_d^2}{4\Delta} - \frac{g^2|\mathcal{C}|^2}{\Delta} + \omega_{eg}\right)\right)J_{ge} \\ &+ i2\frac{g\Omega_d}{2\Delta}J_z\mathcal{C}e^{i\omega_d t} \end{aligned} \tag{4.27}$$

$$\dot{J}_z = W(N/2 - J_z) + i\frac{g\Omega_d}{2\Delta}(\mathcal{C}^* J_{ge}e^{-i\omega_d t} - \mathcal{C}J_{eg}e^{i\omega_d t}) \tag{4.28}$$

Here $\gamma_\perp = W/2$ and $\Delta = \Delta_d + (\delta_0/2)$, which is also the average of $\Delta_d$ and $\Delta_c$. The Eqns. 4.26-4.28 are general equations, valid without assuming a good-cavity or bad-cavity laser.

### 4.2.2 Defining Effective Two Level Parameters for the Raman System

We can now identify the effective two-photon atom-cavity coupling constant

$$g_2 = \frac{g\Omega_d}{2\Delta} \ . \tag{4.29}$$

The effective Rabi flopping frequency between $|e\rangle$ and $|g\rangle$ is just $2g_2$.

Using this coupling constant, we can also construct an effective cooperatively parameter for the two-photon transition using $C_2 = (2g_2)^2/\kappa\gamma$, where

$$\gamma = \frac{\Gamma}{4}\left(\frac{\Omega_d}{\Delta}\right)^2 \tag{4.30}$$

is the decay rate for an atom in $|e\rangle$ to $|g\rangle$ induced by the dressing laser, calculated for large detunings. Substituting Eqns. 4.29 and 4.30 into the above expression for $C_2$, one finds that the two-photon cooperatively parameter and the one-photon cooperatively parameter (Eqn. 4.17) are identical $C_2 = C = (2g)^2/\kappa\Gamma$. This is explained by the geometric interpretation of $C$, a ratio which is determined by the fractional spatial solid angle subtended by the cavity mode and the enhancement provided by the cavity finesse $F$ which enters through the value of $\kappa \propto 1/F$ [149].

The adiabatic elimination yields the two-photon differential ac Stark shift of the frequency difference between $|e\rangle$ and $|g\rangle$

$$\omega_{ac} = \frac{\Omega_d^2}{4\Delta} - \frac{g^2|\mathcal{C}|^2}{\Delta} \ , \tag{4.31}$$

seen in Eqn. 4.27. The two contributions to $\omega_{ac}$ correspond to virtual stimulated absorption and decay. The same virtual process also acts back on the cavity mode creating a cavity frequency as seen in Eqn. 4.26. The shift corresponds to a modification of the bare cavity resonance frequency, leading to a new dressed cavity resonance $\omega_D$ given by

$$\omega_D = \omega_c + N_g \frac{g^2}{\Delta} \ . \tag{4.32}$$

This is the cavity frequency tuning in response to atomic populations artificially introduced in Sec. 4.1. We have assumed that only an atom in $|g\rangle$ couples to the cavity mode, but in reality both states may couple to the cavity mode such that in general $\omega_D = \omega_c + N_g \frac{g_g^2}{\Delta_g} + N_e \frac{g_e^2}{\Delta_e}$, where we have specified independent populations, coupling constants, and detunings for the two states $|e\rangle$ and $|g\rangle$ denoted by subscripts. For tractability in Sec. 4.1's three-level model, we assumed the pre-factors $g^2/\Delta$ were equal in magnitude but opposite in sign so that cavity frequency tuning could be written as $\frac{g^2}{\Delta}(N_e - N_g) = \alpha J_z$.

As in Sec. 4.1, we also determine the steady-state frequency of the laser

$$\omega_\gamma = \frac{2\gamma_\perp}{2\gamma_\perp + \kappa}\omega_D + \frac{\kappa}{2\gamma_\perp + \kappa}(\omega_{eg} + \omega_d - \omega_{ac}) \ . \tag{4.33}$$

and define $\delta = \omega_D - \omega_\gamma$ as the detuning of the emission frequency $\omega_\gamma$ from the dressed cavity mode $\omega_D$.

Here we see that, in general, both the atomic transition frequency tuning from $\omega_{ac}$ and the cavity frequency tuning in $\omega_D$ are important for the laser amplitude dynamics. Comparing the expressions for $\omega_{ac}$ and $\omega_D$, both scale with $g^2/\Delta$, and the determining degrees of freedom are the relative number of atomic to photonic quanta. In good-cavity systems, a large number of photons can build up in the cavity, and the frequency tuning dynamics are dominated by the ac Stark shift [156]. Superradiant lasers, operating deep in the bad-cavity regime, can operate with less than one intracavity photon on average [24], resulting in a system with amplitude dynamics dominated by dispersive tuning of the cavity mode from population [21]. Additional energy levels that couple to the dressed cavity mode $\omega_D$ can result in a proliferation in the degrees of freedom for dispersive cavity tuning, resulting in a much richer system than one dominated by ac Stark shifts, which depend only on $|\mathcal{C}|^2$.

To complete the analogy to the non-Raman lasing transitions from the previous section and arrive at equations for the bad-cavity laser dynamics, here we make the bad-cavity approximation $\kappa \gg 2\gamma_\perp$. We again adiabatically eliminate the cavity field amplitude, assuming that it varies slowly compared to the damping rate. We define a normalized detuning $\delta' = \delta/(\kappa/2)$, and use the cooperativity parameter $C$ to describe the coupling. After simplifying, we have a two-level system analogous to Eqns. 6.1 and 6.2 in Sec. 4.1

$$\frac{\mathrm{d}}{\mathrm{d}t}|J_{ge}|^2 = -2\gamma_\perp |J_{eg}|^2 + \frac{2C\gamma}{1+\delta'^2} J_z |J_{ge}|^2 \tag{4.34}$$

$$\frac{\mathrm{d}}{\mathrm{d}t} J_z = W(N/2 - J_z) - \frac{C\gamma}{1+\delta'^2} |J_{ge}|^2 \ . \tag{4.35}$$

Note that in the bad-cavity limit, the detuning of the dressed cavity mode from the emission frequency $\delta$ is to good approximation the difference of the dressed cavity resonant frequency and the dressed atomic frequency, modified by a small cavity pulling factor

$$\delta \approx (\omega_D - (\omega_{eg} - \omega_{ac} + \omega_d)) \left(1 - \frac{W}{\kappa}\right) \ . \tag{4.36}$$

Our conclusion is that a Raman superradiant laser can perform as a single-photon superradiant laser with $C_2 = C$, but with a transverse collective coherence that evolves a quantum phase at a frequency set by the separation of the two ground states. This means that while superradiant Raman lasers based on hyperfine transitions may not be useful for optical frequency references, their tunability and control make them excellent physical "test-bed" systems for studying cold atom lasers [156, 24, 21]. In addition, the switchable excited state lifetime in a Raman system introduces the possibility of dynamic control in the superradiant emission, useful for novel atomic sensors [23, 160].

## 4.3 Full Model in $^{87}$Rb

In this section, we give the results of a model for a superradiant Raman laser using the ground state hyperfine clock transition ($|g\rangle = |5^2S_{1/2}, F = 1, m_f = 0\rangle$, $|e\rangle = |5^2S_{1/2}, F = 2, m_f = 0\rangle$) in $^{87}$Rb, including all eight ground state levels for repumping. The results include specific values

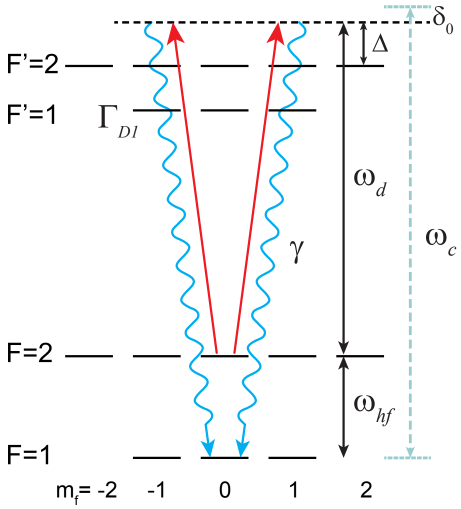

Figure 4.7: Lasing transition and Raman dressing scheme on the $^{87}$Rb D1 line (795 nm). The dressing light (red) and collective emission (blue) are a superposition of $\sigma^+$ and $\sigma^-$ polarizations because the direction of propagation of the light is along the quantization axis defined by the direction of the magnetic field at the atoms. The Raman dressing laser is detuned by $\Delta$ from the atomic transition. The bare cavity detuning is $\delta_0 = \omega_c - (\omega_d + \omega_{hf})$. The optically excited state on the D1 line has a linewidth $\Gamma_{D1}/2\pi = 5.75$ MHz. The effective population decay from $|F=2, m_f=0\rangle$ to $|F=1, m_f=0\rangle$ is $\gamma = \frac{\Gamma_{D1}}{4}\left(\frac{\Omega_d}{\Delta}\right)^2$.

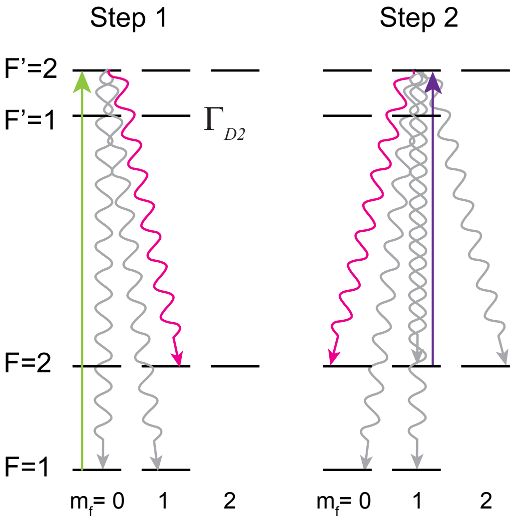

Figure 4.8: Two step repumping process on the $^{87}$Rb D2 line (780 nm). The diagram is drawn showing on only positive Zeeman states, but the process is symmetric with respect to $m_f = \pm1, \pm2$. The desirable decay branches (magenta) show the most direct repumping sequence, although any particular repumping sequence could go through many ground hyperfine states. The optically excited state on the D2 line has a linewidth $\Gamma_{D2}/2\pi = 6.07$ MHz.

of parameters taken from the superradiance experiments in this thesis. The model combines the three-level repumping from the model in Sec. 4.1 and the Raman transition between $|e\rangle$ and $|g\rangle$ of Sec. 4.2. After summarizing the key steady-state results, we use linear response theory similar to Sec. 4.1 to examine the stability of the laser, identifying the important parameters for stable operation in superradiant Raman lasers.

### 4.3.1 Continuous Superradiant Raman Laser in $^{87}$Rb

We model steady-state superradiance in the full $^{87}$Rb Raman system by first including incoherent repumping among the eight ground $5\,^2S_{1/2}$ hyperfine populations $N_{F,m_F}$ (Fig. 4.8). We use $\lambda = \{F, m_F\}$ to refer to a generic set of population quantum labels as $N_\lambda$.

The repumping is performed using single particle scattering off optically excited states to result in Raman transitions to move population from $F = 1$ to $F = 2$ (Fig. 4.8). The repumping has a clear analogy to the three-level model from Sec. 4.1 because population cannot be directly transfered from $|e\rangle$ to $|g\rangle$, meaning some finite population accumulates outside the coherent lasing levels. Separate lasers repump atoms in the $F = 1$ state (green) and the $F = 2$ state (purple). The lasers are characterized by Rabi frequencies $\Omega_{1,0,2,0}$ and $\Omega_{2,1,2,1}$ respectively. The rate of population transfer out of $|g\rangle$ is proportional to the total scattering rate $W$, which includes the Rayleigh scattering rate. The transverse decoherence rate $\gamma_\perp = W/2$ is dominated by the necessary scattering from repumping. In analogy with the model in Sec. 4.1, the repumping rates out of the states in $F = 2$ are proportional to $rW$, where $r = \Omega^2_{2,1,2,1}/\Omega^2_{1,0,2,0}$. The detailed equations for the repumping are given in Appendix B.

To include the collective emission in our $^{87}$Rb Raman laser model, we reduce the Raman transition dynamics to an effective two-level model by eliminating the optical intermediate state (see Sec. 4.2). The hyperfine ground states $|g\rangle$ and $|e\rangle$ form the effective two-level transition shown in Fig. 4.7. The optical transition is induced by a 795 nm dressing laser with Rabi frequency $\Omega_d$ far detuned from the $|e\rangle \rightarrow \left|5^2P_{3/2}, F' = 2, m'_F\right\rangle$ transition ($\Delta$ is typically 1-2 GHz). The dressing laser creates an effective spontaneous scattering rate from $|e\rangle$ to $|g\rangle$ $\gamma = \frac{\Gamma_{D1}}{4}\left(\frac{\Omega_d}{\Delta}\right)^2$ (see Eqn. 4.30

in Sec. 4.2). The fraction of this single particle scattering that goes into the cavity mode is given by the cooperativity parameter $C = 8 \times 10^{-3}$.

Single particle scattering in the cavity mode results in a build up of collective coherence $J_\perp^2$ between $|e\rangle$ and $|g\rangle$. The collective emission has an enhanced scattering rate which dominates the population transfer from $|e\rangle$ to $|g\rangle$. We include the population transfer from collective emission along with the equation for the collective coherence Eqn. 4.34 with the population equations from repumping to form the set of equations used to obtain the steady-state solutions and perform the linearized analysis. We give the details in Appendix B.

### 4.3.2 Steady-state Solutions

In analogy to the model in Sec. 4.1, we are concerned with steady-state values of the inversion $J_z = \frac{1}{2}(N_{2,0} - N_{1,0})$, the collective transverse coherence $J_\perp^2$, and the population that occupies energy levels outside the laser transition $N_{other} = N - N_{2,0} - N_{1,0}$. The steady-state solutions of the system equations are

$$\bar{J}_\perp^2 = \left(\frac{N}{2}\right)^2 \left(\frac{\frac{3}{13}r}{\frac{27}{104}+r}\right)\left(\frac{2W(1+\delta'^2)}{NC\gamma}\right)\left(1-\frac{W(1+\delta'^2)}{NC\gamma}\right) \tag{4.37}$$

$$\bar{J}_z = \frac{W(1+\delta'^2)}{2C\gamma} \tag{4.38}$$

$$\bar{N}_{other} = N\left(\frac{4}{13}\right)\left(\frac{\frac{27}{32}+r}{\frac{27}{104}+r}\right)\left(1-\frac{W(1+\delta'^2)}{NC\gamma}\right) \tag{4.39}$$

$$\bar{M}_c = \bar{J}_\perp^2 \frac{C\gamma}{1+\delta'^2} \; . \tag{4.40}$$

Here $\delta'$ is the detuning of the dressed cavity mode from the laser emission frequency.

As in Sec. 4.1, there is again both a repumping rate that maximizes the coherence (along with the output photon flux) and a repumping threshold for laser turnoff

$$W_{opt} = \frac{NC\gamma}{2(1+\delta'^2)}, \tag{4.41}$$

$$W_{max} = 2W_{opt}. \tag{4.42}$$

To understand the effect of repumping in the full $^{87}$Rb model, we compare Eqn. 4.37 to the steady-state coherence in the three-level model, Eqn. 4.19 in Sec. 4.1. While the form of the expression versus the ground state repumping rate $W$ is the same as the three-level model, the scale factor associated with the repumping ratio is modified. The power reduction factor

$$R_{Rb}(r) \equiv \frac{3}{13}\left(\frac{r}{\frac{27}{104}+r}\right) \tag{4.43}$$

is the modification to the steady-state photon flux compared to the ideal model in Refs. [115]. $R_{Rb}$ has a maximum value of 3/13 contrasted with $R$, Eqn. 4.22, which has a maximum of 1.

While the repuming ratio $r \not\ll 1$, most of the population remains in $N_{2,0}$ and $N_{1,0}$ (Eqn. 4.39). The inversion $J_z$ is the same as the model from Sec. 4.1 (Eqn. 4.18), as here $W$ corresponds to $2\gamma_\perp$. Thus, the results of Figs. 4.3-4.5 give a good qualitative understanding of the steady-state behavior of the $^{87}$Rb system as well.

## 4.4 Conclusion

We have developed a minimal model for a steady-state, superradiant laser that includes key features of observed in recent experiments using $^{87}$Rb [24, 21, 23, 160]. The model describes the reduction in the laser output power with the repumping ratio $r$, the cavity-atomic transition detuning $\delta$, and an additional source of decoherence, such as caused by Rayleigh scattering $\Gamma_R$. The explicit elimination of an intermediate excited state in our Raman laser theory shows that a Raman laser can serve as a good physics model for lasers operating deep into the bad-cavity regime. The adiabatic elimination also reveals the source of the crucial atomic and cavity frequency tunings that can play a key role in the amplitude stability of Raman lasers, both in the bad-cavity [21] and good-cavity [156] regimes.

In addition to explaining experimental observations in previous work, this paper serves as a guide for the design of other cold-atom lasers and superradiant light sources that utilize nearly-forbidden optical transitions [115, 33]. Our minimal model includes a multi-step repumping process and shows the path to adding more energy levels or repumping steps as required for realistic experimental systems. Many of the results here do not assume a good-cavity or bad-cavity laser, making them general results that can be followed until simplified expressions based on a particular laser regime are required.

In general, superradiant laser designs should strive to eliminate sources of decoherence, such as Rayleigh scattering or differential ac Stark shifts from repumping light, while maintaining efficient repumping that avoids accumulation of population outside the atomic energy levels of the lasing transition. The steady-state and amplitude stability properties of cold-atom lasers can be significantly modified by their repumping scheme.

Future designs may also apply optical dressing techniques to induce decay of the excited state [160, 23]. In such Raman systems, the dressing of the cavity-mode can provide positive or negative feedback for stabilizing the output power of the laser. The dressed cavity mode also can pull the laser emission frequency, serving as an amplitude noise to phase noise conversion mechanism. Future theoretical and experimental work, beyond the scope of this paper, can extend the linear response theory presented here to incorporate quantum noise in the repumping process. Cavity frequency pulling and quantum noise in the dressing of the cavity mode are possible sources of the laser linewidth broadening observed in Ref. [24], where the observed linewidth exceeded the simple Schawlow-Townes prediction [115].

# Chapter 5

## A steady state superradiant laser with less than one intracavity photon

In this chapter, I describe the experimental implementation of a superradiant Raman laser source in which spontaneous synchronization of more than $10^6$ $^{87}$Rb atomic dipoles is continuously sustained by as few as 0.2 photons on average inside the optical cavity. By operating at low intracavity photon number, I demonstrate isolation of the collective atomic dipole from the environment by a factor $> 10^4$. The emitted light has a frequency linewidth, measured relative to the Raman dressing laser, below that of single-particle decoherence rates and more than $10^4$ times below the quantum linewidth limit typically applied to good-cavity, optical lasers [136]. These results demonstrate several key predictions relevant for future superradiant lasers that may be used to improve the stability of passive atomic clocks [78] and have the potential to open up searches for new physics [16, 55]. This chapter is based on the work in Ref. [24].

### 5.1 Superradiant Lasers

The fundamental linewidth of a laser is given by a generalized expression for the Schawlow-Townes full width at half maximum (FWHM) $\Delta f_{\mathrm{ST}}$ in Hertz by Kolobov *et al.* [92] and in a simplified form by Kuppens *et al.* [97] as

$$\Delta f_{\mathrm{ST}} = \frac{1}{4\pi}\frac{hf}{P_{\mathrm{out}}}\left(\frac{2\gamma_{\perp}\kappa}{2\gamma_{\perp}+\kappa}\right)^2, \tag{5.1}$$

where $P_{\mathrm{out}}$ is the power exiting the cavity, $f$ is the oscillation frequency, $h$ is the Planck constant, and $\kappa$ is the cavity power decay rate. The transverse decoherence rate of the lasing optical transition is

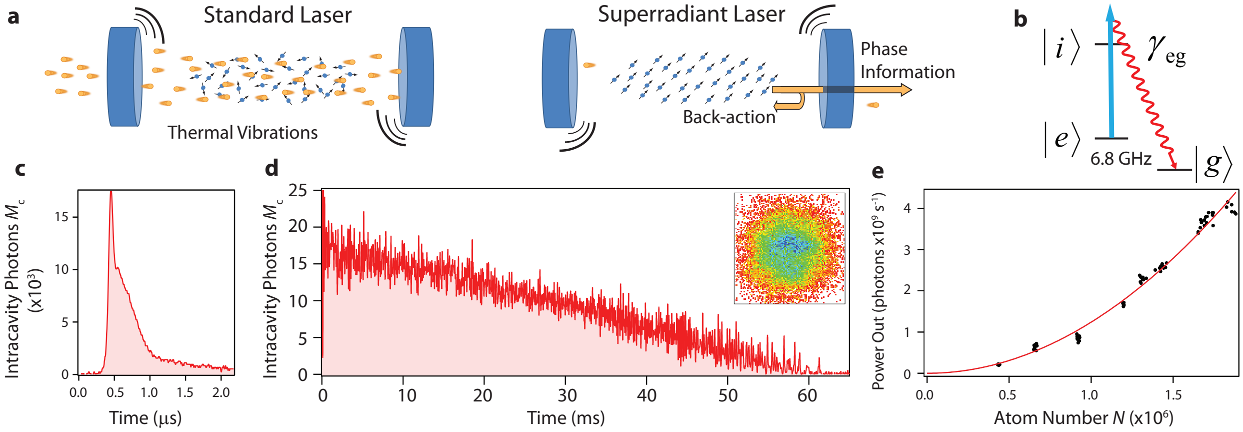

Figure 5.1: **A steady state superradiant laser.** **a,** (left) In a good-cavity laser far above threshold, many photons (yellow) circulate inside the cavity, extracting energy from the largely incoherent atomic gain medium (blue). Thermal vibrations of the mirror surfaces modulate the cavity resonance frequency, limiting the linewidth of the laser. In a superradiant laser (right), the collective atomic dipole stores the coherence, and continuous stimulated emission can be achieved even with less than one photon in the cavity. The stimulation enables phase information to be extracted at a useful rate, while the small intracavity photon number leads to only weak cavity-induced backaction on the collective atomic dipole. **b,** To mimic a narrow optical atomic transition, we dress the metastable ground state labeled $|e\rangle$ with a laser (blue) to induce a spontaneous two-photon Raman transition to $|g\rangle$, with tunable rate $\gamma_{\mathrm{eg}}$. With no repumping light, a single superradiant pulse is emitted. **d,** With repumping light applied, we observe quasi-continuous emission limited by atom loss. The atoms emit into a single spatial mode of the cavity ($\mathrm{TEM}_{00}$) imaged on a CCD (inset). **e,** The measured peak power output (black circles) scales as the number of atoms squared.The red line is a quadratic fit to the data.

$\gamma_\perp = \gamma_{\text{eg}}/2 + 1/T_2$, where $\gamma_{\text{eg}}$ is the decay rate from excited to ground state and $1/T_2$ parameterizes additional atomic dephasing mechanisms.

Optical lasers have typically operated in the good-cavity limit $2\gamma_\perp >> \kappa$ (Fig. 5.1a) due to Doppler broadening or broadening due to interactions with crystal lattices, for instance. In this limit, the generalized linewidth expression reduces to $\Delta f_{\text{GST}} = \kappa/(4\pi M_{\text{c}})$, where $M_{\text{c}}$ is the average intracavity photon number (see Sec. 5.6).

If the cavity and atomic transition frequencies, $f_{\text{cav}}$ and $f_{\text{atomic}}$, are not identical, the system oscillates at a weighted average frequency $f_\gamma = (2\gamma_\perp f_{\text{cav}} + \kappa f_{\text{atomic}})/(2\gamma_\perp + \kappa)$. The cavity frequency pulls the oscillation frequency away from the atomic transition frequency by an amount $P \equiv df/df_{\text{cav}} = 2\gamma_\perp/(2\gamma_\perp + \kappa)$. In the good cavity limit, the emission frequency tracks the empty cavity frequency as $P \approx 1$.

In the bad-cavity limit ($2\gamma_\perp \ll \kappa$), the FWHM linewidth reduces to $\Delta f_{\text{BST}} = \gamma_\perp^2/(\pi\kappa M_{\text{c}})$, a result intimately connected to cavity narrowing using slowed light [97, 158]. The collective atom-light excitation is stored predominantly in the gain medium, making the atoms the primary carrier of phase information (Fig. 15.1a). The weak intracavity photon field acts mainly as a communication bus to drive spontaneous synchronization of the atomic dipoles and to extract information about the phase stored in the collective atomic dipole. The synchronized atomic dipoles radiate at an enhanced rate, a phenomenon known as superradiance or superfluorescence [43]. In addition, the frequency pulling becomes $P \approx 2\gamma_\perp/\kappa \ll 1$, dramatically reducing the impact of noise in the cavity frequency. This isolation of the oscillator from the environment is the key to reducing the sensitivity of such a laser to thermal and technical noise.

## 5.2 Experimental System

Our experimental system, described in Sec. 5.6 and Chapter 2, operates deep into the optical bad-cavity regime, with $2\gamma_\perp/\kappa = 2 \times 10^{-5}$ to $10^{-3}$. The effective excited state scattering rate $\gamma_{\text{eg}} \approx 2$ to $60\ s^{-1}$ is comparable to some optical clock candidates, and the average intracavity photon number $M_{\text{c}}$ ranges from 0.2 to 60. The system consists of an ensemble of $N \approx 10^6$ $^{87}$Rb atoms confined to the $\mathrm{TEM}_{00}$ mode of a medium finesse ($F = 710$) optical cavity with cavity power decay rate $\kappa = 2\pi \times 11$ MHz. Optomechanical effects are suppressed by tightly trapping the atoms using a one-dimensional intracavity optical lattice at 823 nm. We observe no lasing at the vibrational sideband frequencies.

The cavity is coupled to an optically dressed atomic ground state engineered to imitate a long-lived, optically excited atomic state [115, 33] (Fig. 15.1b). The effective excited $|e\rangle$ and ground $|g\rangle$ states are the magnetic field insensitive ground hyperfine clock states. The upper state $|e\rangle$ is metastable and separated from $|g\rangle$ by only 6.8 GHz, but we induce an optical Raman decay from $|e\rangle$ to $|g\rangle$ by applying a linearly polarized 795 nm dressing laser tuned 1 to 2 GHz higher in frequency than the optically excited intermediate state $|i\rangle$. The cavity is tuned to resonance with the spontaneously emitted photon. The combination of detuning and dressing laser power sets a tunable single particle decay linewidth $\gamma_{\mathrm{eg}}$, the rate from $|e\rangle$ to $|g\rangle$. The cycle is completed using 780 nm light to incoherently repump atoms from $|g\rangle$ to $|e\rangle$ at a rate proportional to the single particle rate,$w$, out of the ground state.

The superradiant linewidth $\Delta f_{\mathrm{BST}}$ reduces to $C\gamma_{\mathrm{eg}}/\pi$ at a peak repumping rate $w_{\mathrm{pk}} = NC\gamma_{\mathrm{eg}}/2$. The cooperativity is $C = (2g_2)^2/\kappa\gamma_{\mathrm{eg}}$, where $g_2$ is the single particle, two-photon coupling of the atoms to the cavity emission mode after adiabatic elimination of the intermediate state $|i\rangle$. It should be possible to obtain $\Delta f_{\mathrm{BST}} \ll \gamma_{\mathrm{eg}}$ by operating in the single particle, weak coupling regime $C \ll 1$, a limit that contrasts with the trend in quantum optics to engineer systems with single-particle, strong-coupling $C \gg 1$. It is predicted that strong collective coupling $NC \gg 1$ is sufficient for self-sustained stimulated emission. In this work, we operate with $C = 7.7(4) \times 10^{-3}$ and $NC \approx 10^4$ (all reported uncertainties describe 68% confidence intervals).

## 5.3 Results

A laser operating in the superradiant regime assumes continuous light generation, but optical superradiance is regularly regarded as an intrinsically pulsed process with no phase coherence between the pulses. A single superradiant pulse of photons is emitted if all atoms are initial-

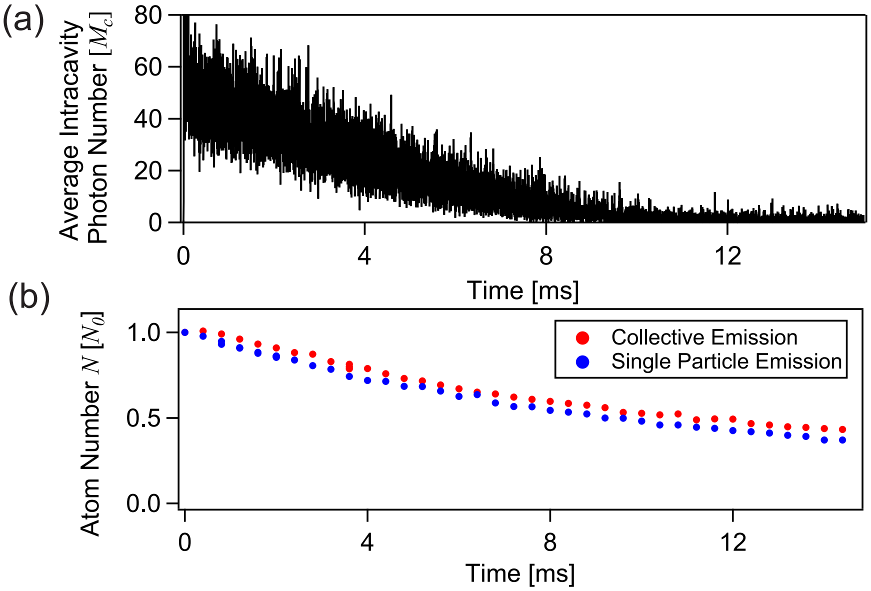

Figure 5.2: The laser can operate in a quasi-steady-state mode in that each atom can go through an emission-repumping cycle multiple times. However, the emitted power decreases over time, eventually going to zero. In (a), we show one example of emission lasting ~ 10 ms. Under other conditions, we have observed emission lasting up to 120 ms. We verify that atoms are being lost from the trap (b) by measuring a changing frequency shift of the cavity mode consistent with atom loss. The loss is not associated with collective emission, as shown by the equivalence of the loss observed with (red) collective emission or (blue) induced single particle emission from $|e\rangle$ to $|g\rangle$ via free space scattering at the same rate as the collectively enhanced decay rate. The atom number is in units of the initial atom number $N_0$.

ized in $|e\rangle$ and the dressing laser is applied (Fig. 5.1c). This pulse contains approximately 0.9(1) photons/atom. Without a pump to recycle the atoms to $|e\rangle$, this pulse is the full extent of the superradiance.

If instead we apply continuous optical repumping from $|g\rangle$ to $|e\rangle$ along with the dressing laser, we observe a transition to quasi-continuous superradiance. We verify that the signal is not just a single pulse as the integrated number of photons emitted into the cavity mode is approximately 35(4) photons/atom for the data in Fig. 5.1d. By varying the excited state lifetime and repumping rates, we were also able to observe superradiant emission lasting as long as 120 ms. By measuring a temperature of the atoms both before and after the superradiant emission, we see a increase in temperature from 16(1) $\mu$K to 30(2) $\mu$K. Given the trap depth of 351 $\mu$K, this is only a minor increase in temperature. The light source shuts off as atoms are lost from the lattice, most likely due to light assisted atomic collisions.

We measure the atom loss by starting superradiant emission and then switching off the dressing and repumping laser after a variable emission time. Turning off the lasers stops the emission and freezes the state populations. Immediately afterwards, we probe the resonance frequency of the cavity, which is dispersively shifted by the atoms. The non-destructive probing is similar to the probing used in spin squeezing experiments described in Chapter 3, and the details for this experiement are included in Section 5.6.1.

Fig. 5.2(a) shows the emitted power approaching zero after lasing for $\sim 10$ ms. The measured cavity shift decreases the longer the laser is allowed to oscillate, indicating that either atoms are being lost from the trap or are having their coupling to the cavity mode reduced. We verify that atoms are actually being lost from the trap by also performing fluorescence measurements in the same experiment. The decay of the fluorescence signal is consistent with loss of atoms from the trap. The loss of atoms is shown in Fig. 5.2(b).

The lasing quenches after only half the atoms are lost. This is explained by the fact that the fixed repumping rate $W$ was initially tuned to an optimum value $W \approx N_0 C\gamma_{eg}/2$ for the initial $N_0$ atoms in the trap. The maximum repumping rate $W_{max} = NC\gamma_{eg}$, above which lasing is quenched as discussed below, then crosses below the fixed repumping rate $W$ when the changing atom number $N$ meets the condition $N < N_0/2$.

Lastly, in Fig. 5.2(b), we present data showing that the loss of atoms is not enhanced by the superradiant process itself. To observe the loss of atoms without superradiant emission, we tune the dressing laser closer to atomic resonance, increasing the single particle scattering to a rate comparable to the collectively enhanced rate. We also move the cavity resonance frequency far from the atomic transition frequency to inhibit any collective enhancement of the decay. After running this non-collective emission for a variable time, we measured the atom number (Fig. 5.2(b), blue circles). The atom loss was the same as in the case with collective emission (Fig. 5.2(b), red circles). Because we observe loss from the trap that is not connected to collective emission, we suspect that light assisted collisions, either from the dressing laser or the repumping lasers, are

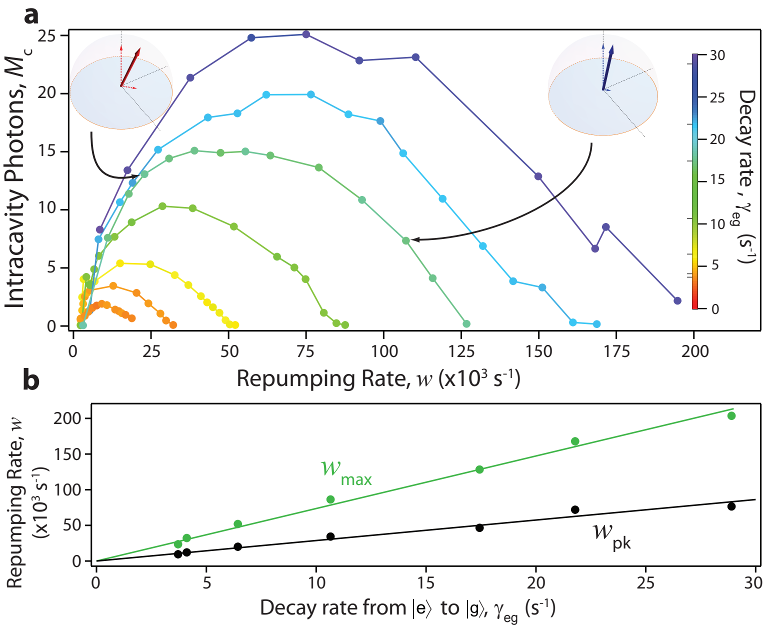

Figure 5.3: **Repumping-induced quenching a,** The average number of intracavity photons $M_c$ versus the repumping rate $w$ for different decay rates $\gamma_{eg}$. The inferred Bloch vector is shown for two operating points. **b,** The repumping rate above which superradiance is quenched $w_{max}$ (green) and the repumping rate at peak output power $w_{pk}$ (black) scale linearly with $\gamma_{eg}$, shown with linear fits to the data.

responsible for the atom loss and ultimately for the shutoff of the laser. Light-assisted collisions could be eliminated in the future using higher dimensional trapping lattices.

Ordinary single-particle fluorescence from an atomic ensemble is too weak to be useful as a phase reference, but the emission rate by the collective dipole is increased into a single spatial mode by approximately $N$. The predicted peak flux of photons out of the cavity is $\dot{M}_{pk} = RN^2C\gamma_{eg}/8$, where $R = 1$ for the two-level model of Ref. [115]. Typically, $R \approx 0.18$ for our multi-level system due to the necessity of optically repumping the atoms through several intermediate Zeeman states. We observe the peak output power scaling as $N^2$ (Fig. 15.1e). For this data, $2\gamma_\perp/\kappa \approx w/\kappa = 3.9(8) \times 10^{-4}$ to $1.4(3) \times 10^{-3}$.

Repumping non-collectively scatters photons transverse to the cavity mode, causing collapse of individual atomic wavefunctions, which are then torqued to rejoin the collective dipole by the weak intracavity field. If the repumping rate is greater than $w_{max} = NC\gamma_{eg}$, the cavity field

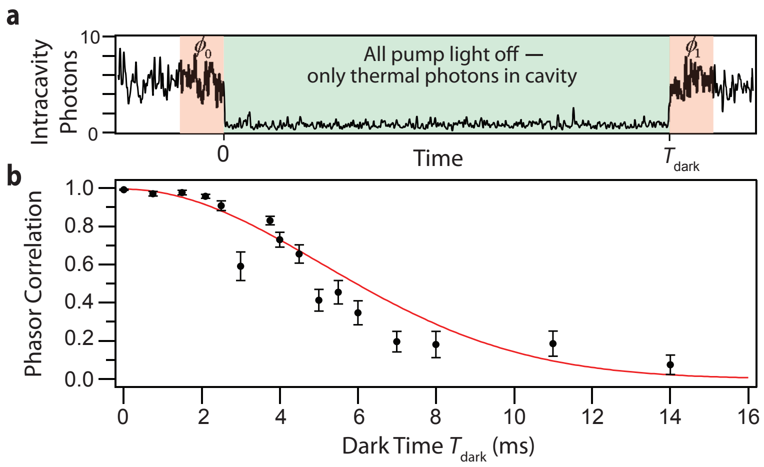

Figure 5.4: **Phase coherence maintained with no intracavity photons.** **a,** The dressing and repumping lasers are shut off for some variable dark time $T_{\text{dark}}$. The phase of the light relative to the dressing laser is measured shortly before and after the dark time. **b,** The phasor correlation function, defined in Sec. 5.6. At times $T_{\text{dark}} < 7$ ms, the phases are correlated because the collective atomic dipole seeds reestablishment of superradiant emission. At longer times, the collective atomic dipole dephases and superradiant emission restarts with a random phase. A gaussian fit is shown in red line. Error bars ±1 s. d.

cannot replenish the collective dipole relative to the rate of repumping induced collapse [115]. The predicted peak output power occurs at $w_{\text{pk}} = w_{\text{max}}/2$. The quenching and linear scaling of $w_{\text{max}}$ and $w_{\text{pk}}$ with $\gamma_{\text{eg}}$ are shown in Fig. 25.3. The fitted and predicted slopes agree to within the 20% uncertainty on the predicted values.

To explicitly show that the phase memory of the system resides in the collective dipole, we measure the phase of the emitted light just before $\phi_0$ and after $\phi_1$ a dark period $T_{\text{dark}}$ in which both the dressing and repumping lasers are shut off (see Fig. 35.4) During this period, any photons in the cavity exit with exponential time constant $1/\kappa = 14$ ns, rapidly erasing all phase information stored in the light mode. While the phase $\phi_0$ is random from one trial to the next, the phase difference within a single trial $\phi_1 - \phi_0$ is highly correlated, demonstrating that phase information is being stored within the collective atomic dipole.

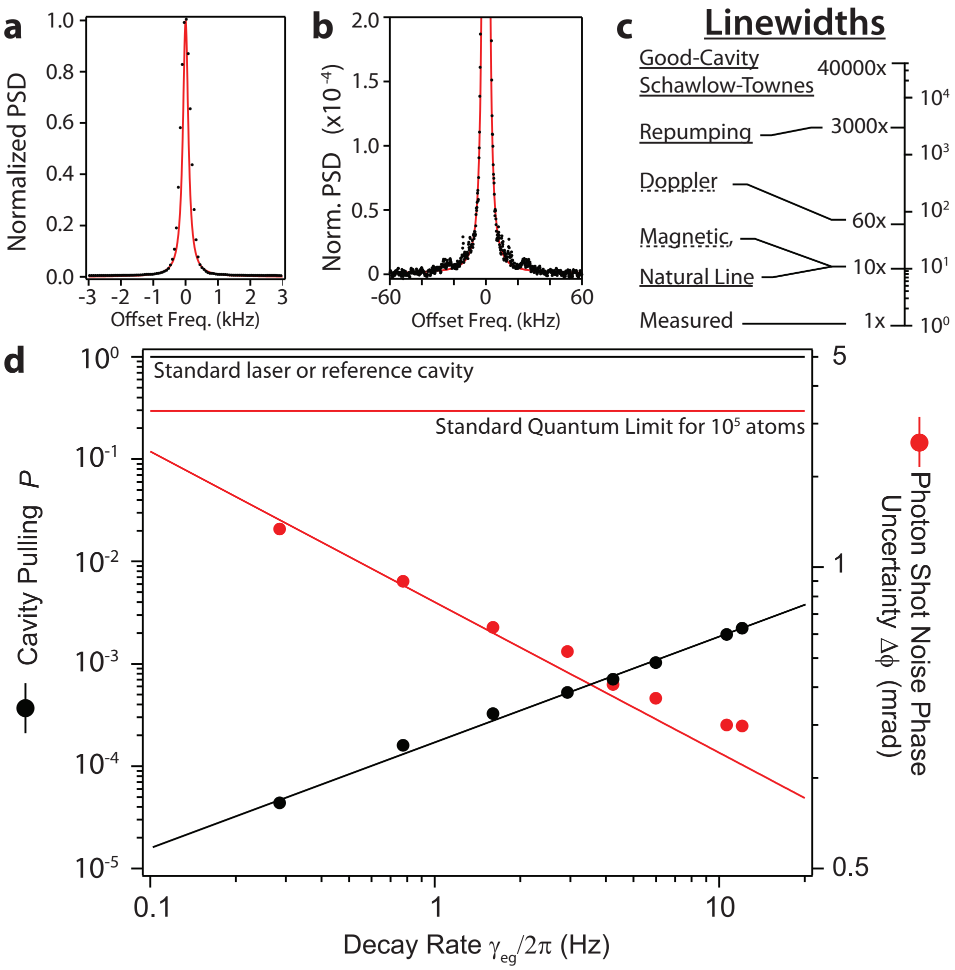

Figure 5.5: **Beyond standard optical laser stability.** **a**, The average power spectrum of the heterodyne signal of the emitted light (black circles) at $M_\mathrm{c} = 0.20(2)$ intracavity photons with a Gaussian fit (red line). **b**, The average power spectrum of the heterodyne signal of the emitted light (black circles) at $M_\mathrm{c} = 30.6(5)$ with a Lorentzian fit that excludes offset frequencies lower than 4 kHz. **c**, The comparison of various characteristic linewidths. Gaussian noise processes are compared to the measured Gaussian FWHM (dashed), and Lorentzian noise processes were compared to the measured Lorentzian FWHM (solid). Details of the experimental configurations are included in Sec. 5.6. **d**, As the decay rate $\gamma_\mathrm{eg}$ decreases, the atomic dipole becomes more isolated from the mirrors, as shown by directly measuring cavity frequency pulling $P$ (black circles). Because of the collectively enhanced emission rate, phase information is still coupled out of the system at a sufficient rate to achieve an ideal RMS phase noise (red circles) sufficient for spectroscopy below the standard quantum limit for $10^5$ atoms. The fitted curves are consistent with the predicted scaling with $\gamma_\mathrm{eg}$.

## 5.4 Expt. Measure: Linewidth

In Fig. 45.5a, we present the power spectrum of the emitted light heterodyned with the dressing laser at $M_{\mathrm{c}} = 0.20(2)$ photons in the cavity mode. The measured Gaussian FWHM, 350(25) Hz, is 4 orders of magnitude below the good-cavity Schawlow-Townes linewidth limit assuming one intracavity photon. The measured linewidth is also below single particle decoherence rates arising from inhomogeneous magnetic field broadening, Doppler decoherence, and the repumping-broadened linewidth $w$ (see Fig. 45.5c). We believe the predicted superradiant linewidth, 2(1) mHz, is not observed primarily due to dispersive tuning of the cavity mode frequency caused by changes in atom number between individual experimental trials, an effect present in this Raman system, but not in proposed active optical clocks, as discussed in Sec. 5.6.

To further probe fundamental noise limits, we note that quantum phase diffusion, as well as single-particle total excited state decay $\gamma_{\mathrm{e}}$ and repumping broadening $w$, all produce a Lorentzian contribution to the power spectrum. After removing low frequency spectral components as described in Sec. 5.6, a Lorentzian fit that excludes offset frequencies below 4 kHz yields a FWHM of 4.5(5) Hz (see Fig. 45.5b). This is still larger than the predicted linewidth, 10(2) mHz, for this particular data set. We believe that the linewidth is limited again by atomic population noise as described above. However, the measured linewidth is less than the total Raman decay linewidth $\gamma_{\mathrm{e}} = 48(16)$ Hz (and the repumping linewidth $w = 13.6(2.0)$ kHz), demonstrating that a collective oscillation can have lower phase noise properties than obtained from a collection of independent atoms fluorescing in free space, as predicted for $C < 1$.

In Fig. 45.5d, we demonstrate small cavity pulling $P \approx 10^{-4}$ for a range of $\gamma_{\mathrm{eg}}$ comparable to the linewidth of several atoms suited for optical clocks, The pulling $P$ is measured by applying small changes in the cavity resonance frequency $df_{\mathrm{cav}}$ and measuring the frequency shift of the light $df_{\gamma}$ exiting the cavity. The measured pulling agrees reasonably well with the predicted pulling $P/P_{\mathrm{pred}} = 1.44(22)$ where $P_{\mathrm{pred}} = 2\gamma_{\perp}/\kappa$. Assuming the suppression of cavity pulling measured in this work, current optical cavities stabilized to $\approx 1$ Hz are sufficient to reach a linewidth of 1 mHz with the appropriate atom.

To decouple the collective atomic dipole from the environment, one can choose an atom with small $\gamma_{\mathrm{eg}}$. However, the emitted light power would also decrease, making the light source too weak to phase stabilize even state-of-the-art narrow lasers. In a 1 kHz bandwidth, we observe a flux of photons sufficient to obtain a quantum-limited phase uncertainty $\Delta\phi \approx 1$ mrad or less (Fig. 45.5d and Sec. 5.6). This phase uncertainty and servo bandwidth would be sufficient to stabilize a bright 1 Hz linewidth laser down to 1 mHz to perform spectroscopy below the standard quantum limit for ensembles of $10^5$ atoms in a state-of-the-art optical lattice clock.

## 5.5 Summary and Conclusions

This work explores a novel regime of optical laser physics in which a highly coherent collective atomic dipole replaces the optical cavity as the high-$Q$ oscillator. Photons play an essential role by establishing atomic correlations, but a macroscopic number of photons need not occupy the intracavity mode. This light source, with $M_{\mathrm{c}} < 1$, $N \gg 1$, and $C \ll 1$, operates in the opposite limit of the single-atom laser [112] with $N = 1$, $M_{\mathrm{c}} > 1$ and $C \gg 1$. The results are particularly relevant for precision measurement science, since we demonstrate such a source operating in the likely “no-photon” limit $M_{\mathrm{c}} < 1$ that may be necessary for superradiant lasers with linewidths $< 1$ mHz. In addition, we show that as an active optical oscillator, stability in excess of the limits imposed by single particle decoherence rates can be achieved. Additional experiments are needed to study photon statistics, atom loss, and possible unforeseen noise that our experiment was unable to resolve at low offset frequencies.

## 5.6 Additional Technical Details

### 5.6.1 Experimental Details

The experimental configuration consists of the cavity (mode waist of 71 $\mu$m and length of 1.9 cm) with a quantization axis defined by a 2.7 G magnetic field along the cavity axis. The

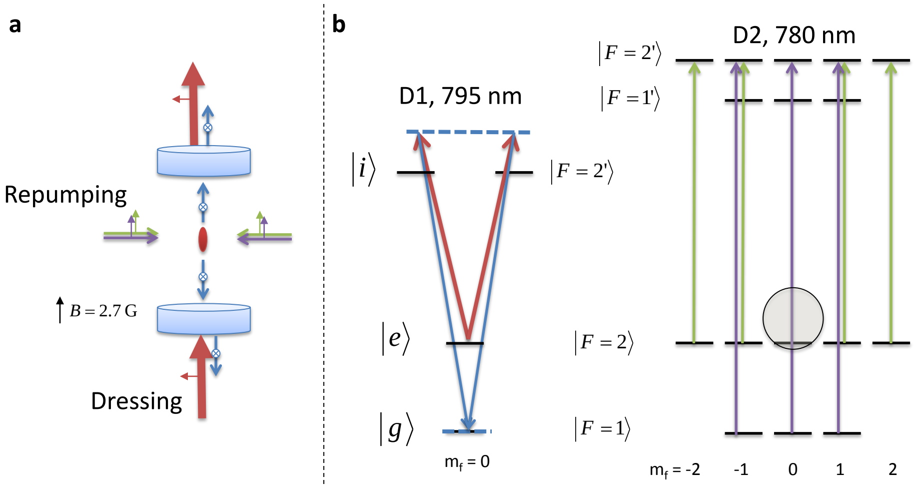

Figure 5.6: **Primary experimental configuration – dressing beam along cavity axis. a,** The physical arrangement of the apparatus. The cavity is vertically oriented, with the quantization axis defined by the magnetic field. The linearly-polarized D1 dressing beam is in red, and the $\pi$-polarized D2 repumping beams are green (F2) and purple (F1). The emitted light, blue, goes into the cavity mode. It has a linear polarization that is rotated 90° from the dressing beam. **b,** The energy level diagram for the D1 and D2 beams. The cavity mode resonance is denoted with a blue dashed line. The repumping dark state is labeled with a gray circle.

atoms are laser cooled to approximately 40 $\mu$K, putting them in the Lamb-Dicke regime along the cavity axis but not perpendicular to the axis. The cooling is not applied during steady state superradiance. We calculate the intracavity photon number via $M_c = 2\dot{M}_d/q\kappa_0$, where $\dot{M}_d$ is the detected photon flux from one end of the symmetric cavity, $q \approx 0.6$ is the quantum efficiency from the cavity mirror to the heterodyne detector, and $\kappa_0/2\pi = 5.3(3)$ MHz is the cavity linewidth due to mirror transmission alone. The fundamental phase noise due to photon shot noise is calculated using $\Delta\phi = 1/\sqrt{4M_d(T)}$ where $M_d(T)$ is the average number of photons measured using homodyne detection in a time interval $T$.

Steady state superradiance was primarily observed in an experimental configuration that was first-order insensitive to Doppler broadening and magnetic field broadening shown in Fig. 5.6. This configuration was used to measure both linewidths quoted in the text, as well as the linewidth comparison to the good-cavity Schawlow-Townes, repumping broadening, and natural linewidths. The 795 nm dressing laser was applied along the cavity axis, and by non-resonantly driving the

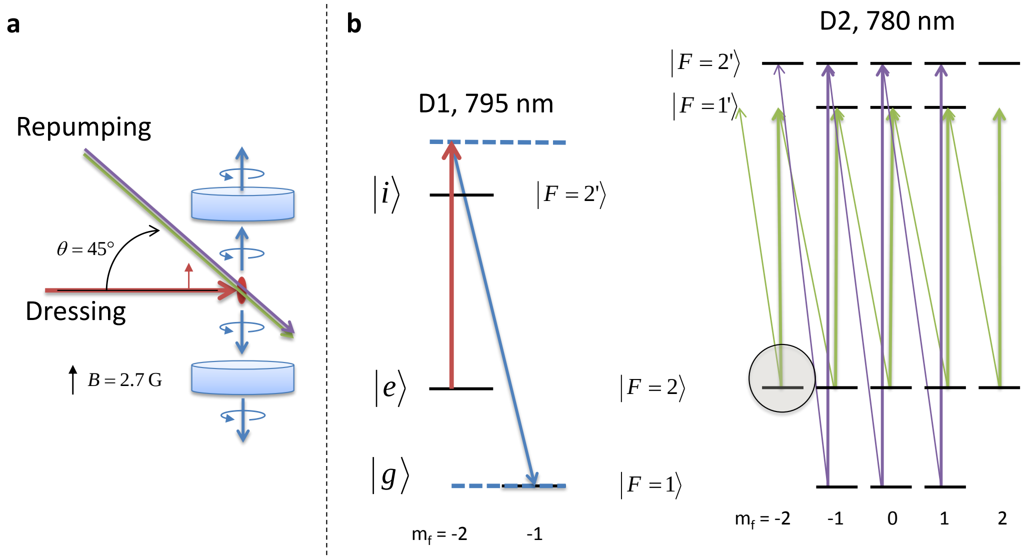

Figure 5.7: **Secondary experimental configuration – dressing beam perpendicular to cavity axis.** **a,** The cavity is vertically oriented, with the quantization axis defined by the magnetic field. The linearly-polarized dressing beam is in red, and the repumping beams are green (F2) and purple (F1). The circularly-polarized emitted light, blue, goes into the cavity mode. **b,** The energy level diagram for the D1 and D2 beams. The cavity mode resonance is denoted with a blue dashed line. The repumping dark state is labeled with a gray circle. The polarization of the repumping beams is a linear combination of $\pi$-polarization (thick lines) and $\sigma^-$ polarization (thin lines).

cavity, we could inject enough intensity to drive the superradiant emission into a resonant cavity mode. The dressing laser is linearly-polarized and appears as a superposition of $\sigma^+$ and $\sigma^-$. The Clebsch-Gordan coefficients on the emission path to $|g\rangle \equiv |F = 1, m_f = 0\rangle$ lead to a cancellation of all emission except for linearly-polarized light, rotated 90° from the polarization of the dressing laser. The polarization orthogonality allows the emitted light to be polarization separated from the dressing light that also emerges from the cavity. The repumping lasers are $\pi$-polarized and tuned such that they create a single state $|e\rangle \equiv |F = 2, m_f = 0\rangle$ dark to the repumping. The F1 repumper moves atoms primarily from $|F = 1\rangle$ to $|F = 2\rangle$, and the F2 repumper pushes population to $|e\rangle$, as the Clebsch-Gordan coefficient for the transition $|F = 2, m_f = 0\rangle \rightarrow |F = 2', m_f = 0'\rangle$ is zero.

In this configuration, the nodes and anti-nodes of the standing waves of the dressing laser and the cavity emission mode do not coincide due to the difference frequency of 6.834 GHz. We define a spatially averaged decay rate $\gamma_{eg} = \left\langle \gamma_{eg}(z)\ \Omega_{ig}^2(z) \right\rangle / \left\langle \Omega_{ig}^2(z) \right\rangle$ weighted by the coupling to the emission cavity mode $\Omega_{ig}^2(z)$.

To measure the amplitude and phase of the emitted light, we combined the superradiant emission with a heterodyne reference. The same laser provides the dressing beam and the heterodyne beam. The schematic and frequencies are described in detail in Fig. 5.8. The beatnote produced on the heterodyne detector is at 50 MHz. The 50 MHz signal is then quadrature demodulated using the signal processing chain described in Chapter 2, resulting in the emitted light amplitude $A(t)$ and phase $\phi_e(t)$ as a function of time.

In order to monitor relative path length fluctuations of the heterodyne detection, we also measure the phase of the Raman dressing beam that passes non-resonantly through the system. Using the polarization filtering, we allow a small amount of the Raman dressing light to pass through to the heterodyne detector, which also creates a beatnote on the detector at 84 MHz. This signal is separately filtered and quadrature demodulated to provide a path length reference phase $\phi_r(t)$.

In a similar way, the dressed cavity resonance frequency is probed to measure the total atom number. A small portion of the heterodyne reference beam is split off to use as a cavity probe (Fig. 5.8). The transmission from this weak beam is detected in heterodyne and the amplitude quadrature is used to identify the cavity resonance frequency while sweeping the EOM modulation frequency $f_m$.

Steady-state superradiance was observed in a second experimental configuration that might be applied for magnetometry, and shown in Figure 5.7. The configuration was first-order sensitive to magnetic field broadening and Doppler decoherence. The quantization axis was still defined by a magnetic field along the cavity axis. The $\pi$-polarized 795 nm dressing laser was applied perpendicular to the cavity axis, a direction in which the atoms were not in the tightly-confined Lamb-Dicke regime. The state $|e\rangle \equiv |F = 2, m_f = -2\rangle$ was the only state dark to the repumping light. This was achieved by applying two different frequency 780 nm lasers at 45° to the cavity axis, such that they consisted of a linear combination of $\pi$ and $\sigma^-$ polarization. Light emitted into

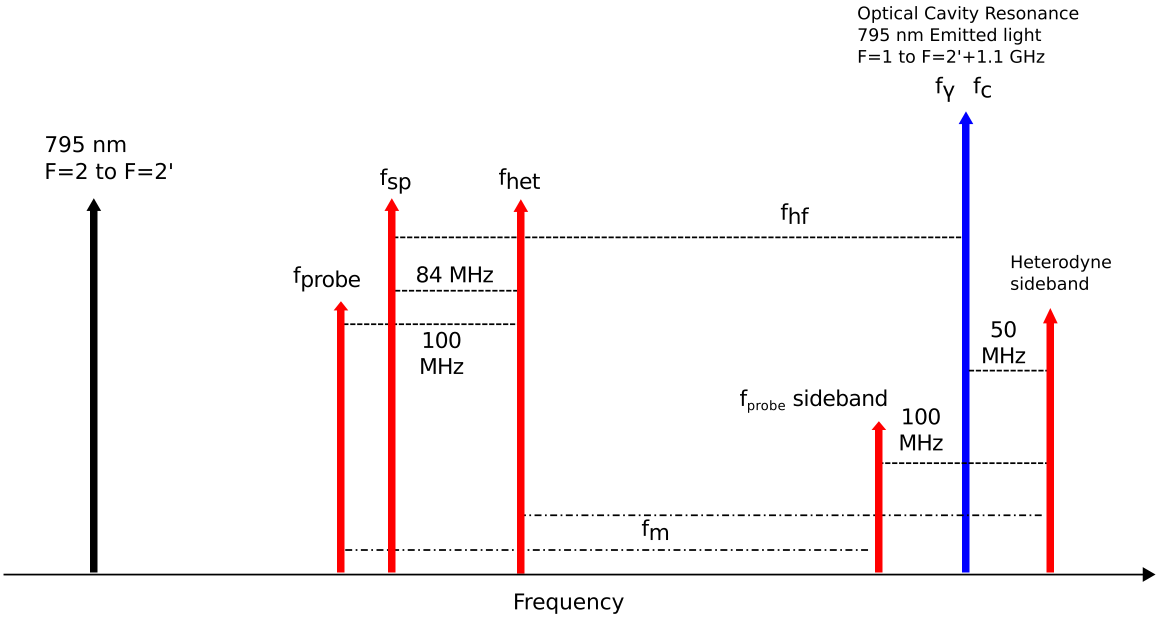

Figure 5.8: A chart of relevant laser frequencies used in the superradiance experiment. The x-axis is frequency, but the y-axis is only used to distinguish different beams. The 795nm reference laser (not shown here) starts the frequency chain, stabilized to the atomic reference, as described in Chapter 2. The second 795 nm laser is then stabilized with respect to the reference 1.184 GHz detuned from the $F = 2$ to $F = 2'$ transition, with the transition indicated by the black arrow. This laser is split into two paths. The first forms the dressing laser $f_{sp}$ after being shifted 84 MHz lower in frequency to give the dressing laser detuning $\Delta = 1.1$ GHz. The other path is ultimately used for both the heterodyne reference beam $f_{het}$ and the dressed cavity frequency probe $f_{probe}$. This second path is modulated using an EOspace high frequency modulator to produce sidebands at $f_m = 6.800$ GHz, placing the higher frequency sidebands near the superradiant emission frequency $f_\gamma$, which is fixed to the be $f_{sp} + f_{hf}$, where $f_{hf}$ is the hyperfine splitting frequency. After high frequency modulation, the probe beam is split from the heterodyne beam, and frequency shifted lower by 100 MHz. The setup produces 3 frequency separated signals on the heterodyne detectors, the emitted light at 50 MHz, the dressing laser leakage at 84 MHz, and the cavity probe at 100 MHz. The high frequency modulation $f_m$ can be swept using the DDS to scan the probe component over the cavity resonance, while keeping the probe signal at a constant 100 MHz.

the standing wave cavity mode could only be $\sigma^+$ or $\sigma^-$ polarized. This polarization constraint, combined with cavity resonance frequency conditions, selected $|g\rangle \equiv |F=1, m_f=-1\rangle$ as a unique ground state for superradiant emission. The dressing laser was tuned 1.1 GHz to the blue of the $|F=2, m_f=-2\rangle \to |F=2', m_f=-2'\rangle$ atomic transition. The cavity mode was tuned 1.1 GHz to the blue of $|F=1, m_f=-1\rangle \to |F=2', m_f=-2'\rangle$ transition. The laser frequency chain was similar for this configuration, with small adjustments to account for the slightly different hyperfine frequency due to Zeeman shifts of the groundstates.

### 5.6.2 Phasor Correlation

We define a phasor correlation function $\mathcal{C}_p = \left\langle \mathrm{Re}\left[\frac{\langle e^{-i\Delta\phi_k}\rangle_k}{|\langle e^{-i\Delta\phi_k}\rangle_k|} e^{i\Delta\phi_k}\right]\right\rangle_k$ where $\Delta\phi_k = \phi_1^k - \phi_0^k$ is the phase difference just before and after the dark time $T_{dark}$ in a single trial $k$. In the case that the phase measurements have no ambiguities due to measuring modulo $2\pi$, $\mathcal{C}_p = \langle \cos[\phi_1^k - \phi_0^k - \langle \phi_1^k - \phi_0^k\rangle_k]\rangle_k$. This definition is chosen such that if there is no noise in the phase difference, $\mathcal{C}_p \to 1$, while if $\phi_1$ is random with respect to $\phi_0$, $\mathcal{C}_p \to 0$. The average incorporated 50 to 100 experimental trials. The phasor correlation function measures the average projection of the final unit length light phasor $e^{i\phi_1}$ onto the initial light phasor $e^{i\phi_0}$. The local oscillator frequency was not equal to the atomic precession frequency in our experiment, so some average relative phase accumulated during the dark time $T_{dark}$. The normalized average difference phasor $\frac{\langle e^{-i\Delta\phi_k}\rangle_k}{|\langle e^{-i\Delta\phi_k}\rangle_k|}$ accounts for this phase accumulation.

### 5.6.3 Lorentzian Fits

In the measurements of the linewidth of the emitted light, we must account for phase noise from relative path length fluctuations. We measure the path length fluctuations in a single trial $k$ using the measured phase of the Raman dressing beam that non-resonantly passes through the cavity $\phi_r^k(t)$. Then we can subtract the path length fluctuations from the phase of the emitted light for each 5.5 ms trial is $\phi_k(t) = \phi_e^k(t) - \phi_r^k(t)$.

In this Raman system, the loss of atoms causes a frequency chirp of the cavity resonance that then chirps the superradiant emission frequency through the cavity pulling effect. The frequency chirp should not be present if an actual highly forbidden optical transition was employed. Because the frequency chirp is a deterministic effect, not a noise process, we attempt to account for the contribution to the measured linewidth by calculating an average phase response as a function of time, averaged over all measured 200 trials $\langle \phi_k(t) \rangle_k$. This average response was then subtracted from each measured phase yielding $\phi'_k(t) = \phi_k(t) - \langle \phi_k(t) \rangle_k$.

Not only does the dispersive cavity shift chirp the emission frequency in a single trial, changes in the atom number between trials also shifts the center frequency of the emitted light. We account for the fluctuation in the center frequency between trials by subtracting a linear fit from each $\phi'_k(t)$, resulting in $\phi''_k(t) = \phi'_k(t) - (m'_k t + b'_k)$. This is equivalent to moving the center frequency of each trial to 0 Hz before calculating the average power spectral density.

The two-sided power spectrum was calculated for each trial from $e^{i\phi''_k(t)}$ using a 4th order Blackman-Harris windowing function to avoid power spectral leakage of the carrier. The resulting bin size in the spectrum is 181.55 Hz as a result of using 5 ms of time data over which the frequency chirp of the laser from atom loss was insignificant. The 4th order Blackman-Harris windowing function gives a very low noise background at the cost of having a large noise background for the first 5 bins from the 0 frequency, so the center 10 bins of data should not be included a fit to the frequency spectrum. The windowing function effectively reduces the close in frequency resolution to gain a lower noise floor further from the carrier.

Due to technical noise processes, we are interested in the Lorentzian signal from from the carrier. We performed Lorentzian fits to the resulting average power spectrum, excluding offset frequencies below 4 kHz to avoid the contributions from these technical noise sources and uncover the underlying Lorentzian linewidth characteristic of quantum noise. Excluding offset frequencies greater than 4 kHz did not significantly change the linewidth measurement.

# Chapter 6

## Linear response theory for a superradiant laser

During the experimental work described in Chapter 5, we observed significant sensitivity of the laser amplitude to the details of the repumping rate and detuning of the cavity from the laser emission frequency. Understanding the laser system's stability is important for guiding the design of future superradiant lasers so they can operate in a stable regime. To study the Raman laser's stability, in this chapter we will extend the theoretical model presented in Chapter 4 to allow for oscillations around the steady state values. Then in Chapter 7, I present our experimental studies demonstrating the relevance of the linear response model in our superradiant Raman laser.

### 6.1 Linear Expansion of Uncoupled Equations

For future applications of steady-state superradiant light sources as precision measurement tools, we are interested in the system's robustness to external perturbations. As is common in laser theory [111, 143, 92], here we analyze the system's linear response to perturbations by considering small deviations from the steady-state solutions. While some previous theoretical expressions in this thesis are valid for both the good-cavity and bad-cavity limit, as no assumptions were made about the relative magnitudes of $\kappa$ and $\gamma_\perp$, it is convenient now to simplify to two equations for the dynamics by assuming that the laser is operating deep in the bad-cavity regime, where $\kappa \gg 2\gamma_\perp$. In this regime, the cavity field adiabatically follows the atomic polarization, providing the physical motivation to eliminate the field from Eqns. 4.8-4.11 [115, 97].

The cavity field is eliminated by assuming that the first time derivative of the complex field amplitude $\breve{\mathcal{C}}$ in Eqn. 4.8 is negligible compared to $\frac{\kappa}{2}\mathcal{C}$. This effectively results in Eqn. 4.12 being the equation for the cavity field. After substituting Eqn. 4.12 into Eqns. 4.9-4.11, we only concern ourselves with the amplitude responses, simplifying the equations by using Eqn. 4.15 and substituting $|\mathcal{J}_{-}|^2$ with $J_\perp^2$. With these simplifications, the dynamical equations for $\dot{J}_z$, $\dot{J}_\perp^2$, and $\dot{N}_3$ are

$$\dot{J}_z = ((\Gamma_{3e} - W/2)\frac{N_3}{2} + \frac{W}{2}(N/2 - J_z)) - \frac{C\gamma}{1+\delta_0'^2}J_\perp^2 \tag{6.1}$$

$$\dot{J}_\perp^2 = -2\gamma_\perp J_\perp^2 + \frac{2C\gamma}{1+\delta_0'^2}J_z J_\perp^2. \tag{6.2}$$

$$\dot{N}_3 = -\left(\Gamma_{3e} + W/2\right)N_3 + W\left(N/2 - J_z\right) \tag{6.3}$$

We perform the linear expansion by re-parameterizing the degrees of freedom in terms of fractionally small perturbations about steady-state: $J_z(t) = \bar{J}_z(1 + j_z(t))$, $J_\perp^2(t) = \bar{J}_\perp^2(1 + 2j_\perp(t))$, and $N_3(t) = \bar{N}_3(1 + n_3(t))$. We also define the response of cavity field through the relationship $A(t) \equiv \sqrt{|\mathcal{C}(t)|^2} = \bar{A}(1 + a(t))$. Since $|\mathcal{C}(t)|^2 = \frac{C\gamma}{1+\delta_0'(t)'^2}J_\perp^2(t)$ from Eqn. 4.12, $A(t)$ follows the atomic polarization, except for the modification from dynamic cavity detuning as will be discussed below. We analyze the response in the presence of a specific form of external perturbation – the modulation of the repumping rate $W(t) = \overline{W}(1 + w(t))$ with $w(t) = \epsilon\mathrm{Re}[e^{i\omega t}]$, where $\epsilon$ is a real number much less than 1. The quantities $j_z(t)$, $j_\perp(t)$, $n_3(t)$, $a(t)$, and $w(t)$ are unitless fractional perturbations around the steady-state values that we assume are much less than 1.

We also include, by hand, an inversion-dependent term in the detuning $\delta_0' = \delta' + \alpha\bar{J}_z j_z(t)$. The cavity mode's frequency is tuned by the presence of atoms coupled to the cavity mode. The tuning is equal but opposite for atoms in the two different quantum states $|e\rangle$ and $|g\rangle$. The detuning $\delta'$ is the steady-state value of the detuning of the dressed cavity from the emitted light frequency. The variation about this steady-state detuning is governed by the second contribution $\alpha\bar{J}_z j_z(t)$. Effects such as off-resonant dispersive shifts due to coupling to other states can lead to this $J_z$

dependent detuning in real experiments. We derived this dispersive shift of the cavity in Chapter 4.

To linearize the resulting equations, we substitute the expansions around steady-state into Eqns. 4.11, 6.1, and 6.2. We neglect terms beyond first order in the small quantities $j_z(t)$, $j_\perp(t)$, $n_3(t)$, $a(t)$, and $w(t)$. For ease of solving the equations, we treat $j_z(t)$, $j_\perp(t)$, $n_3(t)$, and $a(t)$ as complex numbers where the real part gives the physical value. After eliminating the steady-state part of the equations, the equations for small signal responses $j_\perp(t)$ and $j_z(t)$ can be reduced to two uncoupled, third order differential equations

$$\beta\dddot{\jmath}_\perp + \ddot{\jmath}_\perp + 2\gamma_0\dot{\jmath}_\perp + \omega_0^2\jmath_\perp = D_\perp(\omega)\epsilon e^{i\omega t} \tag{6.4}$$

$$\beta\dddot{\jmath}_z + \ddot{\jmath}_z + 2\gamma_0\dot{\jmath}_z + \omega_0^2\jmath_z = D_z(\omega)\epsilon e^{i\omega t}. \tag{6.5}$$

We have written the uncoupled differential equations in a form that suggests a driven harmonic oscillator, with damping rate $\gamma_0$, natural frequency $\omega_0$ and a drive unique to the $\jmath_\perp$ or $\jmath_z$ equation $D_\perp(\omega)$ or $D_z(\omega)$. The drives contain derivatives of the repumping modulation $w(t)$, resulting in frequency dependence. The third derivative term is a modification to the harmonic oscillator response from the third level, characterized by the factor $\beta$ that goes to zero in the two-level limit ($r \to \infty$). To preserve the readability of the text, we have included the full expressions for the coefficients as Appendix C. Each of the terms will be discussed subsequently in physically illuminating limits.

The drive of this harmonic oscillator-like system varies with the modulation frequency and other system parameters. In the case of the two-level model of Ref. [115], with $r = \infty$, $\alpha = 0$, and $\Gamma_R = 0$, the drive terms are

$$D_\perp(\omega) = \frac{\overline{W}}{2}(N\Gamma_c - 2\overline{W} - i\omega) \tag{6.6}$$

$$D_z(\omega) = (N\Gamma_c - \overline{W})\overline{W} + i\omega). \tag{6.7}$$

The modulation-frequency-dependent terms add an extra 90° of phase shift at high modulation frequencies to the observed response. Additionally, the cancellation in $D_{\perp}(\omega = 0)$ results in an insensitivity of the output photon flux to the ground state repumping rate $W$ at $W_{opt}$. The cancellation agrees with the parabolic dependence of $\dot{M}_c$ on $W$, as seen in the steady-state solutions.

The frequency dependent terms in $D_{\perp,z}$ also cause a growing drive magnitude versus $\omega$. This is canceled out in the responses $j_{\perp}$ and $j_z$ by the roll-off from the oscillator, keeping the response finite versus modulation frequency. These characteristic features remain in the response, even as the complexity of the model increases as additional effects are included.

To proceed, we solve the equations for the complex, steady-state response to a single modulation frequency $\omega$, (e.g. $\jmath_{\perp}(t) = \jmath_{\perp} e^{i\omega t}$). The complex response of the cavity field amplitude $a(t)$ results from these solutions,

$$a(t) = \jmath_{\perp}(t) - \frac{\delta \alpha \bar{J}_z \jmath_z(t)}{1 + \delta'^2} \ . \tag{6.8}$$

In contrast to Eqn. 4.12, where $|\mathcal{C}|$ depends only on $J_{\perp}$, including dispersive cavity tuning from the inversion couples the cavity output power to $J_z$ as well.

## 6.2 Transfer Function Analysis

We analyze the response of the cavity field amplitude to an applied modulation of the repumping rates by plotting the amplitude transfer function and the phase transfer function versus the modulation frequency $\omega$, defined as $T_A(\omega) \equiv |a|/\epsilon$ and $T_{\phi}(\omega) \equiv \arctan\left(\frac{Re[a]}{Im[a]}\right)$ respectively. We consider the maximum of the transfer function to define the resonant frequency $\omega_{\text{res}}$. The calculated variation in the transfer functions versus various experimental parameters is shown in Figs. 6.1 - 6.5. All results are given as a series of transfer functions varying a single specified system parameter, with other unspecified parameters set to $\overline{W} = W_{\text{opt}}$, $r = \infty$, $\delta' = 0$, and $\Gamma_R = 0$.

The expressions for the damping $\gamma_0$ and the natural frequency $\omega_0$ guide our understanding of the transfer functions. Holding $r = \infty$, $\delta' = 0$, and $\Gamma_R = 0$, the damping reduces to $\gamma_0 =$

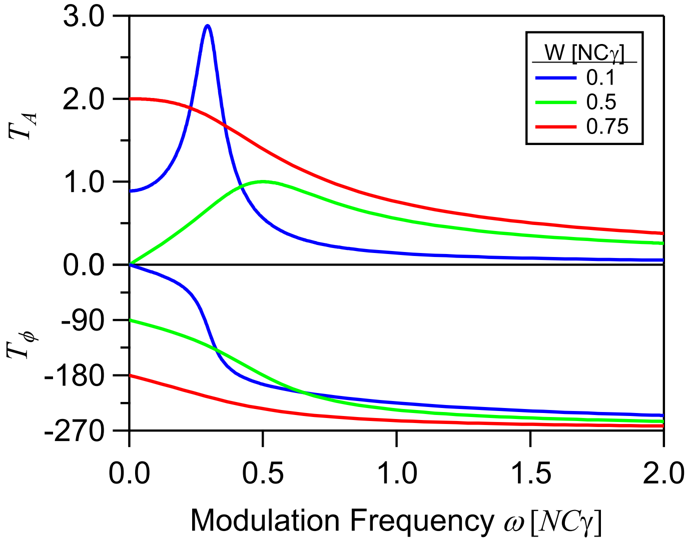

Figure 6.1: Output photon flux transfer function for different ground state repumping rates, with $r = \infty$, $\delta' = 0$, $\alpha = 0$ and $\Gamma_R = 0$.

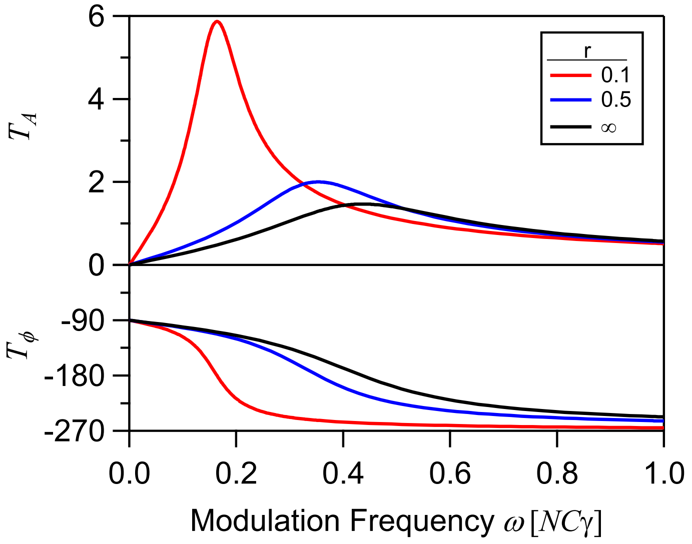

Figure 6.2: Output photon flux transfer function for different repumping ratios $r$, with $W = W_{opt}$, $\delta' = 0$, $\alpha = 0$ and $\Gamma_R = 0$.

$\overline{W}/2$. Physically, the damping enters through the decay of $J_\perp$ at a rate proportional to $\gamma_\perp$. The natural frequency $\omega_0 = \sqrt{\overline{W}(NC\gamma - \overline{W})} = \sqrt{2}\bar{J}_\perp C\gamma$ is set by the steady-state rate of converting collective transverse coherence into atoms in the ground state, $J_\perp^2 C'\gamma$, normalized by the steady-state transverse coherence $J_\perp$.

To examine the effect of the steady-state repumping rate $\overline{W}$ on the response, we plot the transfer functions $T_A$ and $T_\phi$ for different values of $\overline{W}$ in Fig. 6.1. For $\overline{W} < W_{opt}$, we see a narrow resonance feature in the response(blue curve). The frequency of the resonance increases until $\overline{W} = W_{opt}$ (green curve). Also at $\overline{W} = W_{opt}$, the dc amplitude response $T_A(\omega = 0) = 0$, because the drive $D_\perp$ goes to zero (Eqn. 6.6), consistent with the maximum in $\dot{M}_c$ at $W_{opt}$. For $\overline{W} > W_{opt}$, the phase of the response near dc sharply changes sign, as understood from the parabolic response of $\dot{M}_c$ versus $\overline{W}$; on the $\overline{W} > W_{opt}$ side of the parabola, the same change in $W$ produces the opposite change in the output photon flux compared to the $\overline{W} < W_{opt}$ side of the parabola. Meanwhile, the natural frequency has decreased with the increase in $W$ when $W > W_{opt}$. As $\overline{W}$ approaches $W_{\max}$, the response has essentially become that of a single-pole, low pass filter with an additional $\pi$ phase shift.

To examine the effect of population in the third state $|3\rangle$, we now hold $\overline{W} = W_{opt}$ and show $T_A$ and $T_\phi$ for different $r$ in Fig. 6.2. The black curve shows the result for $r = \infty$, which is the two-level model of Ref. [115], as no population accumulates in $|3\rangle$ (recall that $\bar{N}_3/\bar{N}_g = 1/r$). For smaller $r$, the relaxation oscillations grow, shown by the increasing maximum in $T_A$. This response is consistent with the reduced damping rate $\gamma_0$ and increased drive $D_\perp$ seen in the following expressions.

The damping is $\gamma_0 = \frac{r}{1+r}\left(\frac{NC\gamma}{4}\right) - \frac{2\omega^2}{NC\gamma(1+r)}$. The additional $\omega$ dependence, associated with the repumping delay from atoms spending time in $|3\rangle$, results from the third derivative term that scales with $\beta = \frac{1}{\overline{W}(1+r)}$ in Eqns. 6.4 and 6.5.

The complex drive in this limit is $D_\perp = i\omega\frac{NC\gamma}{2}\frac{1+r+2r^2}{(1+r)(1+2r)} - \frac{\omega^2}{1+r}$. The term proportional to $\omega^2$ in $D_\perp$ arises from modulating the rate out of the state $|3\rangle$. Although the $\omega^2$ term in the damping would introduce a roll off in the transfer function $T_A$ with the form $1/\omega^2$, the $\omega^2$ frequency

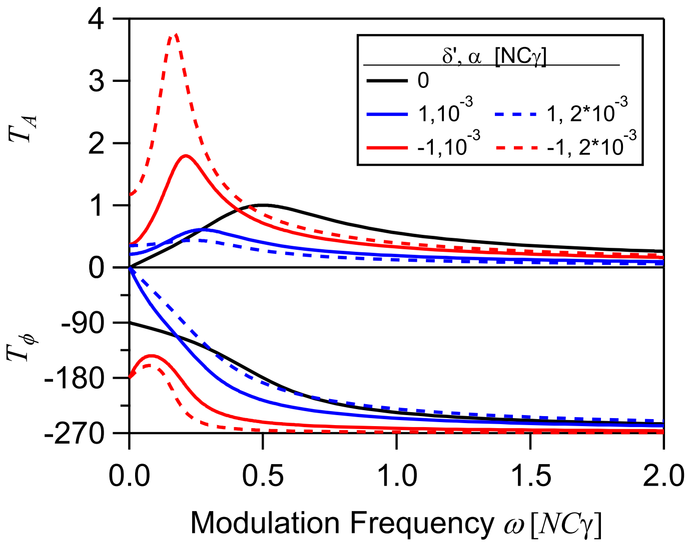

Figure 6.3: Output photon flux transfer function for different dressed cavity detuning from emitted light frequency $\delta$, with $W = W_{opt}(\delta) = \frac{NC\gamma}{2(1+\delta'^2)}$, $r = \infty$, and $\Gamma_R = 0$. The solid (dashed) lines show $\alpha = NC\gamma \times 10^{-3}$ ($\alpha = 2NC\gamma \times 10^{-3}$) to demonstrate the effects of increased cavity feedback.

dependence is canceled. The final transfer function maintains a frequency dependence of $1/\omega$ for $\omega \gg \omega_{res}$, similar to that of the two-level system.

Next we consider the effect of the dynamically tunable cavity mode. The cavity mode response can strongly modify the damping of the oscillator and even lead to instabilities in the cavity light field, eliminating steady-state solutions. We first consider the damping rate of the two-level model ($r = \infty$) with cavity tuning, $\gamma_0 = \frac{\overline{W}}{2}\left(1 + h(\delta')\right)$ where $h(\delta') = 2\alpha\delta'\left(\frac{N}{1+\delta'^2} - \frac{\overline{W}+\Gamma_R}{C\gamma}\right)$. The damping is modified by a detuning dependent feedback factor $h(\delta')$ that is positive or negative depending on the sign of $\delta'$. Because $\overline{W} + \Gamma_R < \frac{NC\gamma}{1+\delta'^2}$ to meet superradiant threshold, $h(\delta')$ has the same sign as $\delta'$. Applying negative cavity feedback, when $h(\delta') > 0$, increases the damping and may be useful for reducing relaxation oscillations and suppressing the effect of external perturbations. When $h(\delta') < 0$, positive feedback decreases $\gamma_0$ and amplifies the effect of perturbations.

We show the effect of this cavity feedback on the transfer functions in Fig. 6.3 for the conditions $r = \infty$, $\overline{W} = W_{opt}(\delta')$, and $\Gamma_R = 0$. The red (blue) curves show positive (negative) feedback, with the black curve serving again as a reference to the model of Ref. [115] with no

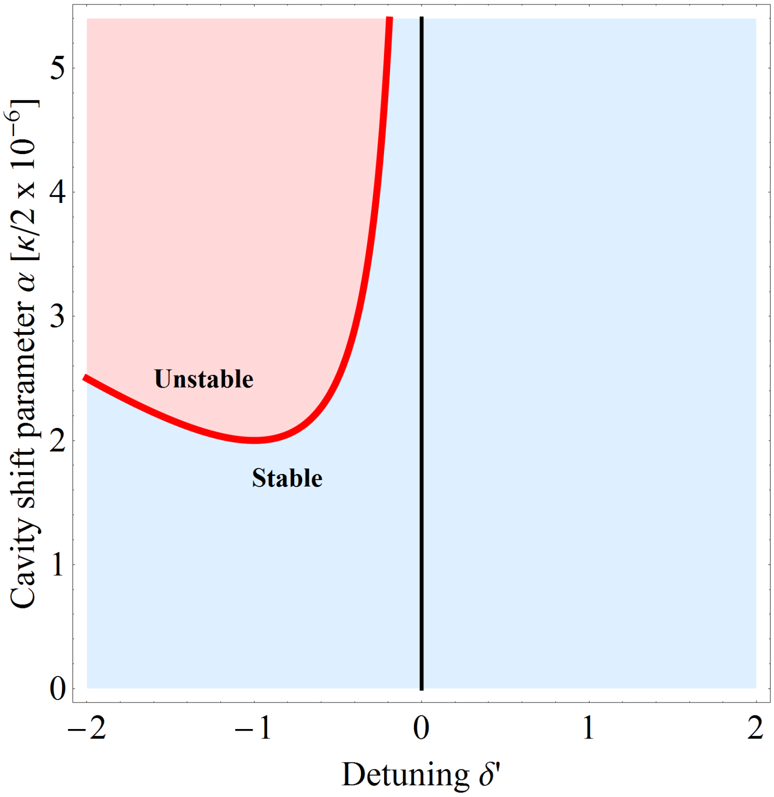

Figure 6.4: Stability plot using $\gamma_0$ stability condition of Eqn. 6.9 as a function of detuning $\delta'$ and the cavity shift parameter $\alpha$, assuming $N = 10^6$. The stability condition also assumes $W = W_{\mathrm{opt}}(\delta', \Gamma_R)$. The region of stability is exact for the two-level model ($r = \infty$), and a good approximation for all values of $r$. The blue region shows where the real part of all the poles of the $\jmath_\perp$ solution are negative, indicating a damped return to steady-state conditions for a perturbation. The red region shows where any of the real parts of the poles become positive, making $J_\perp$ unstable, with no steady-state solutions.

cavity feedback.

Fig. 6.3 also shows the effect of increasing the cavity shift parameter $\alpha$. The solid lines result from $\alpha = NC\gamma \times 10^{-3}$, a cavity shift similar in magnitude to experiments performed in Refs. [24, 21, 23, 160]. The dashed lines result when $\alpha$ is increased by a factor of two.

With enough positive feedback, the system can become unstable, with any perturbations exponentially growing instead of damping, which eliminates steady-state solutions. For a driven harmonic oscillator, the condition for steady-state solutions is $\gamma_0 > 0$. Again assuming $W = W_{\text{opt}}(\Gamma_R, \delta') = \frac{NC\gamma}{2(1+\delta'^2)} - \Gamma_R$, and remaining in the two level limit ($r = \infty$) the stability condition reduces to

$$N\frac{\alpha\delta'}{1+\delta'^2} > -1 \ . \tag{6.9}$$

In Fig. 6.4, we plot the stability condition as a red line.

In general, the stability of a linear system can be determined by examining the poles of the solution. If any pole crosses into the right half of the complex plane, the system is unstable with an oscillating solution that grows exponentially. In the two-level limit ($r = \infty$), this condition on the solutions $\jmath_\perp$ and $\jmath_z$ is mathematically equivalent to the condition on $\gamma_0$, Eqn. 6.9. As the level structure becomes more complex, e.g. $r \neq \infty$ or in the full $^{87}$Rb model in Sec. 6.3, we use the pole analysis to examine the regions of stable operation. For the model here, as $r$ changes, the pole analysis shows that the stability condition in Eqn. 6.9 is no longer exactly correct. However, the change is small enough that Eqn. 6.9 remains a good approximation of the stability condition for all values of $r$.

Finally, in Fig. 6.5 we show the effect of additional decoherence by plotting $T_A$ and $T_\phi$ for different values of $\Gamma_R$. Here $r = \infty$, $\delta' = 0$, and $\alpha = 0$. As a reference, the black curve shows the transfer function with $\Gamma_R = 0$. For the solid curves, the ground state repumping rate $\overline{W} = W_{opt}(\Gamma_R)$ is varied with $\Gamma_R$ to remain at the point of maximum output power (Fig. 4.5) which amounts to holding $\gamma_\perp$ constant. Thus, as the decoherence increases by increasing the rate

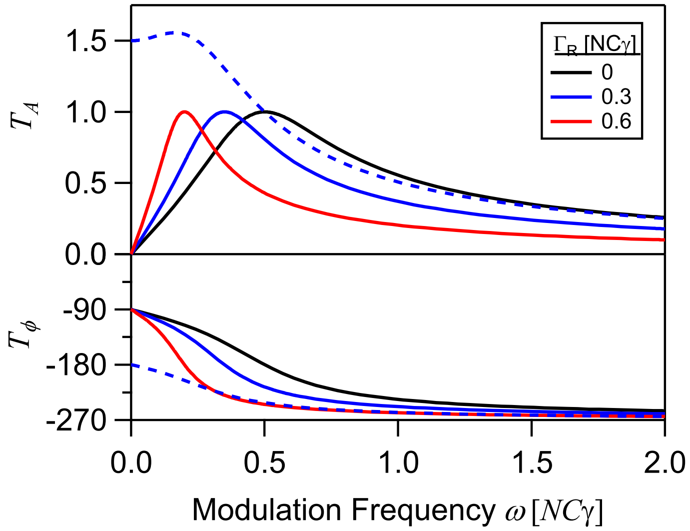

Figure 6.5: Output photon flux transfer function for different Rayleigh scattering rates $\Gamma_R$, with $\overline{W} = W_{opt}(\Gamma_R)$, $r = \infty$, $\alpha = 0$ and $\delta' = 0$. The dashed line shows the transfer functions when $\overline{W}$ is held to $NC\gamma/2$, not varied to remain at $W_{opt}$, and $\Gamma_R = 0.3$. A dashed red curve is not shown, as with $\Gamma_R = 0.6$ and $\overline{W} = NC\gamma/2$ the maximum repumping rate threshold has been exceeded and the output photon flux is zero.

of Rayleigh scattering from the ground state, the resonance frequency only moves because $\overline{W}$ is changing, as seen in the expression for the natural frequency $\omega_0 = W(NC\gamma - 2\gamma_\perp)$. Notice that additional decoherence does not affect the peak size of the relaxation oscillations. Although the damping rate decreases because $\gamma_0 = \overline{W}/2$, this effect is canceled by the drive decreasing with $\overline{W}$ as well, with $D_\perp = -i\omega(\overline{W}/2)$ when $\overline{W} = W_{opt}$.

If we hold $\overline{W}$ constant at $NC\gamma/2$, the resulting transfer function is the dashed line in Fig. 6.5. With $\overline{W}$ constant, the coherence damping rate $\gamma_\perp$ varies with $\Gamma_R$, and the response actually behaves similar to the case where $\overline{W}$ is increased (Fig. 6.1) because of the symmetric roles $W$ and $\Gamma_R$ have in the natural frequency and the drive.

The main conclusion from our examination of the linear response theory of the three-level, bad cavity laser is that most conditions for optimizing the output power are compatible with an amplitude stable laser. Operating at the optimum repumping rate in particular suppresses the impact of low frequency noise on the amplitude stability. However, we also find that because the cavity detuning $\delta'$ couples to the population of the laser levels, cavity feedback can act to suppress perturbations, or cause unstable operation, depending on the sign of $\delta'$. A simple relationship between $N$, $\delta'$, and $\alpha$ gives the condition for stable operation at $\overline{W} = W_{\mathrm{opt}}$.

### 6.2.1 Bloch Vector Analysis of Response

Relaxation oscillations in a good-cavity laser arise from two coupled degrees of freedom, the intracavity field $A$ and the atomic inversion $J_z$, responding to perturbations at comparable rates. Parametric plots of the amplitude and inversion response provide more insight into the nature of the relaxation oscillations than looking at the laser field amplitude response alone [143]. In the bad-cavity regime, the cavity-field $A$ adiabatically follows the atomic coherence $J_\perp$, and the oscillations arise from a coupling of $J_\perp$ and the inversion $J_z$. Thus the relevant parametric plot is the 2D projection of the 3D Bloch vector in the rotating frame of the azimuthal angle. In this section, we study this response of the Bloch vector to better understand the stability of the bad-cavity laser.

The individual plots of Fig. 6.6 show the trajectory of the Bloch vector for the small signal response at different applied modulation frequencies $\omega$ and different repumping rates $\overline{W}$. The trajectory is calculated using the amplitude and phase quadratures of the responses $\jmath_\perp$ and $\jmath_z$ to define the sinusoidal variation of each quadrature with respect to a sinusoidal modulation of $W(t) = \overline{W}(1 + \epsilon \mathrm{Re}[e^{i\omega t}])$. The series of plots show the trend in the responses versus the ground state repumping rate $\overline{W}$ and modulation frequency $\omega$, with $r = \infty$, $\Gamma_R = 0$, and $\delta' = 0$. Although the oscillator characteristics of the two quadratures are identical, they display a differing phase in their response due to the differences in the drives $D_\perp$, $D_z$ on the two quadratures.

At high repumping rates $\overline{W} > W_{\mathrm{opt}}$ and high modulation frequencies $\omega > \omega_{\mathrm{res}}$, the perturbation modulates the polar angle of the Bloch vector, leaving the length largely unchanged. Near $\omega_{\mathrm{res}}$, the two quadratures have large amplitudes and oscillate close to 90° out of phase, leading to the trajectories that encloses a large area. When $\omega < \omega_{\mathrm{res}}$ and with $\overline{W}$ near $W_{opt}$, the cancellation in the drive term $D_\perp$ leads to almost no amplitude of oscillation in the $J_\perp$ quadrature, making the modulation predominately $J_z$-like. For $\alpha = 0$ or $\delta' = 0$, this means the cavity field amplitude $A$

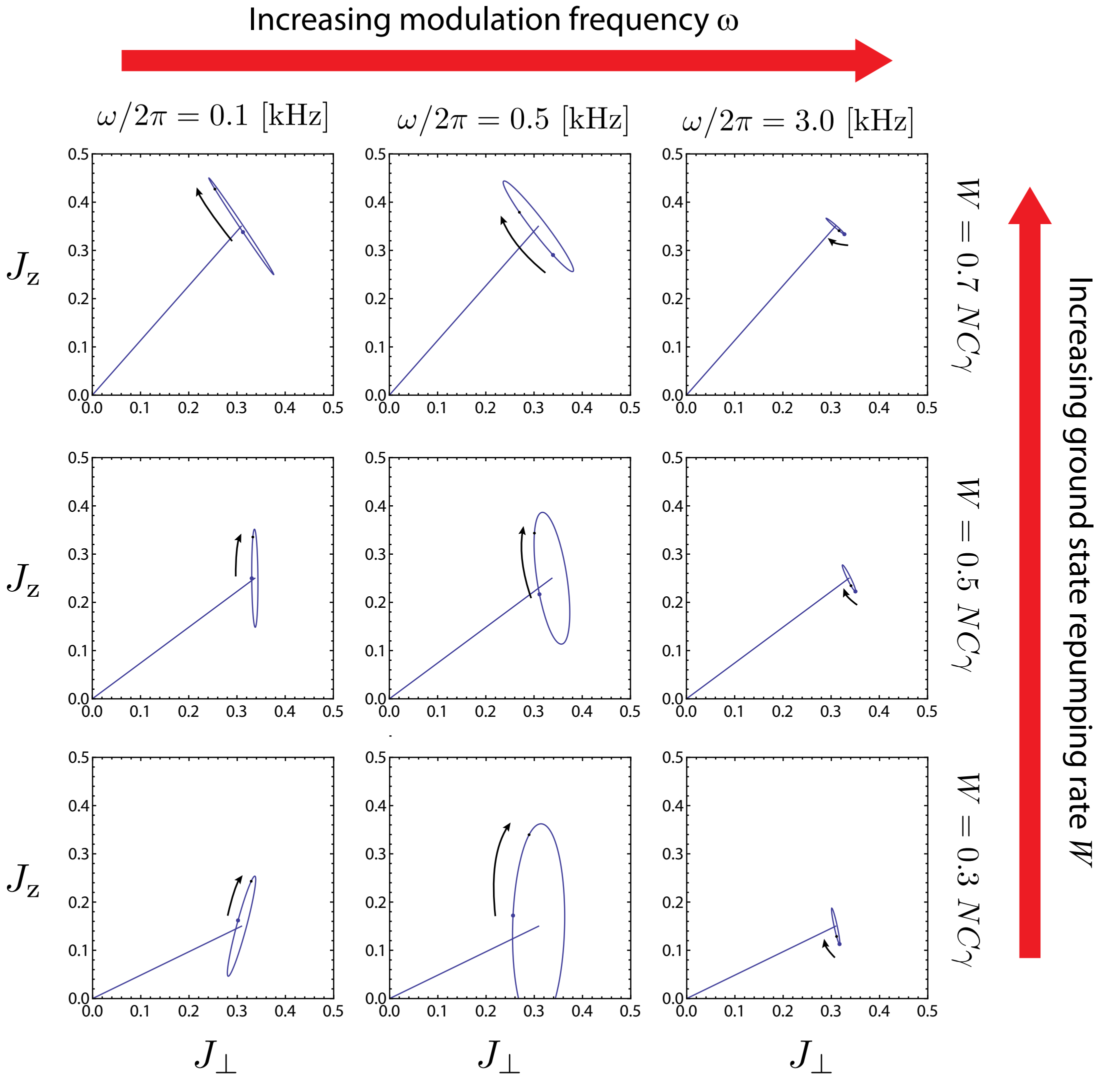

Figure 6.6: Response of the 2D Bloch vector to external modulation of the repumping rate. The steady-state Bloch vector, i.e. $\bar{J}_\perp$ and $\bar{J}_z$ from Eqns. 4.18-4.19, is indicated by the blue line, plotted on the axis with units of $N$, so $N/2$ is the maximum value. The ellipse is the trajectory of the Bloch vector responding to the modulation of the repumping rate $w(t) = \epsilon \mathrm{Re}[e^{i\omega t}]$, described by the small signal responses $\jmath_\perp$ and $\jmath_z$ in Eqns. 6.4 and 6.5. The parameters are $\epsilon = 0.1$, $r = 5$, $\delta' = 0$, $\alpha = 0$, and $\Gamma_R = 0$. The black arrow indicates the direction of the trajectory, starting from the blue dot at $t = 0$. The values of $\omega$ are chosen to show $\omega \ll \omega_{\mathrm{res}}$, $\omega \approx \omega_{\mathrm{res}}$, and $\omega \gg \omega_{\mathrm{res}}$.

will also be stabilized, as it is locked to the transverse coherence $J_\perp$ (Eqn. 6.8).

However, dynamic cavity tuning creates a coupling of the inversion to the cavity field as well, breaking the simple time-independent proportionality of the cavity field amplitude $A$ and the atomic coherence $J_\perp$, as expected from Eqn. 6.8. Fig. 6.7a show the case of $\delta' < 0$. Because of

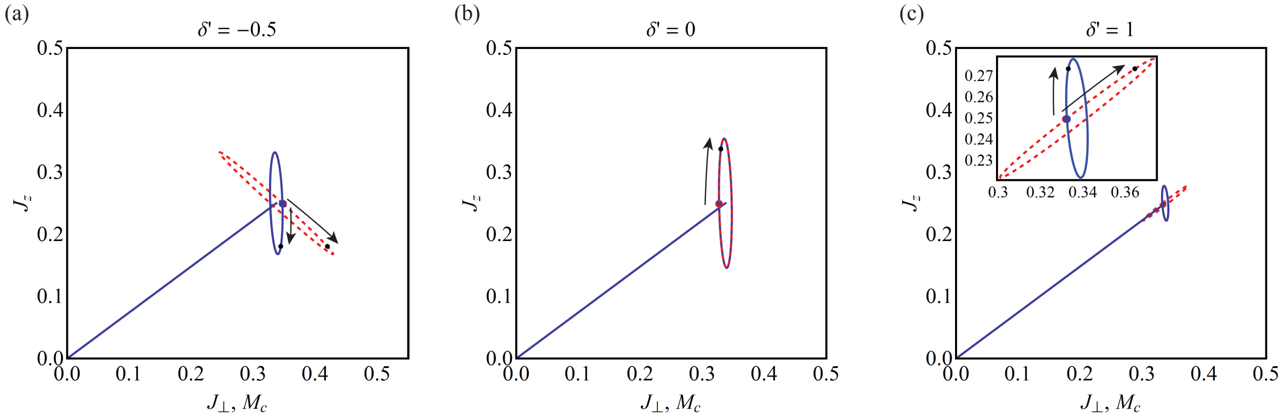

Figure 6.7: Parametric plots of response of the three degrees of freedom $J_z$, $J_\perp$, and $A$, highlighting effect of cavity frequency tuning on response of atomic coherence and output light field. The blue line represents the steady-state atomic Bloch vector, $\bar{J}_z$ and $\bar{J}_\perp$, from Eqns. 4.18-4.19. The blue ellipse shows small single response of the Bloch vector to a modulation of the repumping rate $W$, given by $\jmath_z$ and $\jmath_\perp$ from Eqns. 6.4 and 6.5. The parametric response is plotted with units of $N$, so $N/2$ is the maximum value. The red dashed line is the trajectory formed by the response of the cavity field $a$ (Eqn. 6.8) and $\jmath_z$. The cavity field is plotted as a fraction of the average field, then centered on the steady-state Bloch vector to compare with the atomic response. The arrows indicate the direction of the response with respect to a modulation $W(t) = \overline{W}(1 + \epsilon e^{i\omega t})$. Here $NC\gamma = 10^4\ \mathrm{s}^{-1}$, $r = 5$, $\Gamma_R = 0$, $\overline{W} = W_{\mathrm{opt}}(\delta')$, $\epsilon = 0.1$, and $\omega = 0.02\,NC\gamma$, chosen to show the stable $J_\perp$ response. (a) When $\delta' < 0$, the cavity feedback can be positive, leading to larger oscillations compared to the case of no feedback $\delta' = 0$ shown in (b). Because of the coupling of $J_z$ to the cavity mode frequency, $A$ is not locked to the $J_\perp$ response, as in (b), but is anti-correlated with $J_z$. In (c), where $\delta' > 0$, the negative feedback reduces the response amplitudes in all quadratures. The cavity tuning again shifts the cavity amplitude response, but with the opposite phase relationship due the change in sign of the slope of the Lorentzian, so $A$ follows $J_z$. The inset shows a close up of the response.

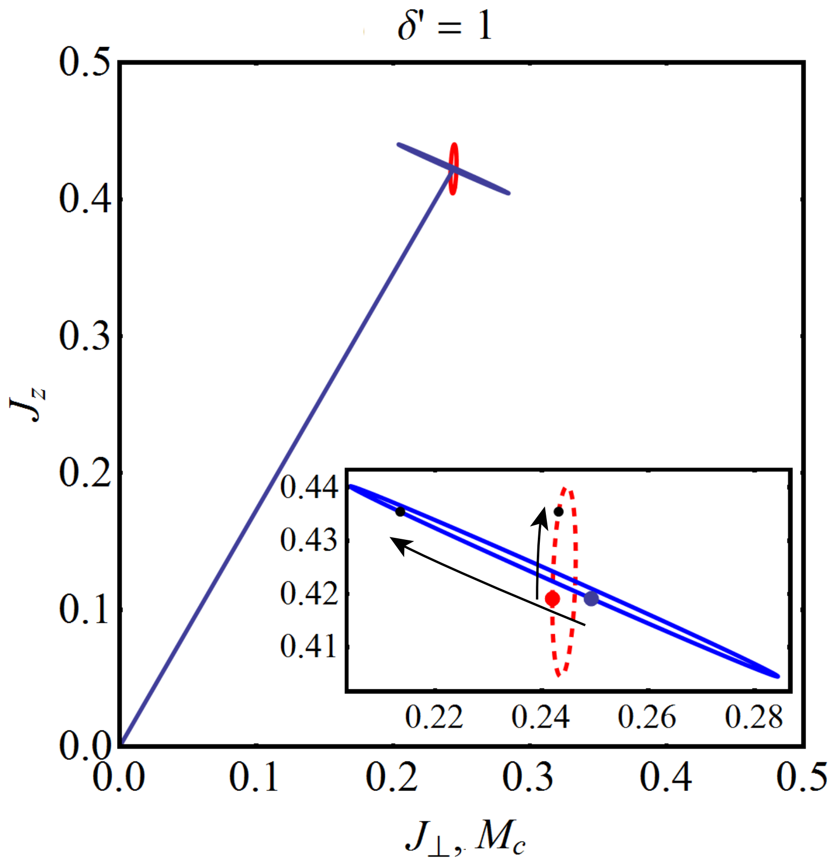

Figure 6.8: Cavity tuning stabilizing the cavity field amplitude. By changing the average repumping rate $\overline{W}$ from $W_{\text{opt}}$ to $0.44 \times 10^4$ for the same parameters as Fig. 6.7c ($NC\gamma = 10^4$ s$^{-1}$, $r = 5$, $\Gamma_R = 0$, $\epsilon = 0.1$, $\delta' = 1$, and $\omega = 0.02\, NC\gamma$), the response of the Bloch vector (blue ellipse) becomes primarily perpendicular to the steady state Bloch vector (blue line). Under these conditions, the cavity field response $A$ (red dashed ellipse) has the smallest fractional deviation of the three degrees of freedom. The inset shows a close up of the response.

the coupling to the inversion, the cavity field response has a larger amplitude than $J_\perp$ response in addition to a phase shift. It is also nearly 180° out of phase with the response of the inversion.We include the case of $\delta' = 0$ (Fig. 6.7b) as a reference. The cavity field is locked to the coherence, even for $\alpha \neq 0$, due to the second order insensitivity in the cavity coupling. For the case of negative feedback $\delta' > 0$, shown in Fig. 6.7c, all the response amplitudes are reduced due to the increased damping. Notice that the inversion and cavity field are now responding in phase.

Because of the coupling between all three degrees of freedom, it is possible to choose parameters that lead to a stabilization of the cavity field. Operating away from $W_{\text{opt}}$, the response of the Bloch vector becomes primarily a modulation of the polar angle as the inversion and coherence respond 180° out of phase. Combined with the cavity tuning, the cavity field is stabilized, as shown in Fig. 6.8, where the parametric plot of $A$ and $J_z$ (dashed red ellipse) shows a response that is primarily $J_z$-like. The response of the cavity field has the smallest fractional variation among the three degrees of freedom.

To conclude our discussion of linear response theory in the three-level model, we point out that the parametric plot analysis highlights the role that the dispersive cavity frequency tuning plays in amplifying or suppressing perturbations in both the atomic degrees of freedom and the cavity field. Crucially, frequency stable lasers may need to seek a configuration that suppresses fluctuations in the $J_z$ degree of freedom to minimize the impact of cavity pulling on the frequency of the laser. We also see that the dispersive tuning breaks the exact proportionality of the cavity field and the transverse atomic coherence, restoring an additional degree of freedom that may be crucial for observing chaotic dynamics in lasers operating deep into the bad-cavity regime [67].

## 6.3 Linear Response Theory in $^{87}$Rb

To analyze the small signal response about these steady-state solutions analytically, we perform the analogous linear expansion as was done in Sec. 6.1. We assume the repumping rates are modulated with $W(t) = \overline{W}(1+\epsilon\text{Re}[e^{i\omega t}])$, and assume the resulting modulation of the populations and coherence take the form $N_\lambda = \bar{N}_\lambda(1 + n_\lambda(t))$ and $J_\perp^2 = \bar{J}_\perp^2(1 + \jmath_\perp(t))$. The equations are then linearized by expanding to first order in the small quantities $n_\lambda(t)$, $\jmath_\perp(t)$, and $\epsilon$, and then re-expressed in terms of $\jmath_z(t) = (\bar{N}_e n_e(t) - \bar{N}_g n_g(t))/(\bar{N}_e - \bar{N}_g)$ and $\jmath_\perp(t)$.

We solve for the steady-state, complex response amplitude at a single drive frequency $\jmath_z(t) = \jmath_z(\omega)e^{i\omega t}$, $\jmath_\perp(t) = \jmath_\perp(\omega)e^{i\omega t} \approx \jmath_\perp^2(\omega)e^{i\omega t}/2$ and $n_\lambda(t) = n_\lambda(\omega)e^{i\omega t}$. The response of the photon amplitude flux is $a(\omega) = \jmath_\perp(\omega) - \frac{\delta'}{1+\delta'} d\delta(\omega)$, where the detuning response is defined by the population response $d\delta(\omega) = \sum_\lambda (\alpha_\lambda/\kappa) N_\lambda n_\lambda(\omega)$ and the $\alpha_\lambda$ are given by elements of the cavity tuning vector $\vec{\alpha}_+$, given in Appendix B. The predicted normalized fractional amplitude response is $T_A(\omega) = |a|/\epsilon$ and phase response function is $T_\phi(\omega) = \arctan\left(\frac{\mathrm{Re}[a]}{\mathrm{Im}[a]}\right)$.

Figs. 6.9 - 6.11 contain surface plots showing the light amplitude transfer function $T_A$ versus modulation frequency. The third dimension shows how the response changes when a single parameter $\overline{W}$, $r$, and $\delta'$ is varied. The lower plots in each figure show the resonant response of the system, following the frequency of the maximum response $\omega_{res}$ and the resonant amplitude response $T_A(\omega_{res})$. The response functions follow the same general trends as the three-level model in Sec. 6.1, showing that the simplified model captures the essential physics of our system. The full model also demonstrates good quantitative agreement with the experimental results as shown in Ref. [21].

In Fig. 6.9, we show the amplitude transfer function versus the repumping rate $\overline{W}$ assuming $r = 0.71$ and $\delta' = 0$. The value of $r$ is chosen to reflect the conditions in Ref. [21]. We see the increasing damping and natural frequency with rising $\overline{W}$ and the dc response suppression appearing near $W_{\mathrm{opt}}$. For $\overline{W} > W_{opt}$, the frequency of the relaxation oscillation moves back towards $\omega = 0$, as expected from the three-level model. Near $W = W_{max}$, the transfer function no longer has a resonance as it monotonically decreases from its maximum at $\omega = 0$.

We show the effect of the repumping ratio $r$ in Fig. 6.10, where $\vec{\alpha}_+ = \vec{0}$, $\delta' = 0$ and $\overline{W} = W_{\mathrm{opt}}$. The trends of lower damping and a lower natural frequency as $r \to 0$ are clearly visible, as expected from the three-level model in Sec. 6.1.

We also note that $T_A$ has a $1/\omega$ roll-off for $\omega \gg \omega_{res}$, even with higher order derivatives in the equations for $\jmath_\perp(\omega)$ and $\jmath_z(\omega)$ that function as a low-pass to the response (analogous to the $\dddot{\jmath}_\perp$

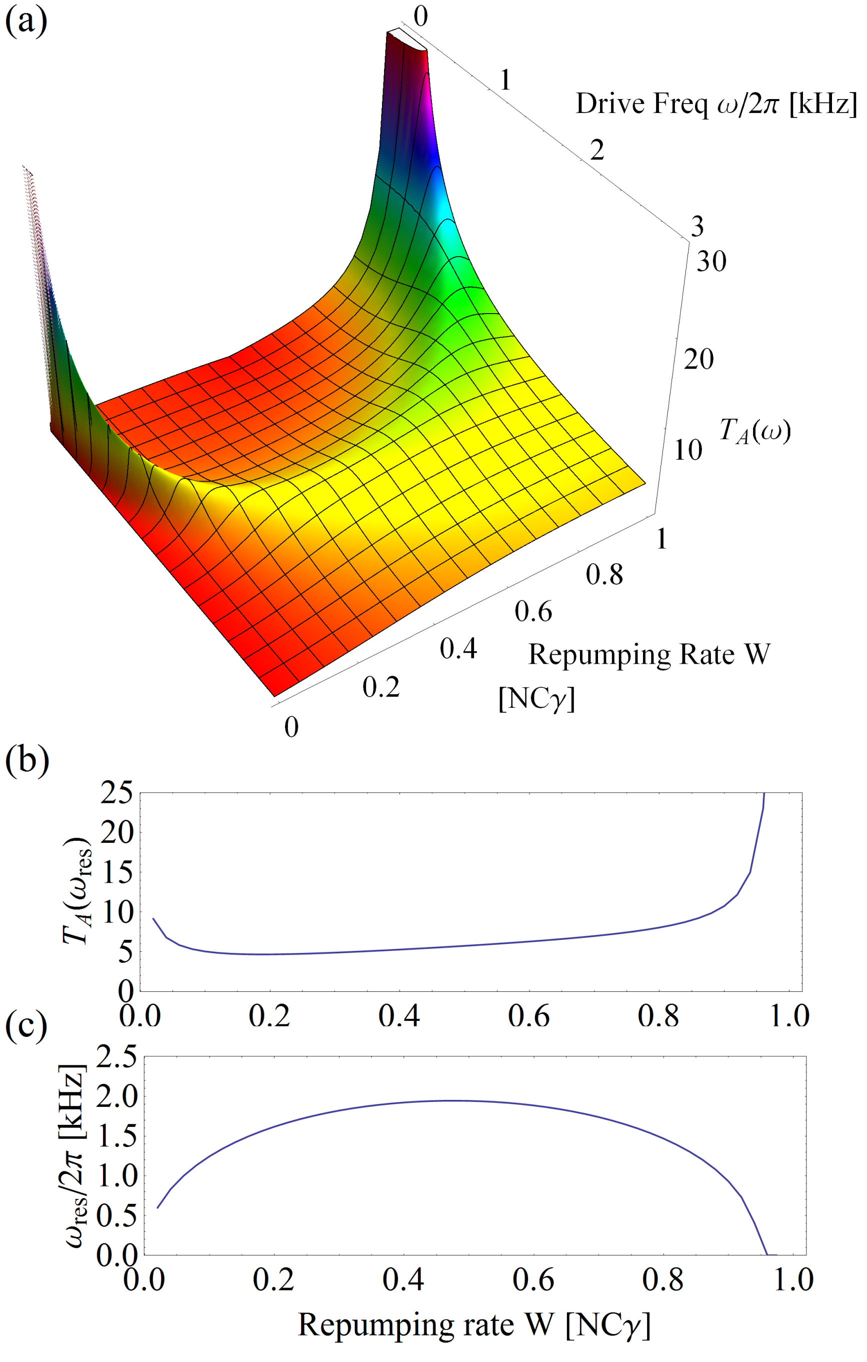

Figure 6.9: Response for different repumping rates. (a) Light field amplitude response transfer function $T_A$ versus repumping rate $W$. (b) Resonant response $T_A(\omega_{max})$ and (c) the resonant modulation frequency $\omega_{max}$ as a function of repumping rate $W$. Here $NC\gamma = 4\times10^5$ s$^{-1}$, $\delta' = \alpha = 0$, and $r = 0.71$.

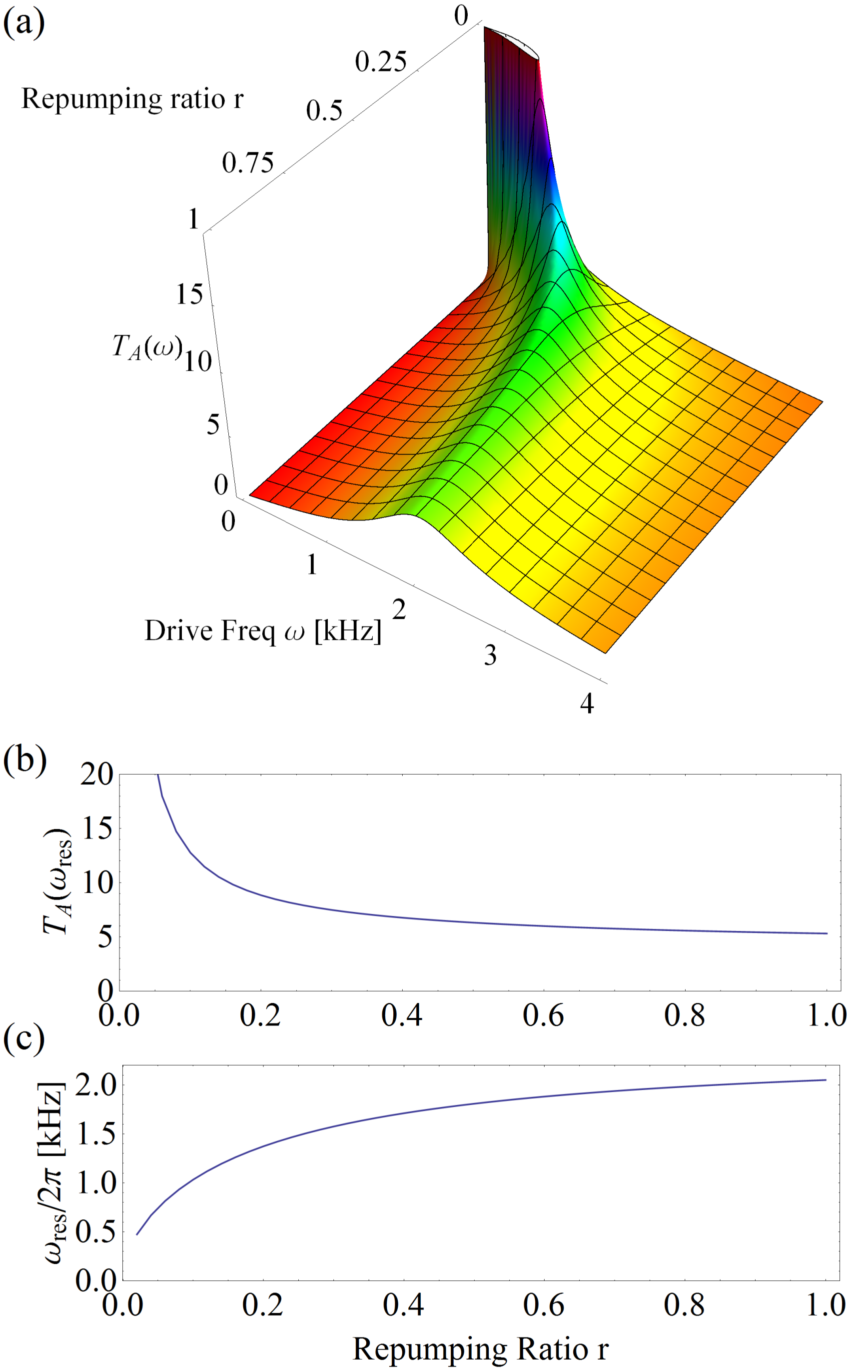

Figure 6.10: Response for different repumping ratio. (a) Light field amplitude response transfer function $T_A$ versus repumping ratio $r$. (b) Resonant response $T_A(\omega_{max})$ and (c) the resonant modulation frequency $\omega_{max}$ as a function of repumping ratio $r$. Here $NC\gamma = 4 \times 10^5$ s$^{-1}$, $\delta' = 0$ and $\overline{W} = W_{opt}$.

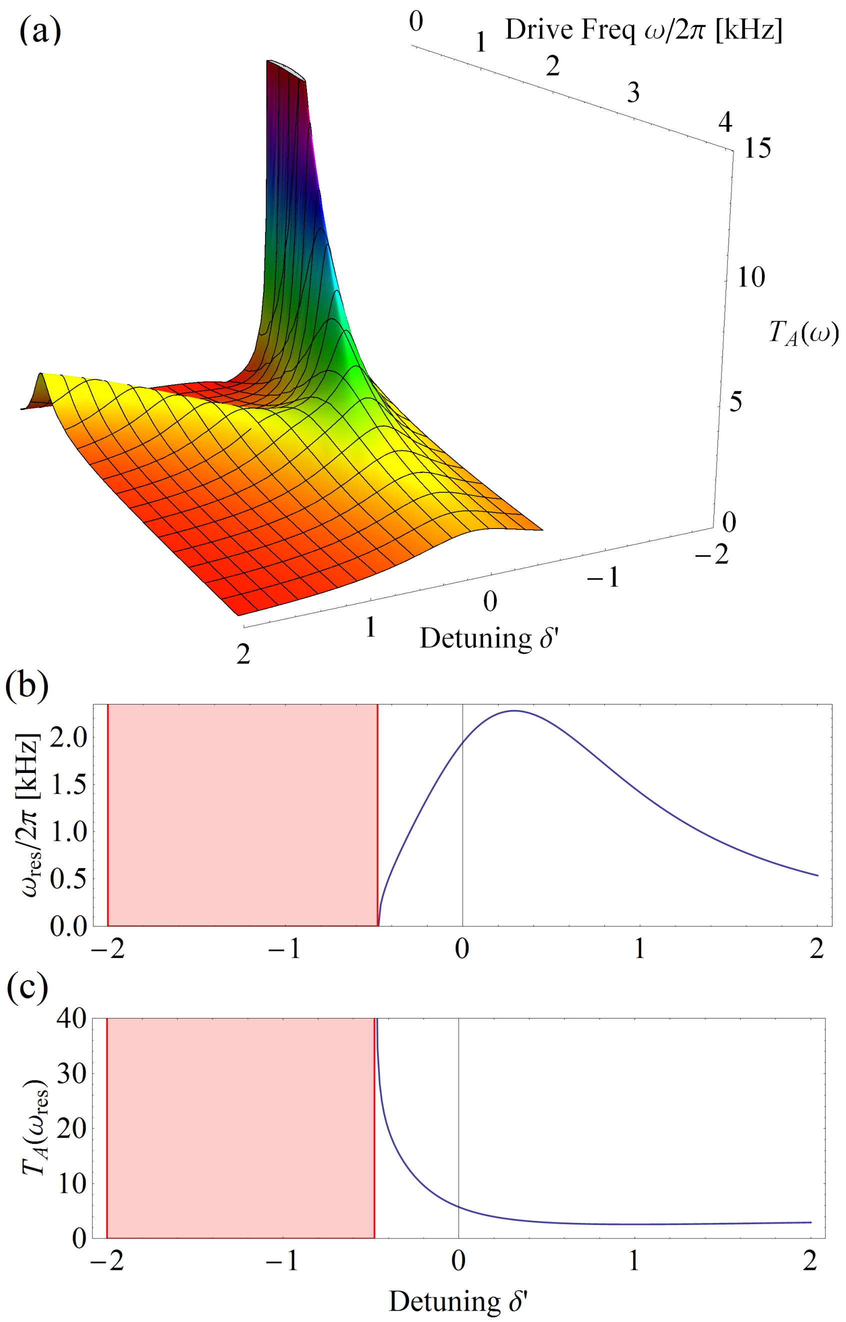

Figure 6.11: Response for different detunings. (a) Light field amplitude response transfer function $T_A$ versus detuning $\delta'$. The transfer function is not plotted in regions of instability. (b) Resonant response $T_A(\omega_{max})$ and (c) the resonant modulation frequency $\omega_{max}$ as a function of $\delta'$. The red shaded regions indicate parameters in which the system is unstable and no steady-state solutions exist. Here $NC\gamma = 4 \times 10^5$ s$^{-1}$, $r = 0.71$ and $\overline{W} = W_{opt}$. The cavity shift parameter is given by $\vec{\alpha}_+$. These parameter values reflect the conditions of the experimental system in Ref. [21].

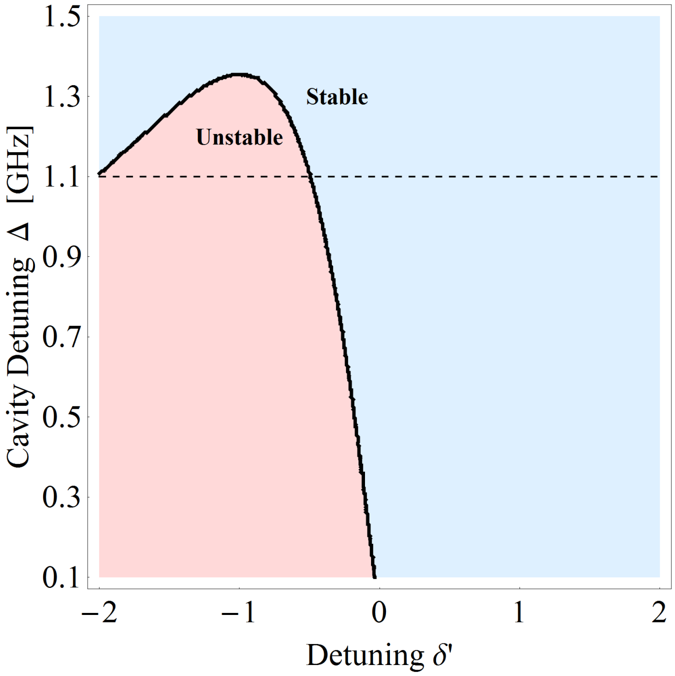

Figure 6.12: Stability diagram for the full model of a superradiant Raman laser in $^{87}$ Rb, plotting the region any of the real parts of the poles of the $\jmath_{\perp}$ solution are positive. When any pole becomes positive, the system is unstable and has no steady-state solutions. The stability regions are shown versus the detuning of the cavity from the emission frequency $\delta'$ and the detuning of the bare cavity frequency from the atomic frequency $\Delta$. The critical contour (bold) marks where the pole changes sign. The dashed line indicates the detuning $\Delta$ of experimental work (Refs. [24, 21]). For the calculation we use $NC\gamma = 10^{-4}$ s$^{-1}$, $\overline{W} = W_{opt}$, and $r = 0.71$.

term in Eqn. 6.4). However, modulation of the repumping rate out of each hyperfine ground state, as was done in Ref. [21], puts higher order derivatives in the drive terms as well. The result is a drive that increases with a higher power of the modulation frequency $\omega$, partially balancing the higher order low-pass filtering. Thus, by modulating the repumping rate out of each hyperfine state, the amplitude transfer function $T_A$ retains $1/\omega$ modulation frequency dependence of the three-level model in Sec. 6.1.

The response as a function of $\delta'$ also qualitatively agrees with the simple picture put forward in Sec. 6.1, as shown in Fig. 6.11. For $\delta' > 0$ around $\delta' = 0$, we see a lower maximum $T_A$ consistent with heavier damping. When $\delta' < 0$, the amplitude of the relaxation oscillations increase as the system becomes less damped. But $\delta'$ continues to decrease, the full model shows a divergence in $T_A$ where the system becomes unstable with no steady-state solutions. In the unstable regime, we do not plot the transfer function and show a red shaded region in Fig. 6.11b and 6.11c. This instability is consistent with our inability to achieve steady-state superradiance experimentally at detuning $\delta' < -0.1$ [21]. The reduction in $\omega_{res}$ with increasing $\delta'$ is a result of maintaining the repumping $\overline{W} = W_{opt}$, which reduces $\overline{W}$ at large detunings and affects the natural frequency.

We also use our linear response model to theoretically predict the stability diagram for the full $^{87}$Rb Raman laser system. We examine the poles of the solution for $\jmath_\perp$ as a function of $\delta'$, the detuning of the dressed cavity resonance frequency from the emission frequency and $\Delta$, the detuning of the bare cavity resonance frequency from the atomic lasing transition $|g\rangle$ to $|i\rangle = |F' = 2, m_f = \pm 1\rangle$. We plot the regions of stability in Fig. 6.12, which is analogous to Fig. 6.4 in Sec. 6.1. However, here the physical parameter $\Delta$ controls $\vec{\alpha}_+$, which roughly scales like $1/\Delta$ (we assume $\Delta$ remains large enough such that the system is well described by the dispersive tuning approximation). Future experiments may benefit from working with larger detuning $\Delta$. However in the standing-wave geometry of Ref. [21], the improved stability would come at the expense of increased inhomogeneous ac Stark shifts from the dressing laser. At fixed scattering rate $\gamma$, the ac Stark shift increases linearly with $\Delta$.

Repumping the atoms through multiple grounds states, quantified by the $r$ parameter, has a

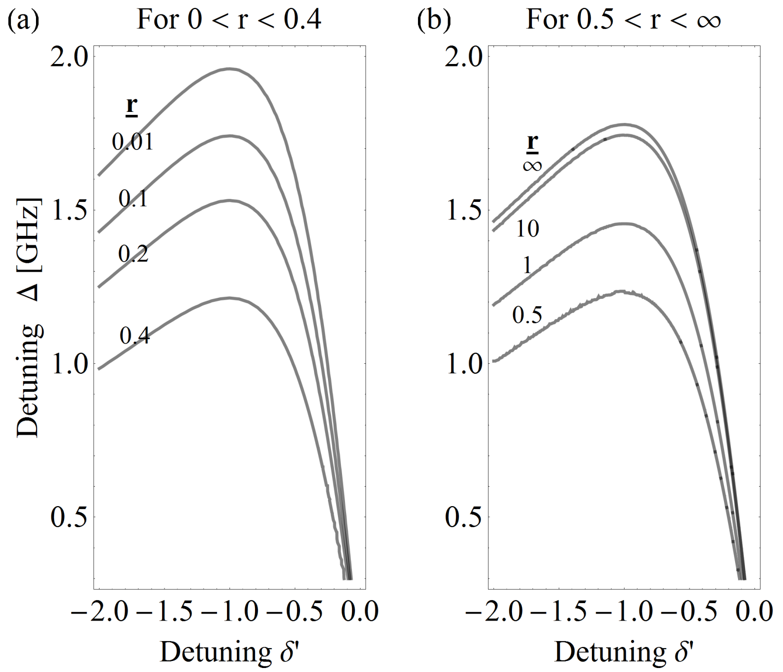

Figure 6.13: Critical stability conditions for variable values of the repumping ratio $r$. Each line shows the contour as a function of $\Delta$ and $\delta'$ separating stable lasing from unstable. The unstable region is defined as any set of parameters that results in a positive value for the real part of any pole of the $J_\perp$ response solution. The stability conditions change as a function of the repumping ratio $r$. (a) As $r$ increases from 0, the unstable region gets smaller until it reaches some value between 0.4 and 0.5, after which (b) the unstable region grows to its asymptotic value.

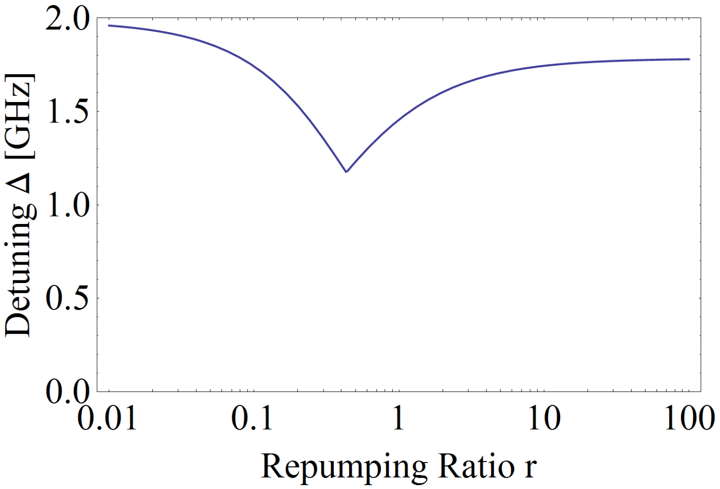

Figure 6.14: The value of $\Delta$ for the critical contour versus $r$, assuming $\delta' = -1$. Lower $\Delta$ indicates that more of the parameter space has stable, steady-state solutions. Here we assume $NC\gamma = 10^{-4}$ s$^{-1}$ and $\overline{W} = W_{opt}$.

larger impact on the stability digram in this full model than on three level model in Sec. 6.1. To study the effect repumping through the multiple ground states of $^{87}$Rb has on the stability of the laser amplitude, we follow the contour of the stability diagram for different values of $r$, shown in Fig. 6.13. The figure is separated into two parts because the contour does not change monotonically. In part (a), $r$ is low, indicating much of the population building up outside of the lasing levels, and the stable region grows in size as the repumping becomes more efficient. However, as $r$ continues to grow, the contour asymptotes to an unstable region about the same size as if $r = 0.1$. In Fig. 6.14, we plot the value of $\Delta$ for the critical contour, holding $\delta' = 1$, indicating that the largest stable region occurs when $r \approx 0.45$. Here the cavity shift caused by atoms accumulating in the other hyperfine states acts to partially balance the shift from atoms in the $|g\rangle$ and $|e\rangle$ states, enhancing the amplitude stability.

# Chapter 7

# Relaxation oscillations, stability, and cavity feedback in a superradiant Raman laser

## 7.1 Introduction

We experimentally study the relaxation oscillations and amplitude stability properties of an optical laser operating deep into the bad-cavity regime using a laser-cooled $^{87}$Rb Raman laser. By combining measurements of the laser light field with non-demolition measurements of the atomic populations, we infer the response of the gain medium represented by a collective atomic Bloch vector. The results are qualitatively explained with a simple model. Measurements and theory are extended to include the effect of intermediate repumping states on the closed-loop stability of the oscillator and the role of cavity-feedback on stabilizing or enhancing relaxation oscillations. This experimental study of the stability of an optical laser operating deep into the bad-cavity regime will guide future development of superradiant lasers with ultranarrow linewidths.

Optical lasers operating deep in the bad-cavity or superradiant regime, in which the cavity linewidth $\kappa$ is much larger than the gain bandwidth $\gamma_\perp$, have attracted recent theoretical[115, 33, **?**] and experimental [24, 23, 160] interest. The interest has been partially driven by the possibility of creating spectrally narrow lasers with linewidths $\leq 1$ millihertz and dramatically reduced sensitivity to the vibrations that limit state of the art narrow lasers and keep them from operating outside the laboratory environment[78]. These lasers may improve measurements of time[74, 19], gravity[38], and fundamental constants[55, 16] aiding the search for physics beyond the standard model. The cold-atom Raman superradiant laser utilized here operates deep into the bad-cavity regime ($\kappa/\gamma_\perp \approx$

$10^3 \gg 1$), making it an important physics test-bed for fundamental and practical explorations of bad-cavity optical lasers.

In the interest of fundamental science and in light of the potential applications, it is important to understand the impact of external perturbations on lasers operating deep into the bad cavity regime. In this Chapter, I present an experimental study of the response to external perturbations of the amplitude, atomic inversion, and atomic polarization of an optical laser operating deep into the bad-cavity regime. In contrast, experiments have extensively studied the amplitude stability properties of good-cavity lasers ($\kappa \ll \gamma_\perp$) (See Ref. [111] and references therein). Previous experimental work in the extreme bad cavity[24] and crossover regime[97] focused on the phase properties of the light and atomic medium. Amplitude oscillations, intensity noise, and chaotic instabilities have been observed in gas lasers operating near the cross-over regime ($\kappa/\gamma_\perp \leq 10$)[30, 154, 70, 161]. Relaxation oscillations of the field have been studied deep into the bad cavity regime using masers[142] in which the radiation wavelength is comparable to the size of the gain medium, unlike in the present optical system. Previous theoretical studies of amplitude stability deep in the bad-cavity regime include studies of relaxation oscillations[92], chaotic instabilities[67], and intensity fluctuations characterized by correlation functions[92, 113].

In good-cavity optical lasers, the atomic polarization (proportional to $J_\perp$) can be adiabatically eliminated and the relaxation oscillations are associated with the flow of energy back and forth between the gain inversion (proportional to $J_z$) and the cavity field $A$, where $J_z$, $J_\perp$ are components of the collective Bloch vector $\vec{J}$ describing the atomic gain medium. In contrast, in a bad-cavity laser, the cavity field can be adiabatically eliminated, and the oscillations are driven by the coupling of $J_\perp$ and $J_z$. Here, we will measure and infer not only the light field $A(t)$, but also the atomic degrees of freedom $J_\perp(t)$ and $J_z(t)$ using non-demolition cavity-aided measurements[35, 34] to give the complete picture of the dynamics of relaxation oscillations in a bad-cavity laser.

We will also consider the effects on the laser's amplitude stability of non-ideal repumping through multiple intermediate states. Intermediate repumping states were not included in previous simple theoretical models[115], but are present in most actual realizations. In addition, we

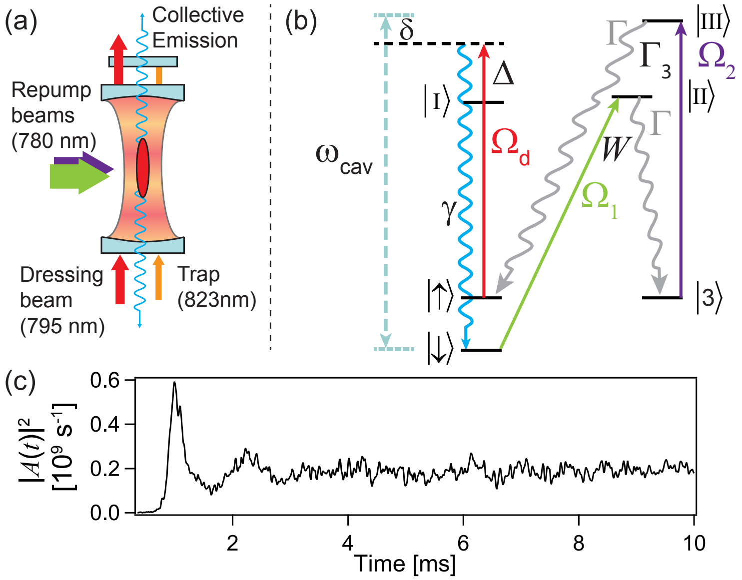

Figure 7.1: (a), (b) Physical setup and energy level diagram. The trapping light (orange) and Raman dressing laser (red, power ∝ $\Omega_d^2$) are injected along the cavity axis. The repumping light (purple, green) is applied perpendicular to the cavity axis. The emitted optical laser light (blue) is nearly resonant with the cavity mode (dashed lines) detuned from $\omega_{\mathrm{cav}}$ by $\delta$. The repumping is accomplished through a pair of two-photon transitions through intermediate optically excited states $|\mathrm{II}\rangle$ and $|\mathrm{III}\rangle$ with incoherent decay rates $\Gamma$. We individually control the two-photon rates $W$ and $\Gamma_3$ with the repumping laser powers $\propto \Omega_{1,2}^2$. $|3\rangle$ represents other metastable ground states besides the laser levels. (c) Example emitted laser photon flux $|A(t)|^2$ versus time showing spiking and relaxation oscillations at turn-on.

demonstrate that the cavity frequency tuning in response to the distribution of atomic population among various ground states can be used to suppress or enhance relaxation oscillations in the Raman transition configuration or other configurations with atomic transitions near-detuned from the lasing mode. As evidence, we show stabilization of $J_z$, $J_\perp$, and $A$ similar to observations of the suppression of relaxation oscillations in good-cavity lasers[146]. The cavity frequency tuning mechanism is related to other applications of cavity feedback including the creation of nonlinearities for generating spin-squeezed atomic ensembles [104], cavity cooling and amplification in atomic and opto-mechanical systems [86], and the control of instabilities in gravitational wave detectors [79].

## 7.2 Experimental System

Our experimental system consists of a quasi-steady-state Raman laser described in Fig. 7.1 and in Chapter 2. The laser uses $N = 1 \times 10^6$ to $2 \times 10^6$ $^{87}$Rb atoms as the gain medium. The atoms are trapped and laser cooled into the Doppler-insensitive Lamb-Dicke regime (40 $\mu$K) in a 1-D optical lattice at 823 nm formed by a standing wave in a moderate finesse $F \approx 700$ optical cavity with a cavity power decay rate $\kappa/2\pi = 11$ MHz. The single-atom cavity cooperativity parameter is $C = 8 \times 10^{-3} \ll 1$, and is equivalent to the Purcell factor[149].

Fig. 7.1b shows a simplified energy level diagram of a three level Raman laser system. The lasing transition is a spontaneous optical Raman transition with single-particle rate $\gamma$ from $|\uparrow\rangle \equiv \left|5\,^2S_{1/2}\,F = 2, m_F = 0\right\rangle$ to $|\downarrow\rangle \equiv \left|5\,^2S_{1/2}\,F = 1, m_F = 0\right\rangle$. The decay is induced by a 795 nm dressing laser injected into the cavity non-resonantly, and detuned from the $|\uparrow\rangle$ to $|\mathrm{I}\rangle \equiv \left|5\,^2P_{1/2}\,F' = 2\right\rangle$ transition by $\Delta/2\pi = +1.1$ GHz. The atoms are incoherently repumped back to $|\uparrow\rangle$ in two steps: from $|\downarrow\rangle$ to $|3\rangle$ and then from $|3\rangle$ to $|\uparrow\rangle$, at single-particle rates $W$ and $\Gamma_3$ respectively. The third metastable ground state $|3\rangle$ here represents the sum of all other hyperfine ground states in $^{87}$Rb. The full energy level diagram with details of the dressing and repumping lasers is provided in Sec. 7.4.

We control $\gamma$ (typical value 60 s$^{-1}$) using the intensity of the dressing laser. We control the repumping rates $W$ and $\Gamma_3$ using two 780 nm repumping lasers tuned near resonance with the $\left|5\,^2S_{1/2}\,F = 1, 2\right\rangle \rightarrow \left|5\,^2P_{3/2}\,F' = 2\right\rangle$ transitions. The repumping intensities are independently controlled allowing us to set the proportionality factor $r \equiv \Gamma_3/W$. In our experiments, $W$ ranges from $10^3$ s$^{-1}$ to $10^5$ s$^{-1}$, and $r$ ranges from 0.01 to 2. The repumping dominates all other homogenous broadening of the $|\uparrow\rangle$ to $|\downarrow\rangle$ transition such that $\gamma_\perp \approx W/2$. The inhomogenous broadening of the transition is $\gamma_{\mathrm{in}} \approx 10^3$ s$^{-1}$. To summarize, the relevant hierarchy of rates characterizing our system is $\kappa \gg \gamma_\perp \approx W/2 \sim NC\gamma > \gamma_{\mathrm{in}} \gg \gamma$. The rate $NC\gamma$ sets the scale for the single-particle, collectively-enhanced decay rate from $|\uparrow\rangle$ to $|\downarrow\rangle$. Coupling to other transverse and longitudinal cavity modes is negligible.

The frequency of the superradiantly emitted light $\omega_\gamma$ is set by the frequency of the dressing laser and the hyperfine splitting $\omega_{\mathrm{HF}}/2\pi = 6.834$ GHz. The detuning of light and cavity resonance frequency is $\delta = 2(\omega_{\mathrm{cav}} - \omega_\gamma)/\kappa$, normalized to the cavity half linewidth. The single particle scattering rate from the dressing laser into the cavity mode is $\Gamma_c(\delta) = C\gamma/\left(1+\delta^2\right)$.

The cavity frequency is dispersively tuned by the atomic ensemble $\omega_{\mathrm{cav}} = \omega_{\mathrm{bcav}} + \sum_k \alpha_k N_k$, where $\omega_{\mathrm{bcav}}$ is the bare cavity frequency and $\alpha_k$ is the cavity frequency shift for a single atom in the $k$th ground Zeeman state resulting from dispersive phase shifts of the intracavity light field.

Since the cavity frequency shift from atoms in the $F = 1, 2$ hyperfine states are not equal, the cavity frequency can provide a measurement of the atomic populations. We can suddenly switch off the repumping and dressing lasers to effectively freeze the atomic populations[23]. We then combine repeated non-demolition cavity frequency measurements like those describe in Chapter 3 and Refs. [152, 139, 35, 34] with NMR-like rotations[36] to determine $J_z(t) = \langle \frac{1}{2} \sum_{i=1}^{N} (|{\uparrow_i}\rangle\langle{\uparrow_i}| - |{\downarrow_i}\rangle\langle{\downarrow_i}|)\rangle$ and $\delta(t)$, described in detail in Sec. 7.4.2. We measure the amplitude of the light field emitted from the cavity $A(t)$ in heterodyne just prior to freezing the system, along with the measurement of the cavity frequency detuning $\delta$ provides an inferred value of $J_\perp = \left|\left\langle \hat{J}_- \right\rangle\right|$ using the relation $A(t) = \sqrt{\Gamma_c(\delta(t))}J_\perp(t)$, where $\hat{J}_- = \sum_{i=1}^{N} |{\downarrow_i}\rangle\langle{\uparrow_i}|$.

We observe characteristic laser spiking and relaxation oscillation behavior in $|A(t)|^2$ as the laser turns on and settles to steady state (Fig. 7.1c). To systematically study small amplitude deviations about the steady-state values $\bar{J}_z$, $\bar{A}$, and $\bar{J}_\perp$, we apply a swept sine technique, similar to Ref. [157]. We apply a simultaneous small amplitude modulation of the repumping rates as $W(t) = \bar{W}(1 + \epsilon\ \mathrm{Re}[e^{i\omega t}]))$ and $\Gamma_3\,(t) = rW(t)$. The modulation frequency $\omega$ is scanned over frequencies of order $\bar{W}$, such that $\gamma < \omega \ll \kappa$. We then measure and infer the quantities $A(t)$, $J_\perp(t)$, and $J_z(t)$ as described earlier.

To calculate the transfer function of the applied modulation, the measured light field amplitude $A(t)$ exiting the cavity as a function of time is fit to $A(t) = \bar{A}(1 + a(\omega)\cos(\omega t + \phi_a(\omega)))$. The normalized fractional amplitude response transfer function is $T_A(\omega) \equiv a(\omega)/\epsilon$ and the phase response transfer function is $T_\phi \equiv \phi_a(\omega)$. We also define the modulation frequency that maximizes

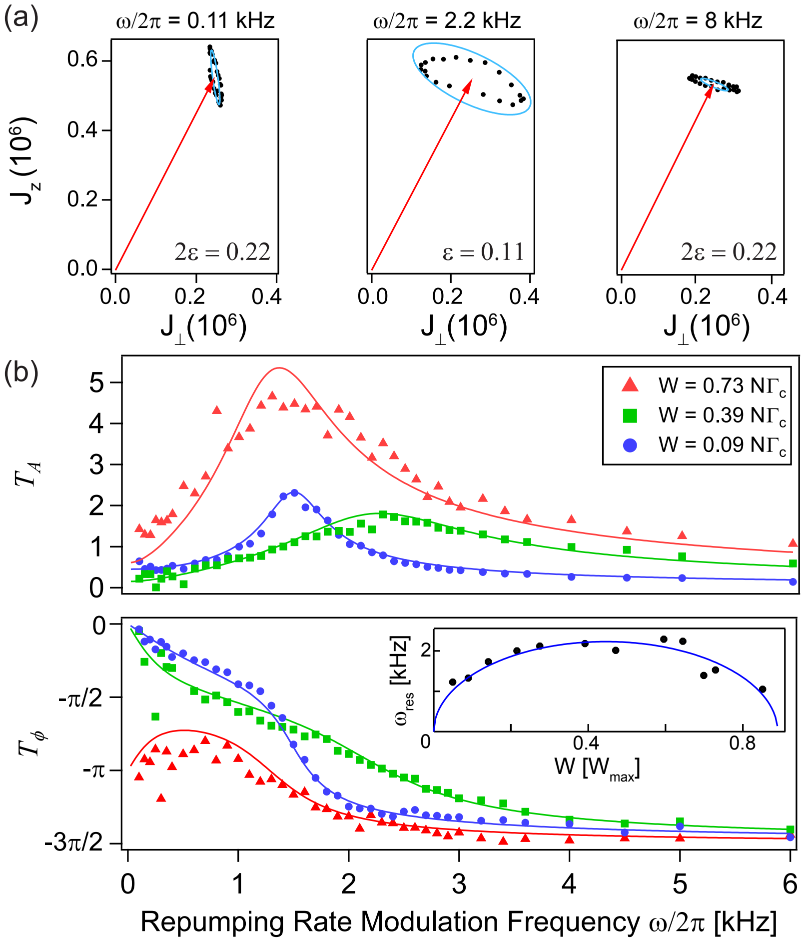

Figure 7.2: (a) Parametric plots of the Bloch vector components $J_z(t)$ and $J_\perp(t)$ over a single cycle of modulation of the repumping rate $W$ for modulation frequencies below, near, and above resonance or $\omega/2\pi = 0.11, 2.2, 8$ kHz, from left to right. The black points are the measured small-signal deviations about the measured steady-state Bloch vector (red arrow). The blue curve is the predicted deviation from steady-state given the experimental parameters $N = 1.3 \times 10^6$, $r = 0.71$, $\bar{\delta} = 1$, $\bar{W} = 0.35\, NC\gamma$, and $NC\gamma = 125 \times 10^3$ s$^{-1}$. The modulation depth $\epsilon$ for data below and above resonance was doubled to make the response more visible. (b) The amplitude (upper) and phase (lower) response transfer functions $T_A(\omega), T_\phi(\omega)$ of the light field for three values of the repumping rate $W$. The points are measured data, and the lines are zero free-parameter predictions of the response. (Inset) $\omega_{\text{res}}$ versus $W$ (points) and a fit to $\omega_0$ (line) showing the expected frequency dependence of the relaxation oscillations on repumping rate.

$T_A(\omega)$ as the resonance frequency $\omega_{\text{res}}$.

## 7.3 Results

We present the measured transfer functions and atomic responses in Figs. 7.2, 7.3, and 7.4, with theoretical predictions from a full model for $^{87}$Rb for quantitative comparison. To guide the interpretation of the measurements, we present an analogous 3-level model for the system shown in Fig. 7.1b that captures qualitative features of the full model, described in detail in Chapters 4 and 6. The 3-level model uses semi-classical optical Bloch equations to describe the lasing transition and the repumping process. Since $\kappa \gg W, \gamma$, the cavity field can be adiabatically eliminated from the system of equations. Additionally, we have adiabatically eliminated the populations in the optically excited states $|\text{I}\rangle, |\text{II}\rangle, |\text{III}\rangle$, arriving at the steady state solutions for the inversion $\bar{J}_z$ and collective atomic coherence $\bar{J}_\perp$[115, 114]. The steady state amplitude $\bar{A}$ is maximized at $W = W_{\text{pk}} = \frac{1}{2}N\Gamma_c(\bar{\delta})$ where $\bar{\delta}$ is the steady state cavity detuning.

To predict relaxation oscillations and damping, we do a straightforward expansion about the steady state values $\bar{J}_z$, $\bar{J}_\perp$, and $\bar{N}_3$ as $J_z(t) \approx \bar{J}_z(1 + \text{Re}[\jmath_z(t)])$, $J_\perp(t) \approx \bar{J}_\perp(1 + \text{Re}[\jmath_\perp(t)])$, and $N_3 \approx \bar{N}_3(1+\text{Re}[n_3(t)])$ and ignore terms that are second order in small complex quantities $\jmath_\perp, \jmath_z, n_3$ and repumping modulation amplitude $\epsilon$, as is described in Chapter 6, similar to work analyzing the small signal response of a laser in Refs. [92, 143]. The coupled quadratures $\jmath_z$ and $\jmath_\perp$ respond like the two coupled quadratures of a harmonic oscillator, slightly modified by the presence of the intermediate repumping state $|3\rangle$. In the limit of ideal repumping ($r \to \infty$) as is considered in Ref. [115], we can recast the equations as two uncoupled, second order differential equations

$$\ddot{\jmath}_{z,\perp} + 2\gamma_0 \dot{\jmath}_{z,\perp} + \omega_0^2 \jmath_{z,\perp} = D_{z,\perp}(\omega)\epsilon e^{i\omega t}. \tag{7.1}$$

When $\bar{\delta} = 0$, the damping rate $\gamma_0 = \bar{W}/2$ is set by the damping of the transverse component $\jmath_\perp$ caused by single-particle wave function collapse associated with the repumping. The natural frequency $\omega_0 = \sqrt{\bar{W}(NC\gamma - \bar{W})} = \sqrt{2}\bar{J}_\perp C\gamma$ is set by the steady-state rate of converting collective

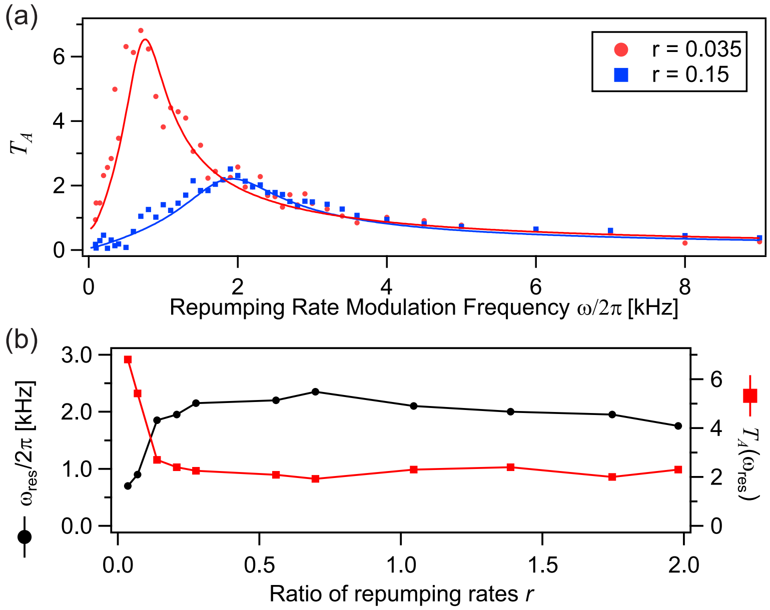

Figure 7.3: Effects of finite ratio of repumping rate $r$ (a) Comparison at two values of $r$ of $T_{\mathrm{A}}(\omega)$versus modulation frequency. The points are measured data in good agreement with the zero-free parameter fit (lines). (b) Plot of the resonance frequency $\omega_{\mathrm{res}}$ (black) and the peak value $T_A(\omega_{\mathrm{res}})$ (red) versus $r$.

transverse coherence into inversion $\bar{J}_\perp^2 C\gamma$, normalized by the total steady state coherence $\bar{J}_\perp$.

The responses of the two quadratures to the modulation are different because the effective drives are different with $D_\perp(\omega) = \frac{\bar{W}}{2}(NC\gamma - 2\bar{W} - i\omega)$ and $D_z(\omega) = (NC\gamma - \bar{W})(\bar{W} + i\omega)$. Note that the magnitude and phase of the drives change with the modulation frequency and repumping rate, even as the modulation depth $\epsilon$ remains constant.

We show this driven oscillator response in Fig. 7.2a with the measured and predicted parametric plot of $J_z$ and $J_\perp$ at three different applied modulation frequencies, with repumping near $\bar{W} = W_{\mathrm{pk}}$ . Although the characteristic frequencies and rates of the atomic oscillator do not change, the differing drives lead to a change in the phase relationship between the response of the two quadratures. We believe the discrepancy with theory in the center panel of Fig. 7.2a is the beginning of nonlinearity in the system as it responds beyond the small perturbation regime near resonance.

In Fig. 7.2b, we focus on the light field's transfer functions $T_{\mathrm{A}}(\omega)$ and $T_\phi(\omega)$. Data for

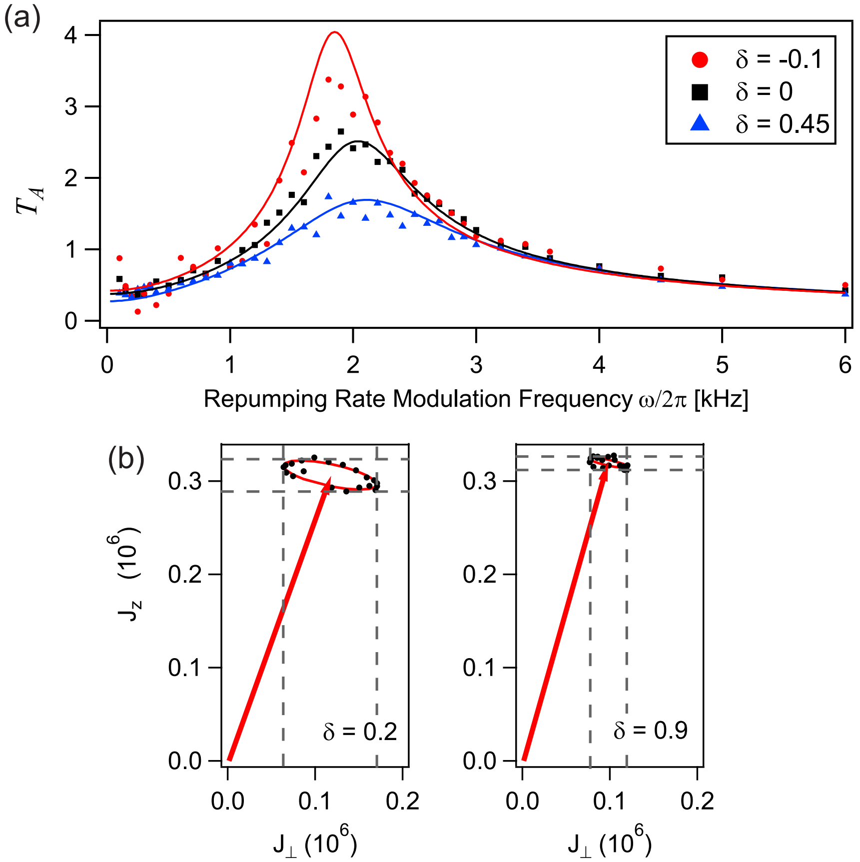

Figure 7.4: Evidence of negative and positive cavity feedback. (a) Amplitude transfer functions of the emitted electric field for three detunings from cavity resonance. The data points are the average of 4 experimental trials. The lines are fitted transfer functions with N as a free parameter. (b) Cavity damping of collective atomic degrees of freedom. The response going from $\bar{\delta} = 0.2$ (left) where the $\gamma_0$ is small to $\bar{\delta} = 0.9$ (right) where the system is expected to be critically damped. The red lines are sinusoidal fits to the data (circles). The dashed lines highlight the damping in both $J_\perp$ and $J_z$.

three different average repumping rates $\bar{W}$ are shown. The data displays the features of the simple 3-level model, namely increased damping with $\bar{W}$, $\omega_0$ scaling with $\bar{W}$ (inset), the 270° phase shift of $T_\phi$ at high modulation frequencies, the small response near $\omega = 0$ and $\bar{W} = W_{pk}$ caused by the cancellation in the drive term $D_\perp(\omega)$, and finally the phase reversal of the response near $\omega = 0$ going from below to above $W_{pk}$. The data also quantitatively agrees with the displayed theory calculated for the full model including all $^{87}$Rb levels. We suspect the deviation for $\bar{W} = 0.73 N\Gamma_c$ is a result of a systematic error in measuring the total atom number.

In this work, the repumping ratio $r \neq \infty$, and the theory must be extended to quantitatively describe the data. The physical effect of finite $r$ is that population builds up in $|3\rangle$. The ratio of steady state populations is simply $\bar{N}_3/\bar{N}_\downarrow = 1/r$. As a result of a non-negligible $\bar{N}_3$, the natural frequency is slightly modified as $\omega_0 = \sqrt{\frac{r}{1+r}\bar{W}(NC\gamma - \bar{W})}$. The effective damping in the presence of a harmonic drive at frequency $\omega$ is $\gamma_0 = \frac{\bar{W}}{2}\frac{r^2}{(1+r)(1/2+r)} + \frac{r(NC\gamma-\bar{W})}{2(1+r)(1/2+r)} - \frac{\omega^2}{\bar{W}(1+r)}$. The frequency dependent term results from the additional phase shift introduced into the oscillating system as a result of time spent in $|3\rangle$. Despite the frequency-dependent reduction of the damping, as long as $\gamma_0 > 0$ near $\omega = \omega_0$, the system will remain stable. We can experimentally observe a reduction in damping as $r \to 0$, shown in Fig. 7.3. From the form of $\omega_0$ and $\gamma_0$, we expect to see the resonance frequency sharply decrease, and an increase in the peak relaxation oscillation amplitude, as $r \to 0$, which we observe in Fig. 7.3b.

To understand the dynamic tuning of the cavity resonance frequency $\omega_{\text{cav}}$ in response to changes in the atomic populations, we consider the case $r \to \infty$ and $\bar{\delta} \neq 0$. We also assume the cavity frequency is tuned by the atomic inversion $J_z$ as $\alpha = \alpha_\downarrow = -\alpha_\uparrow > 0$. The dynamic cavity tuning then modifies the damping rate as $\gamma_0 = \frac{\bar{W}}{2}\left(1 + 2\alpha\bar{\delta}\left(\frac{N}{1+\bar{\delta}^2} - \frac{\bar{W}}{C\gamma}\right)\right)$. The dispersive tuning of the cavity frequency can act as either positive or negative feedback on the oscillations of $\jmath_{\perp,z}$ for $\bar{\delta} < 0$ and $> 0$ respectively. As an example, in the case of negative feedback, if the inversion $J_z$ decreases, the cavity tunes away from resonance with the Raman transition, reducing the superradiant emission from $|\uparrow\rangle$ to $|\downarrow\rangle$, and allowing the repumping to restore the inversion more quickly. We observe both positive and negative feedback in the measured transfer function $T_A(\omega)$ and the atomic responses $J_z(t)$ and $J_\perp(t)$ as shown in Fig. 7.4.

We have studied the dynamics of the polarization, inversion, and field of an optical laser operating deep in the bad-cavity regime. We have shown that dispersive cavity frequency tuning can suppress or enhance relaxation oscillations. Having experimentally validated our model for optical lasers in the extreme bad-cavity regime, future work can now extend the formalism to realistic models of proposed ultrastable lasers using ultranarrow atomic transitions in atoms such as Sr and Yb[115]. In the future, it should be possible to directly monitor $J_\perp$ using techniques similar

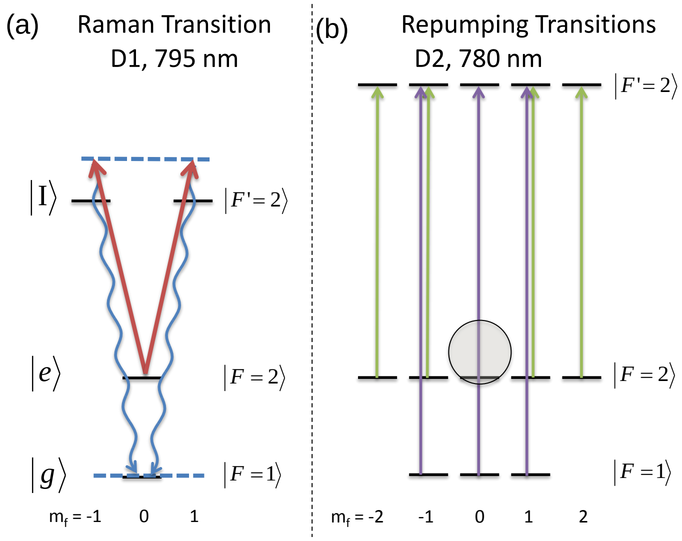

Figure 7.5: (a) The energy level diagram for the D1 Raman transition used for lasing. The linearly polarized Raman dressing laser is shown in red and the superradiantly emitted light in blue. The cavity mode resonance frequency $\omega_{cav}$ is denoted with a blue dashed line. With the quantization axis defined by a 2.7 G magnetic field oriented along the cavity axis, the linearly polarized light is a linear combination of $\sigma_+$ and $\sigma_-$ polarizations. (b) The energy level diagram for the D2 repumping beams F2 (green) and F1 (purple). The dark state with respect to the repumping lasers is labeled with a gray circle and corresponds to $|\uparrow\rangle$.

to those presented here to monitor $J_z$. Further studies of the nonlinear dynamics of the extreme bad-cavity laser system will include investigations of chaos[67] and squeezed light generation[101].

## 7.4 Additional Details

### 7.4.1 Technical Experimental Details

The optical cavity has a mode waist of 71 $\mu$m, mirror separation of 1.9 cm, and a finesse of $F = 700$. The atoms are trapped by a 1-D intracavity optical lattice at 823 nm and laser cooled to approximately 40 $\mu$K. The sub-wavelength localization of the atoms along the cavity-axis ensures that the atoms are in the Lamb-Dicke regime along this direction. However, the atoms are not in the Lamb-Dicke regime with respect to motion transverse to the cavity axis.

We first note that the energy levels, dressing laser, repumping lasers, and relative frequency tunings are the same as the primary configuration presented in Chapter 5. We include the details here again for clarity. The $|{\downarrow}\rangle \equiv \left|5\,^2S_{1/2}\,F=1, m_F=0\right\rangle$ and $|{\uparrow}\rangle \equiv \left|5\,^2S_{1/2}\,F=2, m_F=0\right\rangle$ hyperfine ground states of $^{87}$Rb form the basis of our Raman laser (energy level diagram shown in Fig. 7.5). The $|{\uparrow}\rangle$ state is dressed with an optical Raman laser at 795 nm that induces an optical decay to $|{\downarrow}\rangle$, with the cavity tuned to be resonant or near-resonant with the emitted light. The intensity of the dressing beam and the detuning by $\Delta/2\pi = +1.1$ GHz from the optically excited intermediate states $|\mathrm{I}_\pm\rangle \equiv \left|5\,^2P_{1/2}\,F'=2, m_F'=\pm1\right\rangle$ set the single-atom scattering rate into all of free space $\gamma$. The induced single-atom scattering rate into the cavity mode is $\Gamma_c = \frac{C\gamma}{1+\bar{\delta}^2}$ where $\bar{\delta}$ is the detuning of the cavity resonance frequency from the emitted light in units of the cavity half-linewidth, and $C$ is the single particle cooperativity parameter of cavity QED[35], equivalent to a Purcell factor[149]. The branching ratio for decay to $|{\downarrow}\rangle$ are included in the definition of $C$.

The quantization axis is set by a 2.7 G magnetic field along the cavity axis. The Raman dressing laser is injected non-resonantly along the cavity axis (experimental setup shown in Fig. 7.6a). For this quantization axis, the linearly polarized Raman dressing laser is an equal combination of $\sigma^+$ and $\sigma^-$ light. Constructive interference between the two decay paths from $|{\uparrow}\rangle$ to $|{\downarrow}\rangle$ through the two states $|\mathrm{I}_\pm\rangle$ leads to enhancement of light emission with linear polarization rotated 90° from the polarization of the dressing laser. Conversely, emission of light into the cavity with the same polarization as the dressing laser is highly suppressed by destructive interference of the two decay paths.

Two repumping lasers control the rate out of $|{\downarrow}\rangle$ and back into $|{\uparrow}\rangle$. The laser powers are independently set using acoustic optic modulators (AOMs) 1 and 2 shown in Fig. 7.6a. Both repumpers are $\pi$-polarized, applied perpendicular to the cavity, and separately tuned near the $\left|5\,^2S_{1/2}\,F=1,2\right\rangle$ to $\left|5^2P_{3/2}, F'=2\right\rangle$ transitions. The F1 repumper moves atoms primarily from the ground $\left|5\,^2S_{1/2}F=1, m_F\right\rangle$ states to the ground $\left|5\,^2S_{1/2}F=2, m_F\right\rangle$ states, and sets the scattering rate $W$ out of $|{\downarrow}\rangle$. The F2 repumper pushes population to $|{\uparrow}\rangle$ as the dipole matrix element for the transition $|5^2S_{1/2}, F=2, m_f=0\rangle \rightarrow |5^2P_{3/2}, F'=2, m_f'=0\rangle$ is zero. We quantify the F2 repumping rate by calculating the single particle scattering rate for an atom in $|5^2S_{1/2}, F=2, m_f=1\rangle$ state as $\Gamma_3$. We define the pump ratio $r \equiv \frac{\Gamma_3}{W}$ to quantify the degree of population buildup outside of the two level manifold $|\uparrow\rangle$ and $|\downarrow\rangle$, with the ideal repumping case being $r \to \infty$. Though $\Gamma_3$ is not perfectly equivalent to $\Gamma_{3\uparrow}$ from the three level model, it allows us to define $r$ in an analogous way. Population will still remain in the states $|5^2S_{1/2}, F = 1, m_f = \pm 1\rangle$ even as $r \to \infty$, unlike in the ideal three-level model. This why the output power correction factor $R$ does not asymptote to 1 as $r \to \infty$. Also note that unlike the simple three-level model, here, $W$ includes Rayleigh scattering back to $|\downarrow\rangle$, contributing damping of the coherence $J_\perp$ without affecting the inversion $J_z$.

### 7.4.2 Response Function Measurement Sequence

In Sec. 7.3, we measure three quantities to characterize the response of the superradiant laser to small perturbations: the light field amplitude $A(t)$, the magnitude of the coherence $J_\perp(t)$, and the inversion $J_z(t)$. As shown in Fig. 7.6, the perturbation is created by a small fractional modulation of the F1 and F2 repumping laser power at frequency $\omega$ such that $W(t) = \bar{W}(1+\epsilon\cos\omega t)$ while $r(t)$ remains constant. At time $t_3$, we shut off the repumping and dressing lasers in less than 100 ns, freezing the atomic populations[23]. The amplitude of the light just before shut off $A(t_3)$ is determined from the IQ-demodulated heterodyne signal shown in Fig. 6a.

We then use methods similar to those in Chapter 3 to non-destructively probe the cavity-mode to determine the cavity resonance frequency $\omega_{cav1}$ and hence detuning from the emitted light frequency $\delta(t_3)$. We then calculate the coherence $J_\perp(t_3)$ using the relation $A(t_3) = J_\perp(t_3)\sqrt{C\gamma/(1+\delta^2(t_3))}$. The probe is non-destructive in that a small fraction of the atoms are lost or Raman scattered to other states during the measurement.

The inversion $J_z(t_3)$ is determined by using a microwave $\pi$-pulse to swap the populations between $|\uparrow\rangle$ and $|\downarrow\rangle$, and then measuring the cavity resonance frequency a second time $\omega_{cav2}$. Shifts in the cavity frequency due to atoms in other states are common mode to both measurements, such that the difference between the two cavity frequency measurements is only proportional to the inversion $\omega_{cav1} - \omega_{cav2} = 2(\alpha_\uparrow - \alpha_\downarrow)J_z(t_3)$. The frequency tuning of the cavity resonance per atom in each state $\alpha_{\uparrow,\downarrow}$ is calculated from the known cavity geometry, atomic dipole moments, and bare

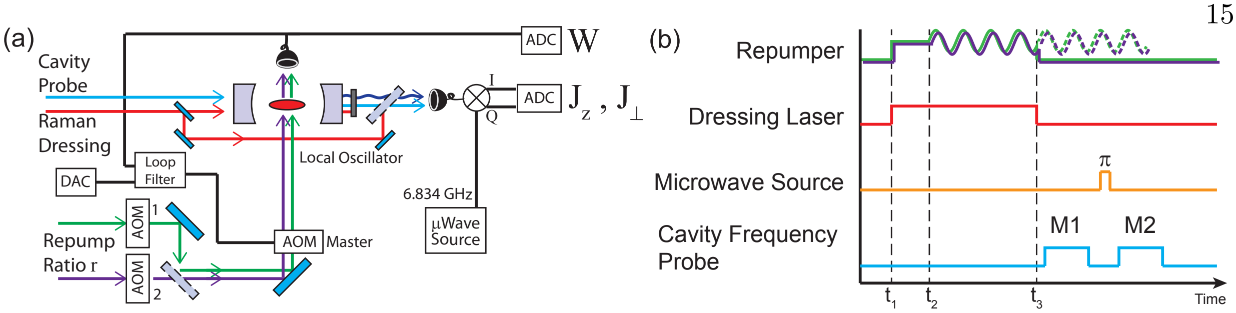

Figure 7.6: Measurement setup and sequence timing diagram. (a) The physical setup for measuring the light field amplitude response $A(t)$ and the atomic responses $J_z(t)$, $J_\perp(t)$ to a small modulation of the repumping rate $W(t)$. Optical beams are colored with arrows; RF and microwave signals are in black. (b) Timing diagram for measurements. Superradiance is started at $t_1$, and the repumping rate $W(t)$ is modulated (with $r$ constant) starting at time $t_2$. At $t_3$, the repumper and dressing lasers are shut off, freezing the atomic populations. The microwave $\pi$-pulse corresponds to a 12 $\mu$s pulse of 6.834 GHz microwaves resonant only with the ground hyperfine state transition $|\uparrow\rangle$ to $|\downarrow\rangle$. The pulse completely swaps the populations $N_e$ and $N_g$ of states $|\uparrow\rangle$ and $|\downarrow\rangle$. The cavity frequency probe windows M1 and M2 used to determine the dressed cavity frequency $\omega_{cav1}$ and $\omega_{cav2}$, and from which we can determine $J_z(t_3)$.

cavity detuning from resonance with nearby optical atomic transitions at 795 nm. The process is repeated for different stopping times $t_3$ in order to sample the modulation period for a set of times $t_i$. The data $J_z(t_i)$ versus $J_\perp(t_i)$ are shown in several parametric plots in the main text.

In the case of the field transfer functions $T_A(\omega)$ and $T_\phi(\omega)$, continuous time traces $A(t)$ are averaged over several trials at the same modulation frequency and phase to enhance signal to noise. The average response is then fit to $A(t) = A_s(1 + a(\omega)\cos(\omega t + \phi_A(\omega)))$, with transfer functions calculated as $T_A(\omega) = a(\omega)/\epsilon$ and $T_\phi(\omega) = \phi_A(\omega)$. The measurement is then repeated for different $\omega$.

### 7.4.3 Real time cavity probe

For the data presented here, we measured the state population by probing the dressed cavity frequency when superradiant emission had been extinguished by turning off the dressing and repumping laser. However, leading up to these results, we also developed a method to measure the dressed cavity frequency in real-time during superradiant emission using the transmission of a weak probe through the atom-cavity system. Here I will describe the details of this real time cavity probe (RTCP).

The basic idea of the real time probe is to weakly phase modulate the dressing laser at the hyperfine frequency, producing a small component of the light at the dressed cavity frequency. We can then detect the transmission of this probe to measure the probe sideband detuning from the dressed cavity resonance $\delta = f_{probe} - f_c$. The sideband is created using the EOspace phase modulator in the dressing path as described in Chapter 2. The basic detection scheme is complicated by presence of the strong off-resonant dressing laser and superradiant emission exiting the cavity along with the weak probe. The superradiant emission is orthogonally polarized with respect to the dressing laser, so it is polarization filtered and sent to the heterodyne detection. The dressing laser and the RTCP are then directed to the APD detector.

There are two difficulties we dealt with in directly detecting the transmission of the weak probe. The first is that the signal from the off-resonant dressing laser provides a large background, $V_{bck}$ which could fluctuate due to detailed higher order mode structure of the cavity. The second difficulty is that the transmission only from a single RTCP does not distinguish the sign of the detuning $\delta$. To address these issues, we implemented a two stage lock-in detection.

The first stage consisted of switching the modulation that created the probe component on the dressing laser on and off at 100 kHz. This switching allows us to measure the total average power transmitted with the Raman dressing laser background subtracted out. The second stage consisted of switching between two different frequencies for the modulation of the dressing laser to create the weak probe components separated from the 'probe center' by $\delta_m = \pm 20$ MHz. We alternated between the two modulation frequencies $f_h$ and $f_l$ at a rate of 50 kHz. Each frequency component produces a signal from the APD, $V_h$ and $V_l$ respectively, that have a Lorentzian shape as a function of the cavity detuning. By mixing the APD signal with the 50 kHz modulation frequency, we can extract the difference in the power transmitted at these two frequencies, which contains information about the sign of the cavity detuning with respect to the center of the two probe components. This assumes that the dynamics of the cavity are stable on timescales of order 20 $\mu$s. The slowly varying signal from the APD after mixing with the 50 kHz reference frequency is

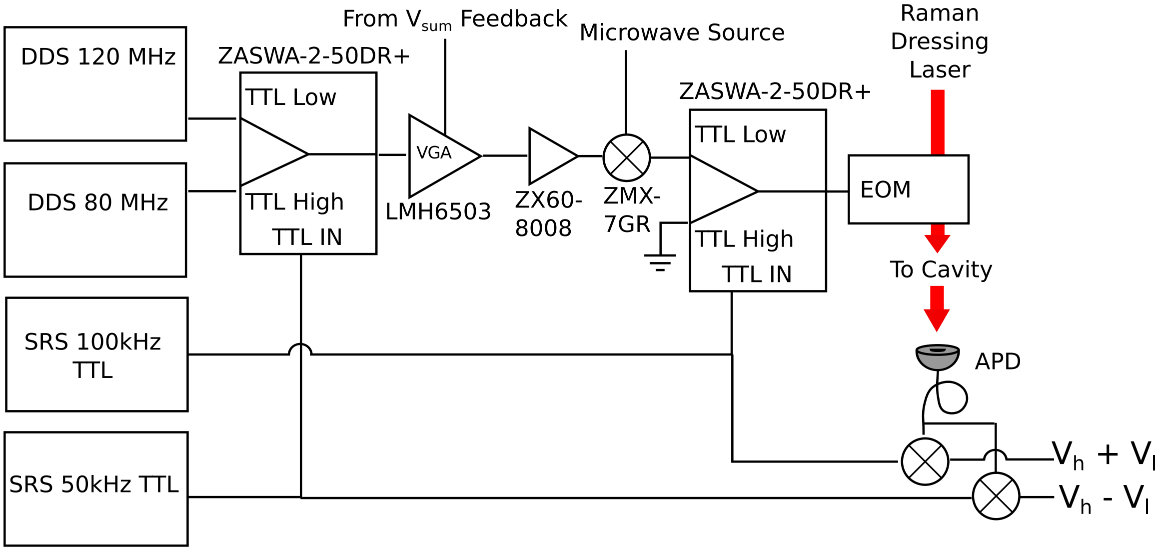

Figure 7.7: A schematic of the real time cavity probe RF setup. The two ZASWA-2-50DR+ switches provide the modulation of the signals, controlled by the two SRS frequency generators locked to the atomic clock reference. The signal generated by the light transmitting the cavity is then demodulated to produce the signals used to determine the dressed cavity detuning.

$V_{\text{diff}} = (V_{bck1} + V_h)/2 - (V_{bck2} + V_l)/2$. Notice the background signal largely subtracts out, so $V_{\text{diff}}$ is proportional to the difference of two Lorentzians. We filter high frequency components above 25 kHz so we can still detect modulations in the cavity mode on the 7 $\mu$s timescale.

The difference in powers provide a dispersive-like signal over a range of 30-40 MHz for the cavity frequency. However, depending on the cavity frequency, the total power transmitted varies as the sum of two Lorentzians. By separately mixing the APD signal with the 100 kHz reference frequency and filtering the signal at 50 kHz, we obtain a slowly varying signal $V_{\text{sum}} = (-V_{bck1} + V_h)/2 + (-V_{bck2} + V_l)/2$ that is proportional to the average transmitted power. We implemented a power stabilization feedback loop to keep the total transmitted power constant at a level that does not interfere with the superradiant emission. The final signal used for measuring the probe-cavity detuning is the ratio $S = V_{\text{diff}}/V_{\text{sum}}$, to normalize out any residual total power variation not accounted for in the feedback loop. We fit $S$ to a signal $y_0 + \frac{8\delta_m\delta}{(\kappa/2\pi)^2+4(\delta_m^2+\delta^2)}$ after sweeping the probe components over the resonance, which calibrates the unknown scale factors in the system, allowing us to invert the expression and extract $\delta$ for a given $S$.

The RTCP was useful in first discovering the dynamics of the dressed cavity mode and the impact of the dressed cavity mode on the amplitude stability of the laser. In particular, it provided the first evidence of the instability associated with a negative detuning of the dressed cavity mode from the laser emission frequency, discussed in Chapter 6. This data is shown in Fig. 7.8.

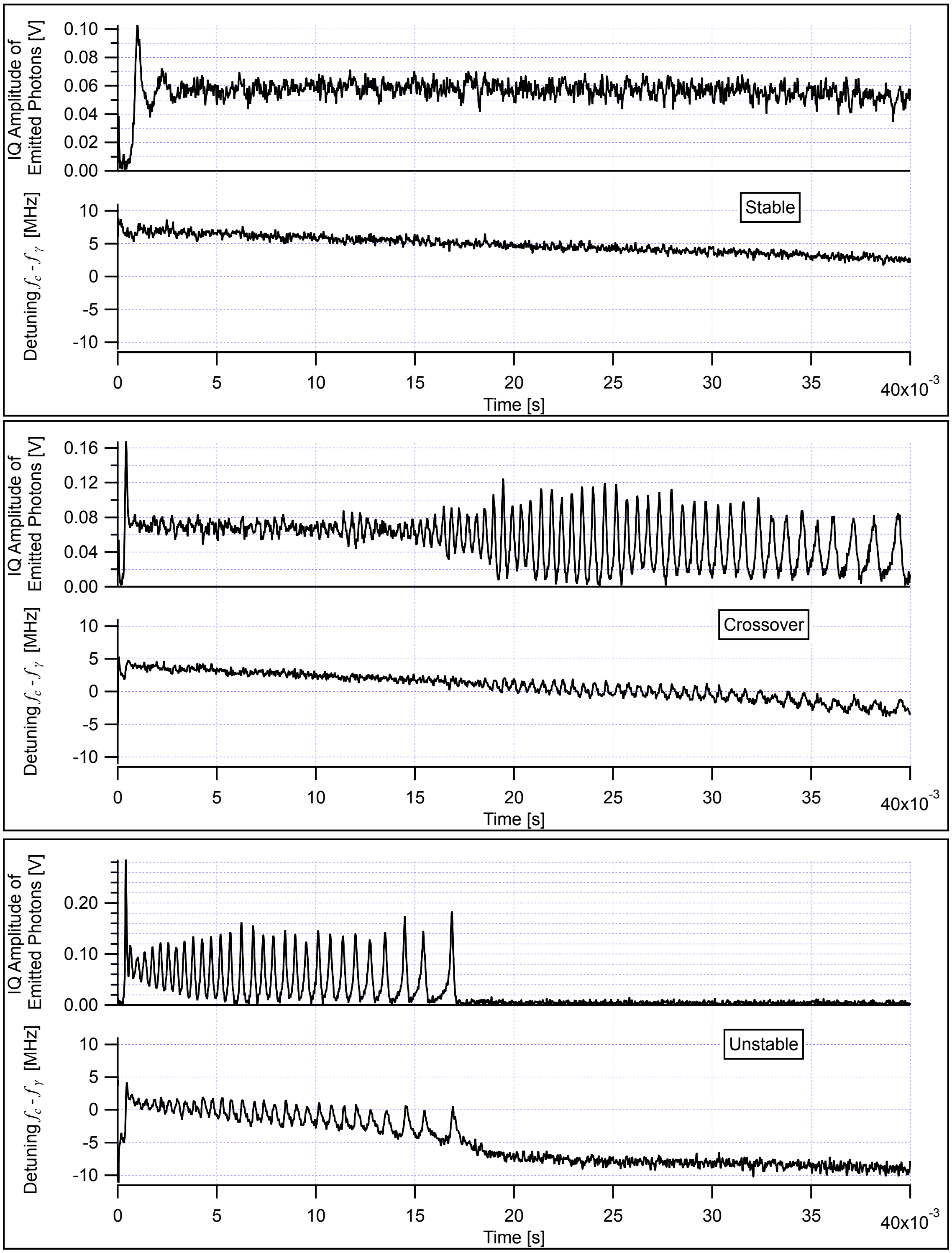

Figure 7.8: Data showing the correlation of amplitude stability of the laser with the cavity detuning from the laser emission frequency. The data in particular highlights the transition from stable operation on when the cavity is positively detuned, but the transition in instability for negative detuning. Here the IQ amplitude of emitted photons is proportional to the emitted light amplitude, $f_c$ is the dressed cavity, and $f_\gamma$ is the emitted light frequency.

# Chapter 8

## Active and passive sensing of collective atomic coherence in a superradiant laser

In this chapter, we explore the idea of the superradiant laser acting as a non-demolition mapping of collective quantum coherence onto a cavity light field. We show theoretically that the fundamental precision of the mapping is near the standard quantum limit on phase estimation for a coherent spin state, $\Delta\phi = 1/\sqrt{N}$, where $N$ is the number of atoms. The associated characteristic measurement timescale $\tau_W \propto 1/N$ is collectively enhanced. The non-demolition nature of the measurement is characterized by only 0.5 photon recoils deposited per atom due to optical repumping in a time $\tau_W$. We experimentally realize conditional Ramsey spectroscopy in our superradiant Raman laser, compare the results to the predicted precision, and study the mapping in the presence of decoherence, far from the steady-state conditions previously considered. Finally, we demonstrate a hybrid mode of operation in which the laser is repeatedly toggled between active and passive sensing.

### 8.1 Introduction

Superradiant lasers have the potential to be the most stable optical frequency references to date, with broad impacts across science and technology [115, 33]. These frequency references derive their stability from an ensemble of atoms spontaneously synchronized by cavity-mediated interactions, achieving collective coherence times greater than single-particle coherence times [24]. Reliance on inter-particle interactions makes superradiant lasing one of the growing number of examples of collective phenomena being explored for enhancing precision measurements [116, 4, 139, 104, 35, 62, 130, 42].

The superradiant laser's defining feature is the storage of the coherence of the laser system in the gain medium. The coherence is mapped onto the cavity field through superradiant emission (Fig. 8.1a). This conceptual Bloch sphere [51] model of the laser has been the key to understanding not only the laser spectrum [24], but also the output field stability properties [21] and ability to use the laser as a sensor of magnetic fields [160]. In a Raman laser configuration, the mapping can be dynamically controlled through the use of an externally applied dressing laser. The storage and recovery of phase information in the atomic ensemble is analogous to quantum memories for quantum communication [47, 25, 145, 37, 125, 105].

In this chapter, I present an analysis of the non-demolition mapping of the coherence in a self-synchronized ensemble of atoms onto a cavity field through superradiant emission that relies on fundamentally collective effects with no single-atom analog. We link the well-known Schawlow-Townes laser linewidth limit [136] to the information gained about the atomic system through the mapping, which sets the fundamental limit to potential superradiant sensors, and study spontaneous synchronization in the presence of decoherence far from steady-state conditions. Theoretically, the output light provides sufficient information to continuously track the evolving phase of the atomic coherence $\phi$ with a precision within a factor of 2 of the standard quantum limit (SQL) on phase resolution for a coherent spin state. The coherence readout rate is collectively enhanced by a factor of $N$ compared to single-particle fluorescence readout. Each measurement also prepares the coherence for the next measurement, while only imparting 1/2 photon recoils per atom in the characteristic measurement time.

Our theoretical analysis is compared to experimental data from our proof-of-principle experimental system using $^{87}$Rb (Fig. 8.1b and 8.1c). The results culminate in a hybrid sensor that combines active sensing of the collective atomic phase during superradiant emission with passive phase measurements using Ramsey-like evolution times. We show the sensor can repeat many measurement cycles in a single experimental trial due to the non-demolition nature of the superradiant mapping.

## 8.2 Theory of the Optimal Estimator

Our theory considers an ideal cold atom Raman laser. Examples of cold atom Raman lasers include Refs. [73, 64, 156, 6]. The ideal laser we consider here operates deep into the bad-cavity, or superradiant, regime [97, 92] where the cavity power decay rate $\kappa$ greatly exceeds all other relevant decay and scattering rates. The laser utilizes $N$ atoms trapped in a one dimension (1D) optical lattice that is formed inside the optical cavity that also mediates the long-range interactions between atoms that drive spontaneous synchronization of the atomic dipoles.

The optical Raman dressing laser induces a decay rate $\gamma$ from $|\uparrow\rangle$ to $|\downarrow\rangle$ (Fig. 8.1c). The dressing laser is detuned from an optically excited intermediate state $|i\rangle$, and the rate a single atom scatters photons from the dressing laser into the resonant cavity mode is $\Gamma_c = C\gamma$, where $C$ is the single-particle cavity cooperativity parameter of cavity quantum electrodynamics (QED)[149]. The collective cooperativity satisfies the necessary condition for superradiance $NC \gg 1$. Single-particle optical repumping proceeds at an optimum repumping rate $w \approx w_{\text{pk}} = N\Gamma_c/2$ [115].

The ensemble of atoms can be represented by a Bloch vector $\vec{J}$ whose azimuthal phase $\phi(t)$ evolves in time at a rate set by $\dot{\phi}(t) = E(t)/\hbar$, where $E(t)$ is the instantaneous energy difference separating $|\uparrow\rangle$ and $|\downarrow\rangle$, and $\hbar$ is the reduced Planck constant. Depending on the sensitivity of $E(t)$ to environmental conditions, precise measurements of $\phi(t)$ correspond to measurements of the environment or time[89].

The quantum phase $\phi(t)$ is not directly measurable and must be mapped onto an observable quantity. Bad-cavity active oscillators, such as masers or superradiant lasers, continuously map the collective phase $\phi(t)$ onto the observable phase $\psi(t)$ of an electromagnetic cavity field, because the rapidly decaying cavity field is slaved to the atomic coherence [21]. Ignoring vacuum noise, the complex electric field phasor is given by $A(t)e^{i\psi(t)} \propto J_\perp(t)e^{i\phi(t)}$ where $J_\perp(t)$ is the projection of the Bloch vector onto the $x$-$y$ plane and $A(t)$ is the amplitude of the electric field phasor. Measuring the cavity field is equivalent to a continuous non-destructive measurement of the evolving atomic coherence.

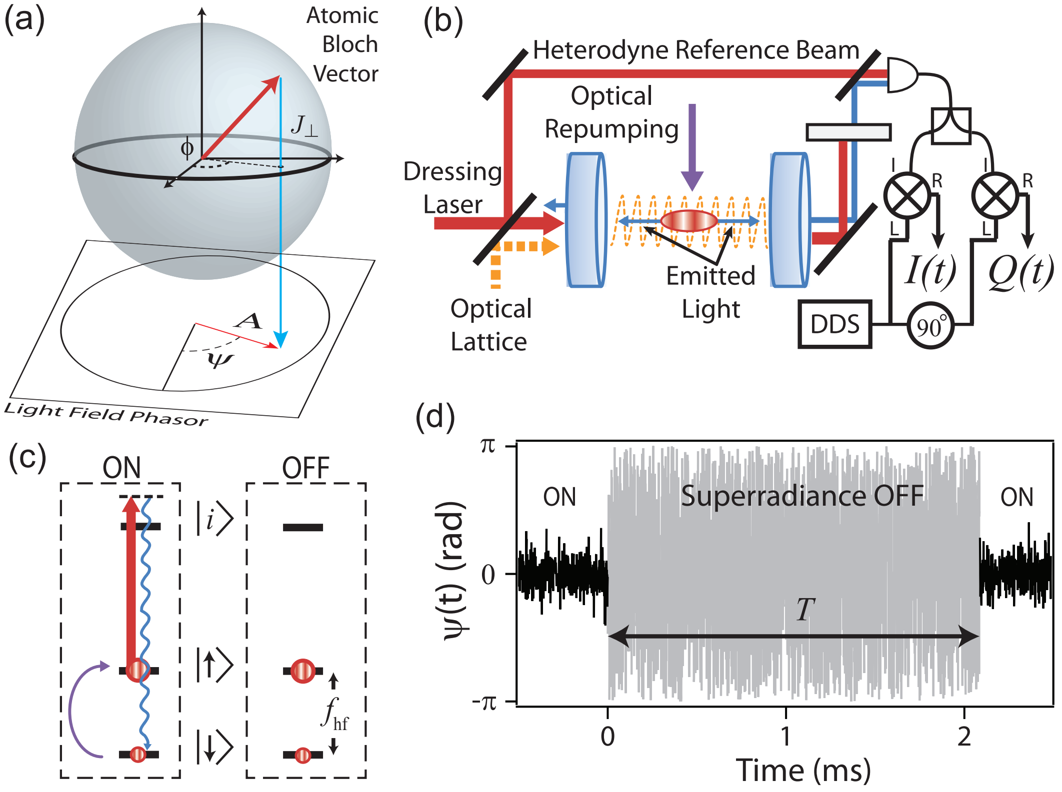

Figure 8.1: (a) Superradiant emission (blue) mapping the collective atomic coherence, represented by a Bloch vector $\vec{J}$ with phase $\phi$ and equatorial projection $J_\perp$, onto the phasor representing the emitted light field defined by a phase $\psi$ and amplitude $A$. (b) The experimental setup. $^{87}$Rb atoms are trapped in a 1D optical lattice (dashed, orange) within an optical cavity. Optical repumping light is applied perpendicular to the cavity axis. The emitted light is detected in heterodyne, then demodulated using a direct digital synthesis frequency reference to obtain both field quadratures, $I(t)$ and $Q(t)$, and calculate the light's amplitude $A$ and phase $\psi$. (c) An energy level diagram of a superradiant Raman laser. The Raman dressing laser (red) detuned from an intermediate state $|i\rangle$ induces optical decay at rate $\gamma$ between ground hyperfine states $|\uparrow\rangle$ and $|\downarrow\rangle$. The atoms are incoherently repumped back to $|\uparrow\rangle$ at rate $w$. When the dressing and repumping lasers are off, the atoms remain in a superposition of $|\uparrow\rangle$ and $|\downarrow\rangle$, and the quantum phase $\phi(t)$ that evolves at $f_{\mathrm{hf}}$. (d) Example data from a Ramsey-like sequence in a superradiant laser. Superradiant emission continuously maps $\phi(t)$ onto $\psi(t)$. We measure a differential light phase $\psi(T) - \psi(0)$ over a free evolution time $T$.

The precision of the $\phi(t)$ to $\psi(t)$ mapping is limited by fundamental quantum noise from Schawlow-Townes phase diffusion of the atomic phase and photon shot noise on the measurement of the light phase. Measuring $\psi(t)$ longer reduces photon shot noise, but diffusion of the atomic phase means later data is less correlated with the initial atomic phase we wish to estimate. Employing a Kalman filter [82] analysis, we find that the optimal estimate $\phi_e(t)$ of the phase $\phi(t)$ is an exponentially weighted average of $\psi(t)$ with a weighting time constant

$$\tau_W = \frac{1}{\sqrt{q} N \Gamma_c} \ , \tag{8.1}$$

assuming $w = w_{\mathrm{pk}}$. The details are included in Sec. 8.5). Here $q$ is the photon detection efficiency. A single-pole, low pass filter can be used to implement such a running weighted average.

The mean squared error of the optimal estimator is

$$\sigma_e^2 = \left\langle \left(\phi_e\left(t\right) - \phi\left(t\right)\right)^2 \right\rangle = \frac{2}{\sqrt{q} N} \ . \tag{8.2}$$

When $q = 1$, the error is only a factor of 2 from the SQL on phase variance for a coherent spin state of $N$ unentangled atoms $(\Delta\phi_{SQL})^2 = 1/N$ and is at the SQL, $2(\Delta\phi_{SQL})^2$, for the steady-state $J_\perp = \frac{N}{2\sqrt{2}}$ projection during superradiance at the optimum repumping rate $w_{\mathrm{pk}}$. Also, the impact of imperfect detection efficiency ($q < 1$) is mitigated by the scaling as $1/\sqrt{q}$ compared to the expected increase from increased photon shot noise alone, which would scale as $1/q$.

The measurement is non-destructive in that an atom experiences only $0.5/\sqrt{q}$ photon recoils on average during the characteristic measurement time $\tau_W$. This degree of recoil heating compares favorably with other sample-preserving [107, 20, 58, 56] and coherence-preserving [4, 139, 35, 34] probing techniques with precision at the SQL.

This active superradiant mapping provides a continuous measurement of the atomic phase, in contrast to the standard technique for mapping a quantum phase onto the observable difference in state populations, as is done in passive Ramsey spectroscopy [126] with atomic fountain and optical lattice clocks, for example [11, 109]. In Ramsey spectroscopy, the atoms accumulate a quantum phase $\phi(t)$ during free evolution periods after which $\phi(t)$ is mapped onto the atomic state populations. The state population is measured through fluorescence detection, which destroys the coherence and often destroys the ensemble [10], though the loss of the sample is not fundamental [107, 20, 57, 56, 58, 155, 170, 22]. Passive Ramsey spectroscopy has the benefit of being free from perturbations necessarily introduced in the active mapping that disturb the accuracy of the measurement. By implementing dynamic control of the superradiant mapping, a passive Ramsey-like sequence can be realized in a superradiant laser, combining both active and passive sensing into a single hybrid system[160].

A single cycle of the hybrid sequence (Fig. 8.1d) consists of running steady-state superradiance and estimating the light phase $\bar{\psi}(0)$ just before temporarily shutting off the dressing and repumping lasers at time $t = 0$, quenching the superradiant emission. However, the collective Bloch vector continues to precess at frequency $f_{\text{hf}}$ separating $|\uparrow\rangle$ and $|\downarrow\rangle$. At time $t = T$, the repumping and dressing lasers are turned on, and the phase of the light can then be estimated as $\bar{\psi}(T)$ using $\psi(t)$ data at times $t > T$. The accumulated atomic phase during the time period $T$ is then $\Delta\phi(T) = \phi(T) - \phi(0) = \bar{\psi}(T) - \bar{\psi}(0)$. The variance on $\Delta\phi(T)$ is $2\sigma_e^2$ because of the measurement necessary to initialize the state at $T = 0$. The initial measurement is unnecessary in traditional Ramsey measurements with perfect state preparation.

The fundamental limit on the estimation of the phase difference $\Delta\phi(T)$ is a factor of 4 larger than for standard interferometry techniques that use traditional Ramsey spectroscopy at the SQL. Still, little fundamental precision needs to be sacrificed in future atomic sensors to utilize the proposed mapping. The collective nature of superradiant emission also results in a characteristic readout rate enhanced by a factor of $N$ compared to the readout rate in the single-atom limit.

## 8.3 Experimental Demonstration

We have implemented a proof-of-principle atomic sensor using a cold-atom Raman laser on the clock transition of the ground hyperfine states of $^{87}$Rb ($|\uparrow\rangle = |F = 2, m_F = 0\rangle$ to $|\downarrow\rangle = |F = 1, m_F = 0\rangle$). For our system, $\kappa/2\pi = 11$ MHz, $N = 10^6$ atoms cooled to 40 $\mu$K, $C = 8 \times 10^{-3}$, and $\gamma/2\pi \approx 1$ Hz. The cavity finesse is $F = 700$. The dressing and repumping lasers can be switched on and off within 100 ns, much faster than the timescale on which atomic dynamics occur. We measure the phase $\psi(t)$ and amplitude $A(t)$ of the emitted light via heterodyne detection with respect to the dressing laser to remove phase noise on the emitted light imposed by phase noise on the dressing laser. By splitting the resulting rf signal and simultaneously demodulating the two quadratures, we obtain both $A(t)$ and $\psi(t)$ simultaneously. Example data of the passive sequence are shown in Fig. 8.1d. We estimate $\phi(0)$ ($\phi(T)$) using linear fits to 0.5 ms of $\psi(t)$ data at times $t < 0$ ($t > T$).

The standard deviation of the light phase difference $\bar{\psi}(T) - \bar{\psi}(0)$ as $T \to 0$ predicted by the optimal estimator $\phi_e$ for our system is $12 \pm 2$ mrad, after accounting for finite quantum efficiency ($q = 0.03$) and the multi-level structure of $^{87}$Rb. The general expression for the superradiant emission rate,

$$R_d = R\left(\frac{N}{2}\right)^2 \frac{2w}{N}\left(1 - \frac{w}{N\Gamma_c}\right) \,, \tag{8.3}$$

accounts for $w \neq w_{\text{pk}}$ and repumping through the multiple levels in the $^{87}$Rb hyperfine structure[24] with the correction factor $R$. Here $N = 9 \times 10^5$ atoms, $\Gamma_c = 0.05$ s$^{-1}$, $R = 0.1$, and $w = 0.2NC\gamma$. The final result of $R \neq 1$ and $w \neq w_{\text{pk}}$ is to reduce $R_d$ by a factor of 0.28. The reduction in the emission rate and the subsequent modification to the phase diffusion increases $\sigma_e$ by a factor of 2.4 compared to Eq. 8.2 (see Sec. 8.5).

The observed standard deviation is $70 \pm 7$ mrad, a factor of 6 above the predicted noise. We assign the discrepancy to the dispersive tuning of the cavity mode described in Ref. [24], an effect present in our system, but not fundamental to the physics of the sensor. Building on this work, we have also demonstrated sensing of applied phase shifts using a superradiant magnetometer [160].

The analysis of the optimal estimator does not consider the impact of decoherence and dephasing in passive sensors with superradiant readout. The process of superradiant emission continually maintains the coherence of the ensemble, but when the emission is turned off, the atoms decohere,

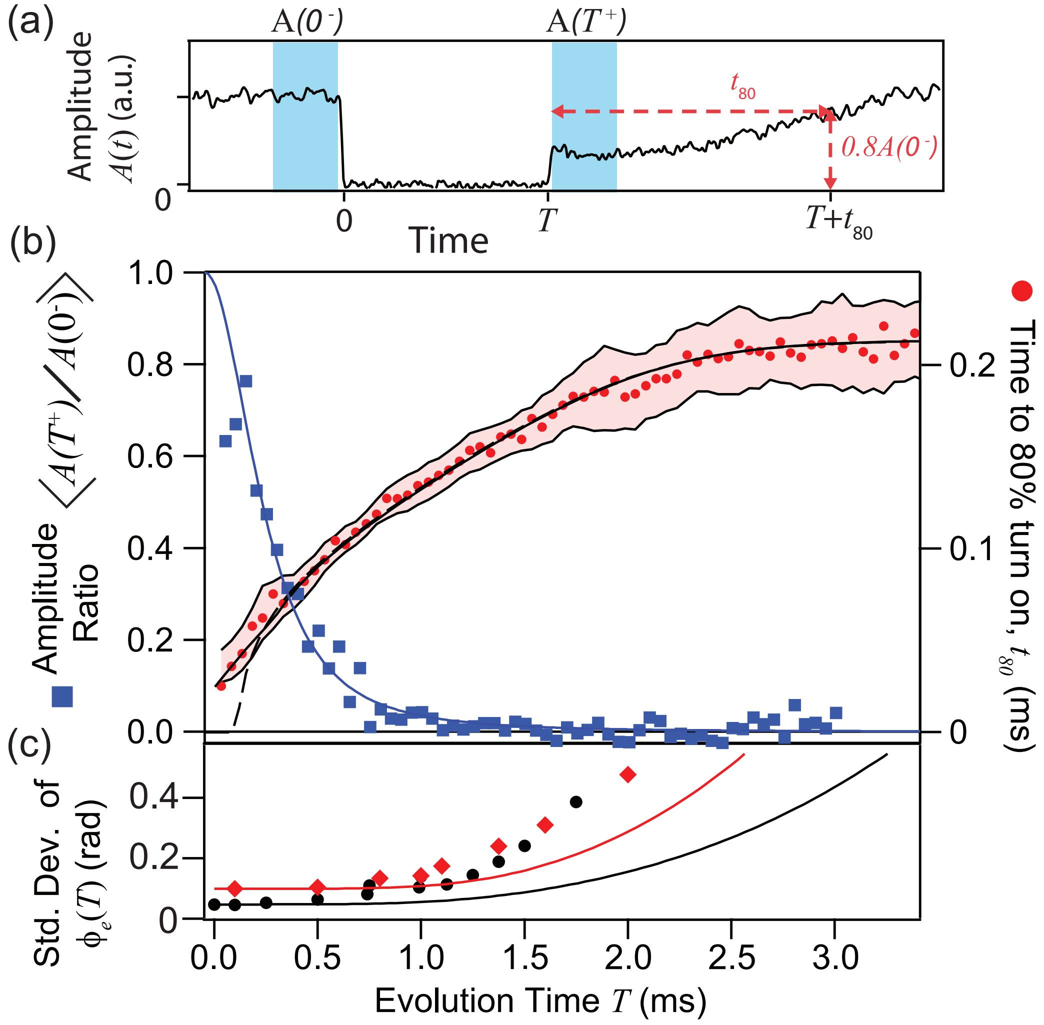

Figure 8.2: (a) Example time trace of the emitted light amplitude with an evolution time $T = 0.4$ ms. $A(0^-)$ and $A(T^+)$ are average amplitudes measured in the blue time windows before and after the evolution time. The characteristic rise time $t_{80}$ is the time when the amplitude has returned to 80% of the steady-state value. (b, left) The decay of $J_\perp$ as estimated by (blue squares) the ratio $A(T^+)/A(0^-)$ and (blue line) a fit to loss of contrast $c(t)$ of traditional Ramsey microwave spectroscopy. (b, right) Measured (red circles) and predicted (line) recovery time $t_{80}$. The solid curve is the prediction accounting for the low-pass filter that was applied to the data. The band around the data indicates 1 s. d. on each side of the data point. We attribute the fluctuations observed at short times to finite measurement precision. Each point is the average of 20 trials. (c) Standard deviation of the phase accumulated in time $T$ as estimated by (diamonds) superradiant mapping and (circle) population mapping. The lines are predictions based on the observed loss of contrast $c(T)$.

decreasing $J_\perp$ and $A$, as illustrated by Fig. 8.1a. In addition to setting the fundamental resolution of the atomic phase, the coherence is vital to the re-establishment of superradiant emission after the evolution time, so the impact of decoherence must be understood for operation of future superradiant sensors.

We use the experimental sequence in Fig. 8.2a to study the decay of coherence. The amplitude of the emitted light field just before turn off, at $t = 0$, is $A(0^-)$ and just after turn on, at $t = T$, the amplitude is $A(T^+)$. When the evolution time $T$ is short, the superradiance promptly returns to $A(0^-)$, but as the atomic coherence $J_\perp$ decays during the evolution time, $A(T^+)$ decreases proportionally. The decay of $J_\perp$ in our system is dominated by dephasing caused by inhomogeneous ac Stark shifts from the optical lattice. The ratio of amplitudes $A(T^+)/A(0^-)$ shown in Fig. 8.2b is well described by a fit to the decay of the contrast fringe $c(T)$ measured in standard microwave Ramsey spectroscopy with population readout [96].

The coherence lost during $T$ is eventually restored as the laser returns to steady-state. In Fig. 8.2b, the time $t_{80}$ at which $A(T + t_{80})/A(0^-) = 0.8$ is compared to a theoretical prediction based on the observed atomic contrast $c(T)$. The prediction is obtained using semi-classical optical Bloch equations and is described in detail in Sec. 8.6. At short times, little coherence is lost, and the laser quickly returns to steady-state because the remaining coherence provides a seed for superradiance.

Ideally, superradiant readout should last long enough to completely restore the coherence and avoid depletion over multiple measurement cycles. We predict an average recovery time $t_{80} < \frac{2}{N\Gamma_C}$, which is confirmed by our experimental results in Fig. 8.2b. Since the characteristic measurement time $\tau_W > \frac{1}{N\Gamma_C}$, each readout will almost fully restore the coherence for the next passive evolution measurement, as long as at least a small fraction of the coherence remains.

The collective atomic coherence $J_\perp(T)$ predominantly seeds subsequent superradiance until $J_\perp(T)$ becomes smaller than the rms equatorial projection of the decohered atoms $J_\perp^{(incoh)} \sim \sqrt{N}/2$. Even for $A(T^+)/A(0^-) \approx 0.05$, $J_\perp(T) > \sqrt{N}/2$, as seen by the relatively small $t_{80}$ (Fig. 8.2b). When $J_\perp(T) < J_\perp^{(incoh)}$, the laser must start an essentially new superradiant emission, resulting

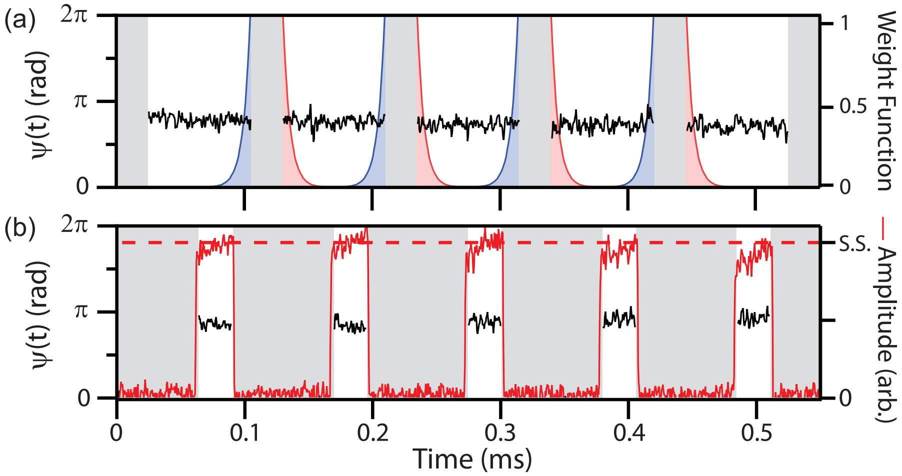

Figure 8.3: Demonstration of non-demolition superradiant measurements enabling a hybrid active/passive oscillator for two different duty cycles shown in (a) and (b). The measured light phase $\psi(t)$ is shown when the superradiance is switched on (black). The periods of evolution time, when the superradiance is switched off, are gray regions (random phase data not shown). The blue and red exponential curves in (a) correspond to the ideal optimal estimate weight functions before and after an evolution period respectively, calculated with our experimental parameters of $N$, $\Gamma_c$, and $q$. (b) The emission amplitude (red) returns to the steady-state value (dashed line) during active oscillation, reflecting restoration of the coherence $J_\perp$.

in large fluctuations in $t_{80}$. We observe fluctuations of 20 $\mu$s, on the same order as the predicted fluctuations in the time to reach the peak intensity of a superradiant pulse after preparation in the fully excited state [63].

We expect the fundamental phase resolution of the sensor to degrade from decoherence, because the signal, set by $J_\perp$, decays as $c(T)$, but the uncertainty from atom shot noise remains fixed. We predict the measurement noise by adding the background measurement noise in quadrature with the fundamental noise limit for both superradiant and population readout of a Ramsey sequence, $2\sigma_e/c(T)$ and $\sigma_e/c(T)$ respectively, shown as the lines in Fig. 8.2c. Experimentally measuring the standard deviation of $\bar{\psi}(T) - \bar{\psi}(0)$ versus $T$, we see that even when $c(T)$ decays to $\approx 5\%$ of the steady-state value at $T = 0.5$ ms, little phase resolution has been lost. The superradiant measurement noise at longer times is not at the decoherence limit due to additional technical noise, confirmed by the appearance of an equal amount of noise on the standard Ramsey population readout as well.

The culmination of these results is a demonstration of the non-destructive measurement technique in which we repeat on/off sequences to create a hybrid active/passive phase reference, shown in Fig. 8.3. The weight functions for the optimal estimate of the phase before and after the evolution periods are shown in Fig. 8.3a. Each measurement both retains a large fraction of the atoms ($> 95\%$, with the loss believed to result primarily from light-assisted atomic collisions) and prepares the atomic coherence for future measurement cycles, as shown by the constant amplitude of the emission in Fig. 8.3b. The free evolution times would ideally have high accuracy, while the active oscillation would have much greater measurement bandwidth, providing the strengths of both active and passive phase references in a single device.

Furthermore, the duty cycle of the measurements could be adjusted in real time for optimal overall phase stability and accuracy given knowledge of the environment. Figures 8.3a and 8.3b show two example experimental trials where only the duty cycle has changed. Real-time adaptation might allow future hybrid phase references to be employed outside of the laboratory for both scientific and commercial applications [38, 103].

## 8.4 Conclusion

In some aspects, our technique is similar to recently demonstrated single-atom [20, 57, 56, 58, 155], sample-preserving [107], and non-demolition [4, 139, 35, 34] readout techniques for neutral atoms where efficient collection of photons allows for detection near the SQL while in principle imparting only a few photon recoils per atom. Compared to fluorescence detection with a high numerical aperture lens, here the solid angle of the mode is small ($\Omega/4\pi = 8.9 \times 10^{-4}$), providing low backgrounds and high optical access.

However, our collective measurement is fundamentally different from the above techniques. Even non-demolition probes cause inevitable decay of the coherence that must be restored via discrete optical pumping and rotation of the state. In the superradiant readout, the active flow of collective information from the cavity also serves to re-prepare the atomic coherence for the next measurement. The atomic phase continuously evolves across passive and active periods, allowing future frequency sources to be phase-locked rather than frequency locked to an atomic reference, effectively eliminating aliasing noise in atomic clocks [163].

Looking forward, the ideas studied here might be applied on strictly-forbidden optical atomic transitions [135], enabling hybrid optical lattice clocks suited for operation outside of carefully controlled laboratory environments. Though the system demonstrated in this work is of limited use for precision measurement, it nevertheless points a way forward to developing a different class of atomic sensors [160] and establishes the theoretical connection between fundamental laser linewidths and the information gained about the underlying system at the heart of the laser. Our work also highlights unique phenomena that emerge from collective coupling of many-body systems, a topic of much recent and future research, e.g. research with quantum dots, superconducting qubits, ions, nitrogen vacancy centers, and mechanical oscillators [137, 52, 72, 95, 167].

## 8.5 Derivation of Optimal Estimator

Here we derive the optimal estimator $\phi_e(t)$ of the quantum phase $\phi(t)$, and its mean squared error $\sigma_e^2$, given a measurement record $\psi(t)$ of the phase of the superradiantly emitted optical field. We use the results from a continuous Kalman filter analysis with uncorrelated process noise and measurement noise [81, 82, 169]. Here the measurement noise corresponds to the photon shot noise that appears in the measurement of the light phase $\psi(t)$ and the process noise corresponds to the phase diffusion of the collective atomic Bloch vector that sets the Schawlow-Townes frequency linewidth limit.

### 8.5.1 Photon Shot Noise

The measured phase of the radiated light is related to the underlying quantum phase $\phi(t)$ by, $\psi(t) = \phi(t) + \Delta\psi(t)$ where the vacuum or photon shot noise adds the noise component $\Delta\psi(t)$. The noise is Poissonian and described by its lowest order moments as $\langle\Delta\psi(t)\rangle = 0$ and $\langle\Delta\psi(t)\,\Delta\psi(t+\tau)\rangle = \delta(\tau)\Phi_m$. Here, $\delta(\tau)$ is the Dirac delta function so that the measurement noise at different times is uncorrelated, but when $\tau = 0$ it is equal to the constant $\Phi_m = \frac{1}{4R_d}$. $S_\phi^{(m)}(\omega)$ is the two-sided power spectral density (PSD) of phase fluctuations due to measurement noise, which for photon shot noise $S_\phi^{(m)}(\omega) = \int_{-\infty}^{\infty} \langle \Delta\psi(t)\, \Delta\psi(t+\tau)\rangle \cos(\omega t) dt = \Phi_m$ [133]. The light phase variance for a measurement time window $\Delta t$ is $\sigma_m^2 = \int_{-\infty}^{\infty} S_\phi^{(m)}(\omega) \left|\frac{\mathrm{Sinc}(\omega\Delta t/2)}{\sqrt{2\pi}}\right|^2 d\omega = \Phi_m/\Delta t = \frac{1}{4R_d\Delta t}$, where $R_d$ is the average rate of detected superradiantly-emitted photons using homodyne detection. At the optimum superradiant photon emission rate [115, 24] $R_d = N^2\Gamma_c/8$, obtained at a repumping rate $w_{\text{pk}} = N\Gamma_c/2$ where $\Gamma_c = \frac{C\gamma}{1+\delta^2}$ is the single-particle natural decay rate into the cavity mode, including a finite detuning of the cavity resonance frequency from the emission frequency $\delta$ in units of the cavity half linewidth $\kappa/2$. Taking into account finite quantum efficiency $q$, we find

$$S_\phi^{(m)}(\omega) = \frac{2}{qRN^2\,\Gamma_c}\,. \tag{8.4}$$

### 8.5.2 Phase Diffusion

In addition to measurement noise, the collective Bloch vector's quantum phase $\phi(t)$ diffuses with time as a result of quantum noise in the repumping process, the same mechanism that sets the Schawlow-Townes frequency linewidth limit in a bad-cavity laser or maser [92, 97, 115]. As a result, values of $\phi(t)$ at different times are less correlated with one another as the time separation grows. Specifically, the two-time phase difference (as measured in an appropriate rotating frame) averaged over many trials is zero $\langle \phi(t+\tau) - \phi(t)\rangle = 0$, but the variance of the phase difference grows linearly with the time difference $\tau$ as

$$\sigma_D^2(\tau) = \left\langle (\phi(t+\tau) - \phi(t))^2 \right\rangle = D^2\,|\tau| \tag{8.5}$$

The phase diffusion coefficient $D$ for the superradiant source can be derived from the expectation value of the two-time raising and lowering atomic operator $\langle \sigma_+(t+\tau)\sigma_-(t)\rangle$ in Ref. [114] and is

$$D^2 = \Gamma_c\left(1 + \frac{2w}{N\Gamma_c}\right) \tag{8.6}$$

Assuming operation at the repumping rate $w_{\mathrm{pk}}$ one finds $D^2 = 2\Gamma_c$. For the Kalman filter analysis to follow, we utilize the PSD of frequency fluctuations defined as

$$S_f^{(p)}(\omega) = \int_{-\infty}^{\infty} \left\langle \dot{\phi}(t+\tau)\dot{\phi}(t) \right\rangle \cos(\omega\tau)\ d\tau \tag{8.7}$$

for the process noise. From Eq. 8.5 and 8.7, one simply finds $S_f^{(p)}(\omega) = D^2$.

### 8.5.3 Optimal Phase Estimation with Kalman Filter

The Kalman filter [81, 82, 169] is designed to provide an optimal estimate $\phi_e(t)$ of the phase $\phi(t)$ that minimizes the mean squared error in the estimate $\sigma_e^2 = \left\langle (\phi_e(t) - \phi(t))^2 \right\rangle$. The Kalman filter assumes the state model and noise sources are well known, and the that the process noise and measurement noise are uncorrelated, an assumption we verify by extending the theoretical work of Ref. [92] to the spectrum of phase fluctuations in a homodyne measurement.

For this simple case, the optimal Kalman filter takes the form of a single pole low-pass filter. In the time domain, this is equivalent to an exponential weighting of the measurement record characterized by the exponential time constant $\tau_W$. The time constant is the inverse of the Kalman gain $K$, which is calculated in steady state by a ratio of the noise power spectral densities

$$\tau_W = \frac{1}{K} = \left( \frac{S_\phi^{(m)}(\omega)}{S_f^{(p)}(\omega)} \right)^{1/2} = \frac{1}{\sqrt{q} N \Gamma_c}\,, \tag{8.8}$$

assuming $w = w_{\mathrm{pk}}$. The optimal estimate is then the exponentially weighted average $\phi_e(t) = \frac{1}{\tau_W} \int_{-\infty}^{t} \psi\left(t'\right) e^{-(t-t')/\tau_W} \mathrm{d}t'$.

The mean squared error in the optimal estimate is given by the geometric mean of the noise spectral densities

$$\sigma_e^2 = \left( S_f^{(p)}(\omega) S_\phi^{(m)}(\omega) \right)^{1/2} = \frac{2}{\sqrt{q} N} \tag{8.9}$$

Here we simply considered portions of the measurement record $\psi(t)$ at times $t \leq t_\circ$, as this is the only information actually available were the superradiance to be shut off at time $t_\circ$ as part of a

Ramsey-like measurement. Conversely, an estimator of the phase just after superradiance is turned back on $\phi_e(t_\circ + T)$ will only include the measurement record at times $t \geq t_\circ + T$. The symmetry of the two noise processes with respect to time reversal makes it sufficient to consider only the first case.

### 8.5.4 Modifications for Experimental Conditions

To obtain a prediction for $\sigma_e^2$ observed here, we must also consider the modifications to $S_\phi^{(m)}(\omega)$ and $S_f^{(p)}(\omega)$ due to imperfections in our experiment. The general superradiant emission rate, Eq. 8.3, clearly modifies $S_\phi^{(m)}(\omega)$ in Eq. 8.4. However, $S_f^{(p)}(\omega)$, given by the phase diffusion of the Schawlow-Townes limit, is also modified. As $S_f^{(p)}(\omega)$ corresponds to the full width at half maximum (FWHM) of the laser linewidth [114], we estimate the general form of the linewidth using Ref. [97]

$$\Delta f_{\text{FWHM}} = \frac{1}{4\pi}\frac{w^2}{R_d}n_{\text{inv}} \tag{8.10}$$

to calculate the modified $S_f^{(p)}(\omega)$. Here, $n_{\text{inv}} = \frac{N_\uparrow}{N_\uparrow - N_\downarrow}$ is an inversion factor that depends on $w$ and $R$ through $N_\uparrow$ and $N_\downarrow$, the steady-state populations of $|\uparrow\rangle$ and $|\downarrow\rangle$ respectively. After simplification, $S_f^{(p)}(\omega)$ reduces to

$$S_f^{(p)}(\omega) = \Gamma_c\left(\frac{3}{2} + \frac{1}{R(\frac{N\Gamma_c}{w} - 1)}\right) \ . \tag{8.11}$$

## 8.6 Prediction of Time to Return to Steady-state Superradiant Emission

To predict the time to restore the superradiant emission to steady state, characterized by $t_{80}$ in the main text, we begin with a model based on semi-classical optical Bloch equations for the collective Bloch vector [114]. The cavity mode is adiabatically eliminated from the set of equations, justified by the cavity damping rate exceeding all other relevant rates in the system. We extend the model to include the full ground hyperfine structure of $^{87}$Rb, which requires repumping lasers on both the $|F=1\rangle \rightarrow |F'=2\rangle$ transition and the $|F=2\rangle \rightarrow |F'=2\rangle$ transition to return atoms from $|\downarrow\rangle$ to $|\uparrow\rangle$. We also account for the Raman transition in our system by adiabatically eliminating the intermediate excited state and defining a two-photon atom cavity coupling $g_2$ as described in Ref. [24]. The model is similar to the cold atom laser in Ref. [156], except that in this work, the cavity decay rate $\kappa$ is much greater than the atomic coherence decay rate $\gamma_\perp \approx w/2$. Compared to the cold atom lasers in Ref. [73, 64], the atomic decoherence rate is much smaller here, because the atoms are confined in a far detuned optical lattice instead of a MOT. Also, here the lasing occurs via a Raman transition between the magnetic field insensitive ground hyperfine states $|\uparrow\rangle = |F=2, m_F=0\rangle$ and $|\downarrow\rangle = |F=1, m_F=0\rangle$, as opposed to different Zeeman states.

To find the characteristic rise time $t_{80}(T)$ as a function of the evolution time $T$, we first solve the system of differential equations under steady-state conditions with the values of $N$, $\Gamma_c$, $w$, and $R$ calculated from the measured shift of the cavity mode and laser powers in our experiment. We then assume that during the dark evolution time all populations remain at their original steady-state values, but that the collective coherence is reduced with respect to the original steady-state coherence $\bar{J}_\perp$ as $J_\perp(T) = c(T)\bar{J}_\perp$, where $c(T)$ is the fractional reduction in the Ramsey contrast fringe measured using traditional microwave spectroscopy and population readout shown in Fig. 3b in the main text. The loss of contrast $c(T)$ is consistent with dephasing caused by differential ac Stark shifts experienced by the trapped atoms [96]. To model the behavior once the coupling is restored at time $T$, we use the steady-state populations and modified coherence $J_\perp(T)$ as initial conditions to numerically integrate the equations and extract a predicted value of $t_{80}$.

# Chapter 9

# Summary and Conclusion

## 9.1 Summary of Results

Throughout this thesis, we have leveraged the additional degree of freedom present in the atom-atom interactions of a large atomic ensemble to generate useful collective states for enhancing precision measurements. Though my work has taken the form of two separate projects over the course of my thesis, both projects are connected by the use of an optical cavity mode as the medium through which the atoms interact.

In Chapter 3, I presented coherence preserving, non-demolition measurements of $4.8 \times 10^5$ $^{87}$Rb atoms using their collective coupling to the optical cavity. The combination of the high measurement precision, more than 12 dB below the projection noise limit, and the reduced measurement back-action enabled by probing on an atomic cycling transition resulted in an ensemble with directly observed phase resolution 10.2(6) dB better in variance than the SQL. By probing the atoms on the $F = 2$ to $F = 3'$ cycling transition, nearly eliminating the Raman spin flip noise that limited our previous attempts to generate spin squeezed states to an equivalent squeezing of 1.1(4) dB [35].

Our measurements of spin flips indicate that they are no longer the limitation in our $^{87}$Rb system, and we have uncovered previously ignored forms of measurement back-action, such as photon recoil heating and opto-mechanical motion.

The other collective phenomena investigated in this thesis is steady-state, collective emission in the superradiant Raman laser. In Chapter 4, I gave a semi-classical model for the superradiant laser including important extensions beyond the model presented in Refs. [115, 33]. Specifically, I included an additional state for the atoms to be repumped through, additional decoherence from the repumping process, and a detuning of the cavity from the emission frequency. Additionally, I motivated the use of the Raman system as a good model for future optical superradiant lasers by doing a explicit adiabatic elimination of the optically excited state in the Raman system, showing it can be reduced to an effective two level system.

The extensions presented in Chapter 4 were key for understanding the experimental results in Chapter 5, where we experimentally realized the first steady-state Raman laser operating deep in the superradiant regime. Using the ensemble of laser cooled and trapped atoms as the gain medium for the laser, we could operate the Raman laser with a ratio of $2\gamma_\perp/\kappa = 5 \times 10^{-5}$. As a result, we observed steady-state lasing and linewidth narrowing even with $< 1$ photon in the optical cavity on average. We also confirmed the prediction that the sensitivity of the laser emission frequency to the cavity frequency should be reduced by $2\gamma_\perp/\kappa$, a crucial feature of superradiant lasers for getting ultrastable optical frequency sources out of stable laboratory environments. Although we were unable to observe the predicted quantum-limited linewidth, we were able to observe spectral features indicating a linewidth below that set by the single particle excited state decay rate, indicating that the collective coherence is driving the coherence of the laser.

Further work in understanding the stability of the laser lead to the results in Chapter 7, where we experimentally investigated the sensitivity of the superradiant Raman laser to fluctuations in the repumping rate by modulating the repumping beam power. We showed that the laser amplitude stability is sensitive how much of the atomic population remains in ground and excited states where the coherence is stored, which we associated with the repumping efficiency. We also investigated a cavity feed-back mechanism by which fluctuations in the ground and excited state populations cause a shift in the cavity mode, and therefore modify the collective coupling. We experimentally demonstrated that this cavity feedback could act to both stabilize the output amplitude or destabilize the system. Finally, using the non-demolition measurement techniques similar to those described in Chapter 3, we were able to gain a unique view of the state of the laser, going beyond just observing the output light and observing the inversion and polarization of the gain medium as well. The using theory laid out in Chapter 6, we could understand all these experimental results in the context of a simple linear response theory. In the future, this linear response theory will be useful for designing superradiant lasers with robust amplitude stability and may help us understand the impact of quantum noise in the repumping process on the phase noise spectrum of a superradiant laser.

Finally, in Chapter 8, I presented a new conceptual view of the superradiant Raman laser, treating it not only as a stable optical frequency source but as a non-demolition mapping of a quantum phase onto the cavity light field phase. This concept of a superradiant laser naturally leads to the question "What is the fundamental precision of the non-demolition mapping?" We theoretically show in this chapter that the fundamental precision is set by the SQL for phase estimation of the coherent spin state, linking the quantum limited linewidth of the laser to atomic projection noise. Combining this superradiant mapping with the ability to dynamically switch on and off the superradiant emission with the Raman dressing laser, we experimentally explore the idea of a hybrid atomic sensor that combines periods of high bandwidth readout of the atomic phase with high accuracy phase measurements using a Ramsey-like sequence. We also observed the decay and re-establishment of atomic coherence during the mapping. Unlike other non-demolition measurements, the superradiant mapping actively establishes coherence during the measurement.

## 9.2 Looking Forward

The concluding message from this thesis is that the future looks promising for using these collective states as tools for precision measurements. As this thesis has shown, effective interactions generated by collective coupling to an optical cavity is particularly well-suited for implementation in precision measurement experiments.

In the case of generating squeezed states, our work demonstrated a large spectroscopic enhancement in an ensemble of cold atoms trapped in an optical lattice, a system very applicable to one of the premier precision measurement devices today, the optical lattice atomic clock. The experimental demonstration of more than an order of magnitude observed enhancement is a true leap forward for quantum measurement science, indicating that entanglement-enhanced spectroscopy has real relevance for future work. Though our technique requires the use of a cycling transition for probing the atoms, current optical clock candidates like Sr or Yb have a readily available, nearly cycling transition in the $^1S_0$ to $^1P_1$ transition. The factor of 10 enhancement in spectroscopic sensitivity represents a real resource for these atomic sensors, in that it is currency that can be spent either improving the precision, accuracy and/or bandwidth. One example would be using a factor of 10 less atoms to achieve the same phase sensitivity while reducing collisional perturbations. In that case, entanglement-enhanced spectroscopic sensitivity is used to reduce a systematic error instead of improving the sensor's precision.

The order of magnitude improvement observed in our experiments is not the fundamental limit possible for our collective pre-measurement scheme. As discussed in Chapter 3, one of the primary limitations is that the effective probe detection efficiency is only $\sim 8\%$. With a few modifications to the apparatus, it should be possible to approach a factor of 100 spectroscopic enhancement in essentially the same system. To address the poor detection efficiency, in the future clean mirrors should be installed and periodically heated to keep rubidium from spoiling their finesse. Furthermore, an single sided cavity (i.e. a cavity with asymmetric transmission properties) could be used to implement a high efficiency homodyne detection in reflection where path lengths can be better stabilized. To realize a factor of 100 in spectroscopic enhancement, we also need narrower linewidth probe lasers, which could be obtained by locking to a stable optical cavity reference. Going further, the sources of measurement induced back-action uncovered in our work will need to be further investigated and understood. For example, opto-mechanical forces associated with the probing appeared significant in our work, and exploring adiabatic turn on and off of the probe may be useful in reducing the impact of the atomic motion on the collective measurement.

Precise non-demolition measurements are also useful in implementing quantum feedback schemes. One possibility going forward is that these precise, non-destructive measurements can be used after a Ramsey sequence to reposition a squeezed state along the equator of the Bloch

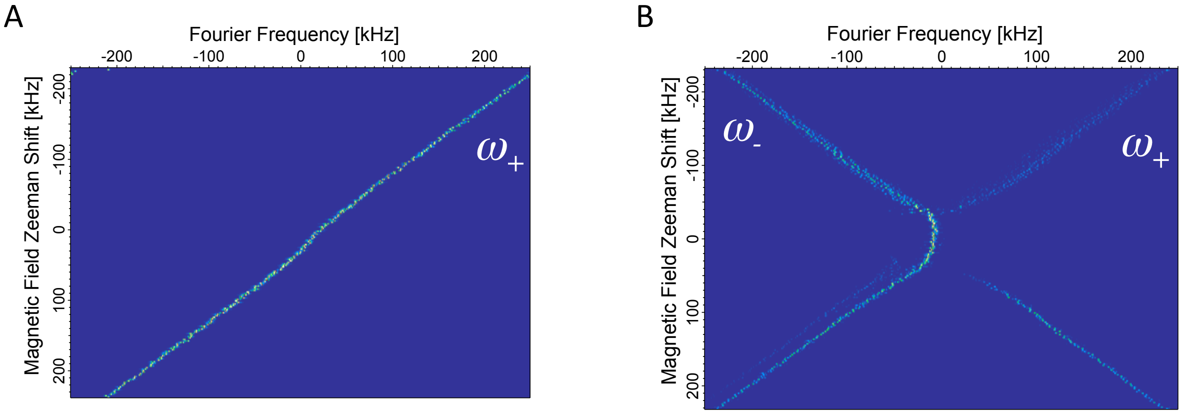

Figure 9.1: Frequency spectrums (horizontal axis) of the superradiantly emitted light, shown as a function of an applied magnetic field (vertical axis) that tunes the lasing transition frequency. Warmer colors indicate more power at a particular frequency. With the atomic ensembles pumping to magnetic field sensitive hyperfine states, as in the secondary configuration discussed in Chapter 5, Sec. 5.6, the laser emission frequency can be controlled with the magnetic field. (A) In the case where all atoms are optically pumped to the same state $F = 2$, $m_F = +2$ (see Fig 9.2a), the laser emission frequency follows nearly linearly with the change in the transition frequency. (B) When two ensembles are pumped to the opposite Zeeman states $F = 2$, $m_F = +2$ and $m_F = -2$, we can observe two distinct superradiant emission frequencies, each associated with one ensemble. As the magnetic field is tuned to bring the laser emission frequencies closer to degeneracy, the ensembles begin to synchronize and eventually lock up, even though their transition frequencies may not exactly the same.

sphere, thus allowing the atomic sensor to circumvent the limitations to spectroscopic enhancement imposed by the curvature of the Bloch sphere [3]. Future work in our system could explore the feasibility of these quantum feedback techniques.

Our work also continues to investigate other collective states with interesting applications for atomic sensors. One example is experiments first conceived during the spin squeezing experiments of Chapter 3 in which state rotation noise could be mitigated by applying controlled dephasing to the ensemble. This work was further developed during the writing of this thesis by colleages in the lab. This use of controlled dephasing is also related to recent theoretical work proposing the enhancement of evolution times in Ramsey spectroscopy using dephased states [121].

Our work with a steady-state superradiant Raman laser investigated an interesting and unusual regime of laser physics, but also serves as an important test bed for future superradiant light

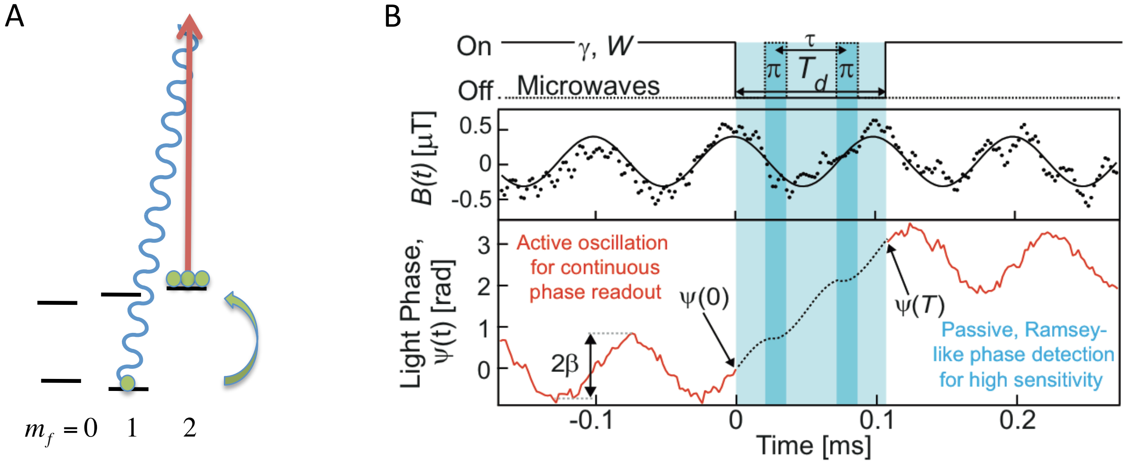

Figure 9.2: Results from a demonstration of a superradiant magnetometer [160]. (A) By operating the superradiant Raman laser in the secondary configuration described in in Chapter 5, Sec. 5.6, the laser emission frequency is sensitive to a magnetic field. (B) We can continuously readout the effects of the oscillating magnetic field applied in the lab during superradiant emission by observing the phase of the emitted light (red). However, for high frequency modulations, a large phase deviation has no time to accumulate, reducing the signal and thus the sensitivity of the magnetometer. By turning off the superradiant emission (blue region), and applying microwave $\pi$ pulses that coincide with the know frequency of magnetic field oscillations, the phase accumulated by the atoms can build up. Then at a later time, the superradiance can be restored and magnetic field can be inferred from the difference in the light phase before and after the turn off. The 'lock-in' detection scheme can theoretically recover the DC sensitivity of the magnetometer.

sources. This thesis presents a promising path forward as we were able to confirm a number of key predictions relevant for future superradiant lasers, such as steady state collective emission and reduced cavity pulling. Our work with the model system has also informed the design of future superradiant lasers. Cavity pulling can still have a significant impact on the laser emission frequency, as seen by the limitation to the observed linewidth in our system. Additionally, the loss of atoms from the trap in our system highlights the need to replenish the ensemble. Schemes with moving optical lattices or continuous atom lasers [147] could be used in the future for reloading the trap. A truly continuous light source will be useful in observing the narrow predicted quantum-limited linewidth that we were unable to observe.

Future work continues in our model system aimed at understanding the role of synchronization in the superradiant laser. Partially motivated by the question of mode competition on multiple transitions in a future superradiant laser, we have developed a scheme in which two spatially separated ensembles act as independent superradiant lasers in the same optical cavity. By independently controlling the lasing frequencies of each ensemble, we can tune the system from a single synchronized ensemble into two independent ensembles, as shown in Fig. 9.1. Recent theoretical work [166] has also investigated this transition, finding interesting connections to phase transitions in open quantum systems. The flexibility and tunability of the superradiant Raman system may provide a good experimental system to investigate aspects of quantum phase transitions in open systems like an optical cavity. Already we have made technical improvements to the experimental apparatus to realize this goal, implementing spatially separated dressing beams to individually control the lasing frequencies.

Our work investigating the dynamic superradiant mapping of atomic coherence onto the cavity field also offers another avenue of future study, as it broadens the idea of what superradiant emission can be harnessed to accomplish. This work emphasizes the idea that the coherence of the laser is stored in the atomic gain medium. This represents yet another new set of possibilities for use in precision measurements because now essentially the laser coherence can be manipulated with all the tools that have been developed for controlling atomic states. In particular, we demonstrated this idea by creating a magnetometer with a superradiant readout out that operate both in a continuous, wideband readout mode or high sensitivity, lock-in detection configuration [160]. The basic idea is illustrated in Fig. 9.2. Ultimately, this work points toward a future in which superradiant lasers can act as both an absolute atomic reference and a frequency source with good short term stability as the detected cavity field is directly phase locked to the atomic reference.

# Bibliography

[1] J Aasi, J Abadie, BP Abbott, R Abbott, TD Abbott, MR Abernathy, C Adams, T Adams, P Addesso, RX Adhikari, et al. Enhanced sensitivity of the ligo gravitational wave detector by using squeezed states of light. Nature Photonics, 7(8):613–619, 2013.

[2] J Abadie, BP Abbott, R Abbott, TD Abbott, M Abernathy, C Adams, R Adhikari, C Affeldt, B Allen, GS Allen, et al. A gravitational wave observatory operating beyond the quantum shot-noise limit. Nat. Phys., 7(12):962–965, 2011.

[3] A. André, A. S. Sørensen, and M. D. Lukin. Stability of atomic clocks based on entangled atoms. Phys. Rev. Lett., 92:230801, Jun 2004.

[4] J. Appel, P.J. Windpassinger, D. Oblak, U.B. Hoff, N. Kjærgaard, and E.S. Polzik. Mesoscopic atomic entanglement for precision measurements beyond the standard quantum limit. Proc. Natl. Acad. Sci., 106(27):10960–10965, 2009.

[5] MD Barrett, J Chiaverini, T Schaetz, J Britton, WM Itano, JD Jost, E Knill, C Langer, D Leibfried, R Ozeri, et al. Deterministic quantum teleportation of atomic qubits. Nature, 429(6993):737–739, 2004.

[6] Quentin Baudouin, Nicolas Mercadier, Vera Guarrera, William Guerin, and Robin Kaiser. A cold-atom random laser. Nat. Phys., 9:357–360, 2013.

[7] K. Baumann, C. Guerlin, F. Brennecke, and T. Esslinger. Dicke quantum phase transition with a superfluid gas in an optical cavity. Nature, 464(9):1301, Apr 2010.

[8] D. Bear, R. E. Stoner, R. L. Walsworth, V. Alan Kostelecký, and Charles D. Lane. Limit on lorentz and $CPT$ violation of the neutron using a two-species noble-gas maser. Phys. Rev. Lett., 85:5038–5041, Dec 2000.

[9] Karim Benmessai, Daniel Creedon, Michael Tobar, Pierre-Yves Bourgeois, Yann Kersalé, and Vincent Giordano. Measurement of the fundamental thermal noise limit in a cryogenic sapphire frequency standard using bimodal maser oscillations. Phys. Rev. Lett., 100(23):233901–233904, Jun 2008.

[10] G. W. Biedermann, X. Wu, L. Deslauriers, K. Takase, and M. A. Kasevich. Low-noise simultaneous fluorescence detection of two atomic states. Opt. Lett., 34(3):347–349, Feb 2009.

[11] S Bize, P Laurent, M Abgrall, H Marion, I Maksimovic, L Cacciapuoti, J Grünert, C Vian, F Pereira dos Santos, P Rosenbusch, P Lemonde, G Santarelli, P Wolf, A Clairon, A Luiten, M Tobar, and C Salomon. Cold atom clocks and applications. J. Phys. B: At., Mol. Opt. Phys., 38(9):S449, 2005.

[12] Gunnar Björk, Henrich Heitmann, and Yoshihisa Yamamoto. Spontaneous-emission coupling factor and mode characteristics of planar dielectric microcavity lasers. Phys. Rev. A, 47(5):4451–4463, May 1993.

[13] Adam T. Black, Hilton W. Chan, and Vladan Vuletić. Observation of collective friction forces due to spatial self-organization of atoms: from rayleigh to bragg scattering. Phys. Rev. Lett., 91(20):203001, Nov 2003.

[14] Eric D Black. An introduction to pound–drever–hall laser frequency stabilization. American Journal of Physics, 69:79, 2001.

[15] R. Blatt and C. F. Roos. Quantum simulations with trapped ions. Nat. Phys., 8(4):277–284, April 2012.

[16] S. Blatt, A. D. Ludlow, G. K. Campbell, J. W. Thomsen, T. Zelevinsky, M. M. Boyd, J. Ye, X. Baillard, M. Fouché, R. Le Targat, A. Brusch, P. Lemonde, M. Takamoto, F.-L. Hong, H. Katori, and V. V. Flambaum. New limits on coupling of fundamental constants to gravity using $^{87}$sr optical lattice clocks. Phys. Rev. Lett., 100(14):140801, Apr 2008.

[17] S. Blatt, A. D. Ludlow, G. K. Campbell, J. W. Thomsen, T. Zelevinsky, M. M. Boyd, J. Ye, X. Baillard, M. Fouché, R. Le Targat, A. Brusch, P. Lemonde, M. Takamoto, F.-L. Hong, H. Katori, and V. V. Flambaum. New limits on coupling of fundamental constants to gravity using $^{87}$sr optical lattice clocks. Phys. Rev. Lett., 100(14):140801, Apr 2008.

[18] Immanuel Bloch, Jean Dalibard, and Sylvain Nascimbène. Quantum simulations with ultracold quantum gases. Nat. Phys., 8(4):267–276, April 2012.

[19] B. J. Bloom, T. L. Nicholson, J. R. Williams, S. L. Campbell, M. Bishof, X. Zhang, W. Zhang, S. L. Bromley, and J. Ye. A new generation of atomic clocks: Accuracy and stability at the $10^{-18}$ level. ArXiv e-prints, September 2013.

[20] J. Bochmann, M. Mücke, C. Guhl, S. Ritter, G. Rempe, and D. L. Moehring. Lossless state detection of single neutral atoms. Phys. Rev. Lett., 104:203601, May 2010.

[21] J. G. Bohnet, Z. Chen, J. M. Weiner, K. C. Cox, and J. K. Thompson. Relaxation oscillations, stability, and cavity feedback in a superradiant raman laser. Phys. Rev. Lett., 109:253602–253606, Dec 2012.

[22] J. G. Bohnet, K. C. Cox, M. A. Norica, J. M. Weiner, and J. K. Thompson. Reduced back-action for phase sensitivity 10 times beyond the standard quantum limit. 2013.

[23] Justin G. Bohnet, Zilong Chen, Joshua M. Weiner, Kevin C. Cox, and James K. Thompson. Active and passive sensing of collective atomic coherence in a superradiant laser. Phys. Rev. A, 88:013826, Jul 2013.

[24] Justin G. Bohnet, Zilong Chen, Joshua M. Weiner, Dominic Meiser, Murray J. Holland, and James K. Thompson. A steady-state superradiant laser with less than one intracavity photon. Nature, 484(6):78–81, 2012.

[25] A. D. Boozer, A. Boca, R. Miller, T. E. Northup, and H. J. Kimble. Reversible state transfer between light and a single trapped atom. Phys. Rev. Lett., 98:193601, May 2007.

[26] Vladimir B. Braginsky, Yuri I. Vorontsov, and Kip S. Thorne. Quantum nondemolition measurements. Science, 209(4456):547–557, 1980.

[27] E Brion, L H Pedersen, and K Mølmer. Adiabatic elimination in a lambda system. J. Phys. A, 40(5):1033, 2007.

[28] Robert Bücker, Julian Grond, Stephanie Manz, Tarik Berrada, Thomas Betz, Christian Koller, Ulrich Hohenester, Thorsten Schumm, Aurélien Perrin, and Jörg Schmiedmayer. Twin-atom beams. Nat. Phys., 7(8):608–611, 2011.

[29] G. K. Campbell, M. M. Boyd, J. W. Thomsen, M. J. Martin, S. Blatt, M. D. Swallows, T. L. Nicholson, T. Fortier, C. W. Oates, S. A. Diddams, N. D. Lemke, P. Naidon, P. Julienne, Jun Ye, and A. D. Ludlow. Probing interactions between ultracold fermions. Science, 324(5925):360–363, 2009.

[30] L. Casperson. Spontaneous coherent pulsations in laser oscillators. Quantum Electronics, IEEE Journal of, 14(10):756 – 761, oct 1978.

[31] Carlton M. Caves. Quantum-mechanical noise in an interferometer. Phys. Rev. D, 23:1693–1708, Apr 1981.

[32] Hilton W. Chan, Adam T. Black, and Vladan Vuletić. Observation of collective-emission-induced cooling of atoms in an optical cavity. Phys. Rev. Lett., 90:063003, Feb 2003.

[33] JingBiao Chen. Active optical clock. Chinese Science Bulletin, 54:348–352, 2009.

[34] Z. Chen, J. G. Bohnet, J. M. Weiner, K. C. Cox, and J. K. Thompson. Cavity-aided non-demolition measurements for atom counting and spin squeezing. arXiv preprint arXiv:1211.0723, 2012.

[35] Zilong Chen, Justin G. Bohnet, Shannon R. Sankar, Jiayan Dai, and James K. Thompson. Conditional spin squeezing of a large ensemble via the vacuum rabi splitting. Phys. Rev. Lett., 106(13):133601–133604, Mar 2011.

[36] Zilong Chen, Justin G. Bohnet, Joshua M. Weiner, and James K. Thompson. A low phase noise microwave source for atomic spin squeezing experiments in 87Rb. Review of Scientific Instruments, 83(4):044701–044701–5, April 2012.

[37] K. S. Choi, A. Goban, S. B. Papp, S. J. van Enk, and H. J. Kimble. Entanglement of spin waves among four quantum memories. Nature, 468(7322):412–416, November 2010.

[38] C. W. Chou, D. B. Hume, T. Rosenband, and D. J. Wineland. Optical clocks and relativity. Science, 329(5999):1630–1633, 2010.

[39] Chin-Wen Chou, H De Riedmatten, D Felinto, SV Polyakov, SJ Van Enk, and H Jeff Kimble. Measurement-induced entanglement for excitation stored in remote atomic ensembles. Nature, 438(7069):828–832, 2005.

[40] Steven T. Cundiff and Jun Ye. *Colloquium*: Femtosecond optical frequency combs. Rev. Mod. Phys., 75:325–342, Mar 2003.

[41] J. Dalibard and C. Cohen-Tannoudji. Laser cooling below the doppler limit by polarization gradients: simple theoretical models. J. Opt. Soc. Am. B, 6(11):2023–2045, Nov 1989.

[42] C. Deutsch, F. Ramirez-Martinez, C. Lacroûte, F. Reinhard, T. Schneider, J. N. Fuchs, F. Piéchon, F. Laloë, J. Reichel, and P. Rosenbusch. Spin self-rephasing and very long coherence times in a trapped atomic ensemble. Phys. Rev. Lett., 105:020401, Jul 2010.

[43] R. H. Dicke. Coherence in spontaneous radiation processes. Phys. Rev., 93(1):99, Jan 1954.

[44] S. A. Diddams, J. C. Bergquist, S. R. Jefferts, and C. W. Oates. Standards of time and frequency at the outset of the 21st century. Science, 306(5700):1318–1324, 2004.

[45] S. A. Diddams, Th. Udem, J. C. Bergquist, E. A. Curtis, R. E. Drullinger, L. Hollberg, W. M. Itano, W. D. Lee, C. W. Oates, K. R. Vogel, and D. J. Wineland. An optical clock based on a single trapped 199hg+ ion. Science, 293(5531):825–828, 2001.

[46] R.W.P. Drever, J.L. Hall, F.V. Kowalski, J. Hough, G.M. Ford, A.J. Munley, and H. Ward. Laser phase and frequency stabilization using an optical resonator. Applied Physics B, 31(2):97–105, 1983.

[47] L.-M. Duan, M. D. Lukin, J. I. Cirac, and P. Zoller. Long-distance quantum communication with atomic ensembles and linear optics. Nature, 414(6862):413–418, November 2001.

[48] Kai Eckert, Oriol Romero-Isart, Mirta Rodriguez, Maciej Lewenstein, Eugene S Polzik, and Anna Sanpera. Quantum non-demolition detection of strongly correlated systems. Nat. Phys., 4(1):50–54, 2007.

[49] J. Esteve, C. Gross, A. Weller, S. Giovanazzi, and M. K. Oberthaler. Squeezing and entanglement in a bose-einstein condensate. Nature, 455:1216–1219, 2008.

[50] M. Evans, L. Barsotti, and P. Fritschel. A general approach to optomechanical parametric instabilities. Physics Letters A, 374(4):665 – 671, 2010.

[51] Richard P. Feynman, Frank L. Vernon, and Robert W. Hellwarth. Geometrical representation of the schrodinger equation for solving maser problems. J. Appl. Phys., 28(1):49 –52, jan 1957.

[52] J. M. Fink, R. Bianchetti, M. Baur, M. Göppl, L. Steffen, S. Filipp, P. J. Leek, A. Blais, and A. Wallraff. Dressed collective qubit states and the tavis-cummings model in circuit qed. Phys. Rev. Lett., 103:083601, Aug 2009.

[53] Jeff Flowers. The route to atomic and quantum standards. Science, 306(5700):1324–1330, 2004.

[54] Seth M. Foreman, Kevin W. Holman, Darren D. Hudson, David J. Jones, and Jun Ye. Remote transfer of ultrastable frequency references via fiber networks. Review of Scientific Instruments, 78(2):021101, 2007.

[55] T. M. Fortier, N. Ashby, J. C. Bergquist, M. J. Delaney, S. A. Diddams, T. P. Heavner, L. Hollberg, W. M. Itano, S. R. Jefferts, K. Kim, F. Levi, L. Lorini, W. H. Oskay, T. E. Parker, J. Shirley, and J. E. Stalnaker. Precision atomic spectroscopy for improved limits on variation of the fine structure constant and local position invariance. Phys. Rev. Lett., 98(7):070801, Feb 2007.

[56] A. Fuhrmanek, R. Bourgain, Y. R. P. Sortais, and A. Browaeys. Free-space lossless state detection of a single trapped atom. Phys. Rev. Lett., 106:133003, Mar 2011.

[57] Roger Gehr, Jürgen Volz, Guilhem Dubois, Tilo Steinmetz, Yves Colombe, Benjamin L. Lev, Romain Long, Jérôme Estève, and Jakob Reichel. Cavity-based single atom preparation and high-fidelity hyperfine state readout. Phys. Rev. Lett., 104:203602, May 2010.

[58] Michael J. Gibbons, Christopher D. Hamley, Chung-Yu Shih, and Michael S. Chapman. Nondestructive fluorescent state detection of single neutral atom qubits. Phys. Rev. Lett., 106:133002, Mar 2011.

[59] Nicolas Gisin, Grégoire Ribordy, Wolfgang Tittel, and Hugo Zbinden. Quantum cryptography. Rev. Mod. Phys., 74:145–195, Mar 2002.

[60] H. M. Goldenberg, D. Kleppner, and N. F. Ramsey. Atomic hydrogen maser. Phys. Rev. Lett., 5:361–362, Oct 1960.

[61] Joel A. Greenberg and Daniel J. Gauthier. Steady-state, cavityless, multimode superradiance in a cold vapor. Phys. Rev. A, 86:013823, Jul 2012.

[62] C. Gross, T. Zibold, E. Nicklas, J. Estève, and M.K. Oberthaler. Nonlinear atom interferometer surpasses classical precision limit. Nature, 464:1165–1169, 2010.

[63] M. Gross and S. Haroche. Superradiance: An essay on the theory of collective spontaneous emission. Physics Reports, 93(5):301 – 396, 1982.

[64] William Guerin, Franck Michaud, and Robin Kaiser. Mechanisms for lasing with cold atoms as the gain medium. Phys. Rev. Lett., 101(9):093002, Aug 2008.

[65] Christine Guerlin, Julien Bernu, Samuel Deleglise, Clement Sayrin, Sebastien Gleyzes, Stefan Kuhr, Michel Brune, Jean-Michel Raimond, and Serge Haroche. Progressive field-state collapse and quantum non-demolition photon counting. Nature, 448(7156):889–893, 2007.

[66] T. L. Gustavson, P. Bouyer, and M. A. Kasevich. Precision rotation measurements with an atom interferometer gyroscope. Phys. Rev. Lett., 78:2046–2049, Mar 1997.

[67] H. Haken. Analogy between higher instabilities in fluids and lasers. Phys. Lett. A, 53(1):77 – 78, 1975.

[68] J. L. Hall, L. Hollberg, T. Baer, and H. G. Robinson. Optical heterodyne saturation spectroscopy. Applied Physics Letters, 39(9):680–682, 1981.

[69] Chris D. Hamley, C. S. Gerving, T. M. Hoang, E. M. Bookjans, and Michael S. Chapman. Spin-nematic squeezed vacuum in a quantum gas. Nat. Phys., 8(4):305–308, February 2012.

[70] R. G. Harrison and D. J. Biswas. Demonstration of self-pulsing instability and transitions to chaos in single-mode and multimode homogeneously broadened raman laser. Phys. Rev. Lett., 55:63–66, Jul 1985.

[71] Peter F Herskind, Aurélien Dantan, Joan P Marler, Magnus Albert, and Michael Drewsen. Realization of collective strong coupling with ion coulomb crystals in an optical cavity. Nature Physics, 5(7):494–498, 2009.

[72] Peter F. Herskind, Aurelien Dantan, Joan P. Marler, Magnus Albert, and Michael Drewsen. Realization of collective strong coupling with ion coulomb crystals in an optical cavity. Nat. Phys., 5(7):494–498, July 2009.

[73] L. Hilico, C. Fabre, and E. Giacobino. Operation of a "cold-atom laser" in a magneto-optical trap. Europhys. Lett., 18(8):685, 1992.

[74] N. Hinkley, J. A. Sherman, N. B. Phillips, M. Schioppo, N. D. Lemke, K. Beloy, M. Pizzocaro, C. W. Oates, and A. D. Ludlow. An atomic clock with 1018 instability. Science, 341(6151):1215–1218, 2013.

[75] JJ Hudson, DM Kara, IJ Smallman, BE Sauer, MR Tarbutt, and EA Hinds. Improved measurement of the shape of the electron. Nature, 473(7348):493–496, 2011.

[76] WM Itano, JC Bergquist, JJ Bollinger, JM Gilligan, DJ Heinzen, FL Moore, MG Raizen, and DJ Wineland. Quantum projection noise: population fluctuations in two-level systems. Phys. Rev. A, 47(5):3554, 1993.

[77] E.T. Jaynes and F.W. Cummings. Comparison of quantum and semiclassical radiation theories with application to the beam maser. Proceedings of the IEEE, 51(1):89–109, 1963.

[78] Y. Y. Jiang, A. D. Ludlow, N. D. Lemke, R. W. Fox, J. A. Sherman, L.-S. Ma, and C. W. Oates. Making optical atomic clocks more stable with $10^{-16}$-level laser stabilization. Nat. Photon., 5:158, Mar 2011.

[79] L Ju, D G Blair, C Zhao, S Gras, Z Zhang, P Barriga, H Miao, Y Fan, and L Merrill. Strategies for the control of parametric instability in advanced gravitational wave detectors. Classical Quantum Gravity, 26(1):015002, 2009.

[80] Brian Julsgaard, Jacob Sherson, J Ignacio Cirac, Jaromir Fiurášek, and Eugene S Polzik. Experimental demonstration of quantum memory for light. Nature, 432(7016):482–486, 2004.

[81] R. E. Kalman. A new approach to linear filtering and prediction problems. Journal of Basic Engineering, 82(Series D):35–45, 1960.

[82] R. E. Kalman and R. S. Bucy. New results in linear filtering and prediction theory. Journal of Basic Engineering, 83(Series D):95–107, 1961.

[83] Savely G. Karshenboim. Precision physics of simple atoms: {QED} tests, nuclear structure and fundamental constants. Physics Reports, 422(1):1 – 63, 2005.

[84] T. Kessler, C. Hagemann, C. Grebing, T. Legero, U. Sterr, F. Riehle, M. J. Martin, L. Chen, and J. Ye. A sub-40-mhz-linewidth laser based on a silicon single-crystal optical cavity. Nat. Photon., 6(10):687–692, Sept 2012.

[85] H J Kimble. Strong interactions of single atoms and photons in cavity qed. Physica Scripta, 1998(T76):127, 1998.

[86] T. J. Kippenberg and K. J. Vahala. Cavity optomechanics: Back-action at the mesoscale. Science, 321(5893):1172–1176, 2008.

[87] Masahiro Kitagawa and Masahito Ueda. Squeezed spin states. Phys. Rev. A, 47:5138–5143, Jun 1993.

[88] Masahiro Kitagawa and Masahito Ueda. Squeezed spin states. Phys. Rev. A, 47:5138–5143, Jun 1993.

[89] John Kitching, Svenja Knappe, and Elizabeth A. Donley. Atomic sensors: a review. IEEE Sensors J., 11(9):1749–1758, September 2011.

[90] Daniel Kleppner, H. Mark Goldenberg, and Norman F. Ramsey. Theory of the hydrogen maser. Phys. Rev., 126:603–615, Apr 1962.

[91] Pieter Kok, W. J. Munro, Kae Nemoto, T. C. Ralph, Jonathan P. Dowling, and G. J. Milburn. Linear optical quantum computing with photonic qubits. Rev. Mod. Phys., 79:135–174, Jan 2007.

[92] M. I. Kolobov, L. Davidovich, E. Giacobino, and C. Fabre. Role of pumping statistics and dynamics of atomic polarization in quantum fluctuations of laser sources. Phys. Rev. A, 47:1431–1446, Feb 1993.

[93] I K Kominis, T W Kornack, J C Allred, and M V Romalis. A subfemtotesla multichannel atomic magnetometer. Nature, 422(6932):596–9, April 2003.

[94] D. Kruse, C. von Cube, C. Zimmermann, and Ph. W. Courteille. Observation of lasing mediated by collective atomic recoil. Phys. Rev. Lett., 91:183601, Oct 2003.

[95] Y. Kubo, F. R. Ong, P. Bertet, D. Vion, V. Jacques, D. Zheng, A. Dréau, J.-F. Roch, A. Auffeves, F. Jelezko, J. Wrachtrup, M. F. Barthe, P. Bergonzo, and D. Esteve. Strong coupling of a spin ensemble to a superconducting resonator. Phys. Rev. Lett., 105:140502, Sep 2010.

[96] S. Kuhr, W. Alt, D. Schrader, I. Dotsenko, Y. Miroshnychenko, A. Rauschenbeutel, and D. Meschede. Analysis of dephasing mechanisms in a standing-wave dipole trap. Phys. Rev. A, 72:023406, Aug 2005.

[97] S. J. M. Kuppens, M. P. van Exter, and J. P. Woerdman. Quantum-limited linewidth of a bad-cavity laser. Phys. Rev. Lett., 72:3815–3818, Jun 1994.

[98] S.J.M Kuppens, M.P van Exter, J.P Woerdman, and M.I Kolobov. Observation of the effect of spectrally inhomogeneous gain on the quantum-limited laser linewidth. Opt. Commun., 126(1-3):79–84, 1996.

[99] A. Kuzmich, N. P. Bigelow, and L. Mandel. Atomic quantum non-demolition measurements and squeezing. Europhysics Letters, 42(5):481, 1998.

[100] Thaddeus D Ladd, Fedor Jelezko, Raymond Laflamme, Yasunobu Nakamura, Christopher Monroe, and Jeremy L OBrien. Quantum computers. Nature, 464(7285):45–53, 2010.

[101] A. Lambrecht, J. M. Courty, S. Reynaud, and E. Giacobino. Cold atoms: A new medium for quantum optics. Applied Physics B: Lasers and Optics, 60:129–134, 1995.

[102] Dietrich Leibfried, Emanuel Knill, Signe Seidelin, Joe Britton, R Brad Blakestad, John Chiaverini, Davi d B Hume, Wayne M Itano, John D Jost, Christopher Langer, et al. Creation of a six-atom schrödinger cat-state. Nature, 438(7068):639–642, 2005.

[103] David R. Leibrandt, Michael J. Thorpe, James C. Bergquist, and Till Rosenband. Field-test of a robust, portable, frequency-stable laser. Opt. Express, 19(11):10278–10286, May 2011.

[104] Ian D. Leroux, Monika H. Schleier-Smith, and Vladan Vuletić. Implementation of cavity squeezing of a collective atomic spin. Phys. Rev. Lett., 104:073602, Feb 2010.

[105] M. Lettner, M. Mücke, S. Riedl, C. Vo, C. Hahn, S. Baur, J. Bochmann, S. Ritter, S. Dürr, and G. Rempe. Remote entanglement between a single atom and a bose-einstein condensate. Phys. Rev. Lett., 106:210503, May 2011.

[106] Qian Lin, Mackenzie A. Van Camp, Hao Zhang, Branislav Jelenković, and Vladan Vuletić. Long-external-cavity distributed bragg reflector laser with subkilohertz intrinsic linewidth. Opt. Lett., 37(11):1989–1991, Jun 2012.

[107] Jérôme Lodewyck, Philip G. Westergaard, and Pierre Lemonde. Nondestructive measurement of the transition probability in a sr optical lattice clock. Phys. Rev. A, 79:061401–061404, Jun 2009.

[108] B Lücke, M Scherer, J Kruse, L Pezzé, F Deuretzbacher, P Hyllus, O Topic, J Peise, W Ertmer, J Arlt, L Santos, A Smerzi, and C Klempt. Twin matter waves for interferometry beyond the classical limit. Science, 334(6057):773–6, November 2011.

[109] A. D. Ludlow, T. Zelevinsky, G. K. Campbell, S. Blatt, M. M. Boyd, M. H. G. de Miranda, M. J. Martin, J. W. Thomsen, S. M. Foreman, Jun Ye, M. Fortier, J. E. Stalnaker, S. A. Diddams, Y. Le Coq, Z. W. Barber, N. Poli, N. D. Lemke, K. M. Beck, and C. W. Oates. Sr lattice clock at $1 \times 10^{-16}$ fractional uncertainty by remote optical evaluation with a ca clock. Science, 319(5871):1805–8, Mar 2008.

[110] D J McCarron, S A King, and S L Cornish. Modulation transfer spectroscopy in atomic rubidium. Measurement Science and Technology, 19(10):105601, 2008.

[111] D. E. McCumber. Intensity fluctuations in the output of cw laser oscillators i. Phys. Rev., 141:306–322, Jan 1966.

[112] J. McKeever, A. Boca, A .D. Boozer, J. R. Buck, and H. J. Kimble. Experimental realization of a one-atom laser in the regime of strong coupling. Nature, 425(16):268, Sept 2003.

[113] D. Meiser and M. J. Holland. Intensity fluctuations in steady-state superradiance. Phys. Rev. A, 81(6):063827, Jun 2010.

[114] D. Meiser and M. J. Holland. Steady-state superradiance with alkaline-earth-metal atoms. Phys. Rev. A, 81(3):033847, Mar 2010.

[115] D. Meiser, Jun Ye, D. R. Carlson, and M. J. Holland. Prospects for a millihertz-linewidth laser. Phys. Rev. Lett., 102(16):163601–163604, Apr 2009.

[116] V. Meyer, M. A. Rowe, D. Kielpinski, C. A. Sackett, W. M. Itano, C. Monroe, and D. J. Wineland. Experimental demonstration of entanglement-enhanced rotation angle estimation using trapped ions. Phys. Rev. Lett., 86:5870–5873, Jun 2001.

[117] Thomas Monz, Philipp Schindler, Julio T. Barreiro, Michael Chwalla, Daniel Nigg, William A. Coish, Maximilian Harlander, Wolfgang Hänsel, Markus Hennrich, and Rainer Blatt. 14-qubit entanglement: Creation and coherence. Phys. Rev. Lett., 106:130506, Mar 2011.

[118] T. L. Nicholson, M. J. Martin, J. R. Williams, B. J. Bloom, M. Bishof, M. D. Swallows, S. L. Campbell, and J. Ye. Comparison of two independent sr optical clocks with $1 \times 10^{-17}$ stability at $10^3$ s. Phys. Rev. Lett., 109:230801, Dec 2012.

[119] S Olmschenk, DN Matsukevich, P Maunz, D Hayes, L-M Duan, and C Monroe. Quantum teleportation between distant matter qubits. Science, 323(5913):486–489, 2009.

[120] Chad Orzel. Searching for new physics through atomic, molecular and optical precision measurements. Physica Scripta, 86(6):068101, 2012.

[121] Laurin Ostermann, Helmut Ritsch, and Claudiu Genes. Protected state enhanced quantum metrology with interacting two-level ensembles. Phys. Rev. Lett., 111:123601, Sep 2013.

[122] CP Pearman, CS Adams, SG Cox, PF Griffin, DA Smith, and IG Hughes. Polarization spectroscopy of a closed atomic transition: applications to laser frequency locking. Journal of Physics B: Atomic, Molecular and Optical Physics, 35(24):5141, 2002.

[123] T. P. Purdy, R. W. Peterson, and C. A. Regal. Observation of radiation pressure shot noise on a macroscopic object. Science, 339(6121):801–804, 2013.

[124] E. L. Raab, M. Prentiss, Alex Cable, Steven Chu, and D. E. Pritchard. Trapping of neutral sodium atoms with radiation pressure. Phys. Rev. Lett., 59:2631–2634, Dec 1987.

[125] A. G. Radnaev, Y. O. Dudin, R. Zhao, H. H. Jen, S. D. Jenkins, A. Kuzmich, and T. A. B. Kennedy. A quantum memory with telecom-wavelength conversion. Nat. Phys., 6(11):894–899, November 2010.

[126] Norman F. Ramsey. A molecular beam resonance method with separated oscillating fields. Phys. Rev., 78:695–699, Jun 1950.

[127] Norman F. Ramsey. Experiments with separated oscillatory fields and hydrogen masers. Rev. Mod. Phys., 62:541–552, Jul 1990.

[128] B. C. Regan, Eugene D. Commins, Christian J. Schmidt, and David DeMille. New limit on the electron electric dipole moment. Phys. Rev. Lett., 88:071805, Feb 2002.

[129] Mark Riebe, H Häffner, CF Roos, W Hänsel, J Benhelm, GPT Lancaster, TW Körber, C Becher, F Schmidt-Kaler, DFV James, et al. Deterministic quantum teleportation with atoms. Nature, 429(6993):734–737, 2004.

[130] M.F. Riedel, P. Böhi, Y. Li, T.W. Hänsch, A. Sinatra, and P. Treutlein. Atom-chip-based generation of entanglement for quantum metrology. Nature, 464(7292):1170–1173, 2010.

[131] D Ristè, M Dukalski, CA Watson, G de Lange, MJ Tiggelman, Ya M Blanter, KW Lehnert, RN Schouten, and L DiCarlo. Deterministic entanglement of superconducting qubits by parity measurement and feedback. arXiv:1306.4002[accepted to Nature], 2013.

[132] T. Rosenband, D. B. Hume, P. O. Schmidt, C. W. Chou, A. Brusch, L. Lorini, W. H. Oskay, R. E. Drullinger, T. M. Fortier, J. E. Stalnaker, S. A. Diddams, W. C. Swann, N. R. Newbury, W. M. Itano, D. J. Wineland, and J. C. Bergquist. Frequency ratio of al+ and hg+ single-ion optical clocks; metrology at the 17th decimal place. Science, 319(5871):1808–1812, 2008.

[133] J. Rutman. Characterization of phase and frequency instabilities in precision frequency sources: fifteen years of progress. Proc. IEEE, 66(9):1048–1075, 1978.

[134] M. Saffman, D. Oblak, J. Appel, and E. S. Polzik. Spin squeezing of atomic ensembles by multicolor quantum nondemolition measurements. Phys. Rev. A, 79:023831, Feb 2009.

[135] Robin Santra, Ennio Arimondo, Tetsuya Ido, Chris H. Greene, and Jun Ye. High-accuracy optical clock via three-level coherence in neutral bosonic $^{88}$sr. Phys. Rev. Lett., 94:173002–173005, May 2005.

[136] A. L. Schawlow and C. H. Townes. Infrared and optical masers. Phys. Rev., 112(6):1940–1949, Dec 1958.

[137] Michael Scheibner, Thomas Schmidt, Lukas Worschech, Alfred Forchel, Gerd Bacher, Thorsten Passow, and Detlef Hommel. Superradiance of quantum dots. Nature Physics, 3(2):106–110, 2007.

[138] Alexander Schilke, Claus Zimmermann, Philippe W. Courteille, and William Guerin. Optical parametric oscillation with distributed feedback in cold atoms. Nat. Photon., 6:101–104, 2012.

[139] Monika H. Schleier-Smith, Ian D. Leroux, and Vladan Vuletić. States of an ensemble of two-level atoms with reduced quantum uncertainty. Phys. Rev. Lett., 104:073604–073607, Feb 2010.

[140] Monika H. Schleier-Smith, Ian D. Leroux, Hao Zhang, Mackenzie A. Van Camp, and Vladan Vuletić. Optomechanical cavity cooling of an atomic ensemble. Phys. Rev. Lett., 107:143005, Sep 2011.

[141] R. J. Sewell, M. Koschorreck, M. Napolitano, B. Dubost, N. Behbood, and M. W. Mitchell. Magnetic sensitivity beyond the projection noise limit by spin squeezing. Phys. Rev. Lett., 109:253605, Dec 2012.

[142] Jon H. Shirley. Dynamics of a simple maser model. American Journal of Physics, 36(11):949–963, 1968.

[143] Anthony E. Siegman. Lasers. University Science Books, Sausalito, CA, first edition edition, May 1986.

[144] Anders S. Sørensen and Klaus Mølmer. Entanglement and extreme spin squeezing. Phys. Rev. Lett., 86:4431–4434, May 2001.

[145] Holger P. Specht, Christian Nlleke, Andreas Reiserer, Manuel Uphoff, Eden Figueroa, Stephan Ritter, and Gerhard Rempe. A single-atom quantum memory. Nature, 473:190193, 2011.

[146] H. Statz, G. A. DeMars, D. T. Wilson, and C. L. Tang. Problem of spike elimination in lasers. Journal of Applied Physics, 36(5):1510–1514, May 1965.

[147] Simon Stellmer, Benjamin Pasquiou, Rudolf Grimm, and Florian Schreck. Laser cooling to quantum degeneracy. Phys. Rev. Lett., 110:263003, Jun 2013.

[148] J. Stuhler, A. Griesmaier, T. Koch, M. Fattori, T. Pfau, S. Giovanazzi, P. Pedri, and L. Santos. Observation of dipole-dipole interaction in a degenerate quantum gas. Phys. Rev. Lett., 95:150406, Oct 2005.

[149] Haruka Tanji-Suzuki, Ian D. Leroux, Monika H. Schleier-Smith, Marko Cetina, Andrew T. Grier, Jonathan Simon, and Vladan Vuletić. Chapter 4 - interaction between atomic ensembles and optical resonators: Classical description. In P.R. Berman E. Arimondo and C.C. Lin, editors, Advances in Atomic, Molecular, and Optical Physics, volume 60 of Advances In Atomic, Molecular, and Optical Physics, pages 201 – 237. Academic Press, 2011.

[150] Michael A Taylor, Jiri Janousek, Vincent Daria, Joachim Knittel, Boris Hage, Hans-A Bachor, and Warwick P Bowen. Sub-diffraction limited quantum imaging of a living cell. arXiv preprint arXiv:1305.1353, 2013.

[151] Agilent Technologies. Low Cost Frequency Multipliers Using Surface Mount PIN Diodes: Application Note 1054. http://literature.agilent.com/litweb/pdf/5966-4998E.pdf.

[152] Igor Teper, Geert Vrijsen, Jongmin Lee, and Mark A. Kasevich. Backaction noise produced via cavity-aided nondemolition measurement of an atomic clock state. Phys. Rev. A, 78:051803, Nov 2008.

[153] Th. Udem, R. Holzwarth, and T. W. Hänsch. Optical frequency metrology. Nature, 416(6877):233–237, 2002.

[154] M. A. van Eijkelenborg, M. P. van Exter, and J. P. Woerdman. Threshold characteristics and intensity fluctuations of lasers with excess quantum noise. Phys. Rev. A, 57:571–579, Jan 1998.

[155] Jürgen Volz, Roger Gehr, Guilhem Dubois, Jérôme Estève, and Jakob Reichel. Measurement of the internal state of a single atom without energy exchange. Nature, 475(7355):210–213, 2011.

[156] Geert Vrijsen, Onur Hosten, Jongmin Lee, Simon Bernon, and Mark A. Kasevich. Raman lasing with a cold atom gain medium in a high-finesse optical cavity. Phys. Rev. Lett., 107(6):063904, Aug 2011.

[157] J. K. Wahlstrand, J. T. Willits, T. R. Schibli, C. R. Menyuk, and S. T. Cundiff. Quantitative measurement of timing and phase dynamics in a mode-locked laser. Opt. Lett., 32(23):3426–3428, Dec 2007.

[158] Hai Wang, D. J. Goorskey, W. H. Burkett, and Min Xiao. Cavity-linewidth narrowing by means of electromagnetically induced transparency. Opt. Lett., 25(23):1732–1734, Dec 2000.

[159] W. Wasilewski, K. Jensen, H. Krauter, J. J. Renema, M. V. Balabas, and E. S. Polzik. Quantum noise limited and entanglement-assisted magnetometry. Phys. Rev. Lett., 104:133601, Mar 2010.

[160] Joshua M. Weiner, Kevin C. Cox, Justin G. Bohnet, Zilong Chen, and James K. Thompson. Superradiant raman laser magnetometer. Appl. Phys. Lett., 101(26):261107, 2012.

[161] C. O. Weiss, N. B. Abraham, and U. Hübner. Homoclinic and heteroclinic chaos in a single-mode laser. Phys. Rev. Lett., 61:1587–1590, Oct 1988.

[162] C. O. Weiss and J. Brock. Evidence for lorenz-type chaos in a laser. Phys. Rev. Lett., 57:2804–2806, Dec 1986.

[163] Philip Westergaard, Jérôme Lodewyck, and Pierre Lemonde. Minimizing the dick effect in an optical lattice clock. IEEE Trans. Ultr. Ferr. Freq. Cont., 57(3):623–628, March 2010.

[164] DJ Wineland, JJ Bollinger, WM Itano, and FL Moore. Spin squeezing and reduced quantum noise in spectroscopy. Phys. Rev. A, 46(11):R6797–R6800, 1992.

[165] R Wynands and S Weyers. Atomic fountain clocks. Metrologia, 42(3):S64, 2005.

[166] Minghui Xu, DA Tieri, EC Fine, James K Thompson, and MJ Holland. Quantum synchronization of two ensembles of atoms. arXiv preprint arXiv:1307.5891, 2013.

[167] André Xuereb, Claudiu Genes, and Aurélien Dantan. Strong coupling and long-range collective interactions in optomechanical arrays. Phys. Rev. Lett., 109:223601, Nov 2012.

[168] Bo Yan, Steven A Moses, Bryce Gadway, Jacob P Covey, Kaden RA Hazzard, Ana Maria Rey, Deborah S Jin, and Jun Ye. Observation of dipolar spin-exchange interactions with lattice-confined polar molecules. Nature, 501:521 – 525, 2013.

[169] Paul Zarchan and Howard Musoff. Fundamentals of Kalman filtering: a Practical Approach. Amer Inst of Aeronautics &, February 2001.

[170] Hao Zhang, Robert McConnell, Senka Ćuk, Qian Lin, Monika H. Schleier-Smith, Ian D. Leroux, and Vladan Vuletić. Collective state measurement of mesoscopic ensembles with single-atom resolution. Phys. Rev. Lett., 109:133603, Sep 2012.

# Appendix A

## Details of Raman laser model

### A.1 Adiabatic Elimination of the Optically Excited State

Here we explicitly derive the adiabatic elimination of an intermediate, optically excited state of a cold atom Raman laser described in Sec. 4.2 and Fig. 4.6. The result is a system of equations describing the laser, Eqns. 4.26-4.28.

The Louivillian $\mathcal{L}[\hat{\rho}] = \mathcal{L}_c[\hat{\rho}] + \mathcal{L}_{ik}[\hat{\rho}] + \mathcal{L}_{ge}[\hat{\rho}]$ includes the cavity decay term $\mathcal{L}_c[\hat{\rho}]$, the spontaneous emission terms from state |i⟩

$$\mathcal{L}_{ik}[\hat{\rho}] = -\frac{\Gamma}{2}\sum_{q=1}^{N}\sum_{k=e,g}(\hat{\sigma}_{ik}^{(q)}\hat{\sigma}_{ki}^{(q)}\hat{\rho} + \hat{\rho}\hat{\sigma}_{ik}^{(q)}\hat{\sigma}_{ki}^{(q)} - 2\hat{\sigma}_{ki}^{(q)}\hat{\rho}\hat{\sigma}_{ik}^{(q)}), \tag{A.1}$$

and an incoherent repumping term that looks like spontaneous decay from $|g\rangle$ to $|e\rangle$

$$\mathcal{L}_{ge}[\hat{\rho}] = -\frac{W}{2}\sum_{q=1}^{N}(\hat{\sigma}_{ge}^{(q)}\hat{\sigma}_{eg}^{(q)}\hat{\rho} + \hat{\rho}\hat{\sigma}_{ge}^{(q)}\hat{\sigma}_{eg}^{(q)} - 2\hat{\sigma}_{eg}^{(q)}\hat{\rho}\hat{\sigma}_{ge}^{(q)}). \tag{A.2}$$

As in Sec. 4.1, we assume we are able to factorize the expectation values $\langle\hat{c}\hat{\sigma}_{ie}\rangle = \mathcal{C}\sigma_{ie}$, $\langle\hat{c}\hat{\sigma}_{ii}\rangle = \mathcal{C}\sigma_{ii}$, $\langle\hat{c}\hat{\sigma}_{gg}\rangle = \mathcal{C}\sigma_{gg}$, $\langle\hat{c}\hat{\sigma}_{eg}\rangle = \mathcal{C}\sigma_{eg}$, $\langle\hat{c}\hat{\sigma}_{ig}\rangle = \mathcal{C}\sigma_{ig}$, and $\langle\hat{c}\hat{\sigma}_{ie}\rangle = \mathcal{C}\sigma_{ie}$.

Applying these assumptions to the master equation results in the equations of motion

$$\dot{\mathcal{C}} = -\,(\kappa/2 + i\omega_c)\mathcal{C} - igJ_{gi} \tag{A.3}$$

$$\dot{J}_{ge} = -\,(W/2 + i\omega_{eg})J_{ge} - i\frac{\Omega_d}{2}e^{i\omega_d t}J_{gi} + ig\mathcal{C}J_{ie} \tag{A.4}$$

$$\begin{aligned} \dot{J}_{gi} =& -\left(\frac{\Gamma + W}{2} + i\omega_{ig}\right)J_{gi} \\ & - i\frac{\Omega_d}{2}e^{-i\omega_d t}J_{ge} + ig\mathcal{C}(N_i - N_g) \end{aligned} \tag{A.5}$$

$$\begin{aligned} \dot{J}_{ei} =& -\left(\frac{\Gamma + W}{2} + i\omega_{ie}\right)J_{ei} \\ & + i\frac{\Omega_d}{2}e^{-i\omega_d t}(N_i - N_e) - ig\mathcal{C}J_{eg} \end{aligned} \tag{A.6}$$

$$\begin{aligned} \dot{J}_z =& \frac{1}{2}(\dot{N}_e - \dot{N}_g) = W(N/2 - J_z) \\ & - i\frac{\Omega_d}{2}(\sigma_{ei}e^{i\omega_d t} - J_{ie}e^{-i\omega_d t}) + ig(\mathcal{C}^* J_{gi} - \mathcal{C}J_{ig}). \end{aligned} \tag{A.7}$$

Here we identity the relevant transverse atomic decay rate $\gamma_\perp = W/2$.

The equation for $\dot{J}_z$ assumes only a negligible fraction of the atomic ensemble resides in $|\mathrm{i}\rangle$, an assumption we justify shortly. For convenience, we go into a rotating frame (often called the natural frame [27]) defined by the transformation of variables:

$$\tilde{\mathcal{C}} = \mathcal{C}e^{i\omega_c t} \tag{A.8}$$

$$\tilde{J}_{ge} = J_{ge}e^{i\omega_{eg} t} \tag{A.9}$$

$$\tilde{J}_{gi} = J_{gi}e^{i(\omega_c + \delta_0/2)t} \tag{A.10}$$

$$\tilde{J}_{ei} = J_{ei}e^{i(\omega_d - \delta_0/2)t} \tag{A.11}$$

$$\tag{A.12}$$

where $\delta_0$ is the two-photon detuning $\delta_0 = \omega_d - \omega_c + \omega_{eg}$. With these substitutions, Eqns. A.3 - A.7 become

$$\dot{\tilde{\mathcal{C}}} = -(\kappa/2)\tilde{\mathcal{C}} - ig\tilde{J}_{gi}e^{-i\delta_0 t/2} \tag{A.13}$$

$$\dot{\tilde{J}}_{ge} = -\gamma_\perp \tilde{J}_{ge} - i\frac{\Omega_d}{2}e^{i\delta_0 t/2}\tilde{J}_{gi} + ig\tilde{\mathcal{C}}\tilde{J}_{ie}e^{i\delta_0 t/2} \tag{A.14}$$

$$\begin{aligned}\dot{\tilde{J}}_{gi} =&(i\Delta - \frac{\Gamma + W}{2})\tilde{J}_{gi} - i\frac{\Omega_d}{2}e^{-i\delta_0 t/2}\tilde{J}_{ge}\\ &+ ig\tilde{\mathcal{C}}e^{i\delta_0 t/2}(N_i - N_g)\end{aligned} \tag{A.15}$$

$$\begin{aligned}\dot{\tilde{J}}_{ei} =&(i\Delta - \frac{\Gamma + W}{2})\tilde{J}_{ei} + i\frac{\Omega_d}{2}e^{-i\delta_0 t/2}(N_i - N_e)\\ &- ig\tilde{\mathcal{C}}e^{i\delta_0 t/2}\tilde{J}_{eg}\end{aligned} \tag{A.16}$$

$$\begin{aligned}\dot{J}_z =&W(N/2 - J_z) - i\frac{\Omega_d}{2}(\tilde{J}_{ei}e^{i\delta_0 t/2} - \tilde{J}_{ie}e^{-i\delta_0 t/2})\\ &+ ig(\tilde{\mathcal{C}}^*\tilde{J}_{gi}e^{-i\delta_0 t/2} - \tilde{\mathcal{C}}\tilde{J}_{ig}e^{i\delta_0 t/2})\end{aligned} \tag{A.17}$$

Here $\Delta = \Delta_d + (\delta_0/2)$ is also equivalent to the average detuning of the Raman dressing laser $\Delta_d$ and the cavity mode $\Delta_c$ from their respective optical atomic transitions.

To reduce these equations to those of an effective two-level system coupled to a cavity field, we assume that we can adiabatically eliminate the collective coherences $\tilde{J}_{gi}, \tilde{J}_{ei}$ and that the population of the intermediate state is small $N_i \ll N_g,\ N_e$. These assumptions are justified due to large detuning $\Delta \gg \Gamma, \gamma_\perp, \delta_0$. The adiabatic elimination of the coherence proceeds as follows [27]: by examining the form of the equations for $\dot{\tilde{J}}_{gi}$ and $\dot{\tilde{J}}_{ei}$, we expect that each one can be written as the sum of a term rapidly oscillating at frequency $\Delta$, and a term varying on the timescale of the population dynamics, much more slowly than $1/\Delta$. By averaging over a timescale long compared to the rapid oscillation, but short compared to the population dynamics, we essentially perform a coarse graining approximation and are left with only slowly varying terms. The derivatives of these coarse-grained collective amplitudes are negligible. Here we consider small fluctuations about steady-state values at frequency $\omega$, so the approximation will be valid when $\Delta \gg \omega$. Thus, to a good approximation for the cases considered here, the derivatives $\dot{\tilde{J}}_{gi}, \dot{\tilde{J}}_{ei}$ can be set to zero. We then solve for $\tilde{J}_{gi}$ and $\tilde{J}_{ei}$ as

$$\tilde{J}_{gi} \approx \frac{\Omega_d}{2\Delta}e^{-i\delta_0 t/2}\tilde{J}_{ge} + \frac{g}{\Delta}e^{i\delta_0 t/2}\tilde{\mathcal{C}}N_g \tag{A.18}$$

$$\tilde{J}_{ei} \approx \frac{\Omega_d}{2\Delta}e^{i\delta_0 t/2}N_e + \frac{g}{\Delta}e^{-i\delta_0 t/2}\tilde{\mathcal{C}}\tilde{J}_{eg} \tag{A.19}$$

where we have approximated $i\Delta + \frac{\Gamma+W}{2} \approx i\Delta$. After including these simplifications and transforming back to the original frame, we arrive at Eqns. 4.26-4.28 in the main text.

## A.2 Steady-state Emission Frequency of the Raman Laser

We find the steady-state cold atom Raman laser frequency from Sec. 4.2 by assuming the laser is oscillating at frequency $\omega_\gamma$, so $\mathcal{C} = \breve{\mathcal{C}} e^{-i\omega_\gamma t}$ and $J_{eg} = \breve{J}_{eg} e^{-i(\omega_\gamma - \omega_d)t}$. Substituting in Eqns. 4.26 - 4.28 gives

$$\dot{\breve{\mathcal{C}}} = (-\kappa/2 - i\delta)\breve{\mathcal{C}} - ig_2 \breve{J}_{ge} \tag{A.20}$$

$$\dot{\breve{J}}_{ge} = \left(-\gamma_\perp - i(\omega_{eg} - \omega_{ac} + \omega_d - \omega_\gamma)\right) \breve{J}_{ge} + i2g_2 J_z \breve{\mathcal{C}} \tag{A.21}$$

$$\dot{J}_z = W(N/2 - J_z) + ig_2(\breve{\mathcal{C}}^* \breve{J}_{ge} - \breve{\mathcal{C}} \breve{J}_{eg}) \tag{A.22}$$

where $\delta$ is the detuning of the emission frequency from the dressed cavity mode

$$\delta = \omega_D - \omega_\gamma \ . \tag{A.23}$$

The steady-state emission frequency $\omega_\gamma$ is constrained by the condition that $J_z$ must be real, and following the procedure in Sec. 4.1, we arrive at the the laser oscillation frequency

$$\omega_\gamma = \frac{2\gamma_\perp}{2\gamma_\perp + \kappa}\omega_D + \frac{\kappa}{2\gamma_\perp + \kappa}(\omega_{eg} + \omega_d - \omega_{ac}) \ . \tag{A.24}$$

Note the insensitivity of the oscillation frequency to changes in the cavity frequency in the bad-cavity limit where $\kappa \gg W = 2\gamma_\perp$.

# Appendix B

## Detailed Equations for $^{87}$Rb Model

### B.1 Repumping Scheme

We begin the description of our model for a cold atom laser in $^{87}$Rb with the details of the repumping process. The equations to describe the repumping are arrived at after adiabatic elimination of the optically excited states $\left|5^2P_{3/2}, F' = 2, m_F\right\rangle$ through which the Raman transitions for repumping are driven. However, unlike in the Sec. 4.2, the scattered photons lack a resonant cavity mode, so the scattering is presumed to be primarily into free space (i.e. non-cavity) modes.

The relevant set of Rabi frequencies describing the resonant repumper laser coupling the ground state $\left|5^2S_{1/2}, F, m_F\right\rangle$ state to an optically excited state $\left|5^2P_{3/2}, F' = 2, m'_F\right\rangle$ is given by the dipole matrix element between the states as

$$\Omega_{F,m_F,2,m'_F} = \left|\left\langle 5^2P_{3/2}, 2, m_F\right| \vec{d} \cdot \vec{E}_F \left|5^2S_{1/2}, F, m_F\right\rangle\right| /\hbar \tag{B.1}$$

where $\vec{d}$ is the atomic dipole moment operator and the electric field of the two repumping lasers are $\vec{E}_1$ and $\vec{E}_2$. If an atom is in the excited state $\left|5^2P_{3/2}, F' = 2, m'_F\right\rangle$ then it spontaneously decays to the ground state $\left|5^2S_{1/2}, F, m_F\right\rangle$ with fractional probability given by the branching ratio

$$B_{F,m_F,F',m'_F} = \left|\langle F\, m_f | F'\, 1\, m'_f\, p\rangle\right|^2 \ , \tag{B.2}$$

where $p$ labels the polarization of the emitted light ($\sigma^+ = -1, \pi = 0, \sigma^- = +1$ and $\sum_{F,m_F} B_{F,m_F,F',m'_F} = 1$.

The repumping rate $W'$ in our model is calculated as the resonant, unsaturated scattering rate

$$W' = \frac{\Omega^2_{1,0,2,0}}{2\Gamma_{D2}}(1 - B_{1,0,2,0}) \tag{B.3}$$

where $\Gamma_{D2}$ is the D2 excited state decay rate $\Gamma_{D2}/2\pi = 6.07$ MHz. Note that the rate $W'$ is the scattering rate out of the ground state, and does not include Rayleigh scattering into free space $\Gamma_R = \frac{\Omega^2_{1,0,2,0}}{2\Gamma} B_{1,0,2,0}$ which causes the scattering atom to collapse into $|g\rangle$ due the optically thin nature of the atomic ensemble along nearly all directions other than the cavity mode. Since $\Gamma_R$ scales with $\frac{\Omega^2_{1,0,2,0}}{2\Gamma}$ as does $W'$, we will group both together into a single rate $W = \frac{\Omega^2_{1,0,2,0}}{2\Gamma_{D2}}$, and distinguish the two rates with branching ratios in our equations for the population equations.

## B.2 Reduced Optical Bloch Equations

Including the coherent dynamics of the effective two-level system adds the coherence $J_\perp^2$ driving the population from $|e\rangle$ to $|g\rangle$ as was seen in Sec. 4.2, Eqn. 4.35

$$\dot{N}_{e,g} = \mp \frac{C\gamma}{1 + \delta'^2} J_\perp^2 \ . \tag{B.4}$$

Here $\delta'$ is the detuning of the dressed cavity mode from the emitted light frequency, normalized by $\kappa/2$, as in Eqn. A.23. In the subsequent equations, we neglect the single particle scattering from $|e\rangle$ to $|g\rangle$ at rate $\gamma$ as it is much less than the collective emission rate.

With these terms, we can write the reduced optical Bloch equations for the the ground state populations as

$$\frac{\mathrm{d}N_{F,m_F}}{\mathrm{d}t} = \frac{W}{\Omega^2_{1,0,2,0}} \sum_{F'=1}^{2} \sum_{m'_F=-F'}^{F'} \left( B_{F,m_F,2,m'_F} - \delta_{F,F'}, \delta_{m_F,m'_F} \right) \Omega^2_{F',m'_F,2,m'_F} N_{F',m'_F} \tag{B.5}$$

$$+ \frac{C\gamma}{1 + \delta'^2} J_\perp^2 \left( \delta_{F,1}, \delta_{m_F,0} - \delta_{F,2}, \delta_{m_F,0} \right) \tag{B.6}$$

where $\delta_{F,F'}$ is the Kronecker delta function. The sums have been reduced using the assumption that the repumping light is $\pi$-polarized.

We also must include the equation for the coherence, driven by the population inversion

$$\dot{J}_{\perp}^{2} = -W\, J_{\perp}^{2} + \frac{C\gamma}{1+\delta'^{2}}(N_{2,0} - N_{1,0})J_{\perp}^{2} \tag{B.7}$$

which is analogous to Eqn. 4.34 in Sec. 4.2, except that here $W$ is the sum of the ground state repumping rate and the Rayleigh scattering rate, where $W$ in Eqn. 4.34 contains only the ground state repumping rate.

Including the equation for the coherence, along with the terms for the effects of collective emission, the resulting equations evaluated for $^{87}$Rb can be compactly expressed as

$$\frac{\mathrm{d}}{\mathrm{d}t}\vec{V} = (M_{cav} + M_{W} + M_{rW})\,\vec{V} \tag{B.8}$$

with the column vector given by

$$\vec{V} = \begin{pmatrix} N_{2,2} \\ N_{2,1} \\ N_{e} \\ N_{2,-1} \\ N_{2,-2} \\ N_{1,1} \\ N_{g} \\ N_{1,-1} \\ J_{\perp}^{2} \end{pmatrix} \tag{B.9}$$

where $N_e = N_{2,0}$ and $N_g = N_{1,0}$ are specially labeled to indicate their importance as the lasing levels.

The matrices governing the time evolution are separated into the evolution governed by the collective coupling to the cavity

$$M_{cav} = \frac{C\gamma}{1+\delta'^2} \begin{pmatrix} 0 & 0 & 0 & 0 & 0 & 0 & 0 & 0 & 0 \\ 0 & 0 & 0 & 0 & 0 & 0 & 0 & 0 & 0 \\ 0 & 0 & 0 & 0 & 0 & 0 & 0 & 0 & -1 \\ 0 & 0 & 0 & 0 & 0 & 0 & 0 & 0 & 0 \\ 0 & 0 & 0 & 0 & 0 & 0 & 0 & 0 & 0 \\ 0 & 0 & 0 & 0 & 0 & 0 & 0 & 0 & 0 \\ 0 & 0 & 0 & 0 & 0 & 0 & 0 & 0 & 1 \\ 0 & 0 & 0 & 0 & 0 & 0 & 0 & 0 & 0 \\ 0 & 0 & J_\perp^2 & 0 & 0 & 0 & -J_\perp^2 & 0 & 0 \end{pmatrix}, \tag{B.10}$$

the repumping of atoms in $F = 1$

$$M_W = W \begin{pmatrix} 0 & 0 & 0 & 0 & 0 & \frac{1}{8} & 0 & 0 & 0 \\ 0 & 0 & 0 & 0 & 0 & \frac{1}{16} & \frac{1}{4} & 0 & 0 \\ 0 & 0 & 0 & 0 & 0 & \frac{3}{16} & 0 & \frac{3}{16} & 0 \\ 0 & 0 & 0 & 0 & 0 & 0 & \frac{1}{4} & \frac{1}{16} & 0 \\ 0 & 0 & 0 & 0 & 0 & 0 & 0 & \frac{1}{8} & 0 \\ 0 & 0 & 0 & 0 & 0 & -\frac{9}{16} & \frac{1}{12} & 0 & 0 \\ 0 & 0 & 0 & 0 & 0 & \frac{3}{16} & -\frac{2}{3} & \frac{3}{16} & 0 \\ 0 & 0 & 0 & 0 & 0 & 0 & \frac{1}{12} & -\frac{9}{16} & 0 \\ 0 & 0 & 0 & 0 & 0 & 0 & 0 & 0 & -1 \end{pmatrix}, \tag{B.11}$$

and the repumping of atoms in $F = 2$

$$M_{rW} = rW \begin{pmatrix} -\frac{8}{3} & \frac{1}{6} & 0 & 0 & 0 & 0 & 0 & 0 & 0 \\ \frac{2}{3} & -\frac{11}{12} & 0 & 0 & 0 & 0 & 0 & 0 & 0 \\ 0 & \frac{1}{4} & 0 & \frac{1}{4} & 0 & 0 & 0 & 0 & 0 \\ 0 & 0 & 0 & -\frac{11}{12} & \frac{2}{3} & 0 & 0 & 0 & 0 \\ 0 & 0 & 0 & \frac{1}{6} & -\frac{8}{3} & 0 & 0 & 0 & 0 \\ 2 & \frac{1}{4} & 0 & 0 & 0 & 0 & 0 & 0 & 0 \\ 0 & \frac{1}{4} & 0 & \frac{1}{4} & 0 & 0 & 0 & 0 & 0 \\ 0 & 0 & 0 & \frac{1}{4} & 2 & 0 & 0 & 0 & 0 \\ 0 & 0 & 0 & 0 & 0 & 0 & 0 & 0 & 0 \end{pmatrix} . \tag{B.12}$$

The repumping rates induced by the F2 repumper are parameterized by repumping ratio $r$ as

$$r = \frac{\Omega^2_{2,1,2,1}}{\Omega^2_{1,0,2,0}} . \tag{B.13}$$

The normalized detuning $\delta'$ of the dressed cavity resonant frequency with the emitted light frequency $\omega_\gamma$ carries implicit dependence on the populations $N_{F,m_F}$ as derived in Sec. 4.2

$$\delta' = 2 \left( \omega_c + \vec{\alpha} \cdot \vec{V} - \omega_\gamma \right) / \kappa . \tag{B.14}$$

The elements of the single-atom cavity tuning vector $\vec{\alpha}$ comes from the cavity dressing as derived from Eqn. 4.32. There we see $\vec{\alpha}$ is set by the detuning of the cavity frequency and the detuning from the atomic transition frequencies $\omega_{F,F'}$ between the ground $\left|5^2S_{1/2}, F\right\rangle$ states and optically excited states $\left|5^2P_{1/2}, F'\right\rangle$ as

$$\alpha_{F,m_F} = \sum_{F'=1}^{2} \frac{(2g_{F,m_F,F',m_F+p})^2}{4(\omega_{bcav} - \omega_{F,F'})} \tag{B.15}$$

where $p = \pm 1$ for the $\sigma^\pm$ polarized cavity mode, and the single-particle vacuum Rabi frequencies are evaluated for each transition. For the quantization axis along the cavity axis, the $\sigma^+$ and $\sigma^-$ polarizations modes will shift in frequency by different amounts specified by two vectors $\vec{\alpha}_\pm$. However, the symmetry of the atomic population equations ensure that the populations are symmetric such that $N_{F,m_F} = N_{F,-m_F}$. Thus, only the shift of the $\sigma^+$ cavity mode needs to be considered. We use the dressing laser detuning $\Delta = +1.1$ GHz as was present in Refs. [24, 21]. The resulting cavity tuning vector is

$$\vec{\alpha}_+ = 2\pi(33.8\ \text{Hz}) \begin{pmatrix} 0 \\ 0.0776 \\ 0.1515 \\ 0.222 \\ 0.289 \\ 1.679 \\ 1 \\ 0.440 \\ 0 \end{pmatrix} . \tag{B.16}$$

We find the steady-state solutions to the system of equations by setting $\mathrm{d}\vec{V}/\mathrm{d}t = 0$ and solving for $\vec{V}$. From the results, we can for the expressions for $\bar{J}_\perp^2$, $\bar{J}_z$, and $\bar{N}_{other}$ in the main text.

# Appendix C

## Full Expressions for the Three-level Model Linear Response Theory

The full expressions for the coefficients in the three-level response equations Eqns. 6.4 and 6.5:

$$\gamma_0 = \frac{r}{2\zeta}\Big( (2N\Gamma_c - 2\gamma_\perp) + 2Wr - \Gamma_R + h(\delta)(4\gamma_\perp + W(1+2r))\Big) \tag{C.1}$$

$$\omega_0^2 = \frac{-r(1+2r)W}{\zeta}\Big( (2\gamma_\perp - N\Gamma_c) - 2\gamma_\perp h(\delta)\Big) \tag{C.2}$$

$$\beta = \frac{(1+2r)}{W\zeta} \tag{C.3}$$

where the denominator factor $\zeta = 2rh(\delta) + (1+r)(1+2r)$ and $h(\delta) = 2\alpha\delta\left(\frac{N}{1+\delta^2} - \frac{2\gamma_\perp}{C\gamma}\right)$.

The drive terms are

$$D_{\perp,z}(\omega) = D_{0,\perp,z} + i\omega D_{1,\perp,z} - \omega^2 D_{2,\perp,z} \tag{C.4}$$

where the coefficients are

$$D_{0,\perp} = \frac{-r(1+2r)W}{2\zeta}\left(W + 2\gamma_\perp - N\Gamma_c - \Gamma_R h(\delta)\right) \tag{C.5}$$

$$D_{1,\perp} = -\frac{W(1+r)(1+2r) + 2r\left(2\gamma_\perp - N\Gamma_c - \Gamma_R h(\delta)\right)/2}{2\zeta} \tag{C.6}$$

$$D_{2,\perp} = -\frac{1+2r}{2\zeta} \tag{C.7}$$

$$D_{0,z} = \left(\frac{W}{2\gamma_\perp}\right)\frac{r(1+2r)W(N\Gamma_c - 2\gamma_\perp)}{\zeta} \tag{C.8}$$

$$D_{1,z} = \left(\frac{W}{2\gamma_\perp}\right)\frac{r(3+2r)(N\Gamma_c - 2\gamma_\perp)}{\zeta} \tag{C.9}$$

$$D_{2,z} = \left(\frac{-2r}{2\gamma_\perp}\right)\frac{N\Gamma_c - 2\gamma_\perp}{\zeta} \tag{C.10}$$

## C.1 Interesting Limiting Cases

Perfect repumping, on resonance:

$$\omega_0^2 = W(NC\gamma - 2\gamma_\perp) \tag{C.11}$$

$$\gamma_0 = W/2 \tag{C.12}$$

$$\beta = 0 \tag{C.13}$$

$$D_\perp(\omega) = \frac{W}{2}(NC\gamma - W - 2\gamma_\perp - i\omega) \tag{C.14}$$

$$D_z(\omega) = \left(\frac{W}{2\gamma_\perp}\right)(NC\gamma - 2\gamma_\perp)(W + i\omega) \tag{C.15}$$

Perfect repumping, with detuning:

$$\omega_0^2 = W\left(N\Gamma_c - 2\gamma_\perp\right)\left(1 + 2\alpha\delta\frac{2\gamma_\perp}{C\gamma}\right) \tag{C.16}$$

$$\gamma_0 = \frac{W}{2}\left(1 + h(\delta)\right) \tag{C.17}$$

$$\beta = 0 \tag{C.18}$$

$$D_\perp(\omega) = \frac{W}{2}\left(N\Gamma_c - W - 2\gamma_\perp - \Gamma_R h(\delta) - i\omega\right) \tag{C.19}$$

$$D_z(\omega) = \left(\frac{W}{2\gamma_\perp}\right)(N\Gamma_c - 2\gamma_\perp)(W + i\omega) \tag{C.20}$$

Imperfect repumping, on resonance:

$$\omega_0^2 = \left(\frac{r}{1+r}\right) W\left(N\Gamma_c - 2\gamma_\perp\right) \tag{C.21}$$

$$\gamma_0 = \left(\frac{r}{(1+r)(1+2r)}\right)(NC\gamma + (r+1/2)W - 2\gamma_\perp) \tag{C.22}$$

$$\beta = \frac{1}{W(1+r)} \tag{C.23}$$

$$\begin{aligned} D_\perp(\omega) = {} & \frac{\omega^2}{2(1+r)} \\ & + \frac{i\omega}{2}\left(\frac{2r}{(1+r)(1+2r)}(NC\gamma - 2\gamma_\perp) - W\right) \\ & + \frac{rW}{2(1+r)}(NC\gamma - 2\gamma_\perp - W) \end{aligned} \tag{C.24}$$

$$\begin{aligned} D_z(\omega) = {} & -\omega^2 \frac{2r(NC\gamma - 2\gamma_\perp)}{2\gamma_\perp(1+r)(1+2r)} \\ & + i\omega\left(\frac{W}{2\gamma_\perp}\right)\left(\frac{r(3+2r)(NC\gamma - 2\gamma_\perp)}{(1+r)(1+2r)}\right) \\ & + \left(\frac{W}{2\gamma_\perp}\right)(NC\gamma - 2\gamma_\perp) \end{aligned} \tag{C.25}$$

# Appendix D

## Heterodyne Photodiode

This circuit diagram contains the details of the photodiode circuit that provided most of the data in the thesis.

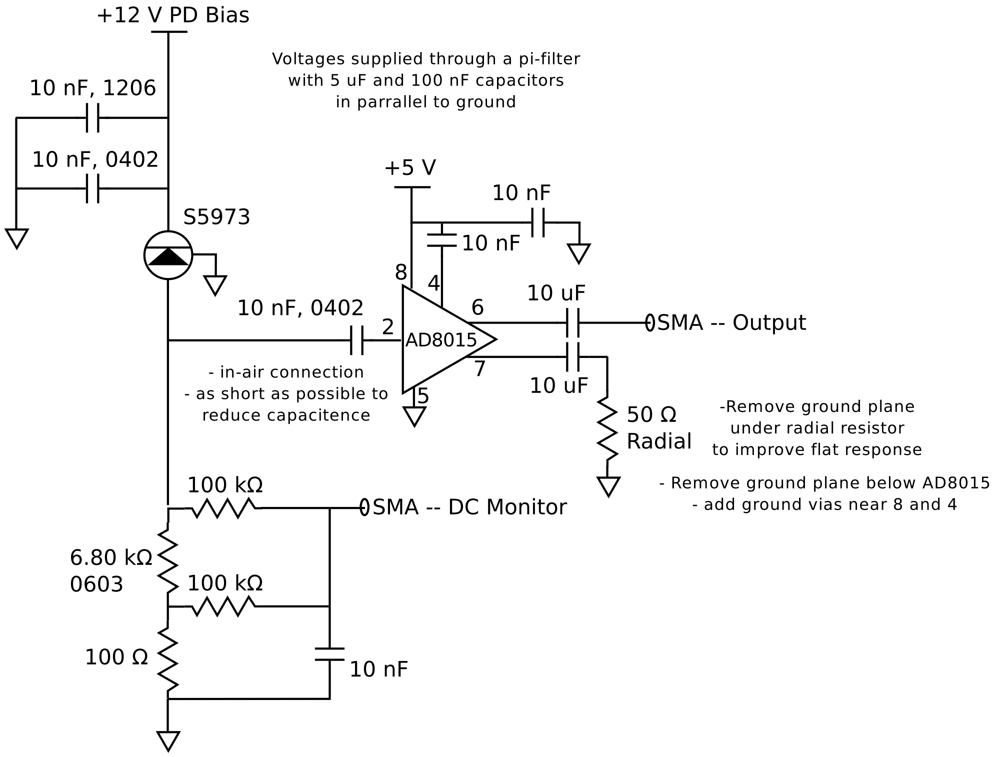

Figure D.1: A schematic of the transimpedance amplifier circuit for the Hamamatsu S5973 photodiode used as the Heterodyne detector in this thesis. Crucial notes about the circuit are noted in text on the schematic. The most important features for a photodiode with a flat gain response up to 200 MHz was robust connections to the ground plane, even adding additional ground connections near the AD8015 transimpedance amplifier. The noise properties of the circuit were also improved by making the capacitance up to the input of the AD8015 low with short, in-air connections from the S5973 output pin to the input of the AD8015. The circuit layout was designed by Terry Brown in the JILA Electronics Shop.